Magnetisation dynamics in magnetostrictive nanostructures

Stuart Robert Bowe

School of Physics and Astronomy
University of Nottingham

This dissertation is submitted for the degree of
Doctor of Philosophy

February 2017

Acknowledgements

First of all I would like to thank to my supervisors Dr. Andrew Rushforth and Dr. Stuart Cavill for their advice and guidance throughout my PhD. I would also like to extend my thanks to Dr. Peter Wadley for the x-rays and Dr Christopher Readon for the loan of his time and excellent e-beam machine. Further thank yous are due to Prof. Václav Holý for his X-ray analysis and Mr Christopher Love for his FMR measurements. I would also like to thank Dr. Francessco Maccherozzi for his help with experiments at the Diamond Light Source.

I would like to express gratitude to Jas Chauhan and David Taylor for their vital assistance in the micro-fabrication facility and Christopher Pallender for the copious supplies of liquid helium and nitrogen.

I would also like to extend a thank you to my colleagues Duncan Parkes for humouring my need to re-invent the wheel, Richard Cousins for humouring me with my bitcoin news and Vicky Hills for the general humour. Also Ryan Beardsley, who I definitely do not owe 'like 11 pints'. Unfortunately I cannot go into detail as to why all of my colleagues deserve my thanks in the space available however I would like to extend apologies and general thanks in no particular order to Mu Wang, Kyle Baldwin, Dan Moss, Steven Hardy, Dave Peat, James Thorpe, Debi Pattnaik, Karl Andrews, Caroline Poyser, Sarah Heywood, Michal Grzybowski, James Moss, Russell Vanhouse, Simon Svatek, Bryn Howells, Josh Whale, Bill York and Eduardo Mendive Tapia.

I would also like to thank Anna for putting up with me and finally thanks to my family, especially Gordon and Dougie for whatever it is they do and my parents for spawning me in the first place and supporting me throughout the years.

Abstract

Spin torque oscillator devices have presented themselves as an energy efficient method of generating microwave frequencies in recent years. These are devices which rely on giant magnetoresistance to create a device resistance which oscillates at microwave frequencies due to the microwave oscillation of a magnetically free layer in the device. A spin torque oscillator can be improved by using a vortex core oscillator as the magnetically free layer offering a narrower linewidth and greater synchronisation possibilities, at the expense of a lower power output. The desire to tune the frequency of oscillation of these devices has been the focus of a great deal of research in recent years and one promising avenue of investigation is to alter the frequency of oscillation by inducing a strain anisotropy in such a device by the use of a piezoelectric transducer. In order for the induced anisotropy to be large a material must be used which exhibits a strong magnetostrictive effect such as $Fe_{1-x}Ga_x$, a material which exhibits strong magnetostrictive properties without the need for rare earth elements.

This thesis describes investigations into the magnetisation dynamics of nanostructures fabricated from magnetostrictive thin films of $Fe_{1-x}Ga_x$ under conditions of in-plane uniaxial anisotropy induced by an applied stress.

Chapter 4 describes investigations into the effects of altering the thickness of sputter grown $Fe_{1-x}Ga_x$ films on the crystalline anisotropy of the films. It was found that the intrinsic magnetocrystalline uniaxial anisotropy within the films increased with film thickness. The cubic anisotropy was shown to be roughly constant with respect to film thickness except when the film was 20nm thick when the cubic anisotropy of the sample was anomalously high. Investigations of the magnetostrictive properties of these materials revealed sputter grown thin films to exhibit similar magnetostrictive properties as bulk material and thin films grown by molecular beam epitaxy. X-ray analysis performed by Dr. P. Wadley and Prof. V. Holy failed to explain the relationships between film thickness and magnetocrystaline anisotropy observed in the samples, but suggested that the average grain size increases as the thickness of the film increases.

Chapter 5 describes the results of time resolved XMCD PEEM measurements performed at the Diamond Light Source synchrotron facility performed in order to investigate the magnetisation dynamics within a series of $Fe_{1-x}Ga_x$ squares. It was found that these squares

demonstrated no significant response to an applied stress, probably due to strong shape anisotropy. Preliminary work to investigate Ni squares revealed that they do exhibit a strong response to stress. The dynamic response of the Ni squares was not successfully measured however.

Chapter 6 presents results of micromagnetic simulations performed to predict the effects of strain-induced anisotropy on magnetic square nanostructures fabricated from $Fe_{1-x}Ga_x$. Time resolved simulations demonstrated the ability of a strain induced anisotropy to modify the frequency of oscillation of the vortex core oscillations and the confined spin wave modes as well as the amplitude of the magnetic field pulse required to induce switching of the polarisation of the vortex core. The effects of size and uniaxial anisotropy on the spin wave modes within square devices was studied and an s shaped spin wave mode was shown to form in the presence of a uniaxial anisotropy.

Table of contents

Chapter 1

Introduction

The aim of this thesis is to present investigations into the use of strain induced anisotropy as a means to modify the properties of spintronic devices such as spin torque oscillators (STOs) and magnetic random access memory (MRAM) based on magnetostrictive materials. $Fe_{1-x}Ga_x$, a material which boasts a high magnetostriction constant and low cost of production, was the material of focus.

1.1 Introduction to spintronics

Nano-structured magnetic materials are the building blocks from which magnetic data storage systems are constructed. The discovery of Giant Magnetoresistance (GMR) [1] in such materials has led to the development of the first spintronic device, the spin-valve, and ensured rapid development of magnetic disc drive technology during the past decade. The spin valve consists of two ferromagnetic layers separated by a non magnetic metallic spacer, as shown in figure 1.1

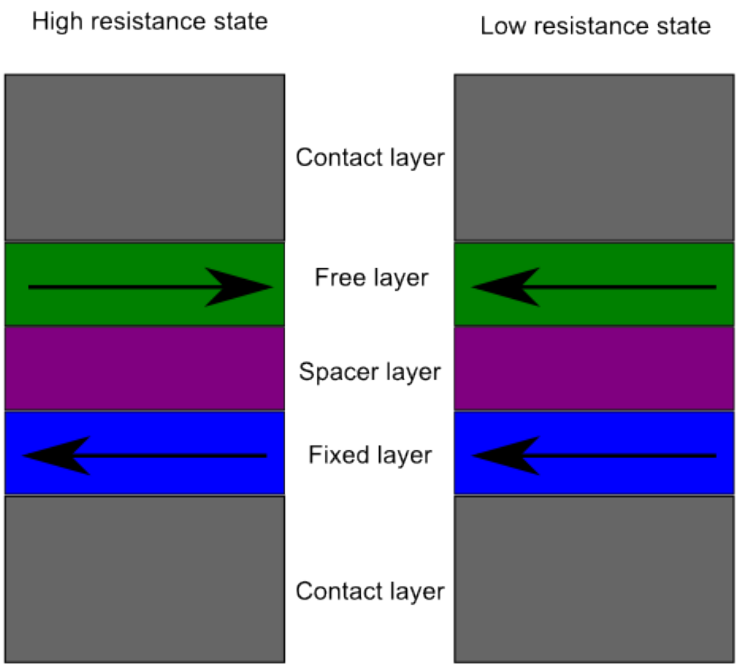

Fig. 1.1 Structure of a typical spin valve [2]. The layers on the top and bottom are contact layers used to connect the spin valve to an external current source. The magnetic free layer has a much lower coercivity than the fixed layer meaning the relative magnetisation of the two layers may be altered by an external magnetic field. The layers are separated by a non-magnetic spacer.

When the magnetisations in the ferromagnetic layers are aligned parallel (P), spin up electrons can pass easily from one layer to another leading to a low resistivity state. If adjacent layers have magnetisations aligned anti-parallel (AP), both spin up and spin down electrons are strongly scattered, and the resistance is high for all electrons. As the saturation /coercive fields of the two layers are different, an external field can switch one layer in isolation of the other, giving parallel or anti-parallel alignment of the magnetisation in the two layers. Thus the magnetic orientations determine low and high resistance states in GMR devices. Recent progress in these devices has concentrated on increasing the magnetoresistance amplitude needed for hard disc drive read sensors. These sensors suffer from signal limitations and added noise due to spin transfer torque induced instabilities [3]. Spin transfer torque (STT), an inverse effect of GMR, occurs for current flowing through two ferromagnetic layers separated by a thin non-magnetic spacer layer, such as in a GMR spin valve. The current becomes spin polarised by passing through the first ferromagnetic layer and interacts with the second ferromagnetic layer (the free layer) by exerting a spin torque on the magnetic moment

[4] . This STT can oppose the intrinsic damping of the free layer causing the magnetisation to precess and even reverse the direction of the magnetisation [5]. Whilst STT can have negative effects on GMR read heads it has important implications for spintronic device applications, such as magnetic tunnel junction based magnetoresistive random access memory (MRAM), since it provides a local means of magnetisation manipulation. MRAM bit switching, the reversal of the free layer magnetisation, is then achieved either by a dual magnetic field pulse at a "cross point" known as toggle writing [6] or using the spin transfer torque from the spin polarised current [7]. STT-MRAM technology has significant advantages over magnetic-field switched (toggle) MRAM that has been widely commercialised [8]. The main hurdles associated with field switched MRAM are its complex cell architecture, high write current and poor scalability below 100 nm. Writing the bits by directly passing a current through the device addresses some of these issues although the main challenges for implementing STT MRAM are the substantial reduction of the intrinsic current density, J_i, required to switch the magnetisation of the free layer and the simultaneous reduction in the reversal time [9]. Given the importance of MRAM to computer memory over the next decade [10], research into magnetic materials and devices is not only topical but directly relevant to industry. Ideally methods to reduce the STT current needed to switch the free layer, or remove the need for current completely, combined with faster switching times are highly desirable.

1.2 Spin torque oscillators

The basic spin valve can be used to produce a spin torque oscillator (STO). STOs are devices which have attracted a great deal of attention over recent years for their potential applications in microwave frequency generation. STOs offer the potential for compact variable microwave generation with very little electronics [11]. A STO is shown in figure 1.2.

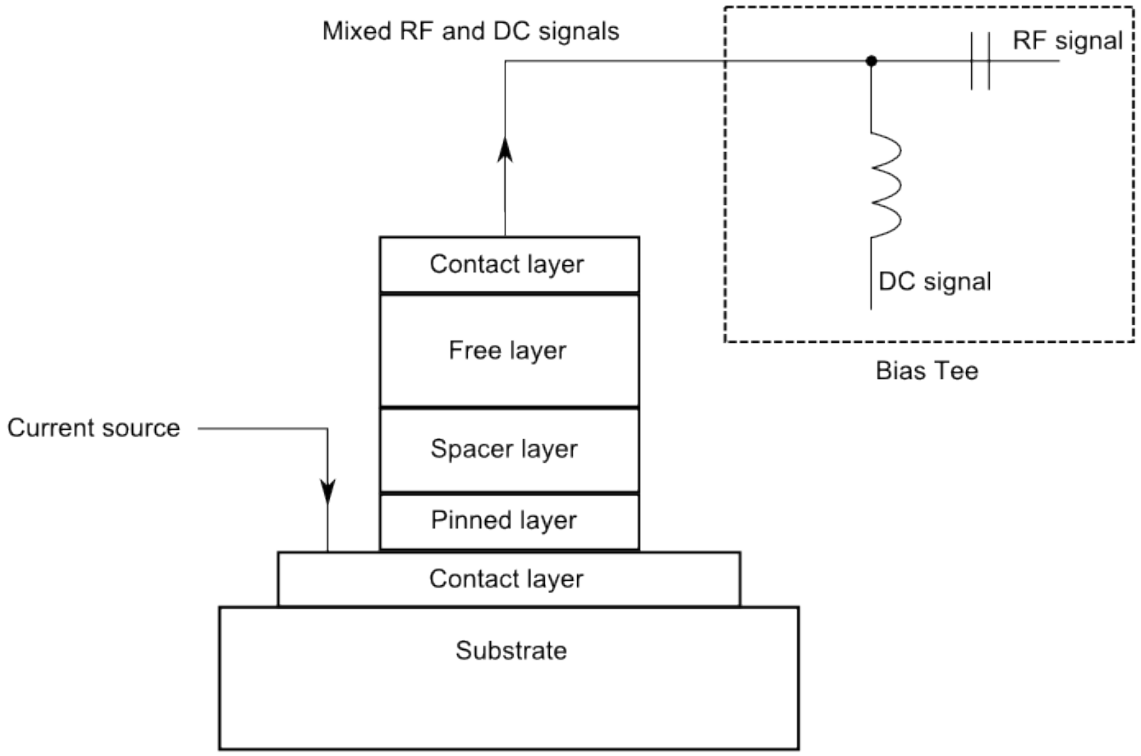

Fig. 1.2 Structure of a typical STO [12]. Electrons passing through the fixed magnetic layer become spin polarised. On entering the free layer these electrons transfer their angular momentum, causing the free layer to precess at microwave frequencies. The resulting fluctuations in giant magnetoresistance result in a microwave frequency component to the voltage output which is then extracted using the bias tee.

A spin polarised current entering the magnetic free layer applies a torque to the magnetisation [12]. This spin transfer torque (STT) acts as an anti-damping term in the Landau-Liftshitz Gilbert equation of motion, see section 2.7. If this anti-damping term is greater than the damping processes in the free layer the STT will cause the magnetisation to precess around the effective field. Due to the GMR effect the device generates an alternating resistance which, due to the constant current running through the device, therefore generates an alternating component in the voltage across the device. This alternating component of the voltage occurs at one of the natural gyromagnetic frequencies of the system and is extracted by the bias tee, also shown in figure 1.2[12].

The magnetic free layer of a STO can either be a non-uniform ground state such as a vortex state described in detail in sections 1.3 and 2.11, or a uniform magnetisation state. A uniform magnetisation state STO will oscillate at a higher frequency than one with a vortex

state (names a vortex core oscillator, VCO) however the output power of the microwave field will be lower [13]. VCO based STOs also exhibit a greater flexibility in their frequency of oscillation [13].

The first advantage of a STO over classical methods of microwave frequency generation is the stability of the frequencies generated by the devices regardless of the temperature of operation. Whilst the linewidth of the generated signals may increase with temperature the central frequency generated will remain constant [14].

STO devices also operate using a DC current making them ideal for microwave frequency generation in mobile devices where a battery is used as the power source.

Further advantages of a STO microwave generator over a typical microwave frequency generator include control over the operating frequency of the device. The operating frequency of a STO can be altered by a number of factors.

The first method of frequency control is an externally applied static magnetic field. The magnetic field is usually applied out of the plane of the device as shown in figure 1.3 which is taken from reference [15].

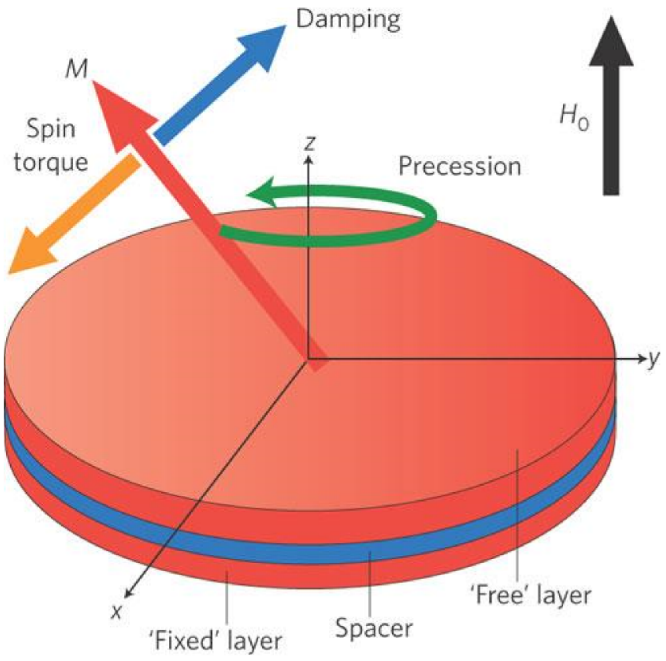

Fig. 1.3 Demonstration of the angles between the direction of precession and the externally applied field in a STO. The image was taken from reference [15].

As the magnetic field is increased the frequency of oscillation increases, causing the amplitude of oscillation, or "cone angle" to decrease, reducing the output power.

The frequency of oscillation as a function of the externally applied magnetic field for a thin film with an externally applied field out of the plane of the sample can be determined by equation 1.1. The resonant frequency is f, H_0 is the externally applied field, M is the magnetisation of the sample and γ is the gyromagnetic ratio [16].

$$f = \frac{\gamma}{2\pi}(H_0 - 4\pi M) \tag{1.1}$$

However this method of frequency control also has its drawbacks in that it requires the energy intensive generation of a static external magnetic field and that if the field is strong enough it can saturate and pin the magnetisation of the magnetic free layer [13].

Alternatively the frequency may be controlled by altering the amplitude of the current applied in order to excite the oscillations [17–19].

As the current increases the frequency of oscillation decreases as a consequence of the increased cone angle with current. For a fixed bias field, the increase in cone angle reduces the frequency of oscillation. This drop in frequency as a function of the applied current is shown in figure 1.4 which shows a theoretical relation between current and frequency for a permalloy like material taken from reference [19].

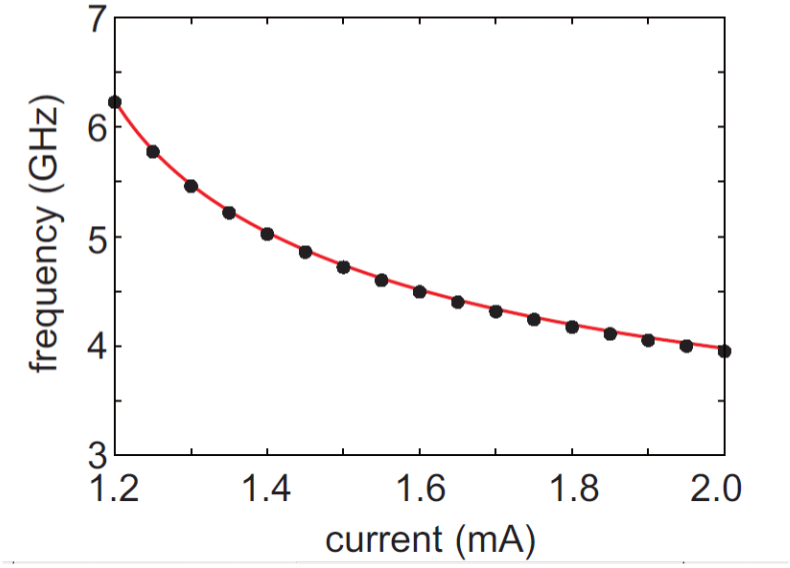

Fig. 1.4 Frequency versus current relation for a theoretical STO taken from reference [19]. The black dots indicate the calculated oscillation frequency at a given current value. The red line serves as a guide to the eye. The values used to calculate this relation are based on the values for permalloy.

Assuming that the magnetisation vector undergoes steady precession the frequency of oscillation can be expressed as a function of the amplitude of the applied current as in equation 1.2. In equation 1.2 H_{appl} is the field applied along the z-axis, H_k is the crystalline anisotropy field along the z-axis, M is the saturation magnetisation and Θ_c is the cone angle and [19], which must be calculated numerically for any given current.

$$f = \frac{\gamma}{2\pi}[H_{appl} + (H_k - 4\pi M)cos\Theta_c] \tag{1.2}$$

Using current to control the frequency of oscillation is energy intensive due to the difficulty in creating a constant current source from the constant voltage sources commonly found in computing. The output power of the microwave signal is also tied to current meaning that the output power will change depending on the desired frequency. The relation between the output power, P_{out}, across a load resistance, R_L against the current applied to the device, I, is given explicitly in equation 1.3 taken from [12]. This equation assumes that the change in the resistance of the device due to the GMR is given by ΔR_{STO} and the average resistance of the device is R_{STOav}.

$$P_{out} = \frac{I^2}{8}\frac{\Delta R_{STO} R_L}{(R_{STOav} + R_L)^2} \tag{1.3}$$

Finally control over the frequency of oscillation of a uniform magnetisation oscillator has been demonstrated using an externally applied strain [20]. This alters the frequency of oscillation by changing the contribution of magnetic anisotropy to the effective magnetic field in equation 1.1. The demonstration of strain control over the frequency of oscillation in a VCO will be extensively discussed in chapter 6 and is briefly mentioned in reference [21].

It is this final method of frequency control which we will focus on in this thesis as the application of a voltage to a piezoelectric transducer on which a sample has been fabricated represents a much more energy efficient method of frequency control requiring no external magnetic field and operating at a constant current applied through the STO device.

With all of these methods the output power of a single STO remains low however. In order to overcome this problem it has been suggested that a number of STOs may be used in conjunction with one another. This presents a problem in that the oscillations must be in phase with one another. When a set of STOs are phase locked the result is a reduced linewidth and a increased power output relative to a single STO or multiple STOs with random phase.

One solution to this problem is to place the STOs in close proximity to one another resulting in phase locking due to the stray dipolar fields of the STOs interacting [22].

This method of phase locking has only been demonstrated in two STO systems due to the difficulties in generating phase locking between STO devices which are further away. Alternatively it has been proposed that phase locking could be accomplished by driving STOs using the RF output from a primary driving STO. The secondary STOs would phase lock to the exciting field and produce the desired increase in output power and reduction in frequency linewidth[23]. This method introduces its own issues however with the time delay between the primary and secondary STOs being non-uniform for larger STO arrays requiring phase delay electronics or a system crafted to ensure distances between STOs designed to ensure phase coherence[24]. Both these methods suffer from issues with the frequency of oscillation of STOs being dependent on number of factors such as the size of the samples and the internal anisotropies of the samples. These problems could be alleviated however by using strain induced anisotropies in the STOs in an array in order to tune the system towards phase coherence.

1.3 Vortex core oscillators

A VCO, similar to a STO, is based on the spin valve, with a non-uniform magnetic state in the free layer. The magnetic domains within a VCO are allowed to form a Landau flux closure state for square geometry as described in section 2.8, and a vortex state for the more common circular geometries. These states have a curling in plane magnetisation with a central core, the vortex core, which has a magnetisation pointing out of the plane. A VCO is commonly excited using STT in the same way as the magnetic free layer in a STO.

In this thesis we studied nanostructures supporting Landau flux closure, or vortex states. These structures could represent the free layer in a VCO. The structures were excited with a magnetic pulse generated by fabricating the samples on a waveguide [25–27]. When a current passes through the waveguide a magnetic field at 90^o to the current is generated exciting the sample. This method of torque generation was used in chapter 5 and modelled in chapter 6. The vortex core precesses in a circular motion due to the balance between restoring force and the action of the excitation.

The frequency of oscillation of a VCO is independent of the strength of an exciting magnetic field pulse [17]. However the oscillation frequency of a VCO may be altered using the internal anisotropy of the system. This may be done either by using fabricating VCOs with different magnetic anisotropies [27, 28] or, as discussed in this thesis, by applying a strain-induced anisotropy to alter the oscillation frequency. Using a strain-induced anisotropy to alter the frequency of oscillation, induced using a piezoelectric transducer, provides a

method of generating an internal anisotropy into the system which can be controlled by the application of a low power voltage making this method both power efficient and practicable.

Vortex states also represent attractive potential candidates for a new generation of MRAM utilising the core's polarisation and its chirality to realise its potential as a four state storage medium [29].

The polarisation of the vortex core may be reversed by causing the vortex core to precess beyond a certain critical velocity [30–32].

The chief advantage of MRAM over electronic memory devices is that MRAM systems are non-volatile. Electronic dynamic random access memory (DRAM) elements rely on capacitive devices to store information, which suffer from the requirement to continuously refresh the memory elements every few milliseconds due to current leakage [33, 34]. The use of non-volatile MRAM would therefore represent a significant improvement in the energy efficiency of computer memory devices representing a non-volatile method of storage. Another potential advantage of MRAM systems is improved read and rewrite times of <1ns [35] compared to rewrite times of a few ns for DRAM devices [36]. An advantage of DRAM memory elements over MRAM is the element density however. DRAM elements as small as 14nm have been produced [37] however effective vortex core MRAM elements are limited to the 100nm size range [17].

A number of problems stand in the way of the realisation of vortex core based STT RAM elements however [32]. First there is the requirement of an external magnetic field pulse, external AC magnetic field or spin polarised current to excite core motion, then there is the problem of reading the polarisation of the vortex cores as quickly and efficiently as a conventional RAM element.

1.4 Materials for strain controlled spintronics

In order to study the effects of strain induced anisotropy a material with a strong response to an applied stress is required, ideally a material like Terfenol-D, an alloy of terbium, dysprosium and iron which exhibits a strong magnetostriction constant of up to $\sim 1.7 \times 10^{-3}$ [38]. Terfenol-D however contains dysprosium and terbium, both rare earth elements making them prohibitively expensive due to their rarity and the difficulty in extracting the raw elements from their ores. For this reason the search for a material in which a strong strain anisotropy can be induced without the need for rare earth elements have been extensive in recent years.

To this end experiments with iron alloys have shown that other materials may be incorporated into the iron lattice and this has been done with silicon, nickel, aluminium and cobalt

[39–41, 39]. The addition of Ga however causes the magnetostrictive properties of Fe to be especially strongly accentuated [39]. The addition of Ga to the lattice was found to produce a tenfold increase in the material's constant of magnetostriction in the [100] direction with a small decrease in the magnetostriction in the [111] direction when the ratio of Ga to Fe is approximately 19:81, a result which is demonstrated in figure 1.5 taken from reference [42].

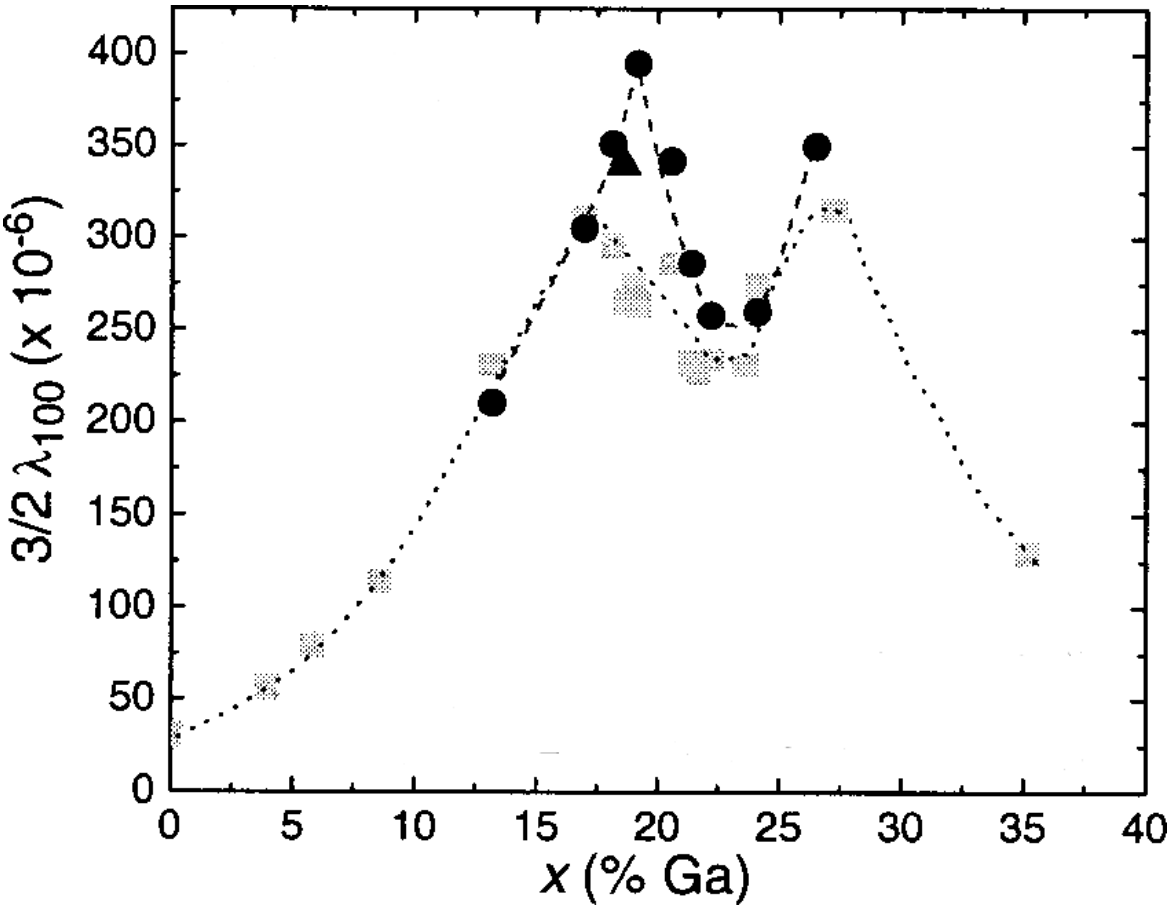

Fig. 1.5 Effect of gallium concentration on the strength of magnetostriction in $Fe_{1-x}Ga_x$. The lower line indicates that the samples were furnace cooled in fabrication whereas the upper line was quenched cooled. This figure was taken from [42].

In order to understand the causes of these two peaks in magnetostriction we must examine the crystal structures that galfenol can take shown in figure 1.6 [43, 44].

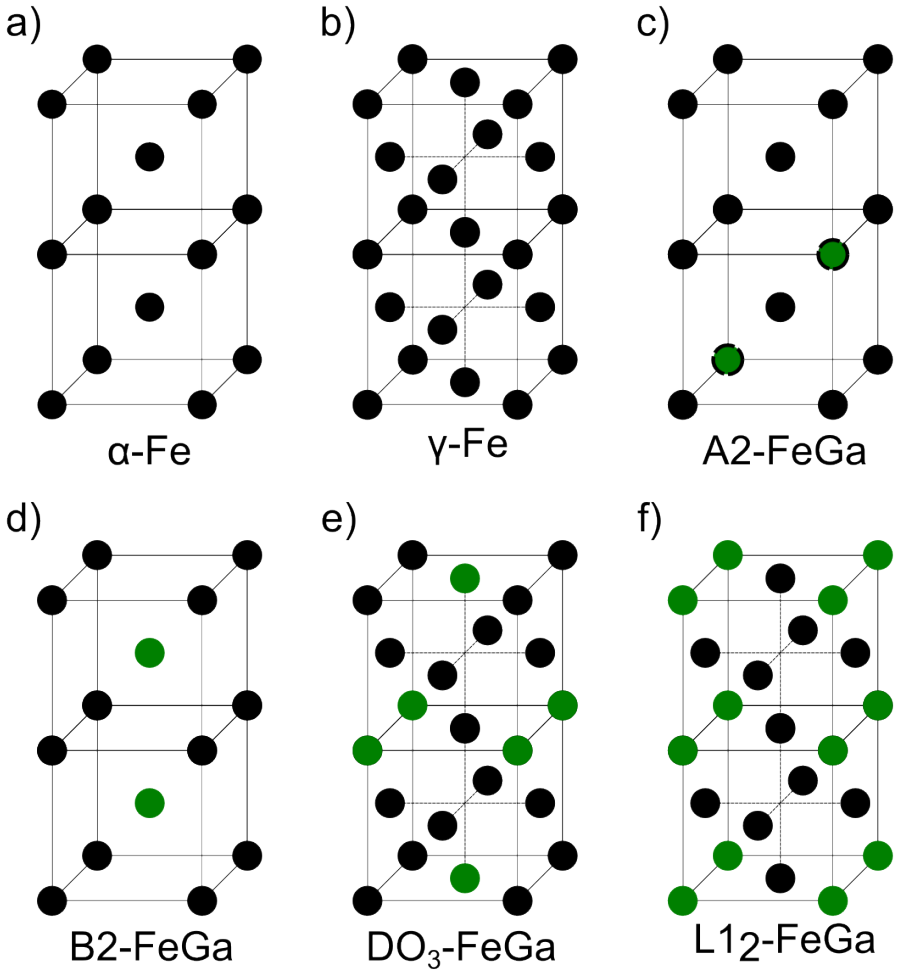

Fig. 1.6 Demonstration of the crystal structures of various phases of Fe and $Fe_{1-x}Ga_x$ with Fe atoms shown in black and Ga atoms shown in green. Shown in a) and b) are the two main allotropes of Fe, α-Fe and γ-Fe which are body centred and face centred cubic respectively. α-Fe is the allotrope to which Ga is added to create A2-$Fe_{1-x}Ga_x$, c) and B2-$Fe_{1-x}Ga_x$, d). In both A2 and B2 $Fe_{1-x}Ga_x$ the body centred cubic structure of α-Fe is retained however in A2 Ga atoms are randomly distributed throughout the lattice and in B2-$Fe_{1-x}Ga_x$ the Ga is consistently located in the body-centred sites. The structures in e) and f) resemble γ-Fe in their face centred cubic structure however $D0_3$-$Fe_{1-x}Ga_x$ (0.19>x>0.27) shown in e) has Ga at the 4a sites and $L1_2$-$Fe_{1-x}Ga_x$ (x>0.27), shown in f) has Ga in place of Fe at the face sites of the structure.

Pure Fe can take on two key allotropes, α-Fe and γ-Fe shown in figure 1.6 a) and b) respectively. When Ga is alloyed with Fe at low concentrations the structure of the galfenol takes on the A2 character shown in figure 1.6 c) where the Fe is in a body centred cubic structure with Ga atoms randomly substituted for Fe atoms [45]. In this structure the magnetostriction has been theoretically described as arising from Ga-Ga pair induced local defects in the crystal lattice [46, 47].

This effect peaks at around $\sim 19\%$ gallium concentration and then decays rapidly as the galfenol crystal becomes a mixture of A2 and D03 phase [48] (with a possible mixture of B2 depending on growth conditions [49, 49]). The magnetostrictive constant peaks again as the structure becomes purely $D0_3$, shown in figure 1.6 e) resulting in lattice softening which is the source of the second, smaller peak in magnetostriction [50]. Finally as the concentration of gallium passes $\sim 27\%$ the $L1_2$ phase, shown in figure 1.6 f) begins to be mixed into the structure resulting in another sharp decline in the magnetostrictive constant of the material [43, 44]. We would expect that the $Fe_{1-x}Ga_x$ films grown in this thesis to take the A2 structure due to the Ga concentration to be approximately 20% or lower.

These strong magnetostriction constants can be compared with the magnetostriction constants of other 3d metals and alloys as shown in table 1.1 which shows the saturation magnetisation of the material, M_s, the constant of magnetostriction constant in the [100], λ_{100} and [111], λ_{111} crystallographic directions and in a polycrystal. Table 1.2 shows the elastic constants $c_{12} - c_{11}$ and c_{44} which correspond to the shear modulus in the [100] and [111] directions respectively.

Material	M_s $(A/m \times 10^6)$	λ_{100} $(\times 10^{-6})$	λ_{111} $(\times 10^{-6})$	λ Polycrystal $(\times 10^{-6})$
BCC-Fe	1.70 [51]	20.5 [52]	-21 [52]	-7 [52]
HCP-Co	1.40 [51]	-140 [52]	50 [52]	-62 [52]
FCC-Ni	0.49 [51]	-46 [52]	-24 [52]	-34 [52]
BCC-$Fe_{20}Ni_{80}$	0.86 [51]	8 [53]	0 [53]	0[53]
BCC-$Fe_{81.3}Ga_{18.7}$	1.38	264 [42]	~ 15 [42]	~ 65 [54]
$Tb_{0.3}Dy_{0.7}Fe_2$	0.8[55]	90 [55]	1640 [55]	1400 [38]

Table 1.1 Various constants pertaining to the magnetostrictive properties of various materials presented as a comparison to the magnetostrictive properties of galfenol.

Table 1.1 shows that galfenol exhibits higher magnetostriction than any other ferromagnetic material not containing rare earth elements. Only terfenol-D has a higher magnetostriction constant. Table 1.1 also demonstrates that the magnetostriction in $Fe_{1-x}Ga_x$ is highly anisotropic. Also shown is the weak magnetostriction in permalloy, this is a contributing

factor to the use of permalloy in the vortex core experiments described in section 1.3 and in the field of magnonics described in section 2.10, since the lack of magnetostriction simplifies the dynamics in the magnetic systems by removing a strain-induced anisotropy from the system.

In order to look at why other magnetic materials may be used in strain resolved experiments we must look at the elastic constants of ferromagnetic materials. These constants are presented in table 1.2.

Material	$c_{11} - c_{12}$ (GPa)	c_{44} (GPa)
BCC-Fe	95 [56]	112 [56]
HCP-Co	141	75 [57]
FCC-Ni	90 [56]	1.185 [56]
BCC-$Fe_{20}Ni_{80}$	8.6 [58]	66 [59]
BCC-$Fe_{81.3}Ga_{18.7}$	39.4[42]	$\sim$ 120 [42]
$Tb_{0.3}Dy_{0.7}Fe_2$	76 [55]	49 [55]

Table 1.2 Elastic constants of various materials presented as a comparison to the elastic properties of galfenol.

The strain-induced magnetic anisotropy is a product of the magnetostrictive constants given in table 1.1 and the elastic constants given in table 1.2 as described in detail in section 2.5. These tables show that whilst Ni has lower magnetostrictive constants than $Fe_{1-x}Ga_x$ it has higher elastic constants. This means that a smaller amount of stress applied to a Ni sample will result in a greater strain than the same stress applied to a $Fe_{1-x}Ga_x$ sample. The greater magnetostrictive constant of $Fe_{1-x}Ga_x$ makes it more attractive than Ni for experiments studying the effects of a strain-induced anisotropy however since the magnetoelastic energy, discussed in detail in section 2.5, is a product of the Youngs modulus (related to the elastic constants) of the material and the magnetostrictive constant in the direction of the strain the sample is experiencing. It can also be seen from table 1.2 that the introduction of Ga into the Fe lattice results in a reduction of the elastic constants in the [100] direction but an slight increase in the elastic constants in the [111] direction as described in our discussion of the structure of $Fe_{1-x}Ga_x$ thin films.

The strength of magnetostriction is also heavily affected by the temperature of the material with high temperatures decreasing the level of magnetostriction in $Fe_{0.81}Ga_{0.19}$ as shown in figure 1.7 which was taken from reference [60].

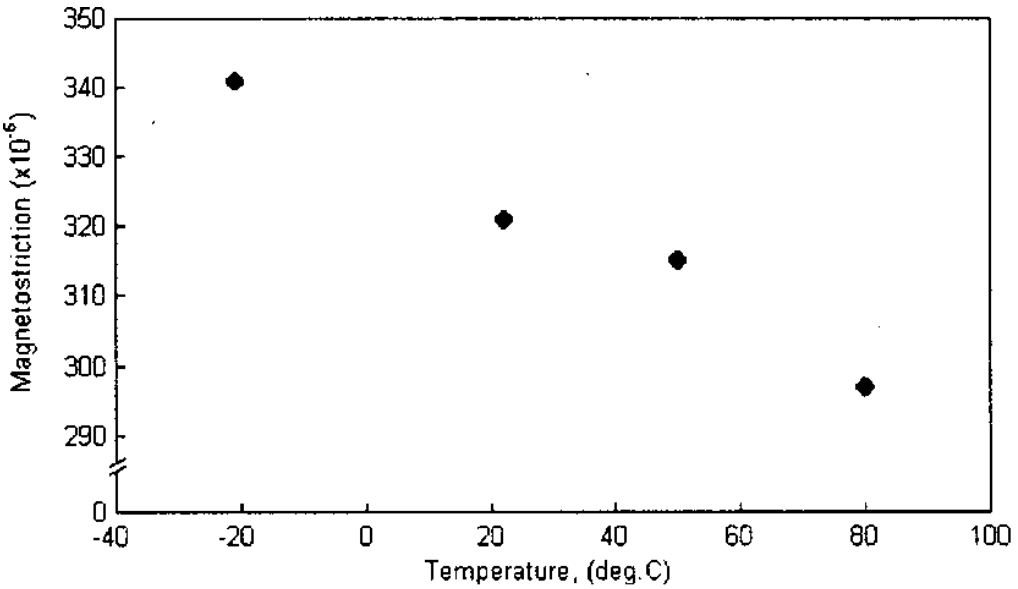

Fig. 1.7 Graph showing the relation between temperature and magnetostrictive constant in $Fe_{0.81}Ga_{0.19}$ taken from reference [60].

However this relation is also dependent on the composition of the sample with reference [42] reporting a positive correlation between temperature and magnetostriction in $Fe_{75.9}Ga_{24.1}$ and $Fe_{77.6}Ga_{22.2}$.

Previous investigations of $Fe_{0.81}Ga_{0.19}$ thin films grown on GaAs by molecular beam epitaxy reveal that the material possesses both in-plane uniaxial anisotropy, arising from the interface with the GaAs and cubic anisotropy, arising from the body centred cubic structure of $Fe_{0.81}Ga_{0.19}$ [61]. The uniaxial easy axis lies along the [110] axis with the hard axis lying along $[1\bar{1}0]$. The cubic easy axes for $Fe_{0.81}Ga_{0.19}$ lie in the [100] and [010] directions, the same as for iron [62, 63].

Investigations into the strain-induced anisotropy of $Fe_{0.81}Ga_{0.19}$ thin films grown on GaAs by molecular beam epitaxy have shown that the strain-induced anisotropy in Molecular Beam Epitaxy (MBE) grown $Fe_{0.81}Ga_{0.19}$ thin films is comparable to the strain induced anisotropy in bulk $Fe_{0.81}Ga_{0.19}$ material. This is shown in figure 1.8 which shows the value of strain anisotropy, K_s, as a function of applied strain and was taken from reference [61].

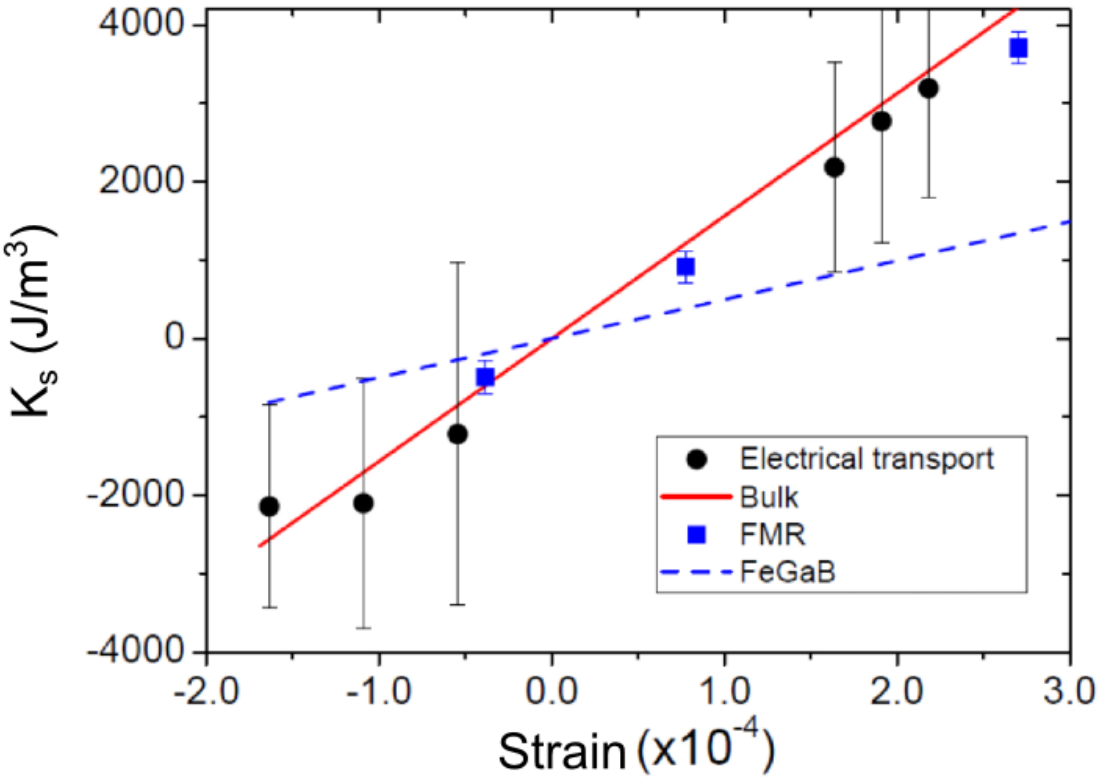

Fig. 1.8 Strain anisotropy verses applied strain for $Fe_{0.81}Ga_{0.19}$ thin films grown on GaAs by molecular beam epitaxy. Data was collected using electrical transport measurements similar to those described in section 3.10 and by Ferro-Magnetic Resonance (FMR) measurements. Also shown are the relations between strain anisotropy and strain for bulk $Fe_{0.81}Ga_{0.19}$ and FeGaB. Taken from reference [61].

The effects of this strain-induced anisotropy can be seen in figure 1.9 taken from reference [64] which shows hysteresis loops for bulk $Fe_{0.81}Ga_{0.19}$ with different levels of compressive strain applied along the [100] axis showing that as the compressive strain increases the [100] axis becomes harder indicating that the strain is altering the anisotropy of the material.

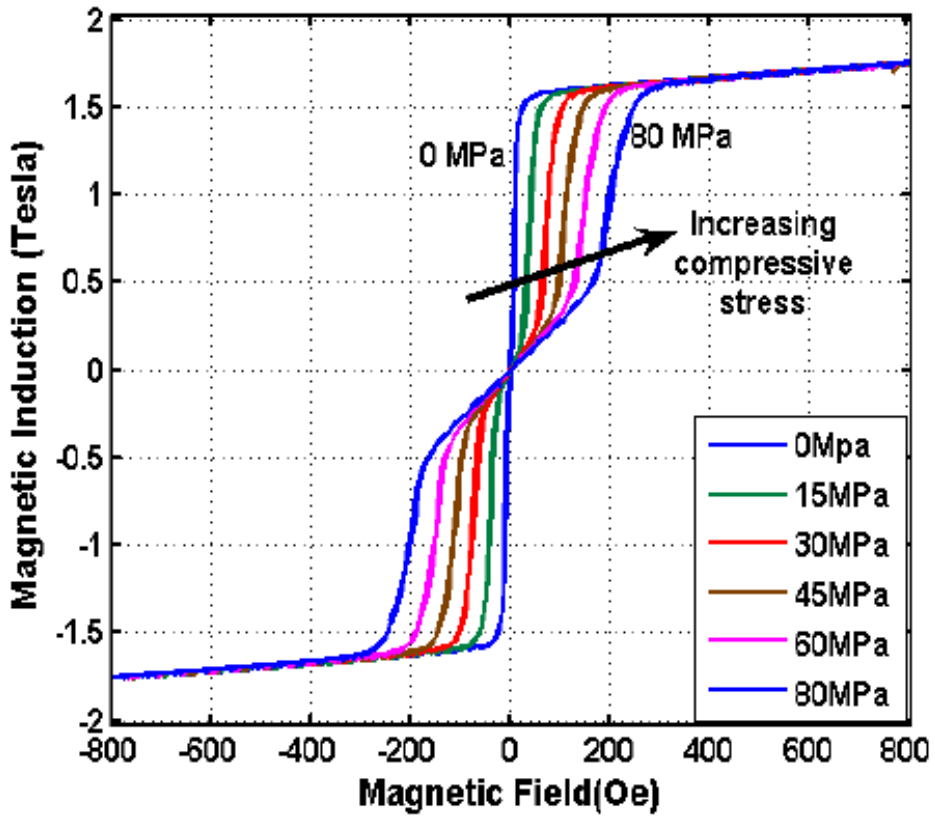

Fig. 1.9 A series of hysteresis loops for $Fe_{0.81}Ga_{0.19}$ orientated along the [100] axis with magnetisation and a variety of different compressive strain values along the [100] axis. The different colours of the lines indicate different amounts of strain. Taken from reference [64].

1.5 Magnetic imaging

In order to minimise the energy within a magnetic material regions of uniform magnetisation, known as domains, may form. These areas form in order to minimise the stray field resulting from the system's internal magnetisation. This is discussed further in section 2.8 however here we will simply state that the magnetic configuration of a material may contain many of these regions of uniform magnetisation. This is particularly true for the meso and macro magnetic elements studied in this body of work.

There are a number of ways of imaging the magnetic state of a material. However, each of these methods has it's own advantages and drawbacks.

1.5.1 Magnetic Force Microscopy (MFM)

Magnetic force microscopy (MFM) is a variety of atomic force microscope where a sharp magnetised tip scans a magnetic sample, the tip-sample magnetic interactions are detected and used to reconstruct the magnetic structure of the sample surface [65].

This method has advantages in terms of the cost effectiveness of the scanning process as well as the flexibility of the method with MFM being used in difficult environments such as ultra high vacuum or at extreme temperatures[66, 67]. The drawbacks of this method are the low speed of measurements with a single magnetic contrast image taking many minutes to produce [68, 69]. The method may only measure the stray field of the sample meaning that it is a poor method for measuring the in-plane magnetisation of a material since only the in-plane magnetisation at the edges of the material, or the out of plane component of the magnetisation may be measured. This method may also lead to back-action between the tip and the sample altering the magnetic configuration of the material as it is imaged. This method is also unsuitable for experiments where a high magnetic field is applied to the sample since the magnetic tip may be affected by the applied magnetic field. The low speed of image collection makes time resolved measurements using MFM impractical.

1.5.2 Magnetic-Optical Kerr Effect (MOKE) magnetometry

Another very popular method for measuring the magnetic field of a sample is Magnetic-Optical Kerr Effect (MOKE) magnetometry and microscopy. This involves reflecting polarised light from the surface of the sample and then measuring the rotation of the polarisation, the Kerr angle, due to the magnetisation of the sample. The change in magnetisation of the sample is detected by observing rotations in the polarisation as experimental conditions are applied, such as the application of an external magnetic field or a change in sample temperature. This method may also be used to measure the magnetisation in or out of the plane of the sample depending on the angle of incidence between the laser and the sample surface.

Time resolution can be added to the experiment by using a pulsed laser in a stroboscopic pump-probe arrangement where the pump can either be another laser pulse [70] or an electronic signal used to create a pulsed magnetic field via a stripline or coplanar waveguide [25]. A delay line is used to ensure a delay between the perturbation to the system and the detection pulse.

Measurements of VCOs have been performed using time resolved MOKE microscopy by the use of a waveguide [25] however the drawbacks of this method include the fact that

any measurement is of a change in magnetisation rather than a direct measurement of the magnetisation. The spatial resolution is limited by the wavelength of light[25].

1.5.3 X-ray Techniques

Transmission X-ray Microscopy (TXM) and Scanning Transmission X-ray Microscopy (STXM)

Another pair of photon techniques are transmission x-ray microscopy (TXM) and scanning transmission x-ray microscopy (STXM). These techniques involve measuring the intensity of x-rays passing through a magnetic sample. Magnetic contrast is obtained via X-ray Circular Dichroism (XMCD), since the circularly polarised x-rays are attenuated by differing amounts depending on the direction of the magnetisation in the region they are passing through. The energy of the X-rays must be tuned, depending on the magnetic material being imaged, to coincide with an absorption edge of the element being studied. Normally in the soft x-ray region these are the $L_{2,3}$ edges of the transition metals i.e electric dipole transitions between p and d orbitals. For a full description of the mechanism of this attenuation see section 3.12.1 however for now we will simply state that the magnetic contrast from TXM and STXM results from this variation in x-ray attenuation depending on the magnetisation of the area the x-rays are passing through.

The difference between the two methods is that in TXM the sample is illuminated using a full field technique whilst STXM is a scanning probe technique. Whilst STXM and TXM have high resolution, approximately 10nm, and produce a direct measurement of the magnetisation of the sample they require thin films grown on X-ray transparent membranes such as SiN. Whilst the technique is used to measure thin films [71, 26] and time resolved TXM is used to measure vortex core dynamics [72] technologically important substrates, such as GaAs and Si, cannot be used [73, 71], nor can the sample be grown on ferroelectric substrates.

XMCD PhotoEmission Electron Microscopy (XMCD PEEM)

Finally time resolved XMCD (TR-XMCD) PhotoEmission Electron Microscopy (PEEM) can also be used to measure magnetic domains with high resolution in both space and time in an element specific manner. The experimental details of this method can be found in section 3.13. In brief it involves forming an image using the elections photo-emitted from the surface due to absorption of X-ray photons. As the number of emitted electrons is proportional to the absorption cross section tuning the X-ray energy to a specific absorption edge allows for an element specific measurement. If the sample is magnetic then the absorption cross

section is dependent on the photon helicity (XMCD) allowing for magnetic contrast imaging. This method gives high resolution and a direct measurement of sample magnetisation with no requirement for transmission through the sample. For these reasons a significant part of the work included in this thesis, specifically the data presented in chapter 5, involved the development of time resolved XMCD-PEEM with a capacity for strain resolved experiments. This development revealed a number of experimental difficulties involved in time resolved XMCD-PEEM, which will be discussed in chapter 3. This method also requires a tunable source of circularly polarised soft x-rays meaning the experiment must be performed at a synchrotron limiting the amount of time in which the apparatus is available. The XMCD PEEM system at Diamond Light Source is not optimised for high frequency experiments with cabling designed for DC experiments and floating on a 20kV supply. This means that a laser system, described in section 3.13, must be used in place of a single high frequency pulse generator. Despite these drawbacks time resolved XMCD PEEM is the only experimental method which allows for the high resolution images with a sufficiently high sampling frequency to collect videos of vortex core oscillations and which does allow for the sample to be mounted on a piezo-electric transducer which can be used to apply a strain to the samples being tested.

Chapter 2

Theory

2.1 Ferromagnetism and the exchange energy

Ferromagnetism occurs in materials in which there are electrons with unpaired spin in the outer d or f orbitals. These spins interact with unpaired spins in the surrounding atoms in the lattice to result in long range magnetic ordering. Heating a ferromagnet beyond a certain temperature, the Curie temperature, causes the spin system to become disordered and transition to a paramagnetic state. A material in which the magnetic ordering leads to the local moments being aligned anti-parallel is referred to as anti-ferromagnetic, which is characterised by an ordering temperature known as the Néel temperature, T_N. When such a system is heated beyond the Néel temperature it will loose its ordering and will again become paramagnetic. Ferromagnetism, anti-ferromagnetism and paramagnetism are all demonstrated in figure 2.1. Not shown here are more exotic forms of magnetic ordering such as helimagnetism (where the spins form a spiral) or ferrimagnetism (a form of anti-ferromagnetism where the atomic moments in one direction are larger than the atomic moments in the other direction).

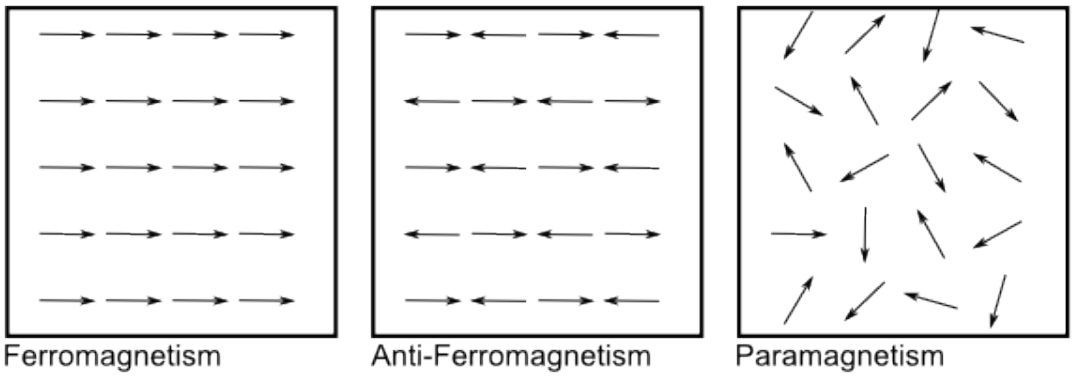

Fig. 2.1 Different forms of magnetism. Ferromagnetism and anti-ferromagnetism both involve long range magnetic ordering with spins aligning in ferromagnetic systems and spins anti-aligning in anti-ferromagnetic systems. In paramagnetism there is no long range ordering without an externally applied field and therefore no net magnetisation. In diamagnetic systems the application of an external magnetic field will result in magnetisation counter to the applied field.[74]

Ferromagnetism arises in Fe, Co and Ni due to a combination of the unpaired electrons in the d orbital and the exchange energy between the unpaired electrons. Electron configurations for a series of metals are shown in figure 2.2.

In figure 2.2 we can see that there are unpaired d electrons in Sc, Ti, V, Cr, Mn, Fe, Co and Ni but that ferromagnetism only occurs in Fe, Co and Ni. The reason for this can be found in the exchange interaction between electrons from neighbouring atoms within the lattice. The exchange interaction between atoms in a lattice is characterised by the exchange constant, J.

This exchange constant is used in the Ising model to determine the interaction energy between two electrons in fixed locations. This is combined with the energy of a free spin to produce the Hamiltonian for a magnetic insulator. This is given in equation 2.1 in which $s_{i,j}$ is the spin on sites i and j, $J_{i,j}$ is the interaction energy between the spins at sites i and j, g is the gyromagnetic ratio, μ_B is the Bohr magneton and H is the externally applied magnetic field.

$$\mathscr{H} = -\frac{1}{2}\sum_{i,j} J_{i,j} s_i \cdot s_j + \sum_i g\mu_B H \cdot s_i \tag{2.1}$$

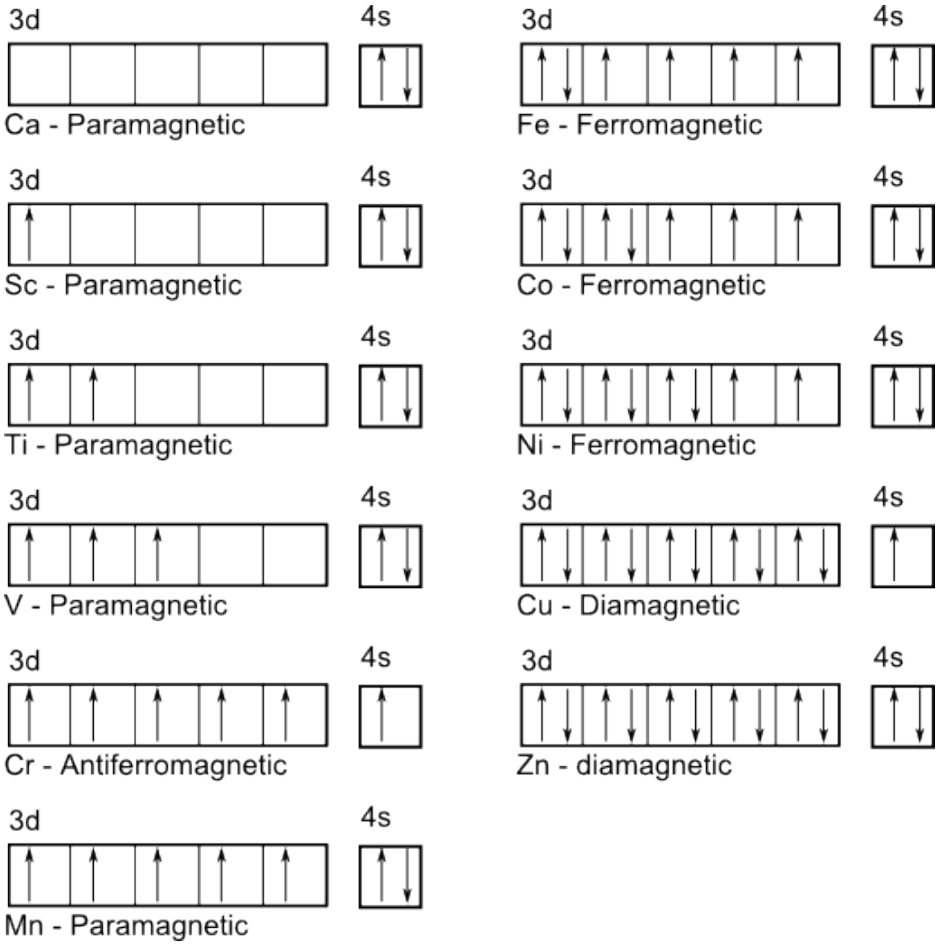

Fig. 2.2 Electron configurations for various metals along with the magnetic state at room temperature that results from the configurations. The arrows represent up and down spin electrons in the outer d and s orbitals of the elements shown with all lower energy levels being filled.

The sign of the spins relative to one another will change in order to minimise the interaction energy. The interaction integral, J, therefore dictates the magnetic character of the material. The relation between the exchange energy and whether a material is para,ferro or anti-ferromagnetic is often demonstrated using the Bethe-Slater curve [75, 76] shown in figure 2.3 which was taken from reference [77].

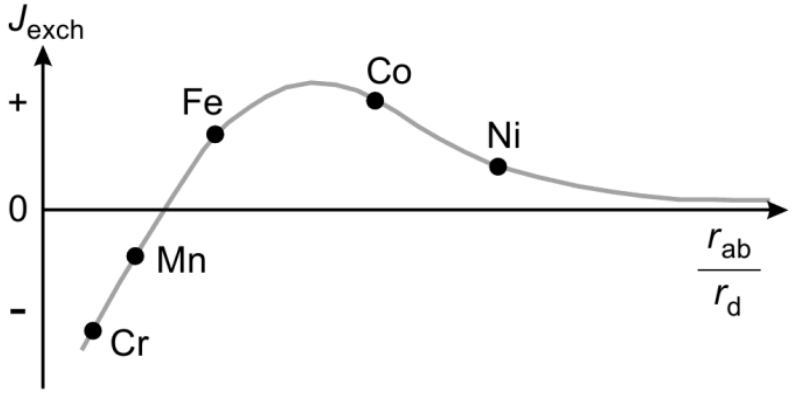

Fig. 2.3 Bethe-Slater curve taken from reference [77]. This is a plot of the ratio between atomic separation in the crystal, r_{ab}, to diameter of the 3d orbital in the material, r_d, against the exchange interaction for a series of materials in which it can be seen that the ferromagnetic materials have positive interaction energies and the anti-ferromagnetic materials have negative interaction energies with the interaction energies of paramagnetic materials tending towards zero.

This is a plot of the ratio between atomic separation in the crystal, r_{ab}, to diameter of the 3d orbital in the material, r_d, against the exchange interaction for a series of materials. It can be seen that ferromagnetic materials can be found in the positive region of the graph and anti-ferromagnetic materials can be found in the negative region. This graph also shows the interaction energy tending to zero as the ration $\frac{r_{ab}}{r_d}$ increases. These materials will exhibit paramagnetism due to their low interaction energy.

Whilst this model may be informative as to the magnetic properties of magnetic insulators the materials studied in this thesis are conductive metals. In order to understand these materials we must expand the Ising model to account for itinerant magnetism using the Hubbard model. In this model the magnetic spins are not confined to specific sites but are free to move throughout the material. Now the magnetic configuration of the system is governed by the potential energy of the system as well as the kinetic energy. This means that kinetic and potential energies are in competition with equal numbers of spin up and spin down electrons minimising the kinetic energy and a spin polarised state minimising the potential energy. This means that the system will become a ferromagnet only if the Stoner criterion is met. The Stoner criterion is given in equation 2.2 in which U is the potential energy of the system, $D(E_F)$ is the total density of states at the fermi surface and V_c is the volume of the unit cell

$$U < \frac{2}{D(E_F)V_c} \tag{2.2}$$

2.2 Magnetic Anisotropy

Magnetic anisotropy arises primarily due to the coupling of the orbital moments of electrons with the crystal field, the static electric field resulting from the local atomic cores and electrons. The interaction of the electrons spin with their orbital moments, the spin orbit interaction, then results in the spins of the electrons also becoming coupled to the crystal field of the material.

The positioning of atoms within the crystal lattice causes asymmetries in the crystal field which makes it easier for the magnetic moments to align to certain crystal directions. Iron can exist in a number of crystallographic states however for the purposes of this thesis we will be ignoring the more exotic allotropes of iron, instead focusing on epitaxially and sputter grown iron which takes on a body centred cubic crystal structure[78]. The anisotropy, known as magnetocrystalline anisotropy, reflects the symmetry of the crystal. BCC iron has predominantly cubic anisotropy. When grown on GaAs, the influence of the interface induces a uniaxial component to the magnetic anisotropy. This will be the subject of further discussion in section 2.5.

The shape of a material may also lead to anisotropy since the high energy cost of producing a stray field will cause the magnetic moments within the sample to lie parallel to the edge of the sample. This means that in the thin films being studied in this thesis magnetic moments aligning out of the plane of the sample will become energetically unfavourable and therefore will align in the plane of the sample. This can be seen explicitly by looking at the magnetostatic energy, E_{mstat}, which is described in equation 2.3 which is a product of the field due to magnetic poles at the surface of the sample, also known as the stray field, $\underline{\mathrm{H}}_{st}$, and the magnetisation of the sample $\underline{\mathrm{M}}$ integrated over the volume of the sample V.

$$E_{mstat} = -\frac{\mu_0}{2}\int_V \underline{\mathrm{M}} \cdot \underline{\mathrm{H}}_{st} dv \tag{2.3}$$

Anisotropy may also form in a material due to strain applied to the sample as described in the next section.

2.3 Magnetostriction

Magnetostriction is the effect of a physical strain, induced in a material by an applied stress, which alters the magnetic anisotropy possibly leading to a change in the direction of the magnetisation of the material.

This can be understood as the strain altering the shape of the crystal field creating an additional magnetic anisotropy thereby moving the magnetic easy axis and causing the direction the magnetisation to change in order to minimise the energy of the system. The phenomenological form of the magnetic free energy will be described in section 2.5.

2.4 The spin orbit interaction

The energy levels within the system are also altered due to the spin orbit interaction (SOI). This can be thought of classically by imagining the electron orbiting the nucleus at relativistic speeds. Since the electron has a negative electric field and the nucleus a positive electric field the result is a magnetic field due to the moving electric fields in accordance with Maxwell's equations. This magnetic field acts to re-orient the electrons spin altering the electron's energy level as described by the hamiltonian given in equation 2.4 in which $\underline{S}$ is the spin angular momentum of the electron, $\underline{B}_{eff}$ is the effective magnetic field on the electron, m_e is the electron mass,$\underline{p}$ is the electron's momentum and V is the electric potential experienced by the electron.

$$H_{SO} = \underline{B}_{eff} \cdot \underline{S} = (\frac{1}{2m_e^2c^2}\nabla V \times \underline{p}) \cdot \underline{S} \tag{2.4}$$

This shift in energy level is dependent on the angular momentum of the electrons leading to energy level splitting between electrons with differing angular momentum quantum numbers. This splitting is exploited to perform XMCD measurements as described in section 3.12. An example of this shift in energy level is seen in equation 2.5 which describes the energy shift due to SOI in hydrogen. V is the potential the electron sits in, r the distance from the nucleus, m the mass of an electron, $\underline{L}$ the orbital angular momentum and $\underline{S}$ the spin moment.

$$\Delta E_{SO} = \frac{1}{2m^2c^2}\frac{1}{r}\frac{\delta V}{\delta r}\underline{L} \cdot \underline{S} \tag{2.5}$$

The SOI results in a number of interesting magnetic properties such as anisotropic magnetoresistance as described in section 2.6, magnetic anisotropy as discussed in section 2.2 or magnetostriction which is described in section 2.3.

2.5 The magnetic free energy

The Stoner-Wolhfarth model is a method of modelling single domain ferromagnets in terms of the internal energy of the system using terms to describe the uniaxial ansiotropy and the Zeeman field. We will be building on this model by introducing additional anisotropy terms and determining the angle of the magnetisation as a function of the applied field by finding the angle at which the free energy of the system is minimised. The model takes into account the angle between the [010] axis and the magnetisation (usually along the direction of the applied field), (θ), and the angle between the net magnetisation and the applied field, (ϕ), as demonstrated in figure 2.4.

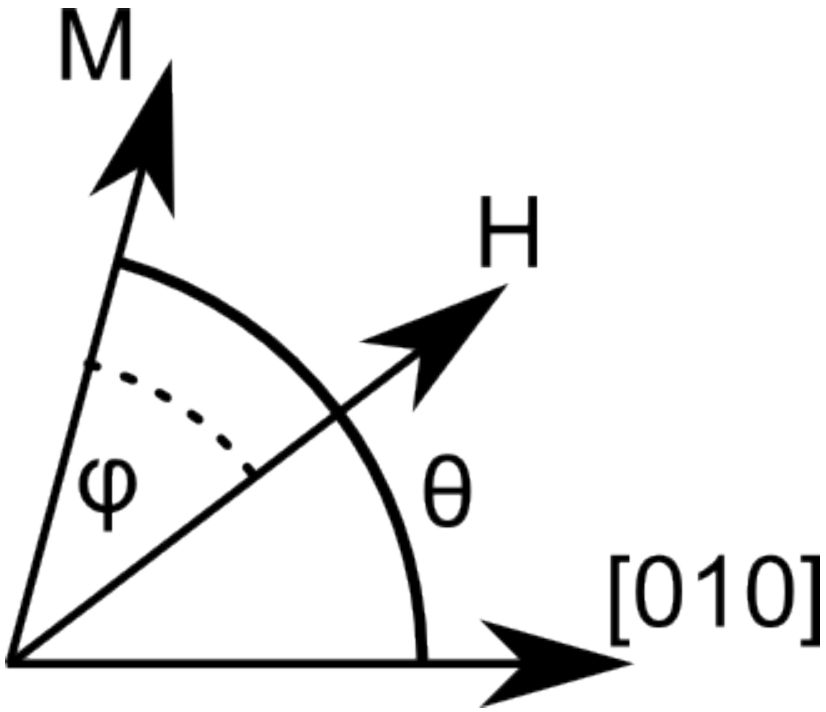

Fig. 2.4 Visual guide for the angles used in modelling the magnetic free energy.

In order to model the magnetic free energy we have to sum all the energy terms that make up the total energy of the system. The first one we will include is the uniaxial anisotropy energy which is defined in equation 2.6 in which E_u is the uniaxial anisotropy energy density, K_i^u is the magnetic uniaxial anisotropy constant in which i is the order of the term [79].

$$E_u = K_1^u \alpha^2 + K_2^u \alpha^2 = K_1^u sin^2(\theta - \frac{\pi}{4}) + K_2^u sin^4(\theta - \frac{\pi}{4}) + ... \tag{2.6}$$

E_u is represented phenomenologically using polar co-ordinates so that α is a direction cosine of the magnetisation with respect to the [010] axis. Since the uniaxial anisotropy is acting on only one axis due to the magnetisation being confined to the plane by the thin film condition α becomes sin(θ). For iron and its alloys (e.g. Galfenol) on GaAs however we must also consider the $\frac{\pi}{4}$ factor coming from the uniaxial easy axis being along the [110] axis which lies at an angle $\frac{\pi}{4}$ from the [010] direction.

The next term to be introduced will be the cubic anisotropy energy, E_c. This is an anisotropy term that appears in cubic systems meaning that we need to extend the treatment of the uniaxial anisotropy to include terms for the other principal crystal axes' cosines, α_i, meaning that the anisotropy energy of a cubic system may be described by equation 2.7.

$$E_a = K_0 + K_1(\alpha_1^2\alpha_1^2 + \alpha_2^2\alpha_3^2 + \alpha_3^2\alpha_1^2) + K_2(... \tag{2.7}$$

If we then express the cubic and uniaxial anisotropy to first order we can separate out the terms and express the cubic anisotropy using equation 2.8.

$$E_c = \frac{K_c}{4} sin^2(2\theta) \tag{2.8}$$

The in plane cubic and uniaxial anisotropies in ferromagnetic materials grown on GaAs, such as those discussed in this thesis, are dependent on film thickness as shown in figure 2.5 which was taken from reference [78]. This figure shows the uniaxial anisotropy decreasing with increasing film thickness and cubic anisotropy increasing with film thickness.

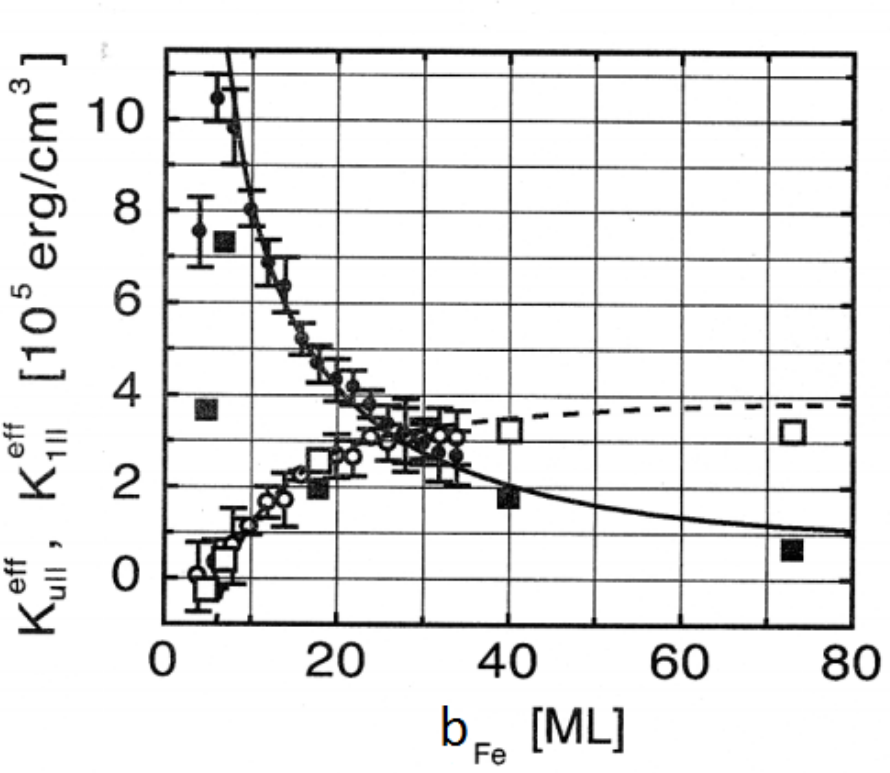

Fig. 2.5 Relation between film thickness (in terms of number of mono-layers) and constants of cubic (hollow symbols) and uniaxial (full symbols) anisotropy for epitaxial iron on GaAs(001) taken from reference [78]. The squares represent data collected using vibrating sample magnetometery and the circles represent data collected by MOKE.

The magnitude of the in plane uniaxial anisotropy, K_u, decreases as thickness increases due to the fact that the uniaxial anisotropy is an effect of the interface between the GaAs substrate and the iron film [80]. The exact microscopic mechanism of this is a subject for debate however with two leading theories as to the effect's origin. The first theory is that the interface effect is due to a strain induced by the lattice mismatch between the iron and the GaAs [81–84]. This is due to the fact that the lattice constant of iron is 2.866Å[85] which roughly half the lattice constant of GaAs which is 5.652Åleading to close lattice matching between the body centered cubic structure of $Fe_{0.81}Ga_{0.19}$ and the cleaved surface of the zinc-blende structure of the GaAs [78, 85]. The structure of the two lattices is the same however since the cleaved surface of the zinc-blende structure of the GaAs substrate matches the cleaved surface of the bcc iron [86]. There is however a mismatch in terms of electronic structure and bonding geometries between the two materials which is the source of the second

theory about the source of the uniaxial anisotropy in iron. This theory states that the uniaxial anisotropy occurs because of the bonding between the As atoms in the GaAs and the Fe atoms at the interface.

It states that the p states in the As hybridise with the d states in the Fe atoms resulting in uniaxial quenching of the magnetic moments of the Fe atoms in the $[1\bar{1}0]$ direction producing the uniaxial anisotropy in the [110] direction [87–90]. The origin of the uniaxial anisotropy in iron has been studied for some time however and there is still no conclusive evidence pointing to either of these explanations meaning that the question remains unresolved.

Next we will add the Zeeman energy, E_z, to our model. This is the energy due to the interaction between the internal magnetisation of the system and the external applied magnetic field H. This term is given by 2.9 and is the only term in our model dependent on the angle and strength of the external magnetic field.

$$E_z = -M \cdot H cos(\phi - \theta) \tag{2.9}$$

The final term we will include is the magnetoelastic energy density, E_{ME} which is given by the resolution of 2.10 which shows the general form of the contribution as well as the contribution in galfenol. In equation 2.10 α_i are the direction cosines of the magnetisation with respect to the cubic axes, B_1 and B_2 are magnetoelastic constants and ε_{ij} are strain tensor components [91].

$$E_{ME} = B_1(\varepsilon_{xx}(\alpha_1^2 - \frac{1}{3}) + \varepsilon_{yy}(\alpha_2^2 - \frac{1}{3})) + B_2(\varepsilon_{xy}\alpha_1\alpha_2 + \varepsilon_{yz}\alpha_2\alpha_3 + \varepsilon_{xz}\alpha_1\alpha_3) \tag{2.10}$$

When we apply equation 2.10 to the thin films which are being examined in this thesis we first assume the out of plane component of the magnetisation to be negligible due to shape anisotropy as described in section 2.2. This means that $\alpha_3 \sim 0$ meaning that it can be eliminated from the equation. We also assume that the cross strain terms, ε_{xy}, ε_{xz}, ε_{yz} are negligible compared to ε_{xx}, ε_{yy} and ε_{zz} making the B_2 section of equation 2.10 disappear as well. The remaining magnetoelastic constant B_1 is then defined using equation 2.11 in which λ_{100} is the magnetostriction constant and c_{12} and c_{11} are elastic constants.

$$B_1 = \frac{3}{2}\lambda_{100}(c_{12} - c_{11}) \tag{2.11}$$

When we substitute equation 2.11 into equation 2.10 and insert the direction cosines we find equation 2.12 in which λ_{100} is the magnetostriction constant along the [100] axis [61].

$$E_{ME} = \frac{3}{2}\lambda_{100}(c_{12} - c_{11})(\varepsilon_{xx} - \varepsilon_{yy})sin^2\theta \tag{2.12}$$

In equation 2.12 the strain terms ε_{xx} and ε_{yy} are dependent upon one another due to Poisson deformation which is described in section 3.10 where it is discussed in relation to the deformation of FeGa samples being subjected to a strain applied by a piezoelectric transducer.

Combining the ε_{xx} and ε_{yy} terms into a single term, ε and combining c_{12} and c_{11} with the magnetostriction constant into the magnetoelastic constant B_1 results in the magnetoelastic energy being expressed as shown in equation 2.13

$$E_{ME} = B_1\varepsilon sin^2\theta \tag{2.13}$$

When we combine all these energy terms the result is equation 2.14 in which E is the total energy of the system, K_c is the cubic anisotropy, K_u is the uniaxial anisotropy and λ_{100} is the strain applied along the [100] axis.

$$E = \frac{K_c}{4}sin^2(2\theta) + K_u sin^2(\theta - \frac{\pi}{4}) - M \cdot H cos(\phi - \theta) + \frac{3}{2}\lambda_{100} Y \varepsilon sin^2(\theta) \tag{2.14}$$

This is a useful tool for predicting and modelling hysteresis loops of materials found using the techniques detailed in chapter 4.2. By fitting this model to experimental data we can find values for the anisotropy constants K_c and K_u and the magnetoelastic coefficient as performed in chapter 4.

2.6 Anisotropic Magnetoresistance

Anisotropic magnetoresistance (AMR) is the property of a magnetic material whereby the resistance of the material changes depending on the angle between the applied current and the magnetisation of the material. AMR can be described using the relation in equation 2.15 where $\delta\rho/\rho$ is the AMR ratio, $\delta\rho$ is the change in resistivity due to the AMR effect, $\rho_{\parallel}$ is the resistivity of the sample with the current parallel to the magnetisation and $\rho_{\perp}$ being the resistivity with the current and magnetisation perpendicular to one another [92, 56].

$$\frac{\delta\rho}{\rho} = \frac{\rho_{\parallel} - \rho_{\perp}}{\rho_{\perp}} \tag{2.15}$$

If we generalise equation 2.15 for any given angle between the magnetisation in the plane and the current, θ_{AMR}, we can express the resistivity using equations 2.16 and 2.17 [93] in which ρ_{av} is the average resistivity of the sample when the magnetisation is rotated over 2π, $\Delta\rho$ is the amplitude of the AMR and θ_{AMR} is the angle between the current and the magnetisation.

$$\rho_{xx} = \rho_{av} + \Delta\rho cos(2\theta_{AMR}) \tag{2.16}$$

$$\rho_{xy} = \Delta\rho sin(2\theta_{AMR}) \tag{2.17}$$

AMR arises due two major influencing factors, the scattering rate being affected by the relative spin alignment between the static d electrons and the s electrons moving on the Fermi surface and the density of states of the s electrons on the Fermi surface. The influence of these factors is captured using equation 2.18 which gives the conductivity tensor σ_{xx} as a function of the density of states at the Fermi surface, $N(E_F)$, and the diffusivity tensor, D_{xx}.

$$\sigma_{xx} = N(E_F)D_{xx} \tag{2.18}$$

The shape of the Fermi surface may be distorted as a function of the magnetisation direction due to the SOI. The diffusivity tensor is determined by the scattering probability between the s and d electrons, which depends on the relative alignment of the spins of the s and d electrons.

2.7 The Landau-Liftshitz Equation

The Landau-Lifshitz-Gilbert equation (LLG equation) describes the rate of change of magnetisation, M, of an individual magnetic particle induced by the effective magnetic field. The LLG equation is a sum of two terms, the Landau-Lifshitz driving field and Gilbert magnetic

damping as shown in equation 2.19 in which α is the phonomenological Gilbert damping coefficient and γ is the gyromagnetic ratio.

$$\frac{d\mathbf{M}}{dt} = -\gamma \mathbf{M} \times \mathbf{H}_{eff} - \frac{\gamma\alpha}{M_s}\mathbf{M} \times (\mathbf{M} \times \mathbf{H}_{eff}) \tag{2.19}$$

$\mathbf{H}_{eff}$ is the effective field arising from the external magnetic field, the internal anisotropies of the sample, the other dipoles within the sample and the net demagnetising field of the sample all being modelled as a single value which is calculated using 2.20 in which E_{av} is the average energy density.

$$\mathbf{H}_{eff} = -\mu_0^{-1}\frac{\partial E_{av}}{\partial \mathbf{M}} \tag{2.20}$$

A visual aid to the form of the terms in the LLG equation is shown in 2.6 with figure 2.6a) showing the form of the driving term and figure 2.6b) showing the form of the damping term.

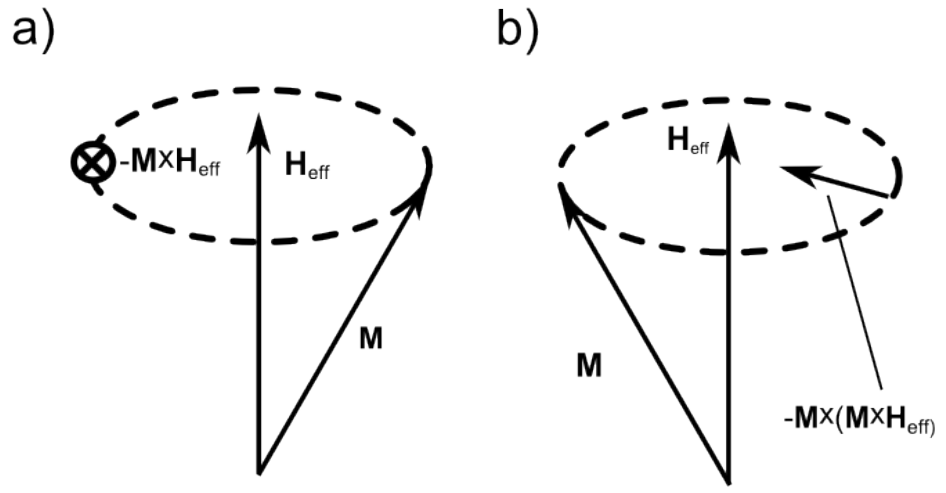

Fig. 2.6 Visual aid to the components of the LLG equation. a) shows the magnetisation precessing about the effective field ($\mathbf{H}_{eff}$) producing the time varying magnetisation by the cross product of $-\underline{\mathrm{M}}$ and $\mathbf{H}_{eff}$. Without damping the magnetisation will precess around the effective external field indefinitely however in b) the damping term is included acting to retard the precession of the spin. This means that the magnetisation will eventually align along the direction of the externally applied field.

This equation can be used for computational modelling of the dynamics of a ferromagnetic system as is performed by the Object Oriented MicroMagnetic Framework (OOMMF) computer program used to simulate magnetisation patterns as described in section 3.8.

2.8 Domain walls

In a magnetic material the magnitude of the individual magnetisation vectors are fixed, however they will still rotate in such a way as to reduce the internal energy of the system as much as possible. This means that regions of uniform magnetisation called magnetic domains will form within a sample. Magnetic domains must still obey the Maxwell equations meaning that the lines of B-field must be continuous due to equation 2.21.

$$\nabla \cdot \underline{B} = 0 \tag{2.21}$$

This means that domains left to settle into a stable state will tend to fall into what is known as a Landau flux closure domain, an idealised example of which is shown in 2.7. Note that this is a generalisation and that if it is energetically favourable to retain a single domain structure the system will do so due to the high energy cost of forming domain walls.

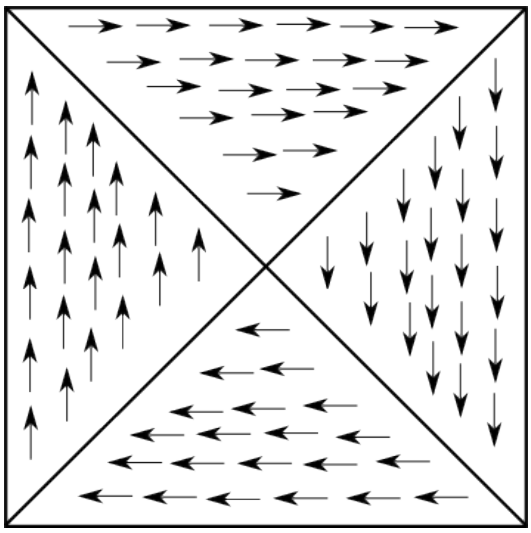

Fig. 2.7 Drawing of a Landau flux closure domain in an ideal square sample

The relation in equation 2.21 also leads to the stray field H_{str}, the magnetic field produced by the magnetisation of the sample. It is this field that we use to measure the magnetisation of a sample by its interaction with some external measurement apparatus (see chapter 3). The

energy associated with the stray field is given by the equivalent integrals given in equations 2.22 and 2.23 [94].

$$E_{str} = \frac{\mu_0}{2} \int_{allspace} H_{str}^2 dV \tag{2.22}$$

$$E_{str} = -\frac{\mu_0}{2} \int_{sample} \mathbf{H}_{str} \cdot \mathbf{M} dv \tag{2.23}$$

These values will always be positive (due to the H_{str}^2 term in 2.22) meaning that in order to reduce the net energy, the magnetisation within the sample will move to reduce the stray field energy. Since lines of magnetisation which end at the surface of the sample require more energy to maintain than lines of magnetisation which run parallel to the edges of the sample the favoured magnetic domain structures will be those which run parallel to the edges of the sample. This, combined with the fact that large areas of uniform magnetisation are also energetically favourable, means that the lowest energy magnetisation structures may not necessarily be those for which all the individual spins of atoms in the lattice are pointing the same way. The structure may therefore contain domain walls, lines along which the magnetisation rotates from one orientation to another. This may happen in two ways referred to a Bloch walls and Néel walls. Néel walls involve a rotation within the plane of the magnetisation and Bloch walls involve a rotation out of the plane of the magnetisation as demonstrated in figure 2.8[95].

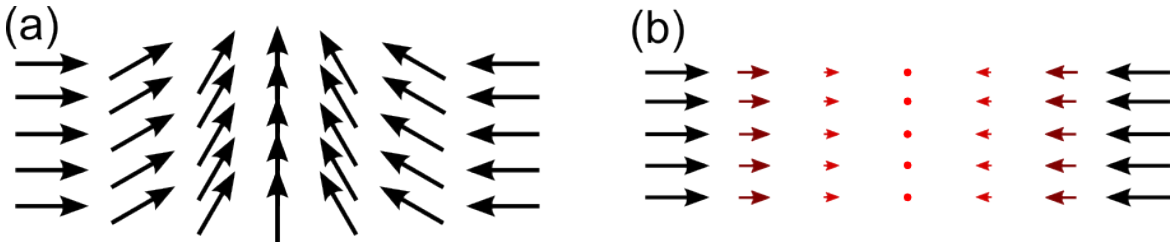

Fig. 2.8 Demonstration of the structure of Bloch and Néel type walls. (a) represents a Néel wall where the rotation is in the plane of the magnetisation and (b) represents a Bloch wall where the colour indicates the out of plane component of the wall.

The Bloch wall, in which the rotation is out of the plane of the material, is the most likely type of wall to form in a bulk sample, this is because $\nabla \cdot \mathbf{M}$=0 throughout the structure meaning that there is no stray field associated with the wall meaning it has the minimum magnetostatic energy possible. The rotation will still cause an increase in the exchange

energy due to the rotations of magnetisation involved, however the magnetisation of the domains will tend to lie along the easy axis meaning that the cost of forming a domain wall will be increased due to the center of the wall containing spins aligned along the hard axis of magnetisation. The energy required to form a Bloch domain wall is given as γ_B in equation 2.24 in which C is the exchange constant of the material, q is the width of the domain wall, b is film thickness and K_1 is a constant describing the anisotropy[95].

$$\gamma_B = \frac{\pi C}{q}(\sqrt{2}-1) + \frac{\pi q}{2}K_1 + \frac{\pi^2 M_s^2 q^2}{b} log(1+\frac{b}{q}) \tag{2.24}$$

When we look at the thin film case we find that Néel walls are much more likely to form since the energy required to form a Néel wall goes down as the thickness decreases since Néel walls exhibit the opposite effect to Bloch walls in that the they contain a volume charge rather than a surface charge. This means that when the volume of the domain walls is reduced by constriction of the film thickness the energy required to form a Néel wall is lower than the energy required to form a Bloch wall. We can see this by an examination of the energy required to form a Néel wall, γ_N, which is shown in equation 2.25.

$$\gamma_N = \frac{\pi C}{q}(\sqrt{2}-1) + \frac{\pi q}{2}K_1 + \pi^2 M_s^2 q[1 - \frac{q}{b} log(1+\frac{b}{q})] \tag{2.25}$$

When we compare the results of equations 2.24 and 2.25 we can see that at a certain thickness the type of wall most energetically favourable will switch as shown explicitly in figure 2.9 showing the energy required to form each type of wall with respect to the film thickness.

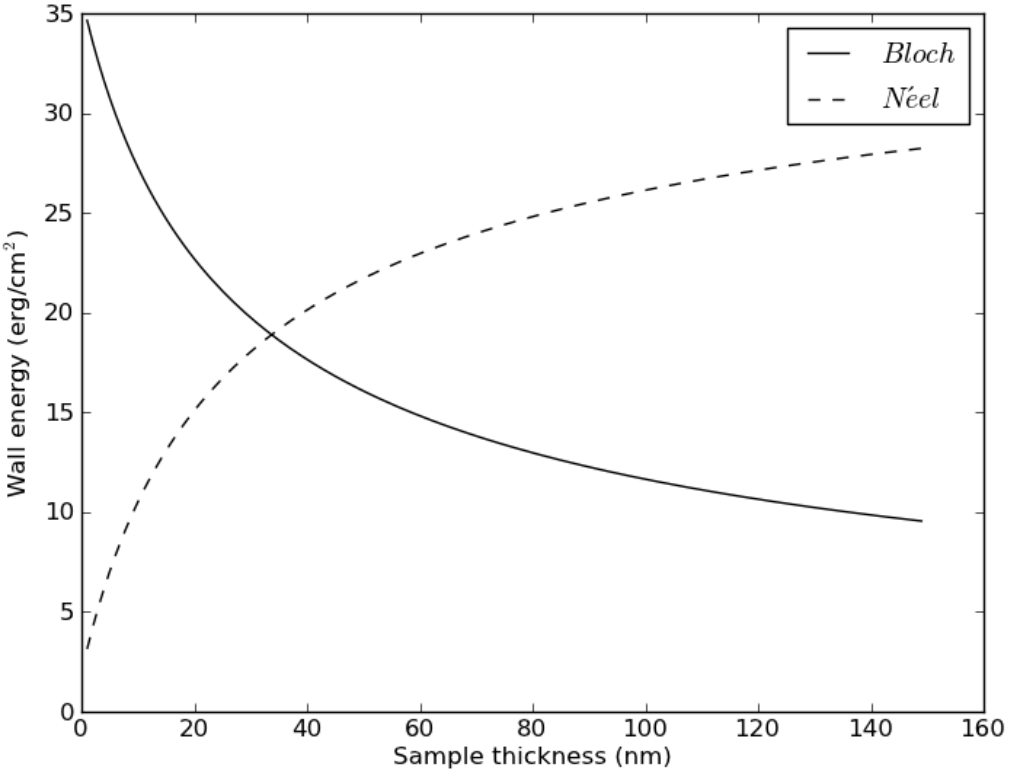

Fig. 2.9 Energy required to form Néel (dotted line) and Bloch (solid line) with respect to film thickness in iron (values taken from references [96, 79]).

The transition between these two types of domain wall is not a direct step with the wall type being Néel at one thickness and block in a film 1Å thicker but rather a gradual transition whereupon Néel walls develop a Bloch component which will form producing an angle between the out of plane component of the wall and the walls magnetisation, ϕ_f as demonstrated in figure 2.10.

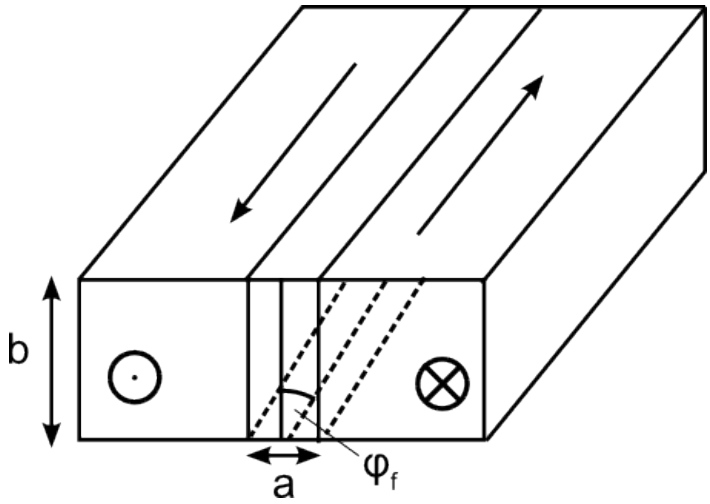

Fig. 2.10 Diagrammatic representation of the dimensions and angles used to describe domain wall behaviour in the text

When ϕ_f is greater than some critical angle ϕ_c the wall will be of the Néel type however when this angle is exceeded the wall will be in some intermediate state and when ϕ_f is equal to $\pi/2$ the wall will be a fully stable Bloch wall formation [97].

2.9 Performing XMCD in PEEM

XMCD relies on the difference in x-ray absorption (XA) spectra obtained using right and left-handed circularly polarised light. XMCD is a well established and powerful technique which utilises the dependence of attenuation coefficients on the relative orientations of the photon helicity and sample magnetization, in ferromagnetic materials, to reveal separate spin and orbital information about the absorbing atom. This combined with the inherent element specificity of XA make XMCD a uniquely revealing probe of the micromagnetic properties of solids.

XMCD results from the conservation of the angular momentum carried by a photon and the spin-orbit interaction. The easiest way to understand this process is to separate it into two sub-processes however this is done solely for demonstrative purposes [98]. The first process is the absorption of a circularly polarised photon by a core electron which is subsequently excited. The photon is circularly polarised and therefore carries an angular momentum of $\pm\hbar$ in the direction of propagation. The sign of $\hbar$ is dependent on the photon's helicity. The photon's angular momentum is then entirely transferred to the electron's orbital moment. In the second sub-process the spin asymmetry of the valence shell acts to detect

the magnetisation direction which, for maximum dichroism effect must be aligned with the photon spin direction. This process is demonstrated by figure 2.11.

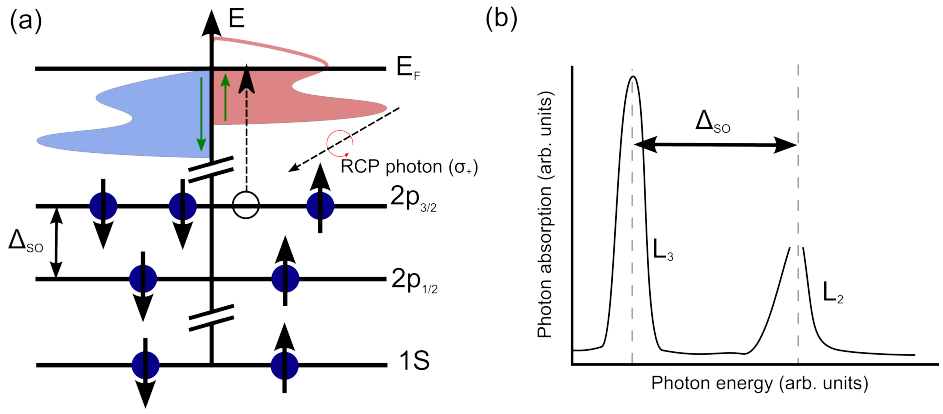

Fig. 2.11 XMCD effect illustrated for L edge absorption in an arbitrary material. a) shows the excitation of an electron in the p orbital into the empty states within the d orbital. b) shows the resulting XA spectrum for the L_3 and L_2 edges [99, 100].

The allowed transitions of the absorbing electron are governed by selection rules which result from symmetry considerations of the initial and final quantum states. In the dipole approximation for circularly polarised light only transitions where $\Delta l_q = \pm 1$ and $\Delta m = \pm 1$ and $\Delta m_s = 0$ are permitted, where l_q is the quantum number of the orbital angular momentum, m is the magnetic quantum number and m_s is the electron spin number. As such XMCD spectra indicate any difference in the occupation of allowed states from both an orbital and spin perspective. In a simplified one electron model, where one spin-band is filled and weak spin-orbit coupling in the d-band is ignored, the origin of the XMCD effect can be seen by considering the angular part of the squared dipole transition from the $2p_{\frac{1}{2}}$ and $2p_{\frac{3}{2}}$ states to the empty d-band states.

2.10 Magnetisation dynamics in confined magnetic structures

Similar to elastic waves in a crystal, spin waves (or magnons) are collective low energy propagating disturbances of a magnetic system. Spin waves broadly break down into two regimes depending on the wave-vector k which are described in terms of the source of the

spin wave. When the value of k is in the μm^{-1} range the spin wave is propagated due to the dipolar interaction between the spins. However when k is in the nm^{-1} range the spin wave is propagated due to the exchange interaction. Spin waves dominated by the dipolar interaction (dipolar spin-waves) tend to have frequencies in the 10s of GHz range, exchange spin-waves tend towards the THz range. This shift in frequencies can be seen in figure 2.12 taken from reference [101] showing the dispersion relations between dipolar spin waves and exchange spin waves.

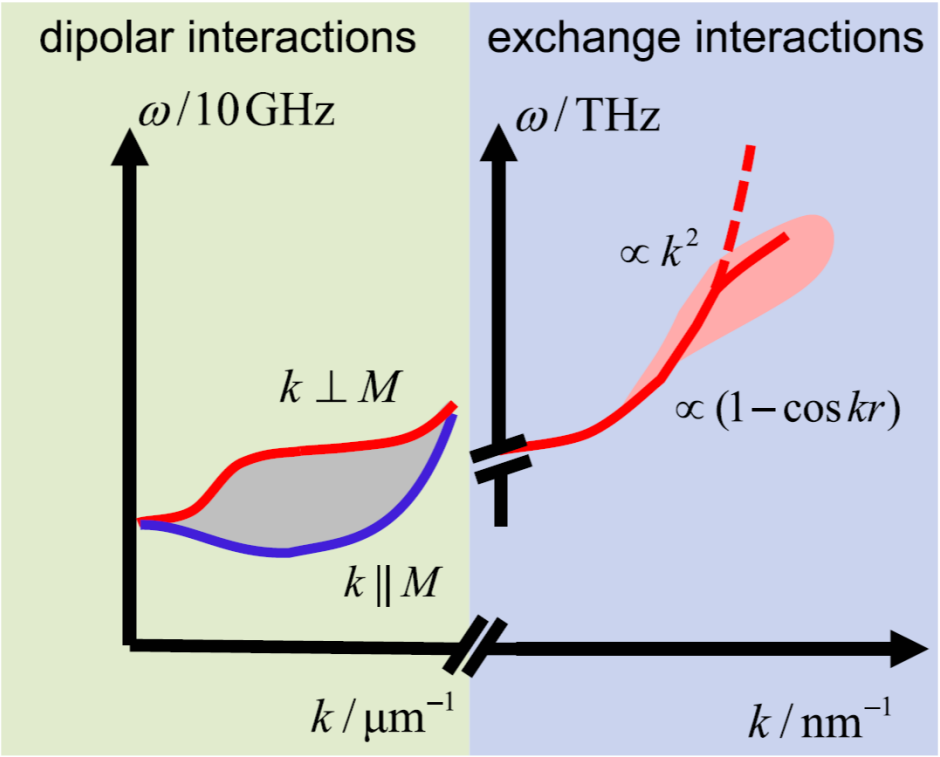

Fig. 2.12 Dispersion curves for magnons in an infinite plane taken from reference [101]. Shown, by the means of a split axis, are the dispersion curves for dipolar spin-waves in the GHz frequency range and exchange spin waves in the THz frequency range. The red line in the dipolar region represents the dispersion relation for magnons with wave vectors perpendicular to the magnetisation and the blue line indicates the dispersion curve for magnons with a wave vector parallel to the magnetisation. The grey region between the two represents magnons with wave vector and magnetisation at some other angle from one another. Shown in the THz range is the dispersion curve for exchange spin-waves roughly following a parabolic relationship at lower energies before the relation changes when the energy becomes high enough that all dipolar effects can be ignored. The red shading represents broadening of the available energy bands due to damping.

Two key points can be seen in figure 2.12. The first is that the dispersion relation for the dipolar spin-waves is dependent on whether the magnetisation is parallel or perpendicular to the wave vector. The second is that the relation for exchange spin-waves is roughly parabolic at low wave vectors but diverges away from this relationship as the wave vector rises. For the work presented in this thesis the important regime is that of the dipolar spin waves so the properties of the dispersion relation for the exchange waves will not be discussed in great detail.

The splitting in the dispersion relation for dipolar-spin waves occurs due to differences in the equations of motion depending on whether the spin waves are parallel or perpendicular to the wavevector. Spin waves with k||M are referred to as backward volume waves due to their negative group velocity. This negative group velocity occurs due to the precession of the spin waves being lower than the natural precession frequency of spins in the system. Dipolar spin-waves with k⊥M are referred to as being in the Damon-Eshbach (DE) geometry. The two types of dipolar spin waves are shown in figure 2.13.

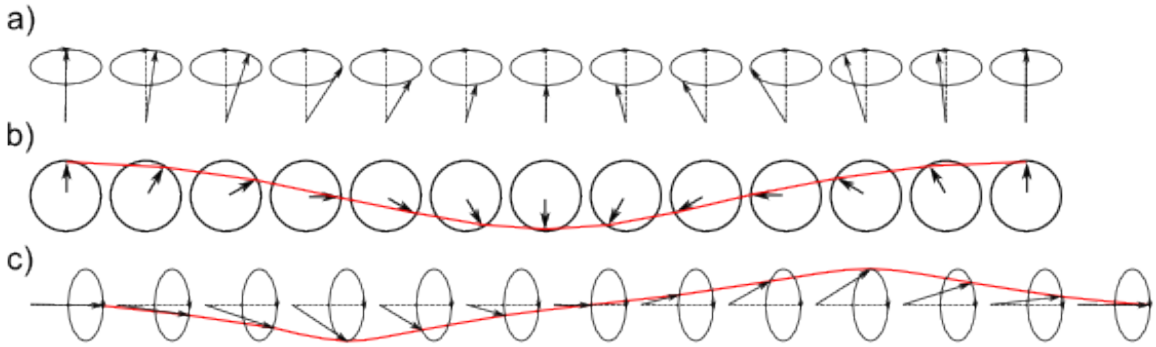

Fig. 2.13 Demonstration of the propagation of dipolar spin waves. a) shows a Damon-Eshbach as seen from the side where the wave is propagating perpendicular to the magnetisation. This is shown from above in b) in which the wave is shown by the red line. c) shows a backward volume wave from the side, once again the red line shows the waveform. [74]

So far we have been describing spin-waves in a general case. We must now move to describe spin-waves when confined in a realistic structure. Once the spin waves are confined the wave vectors become quantised due to the confinement [102]. The confinement limits the wave vectors of standing waves within the material in accordance with equation 2.26 in which n is an integer and d is the width of the confinement.

$$k = n\frac{\pi}{d} \tag{2.26}$$

The frequency of the DE spin waves in an infinite ferromagnetic film of thickness d can then be described by the modified Kittel equation given in equation 2.27 [103].

$$\omega_{DE} = \gamma\sqrt{H(H+M_s)+(M_s/2)^2(1-e^{-2kd})} \tag{2.27}$$

Where ω_{DE} is the frequency of the DE spin wave, γ is the gyromagnetic ratio, H is the applied field and M_s is saturation magnetisation. DE like spin waves in Landau flux closure states have been described forming along domain walls in reference [104] where the oscillation frequency is dependent on the film thickness, domain wall width, length and the effective field along the region of the domain wall. The edges of the material and the vortex core are assumed to act as pinning points, dictating the character of the stationary wave formed. Waves form along the domain walls due to the fact that the domain walls lie along regions of uniform effective field within the sample[105]. Once the spin waves have been excited the effect of the vortex core's motion is much lower than the effective field resulting from the distortion of the domain wall. This means that the spin wave along the domain wall is subject only to the effective field along the domain wall and the core can be approximated to be stationary.

Backward volume spin wave modes are unable to form in confined materials due to the confinement of the travelling waves although spin waves may exist which may be understood as being analogous to a combination of DE modes and back-propagating modes. In an infinite plane these form with wave vectors at some angle Θ to the magnetisation however they only transition from DE spin waves into back propagating spin waves once the angle between the magnetisation and the wave vector drops below the critical angle Θ_{DE} given by equation 2.28 [106].

$$\Theta_{DE} = arctan(\sqrt{H/M_s}) \tag{2.28}$$

2.11 Vortex core oscillators theory

In section 1.3 we saw that vortex core oscillators contain ferromagnetic structures in which the domain structure has settled into a Landau flux closure state. The core may be excited

to move in a circular motion due to the application of an external force and this motion is described in detail by the Thiele equation [107] [108] which is shown in 2.29 in which κ is a positive constant analogous to the core's mass, $\underline{v}$ is the core's velocity and $\underline{\underline{X}}$ is the position of the vortex.

$$\underline{G} \times \underline{v} = \kappa \underline{\underline{X}} \tag{2.29}$$

The term $\underline{G}$ in equation 2.29 represents the Gyrocoupling vector. This represents the correction forces acting on the core and is described by equation 2.30 in which μ_0 is magnetic permeability of free space, M_s is the saturation magnetisation, γ_0 is the gyromagnetic ratio, h is the sample thickness, $\hat{z}$ indicates that the vector is out of the plane and p is the polarisation of the core, either +1 or -1., Also used in equation 2.30 is n, which represents the dynamic winding number for the core's oscillation. This describes the number of times the vortex core travels around the center of the object in a single oscillation and the direction in which it travels with a positive winding number representing an anti-clockwise movement and a negative value indicating a clockwise movement. More information on the dynamic winding number can be found in reference [109].

$$\underline{G} = 2\pi \frac{\mu_0 M_s h}{\gamma_0} np\hat{z} \tag{2.30}$$

The motion of the core can then be determined by finding a general solution to equation 2.29 as shown in equation 2.31 in which $\underline{\underline{X}}(t)$ is the position of the core at time t, ω is the frequency of oscillation, X is the radius of the oscillation and $\hat{r}$ is the radial unit vector.

$$\underline{\underline{X}}(t) = X(cos(\omega t), sin(\omega t))\hat{r} \tag{2.31}$$

Looking at this general solution we can see that the core precesses in a circular motion with a frequency of ω and a radius X. This model makes the assumptions that the core is rigid and that the system is at equilibrium. However, more in depth theoretical models have been developed which show that the core behaves as a harmonic oscillator [110]. The simple model given in equation 2.29 is sufficient for the work described in this thesis and so we will now discuss the results of this general solution.

The general solution to the Thiele equation given in equation 2.31 combined with the formulation of the gyrocoupling vector given in equation 2.30 leads us to the conclusion that

for positive core polarisation the motion is in an anti-clockwise direction clockwise when the core polarisation is negative [111].

The core's polarisation can be used to realise its potential as a storage medium with the direction of the magnetisation being considered its state [29]. The magnetisation of the core may be reversed either by applying a large magnetic field or by exciting it to perform gyrotropic motion with a velocity greater than the critical velocity v_{cri} which is defined as a function of the exchange stiffness, A_{ex}, the gyromagnetic ratio, γ and a constant of proportionality which is unique to any given material, η by equation 2.32 [31].

$$v_{cri} = \eta\gamma\sqrt{A_{ex}} \tag{2.32}$$

This dependence of the critical velocity on the exchange stiffness can be understood by looking at the mechanism of vortex core reversal. When the core moves faster than the critical velocity the distortion of the core resulting from its motion causes it to nucleate into a core/anticore pair which annihilate in order to produce a single core. This single core will have the reverse polarisation of the original core as demonstrated in figure 2.14 which was taken from reference [30].

This means that in order to induce vortex core reversal the speed at which the core propagates must be great enough that the core becomes distorted despite the influence of the exchange stiffness preventing this distortion.

The dependency of core gyrotropic frequency on the anisotropies of the system is due to the effective mass of the core, κ being dependent on the magnetic susceptibility of the sample χ_0 as demonstrated by equation 2.33 in which M_s is the saturation magnetisation, h is the sample thickness and μ_0 is the magnetic permeability of free space.

$$\kappa = \pi\frac{\mu_0 M_s^2 h}{\chi_0} \tag{2.33}$$

This allows for the frequency of oscillation of a vortex core to be controlled by the various anisotropies of the system due to the dependence of χ_0 on the magnetic anisotropies of the sample[27, 28]. The relation between the magnetic susceptibility and the frequency of precession of the core, ω_c, is given explicitly by equation 2.34[111].

$$\omega_c = \frac{1}{2}\frac{\gamma_0 M_0}{\chi_0} \tag{2.34}$$

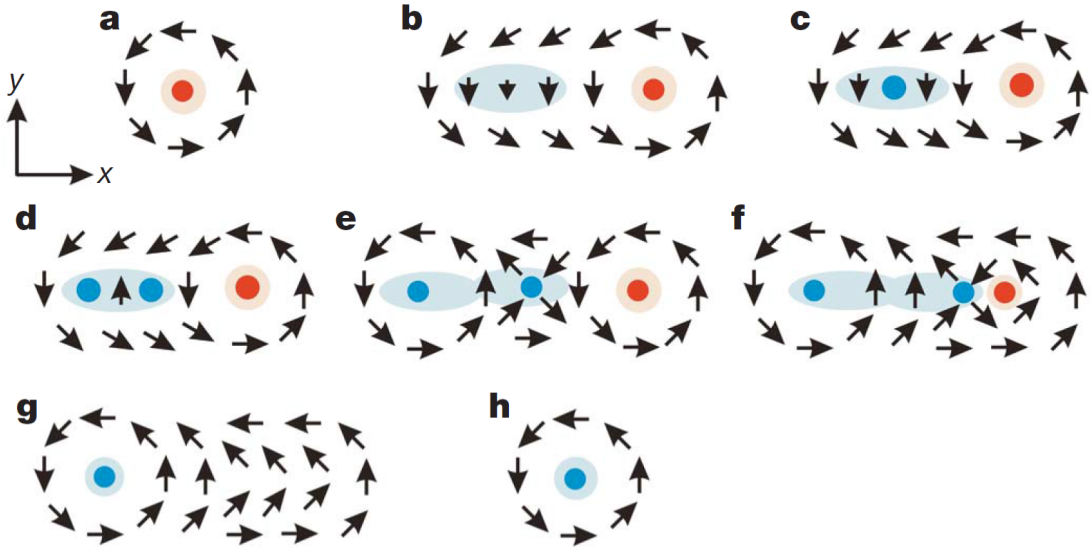

Fig. 2.14 Demonstration of the process of core reversal taken from reference [30]. The core's initial configuration is shown in a). As the speed of the core increases the core begins to distort forming an area with a out of plane component as shown in b). This out of plane component increases in c) causing the in-plane component of the magnetisation to turn with it. This in-plane component results in the formation of a vortex/anti-vortex pair as shown in d) and e). The anti-vortex/vortex pair are attracted to one another and annihilate in f and g resulting in the release of energy in the form of high frequency spin waves leaving a new vortex with a polarisation which is reversed to the initial vortex.

Hence a strain induced uniaxial anisotropy generated by an underlying piezoelectric layer provides a means of low power voltage modification of the oscillation frequency of a vortex core oscillator.

Chapter 3

Methods

This chapter consists of brief explanations of the methods used in order to collect the data presented in the rest of the thesis.

3.1 Photo-lithography and electron beam lithography

In order to fabricate micrometer length scale devices a process known as photolithography was used. Photolithography is a process used in microfabrication to pattern parts of a thin film or the bulk of a substrate. It uses light to transfer a geometric pattern from a photomask to a light-sensitive chemical photoresist on the substrate. A series of chemical treatments then either engraves the exposure pattern into, or enables deposition of a new material in the desired pattern upon, the material underneath the photo resist. In this study both techniques were used with the magnetic material deposited on the substrate after photolithography by evaporation or sputtering, as detailed in sections 3.2 and 3.3 respectively, or the magnetic thin film was milled using ion milling as described in section 3.4.

In order to fabricate materials on the nanometer length scale a e-beam resist was used in place of a photo-resist and the areas to be exposed were irradiated with a beam of electrons instead of UV allowing for higher resolution in the resulting image. The electron beam was controlled using electrostatic deflectors allowing for precise control of the position of the beam allowing for high resolution lithography. All electron beam lithography patterns described in this thesis were performed by Dr. Christopher Reardon at the University of York.

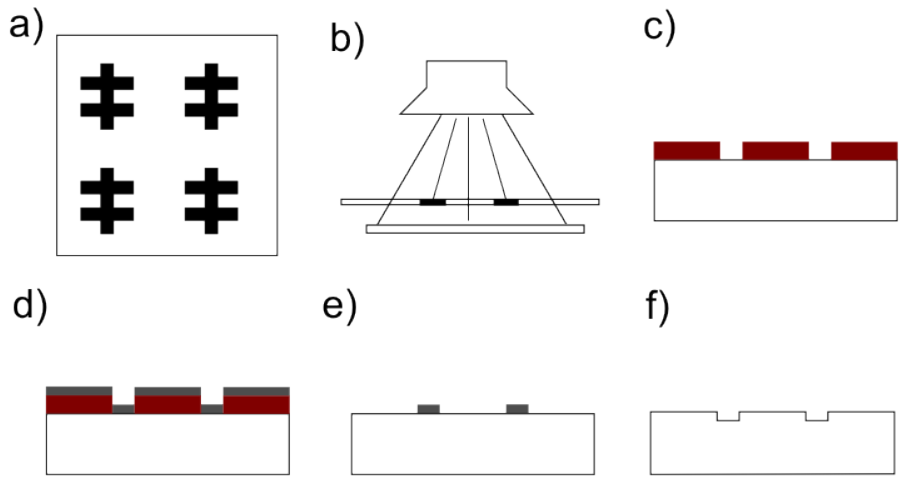

Fig. 3.1 Schematic diagram demonstrating the process of photo-lithography. a) shows a plan view of the photo-lithography mask and b) shows the mask being used to expose the photoresist to UV in selected areas. c) shows the photo-resist post development with the resist having been washed away in the desired areas by the development solution. d) shows the wafer post deposition of material using a process such as evaporation or sputtering. Section e) shows the material being left behind in the desired areas once the resist has been removed with acetone. f) shows the results of etching the material away using a technique such as ion milling.

3.2 Thermal evaporation

Thermal evaporation is a technique used to deposit metals onto a substrate. The metal to be deposited is placed in a coil of wire or 'boat' in a vacuum chamber with the sample suspended above the boat. Once the chamber has pumped down to the order of 5×10^{-7}mbar a high current is passed through the boat in order to heat the metal to the point at which the metal has a significant vapour pressure. Thermally vaporized molecules, with a mean free path of between 10cm and 1m, travel away from the source and condense on the surface of the substrate where they settle to form a metal film as shown in figure 3.2.

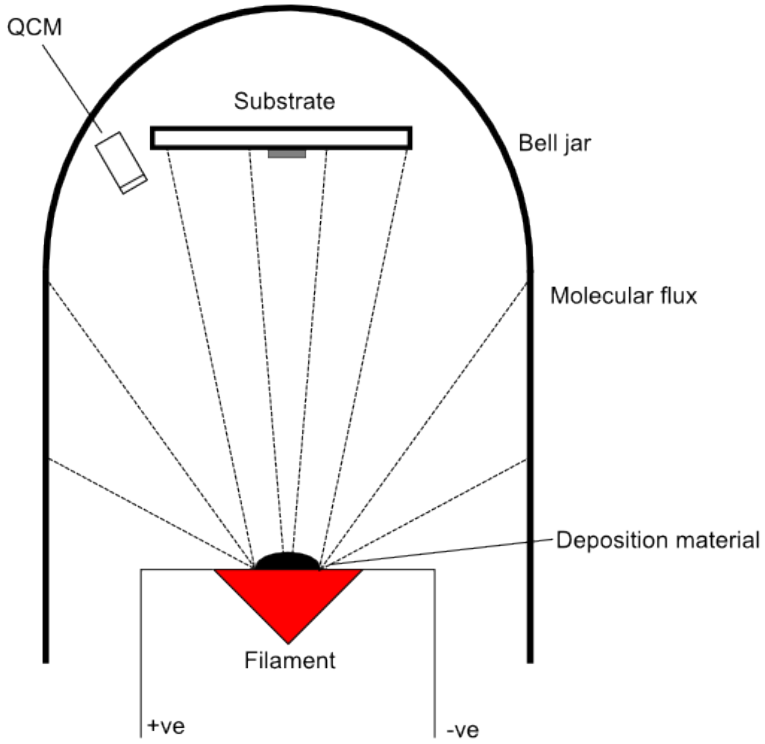

Fig. 3.2 Schematic diagram of the evaporation process used to create thin films of metal on a substrate. The chamber is kept at a vacuum of approximately 1^{-4}Pa and a high current is passed through the boat to heat up the metal to cause it to evaporate. The quartz crystal monitor is used to measure the rate at which the metal is deposited and the current is used to control the rate of deposition accordingly.

The mean free path of the molecules represents the average distance between collisions for a molecule. This distance is found using equation 3.1 in which λ_m is the mean free path, r_x is the radius of the molecule's cross section, K_B is the Boltzmann constant, p is the pressure and T is the temperature [112].

$$\lambda_m = \frac{K_B T}{4\sqrt{2}\pi r_x^2} \tag{3.1}$$

Equation 3.1 indicates the reason for the large variation in mean free path of thermally evaporated molecules since there is a large variation in the size and therefore cross sectional radius of the evaporated molecules.

3.3 Sputtering

Sputtering is a technique used to grow thin metal films on a substrate. The process involves holding an argon plasma above a metal disc using a magnetic field as demonstrated in figure 3.3 a). The argon ions collide with metal atoms at the surface of the target producing metal ions, atoms and clusters which are ejected from the surface of the target as shown in figure 3.3 b) which also shows a cross section of the field lines around the target. These clusters of metal are directed towards the sample substrate which is suspended above the targets and rotated at 30rpm in a vacuum chamber in order grow uniform thin metal films as shown in figure 3.3c). The chamber is pumped down to 1×10^{-7}Pa before sputtering begins giving a mean free path of between 1 and 10^5km, the large variation in mean free path is due to the variability in size of metal clusters being ejected from the surface of the sputter target. When the argon enters the chamber the pressure increases to 0.1Pa giving a mean free path of between 0.1 and 100mm. The rotation ensures an even deposition across the wafer and the vacuum ensures a large mean free path of metal atoms and clusters between the targets and the substrate.

In DC sputtering the argon ions are produced by passing non-ionised argon through a constant electric field in order to ionise it. This electric field is produced by a bias voltage of between 150V-250V. The ions are then trapped as a plasma using a magnetic field above the target using permanent magnets. Since the plasma follows the magnetic field lines it forms a ring of plasma above the target. The ions collide with the surface of the target causing metal clusters to be ejected from the surface of the target which then settle on the surface of the substrate. When the metal used as the target is insufficiently electrically conductive RF sputtering is used. This works the same way as DC sputtering except the electric field used to ionize the argon is oscillating at RF frequency. This is done to prevent charge build up on the surface of the target.

Sputter growth is preferable to MBE growth due to its faster growth rates, lack of need for a ultra high vaccum system and lower equipment costs. Despite the typically lower growth quality of films grown by sputter deposition, sputter grown films have been shown to form epitaxially with their substrates [113]. All sputtering performed in the collection of the data presented in this thesis was performed using a Mantis QPrep500 ultra high vacuum sputter deposition system.

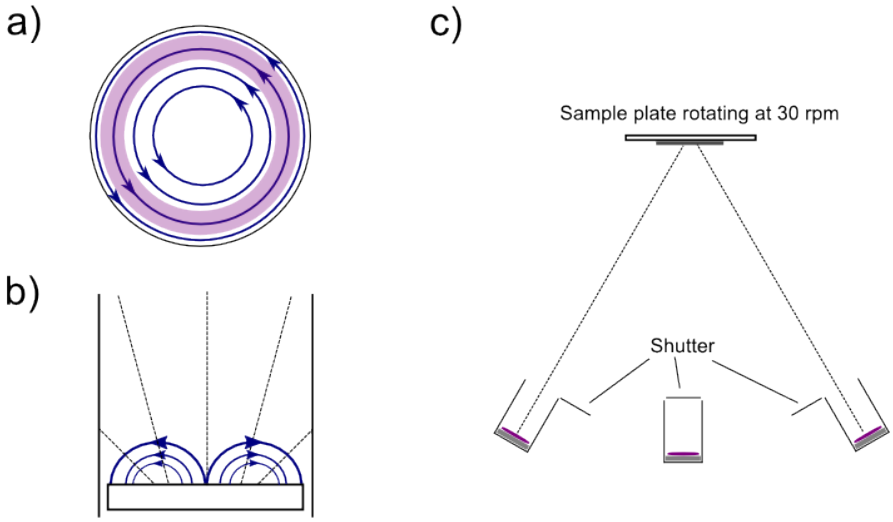

Fig. 3.3 Schematic diagram of the sputtering process used to create thin films of metal on a substrate. Section a) shows the magnetic field lines of the target as seen from above in blue and the plasma following the field lines being shown in purple. The head of the target is magnetised in sections in order to produce a circular magnetic field. Section b) shows the field lines of the target as seen from a cross section through the side as well as the metal clusters being ejected from the surface of the target. Section c) shows the process of sputtering where ions are ejected from the targets and stick to the substrate which is rotated to ensure an even metal film coating.

3.4 Ion milling

In order to etch away acid resistant materials, such as aluminium, ion milling was used. This technique involves irradiating the surface of the sample with a stream of Ar^+ ions produced by reversing the polarity of the sputter machine described in section 3.3. A 630V bias was established between the sample and the target where the plasma was generated within a pressure of 0.16Pa with the distance between the target and the sample being 20cm. A full treatment of this technique can be found with reference [114]. All ion milling described in this thesis was performed using the sputter machine described in section 3.3.

3.5 Substrate thinning

In order to increase the amount of stress transmitted to the samples the back of the substrate was thinned using an acid etch. This process involved mounting the samples face down to

microscope slides and then etching the backs of the samples using an etch solution made up of 5ml water, 40ml of hydrogen peroxide and 5ml of 95% pure sulphuric acid. This process was used to thin GaAs substrates used to grow thin galfenol films in chapters 4 and waveguides in 5.

3.6 SQUID magnetometry

A Super Conducting QUantum Interference Device Magnetometer is a piece of equipment used to measure the magnetisation of materials as a function of applied external magnetic field [115, 116]. The magnetometer used for the experiments in this thesis was a quantum design MPMS XL SQUID magnetometer. A small ($\sim$5$\times$4mm) sample is held on an oscillating wire and is then passed through an induction coil in a magnetic field. The magnetic field aligns magnetisation in the sample so that when the sample passes through the coil the coil experiences a magnetic field due to the magnetisation of the sample as shown in figure 3.4.

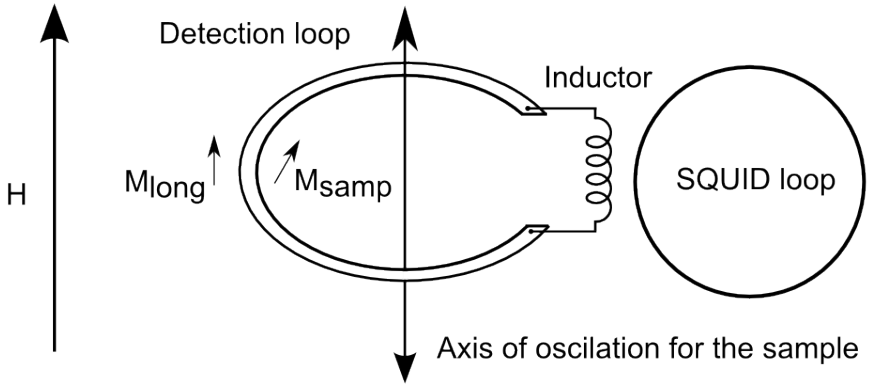

Fig. 3.4 Demonstration of the detection coil in a SQUID. The sample moves through the detection loop which is inductively coupled to the SQUID loop. The magnetisation of the sample induced a current in the detection loop which is transferred to the SQUID loop by the inductor. Since the magnetisation is measured in only one direction the result of this measurement will be the magnetic moment from the movement of the sample's stray field relative to the static detection loop rather than a direct measurement of the sample's magnetisation.

This set-up means that the value measured by the SQUID will be the current induced in the coil by the movement of the stray field lines relative to the static coil, the long moment, M_{long}, of the sample rather than a direct measurement of the magnetisation M_{samp}. Since

we will be measuring the magnetisation in only one vector direction at some distance from the sample the measurement we make will be a projection of the magnetisation rather than magnetisation itself. The detection loop is then inductively coupled to the SQUID loop which is a loop of superconducting material with one or more Josephson junctions in it. A Josephson junction is a link between two superconducting regions which are otherwise isolated from one another. Cooper pairs moving through the superconducting regions can tunnel through the junction with no voltage drop so long as the critical current,i_c, is not exceeded and the length to tunnel through is less than the coherence length, ξ. The current crossing a Josephson junction, i_s is described by equation 3.2 in which $\Delta\phi_{ph}$ is the phase difference between the two pieces of superconductor on either side of the junction.

$$i_s = i_c sin(\Delta\phi_{ph}) \tag{3.2}$$

This means that if the Josephson junction is made to carry an RF current at the critical amplitude, i_c, any difference in electric or magnetic field across the Josephson junction can be easily detected by means of an induction coil linked to a LC or tank circuit as shown in figure 3.5.

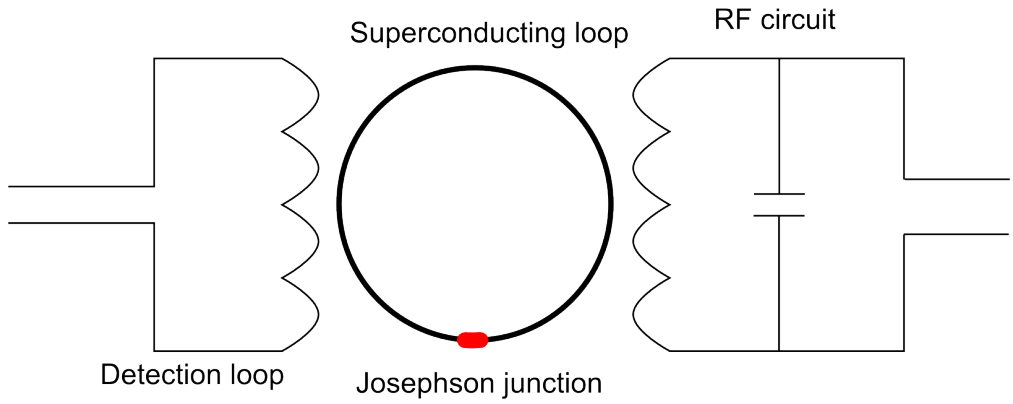

Fig. 3.5 Diagramatic representation of an RF SQUID loop. The superconducting loop is inductively coupled to both the detection loop and the RF tank circuit used to determine the change in current in the superconducting loop.

The LC circuit is a circuit containing an inductor (L_t) and a capacitor (C_t) through which a RF voltage is passed at a resonant frequency given in equation 3.3 in order to produce the lowest possible impedance for the circuit.

$$f_0 = \frac{1}{2\pi\sqrt{L_t C_t}} \tag{3.3}$$

When a current is induced in the detection coil it is passed to the superconducting loop and then passed through to the RF circuit causing the RF oscillations to decrease in amplitude and change in frequency. By measuring the change in amplitude and frequency produced by the sample moving through the detector loop we can find the long moment of the magnetisation. By this method we can register that a change has taken place however to more accurately measure the change in long moment we have to add a feedback loop to the LC circuit allowing us to find the long moment from the current required to counteract the change produced by the detection coil. This feedback loop calculates the change in frequency by considering the change in inductance in the tank circuit due to the change in flux. This change is described by equation 3.4 which describes the new inductance of the inductor in the tank circuit , $\tilde{L}_t$, as a function of flux coupled to the loop, ϕ_e, the coupling constant describing the quality of the coupling between the inductors in the setup, κ, and the constant β_e which is a constant based on the Josephson junction in the SQUID loop.

$$\tilde{L}_t = L_t(1 - \kappa^2 \beta_e cos(2\pi\phi_e)) \tag{3.4}$$

3.7 Modelling magnetic hysteresis loops

In order to find anisotropy values from SQUID magnetometry, hysteresis loops were simulated for a range of K_c and K_u values and then a cost function was calculated for each simulated loop. The cost function, C, describes the difference between the simulated loops and collected data in accordance with equation 3.5 in which x_i is point i on the simulated curve with n points and y_i is point i of the collected data.

$$C = \sum_{i=1}^{n} (x_i - y_i)^2 \tag{3.5}$$

The K_c and K_u values for the loop with the lowest cost function were used as the K_c and K_u data for that SQUID loop. The loops were simulated by setting the applied field to a maximum value and then moving through field values modelling the magnetic free energy as

described in section 2.5 for each field value. The equation for the magnetic free energy is restated in equation 3.6 in the interests of clarity.

$$E = \frac{K_c}{4} sin^2(2\theta) + K_u sin^2(\theta) - M \cdot H cos(\phi - \theta) + \frac{3}{2}\lambda_{100} Y \varepsilon sin^2(\theta) \tag{3.6}$$

Equation 3.6 was solved by finding the energy for θ in the range -190° to +190° in 0.1° steps. Then the energy minimum closest to the previous value of theta was used as the new theta value used to find the magnitude of the projection of the magnetisation along the field direction as shown in figure 3.6 (the first theta value was set to the direction of the field).

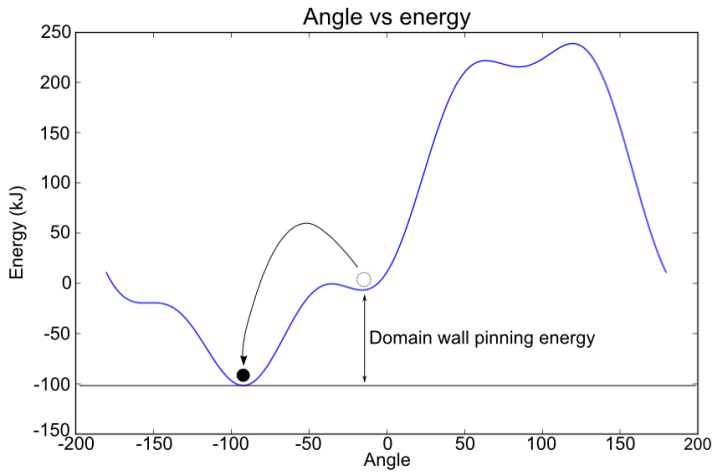

Fig. 3.6 The result of calculating the energy value for all theta values at a 10mT externally applied field with a saturation magnetisation of $1.590 \times 10^6 \mathrm{A}m^{-1}$, a cubic anisotropy value of 2.485×10^4 J/m^3, uniaxial anisotropy value of 2.05×10^3 J/m^3 and a strain anisotropy value of 4.7×10^3J/m^3. When the difference in energy between the local minimum and the global minimum is less than that of the domain wall energy the system will move into the global minimum to simulate domain wall switching.

When the difference in energy between the local energy minimum and the global energy minimum was lower than the domain wall pinning energy the value of θ was adjusted to that corresponding to the global minimum, simulating the depinning of domain walls and invoking a sudden switching event. This means that in our simulation rather than simulating individual regions becoming depinned and forming domain walls the entire system switches at once as shown in figure 3.6. It should be noted that the depinning energy is the distinct from the energy requrired to form a domain wall described in equations 2.24 and 2.25. Once

the θ value for a given external field is determined it is saved in a list which is then converted into a magnetisation value using the projection given in equation 3.7.

$$M = M_s sin(\theta) \tag{3.7}$$

The code sweeps the field between the limits set by the user in order to generate a hysteresis loop which is then compared to the collected data by finding a cost function as described in equation 3.5. The loop with the lowest cost value is then assumed to be the best fit of the collected data and the values used to generate that loop are used for the anisotropy energies or domain wall energies depending on what values were being searched for.

The errors were found using a windowing function, by plotting the fitting result for an amount above and below the value found for the anisotropy and measuring the number of experimentally found points between these two curves. When the number of points within the window exceeded 2 σ of the total number of points, meaning 66% of the total number of points lay inside the window, the value used to create this window was used as the error for that anisotropy for the loop. This is demonstrated in figure 3.7 which shows the curves making up the windows as well as the experimentally found data points.

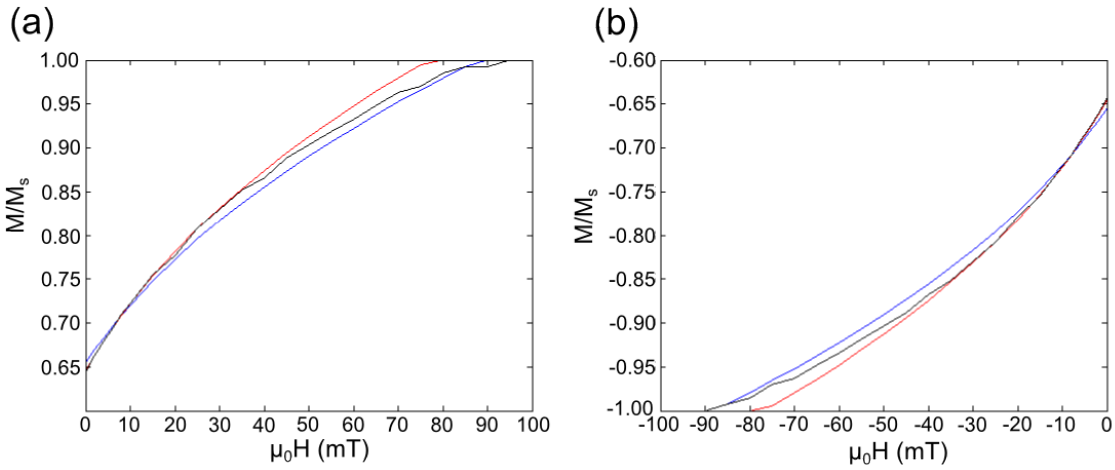

Fig. 3.7 Demonstration of the windowing function used to create the error bars on the anisotropy results from analysis of SQUID data loops. The collected SQUID data is represented by the black line, the blue line represents the fit with the higher anisotropy value and the red line represents the fit with the lower anisotropy. In a) the fitting section of the loop where the field is sweeping from +100mT to 0mT is shown and in b) the fitting section of the loop with the field sweeping from -100mT to 0mT is shown.

3.8 The Object Oriented Micro-Magnetic Framework (OOMMF)

OOMMF is a modelling program developed by the information technology laboratory at the National Institute of Standards and Technology (NIST) in the USA [51]. It is a program designed to perform micromagnetic simulations using a finite differences approach. The program splits a simulated object into a grid of individual magnetic spins and solving the LLG equation, described in section 2.7, for each individual element in the grid. In this way the evolution of a system over time when influenced by a magnetic field can be studied or else the most energetically favourable ground state can be found depending on the conditions the simulation was set in motion with. This system does however make some assumptions such as modelling the system as a grid of highly localised spins and with a zero temperature approximation. The simulation models the grid advancing in discrete time steps, solving the LLG equation at each time step based on any external field combined with material anisotropies and the demagnetising fields.

3.9 Spatial FFT program

In order to study the appearance of magnons within micromagnetic simulations a program was developed that would calculate the Fourier transformation of the magnetisation of each element in the simulation as it changes over time. The simulations produced arrays containing the magetisation in x, y and z as described in section 3.8 which were then converted into bmp images representing the magnetisation in the x, y and z directions where red indicated a large positive magnetisation and blue a large negative magnetisation. These images were then loaded into python and the colour converted back into a 2 dimensional array representing the magnetisation in the direction being investigated. These 2 dimensional arrays were then stacked upon one another into a 3D matrix representing the change in magnetisation in a particular direction changing in time. Next the program ran through the pixels doing a 1D Fourier transform on each one using the fast Fourier transformation algorithm [117]. Every time a row was completed the results were saved as a 2D matrix so that if the program crashed part way through the simulation the results could be salvaged. This process is demonstrated in figure 3.8.

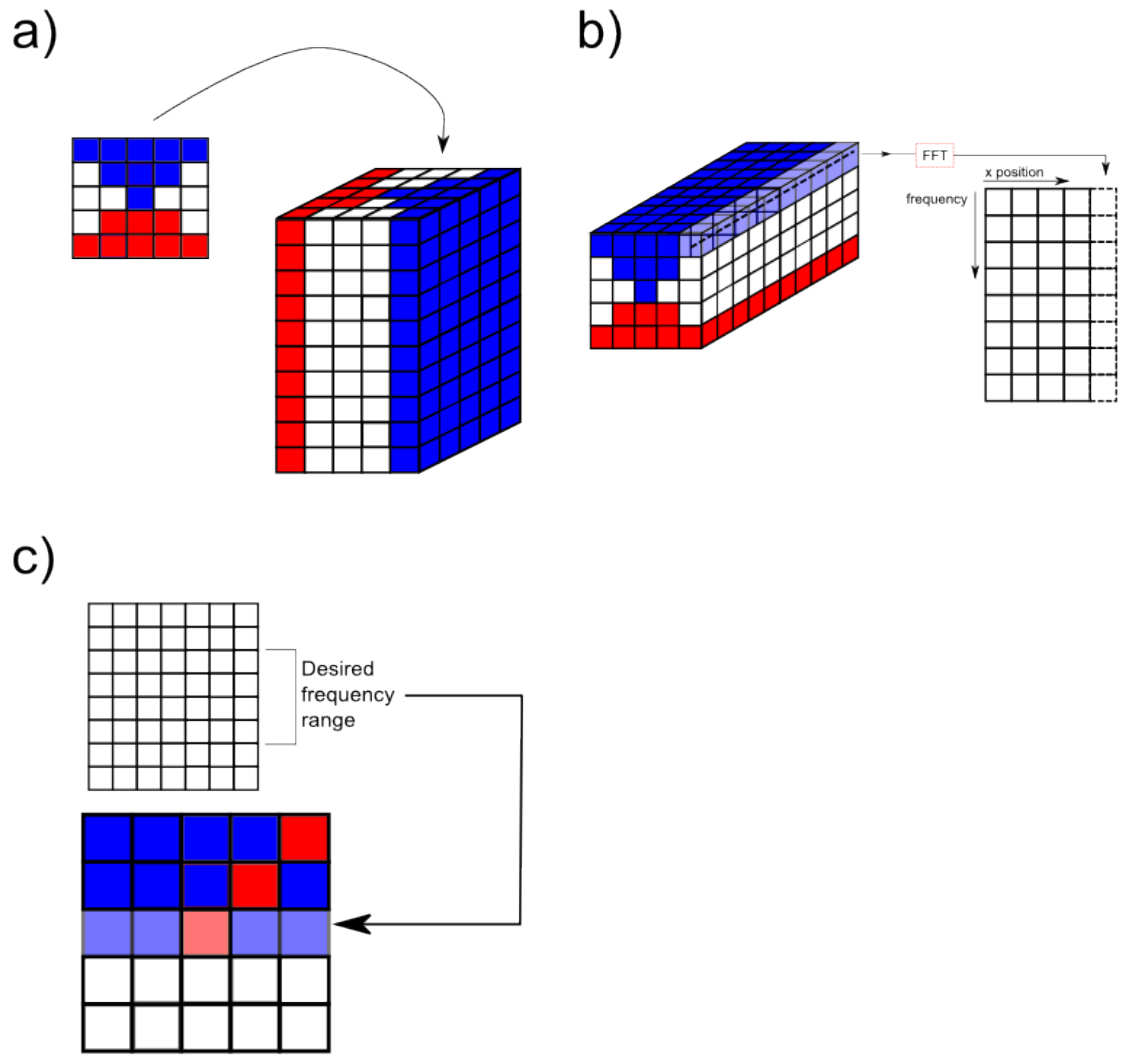

Fig. 3.8 Demonstration of the process of the 3D Fourier transformation program. In part a) the images are stacked one upon another in order to form a 3d stack. In part b) cross sections of 1 pixel are taken through the stack and the result is Fourier transformed to produce the frequency profile of that pixel. This frequency profile is then saved in a 2D matrix containing all the frequency profiles for the pixels with that y position. This process is repeated for all the y positions in order to build up a set of 2D matrices describing the frequency profile for each y position which were saved to the hard disc in order to avoid filling the RAM with 2 large 3D matrices. The final step is shown in c). The 2D matrices are loaded back in and then used to build up heat maps for a set of frequency ranges. These heat maps are built line by line as the 2D matrices are loaded in one at a time.

The final step involved producing a series of heat maps demonstrating which areas of the image oscillated within the frequency range indicated by that heat map. In order to produce

these heat maps the Fourier transformed data was loaded back into the program so that the heat maps could be constructed line by line. This involved summing the amplitude of the Fourier transformations for each pixel across the desired frequency range and since the data was saved line by line it was more expedient to produce the heat maps in this way. Example heat maps for a test piece consisting of four squares which oscillate at different frequencies is shown in figure 3.9.

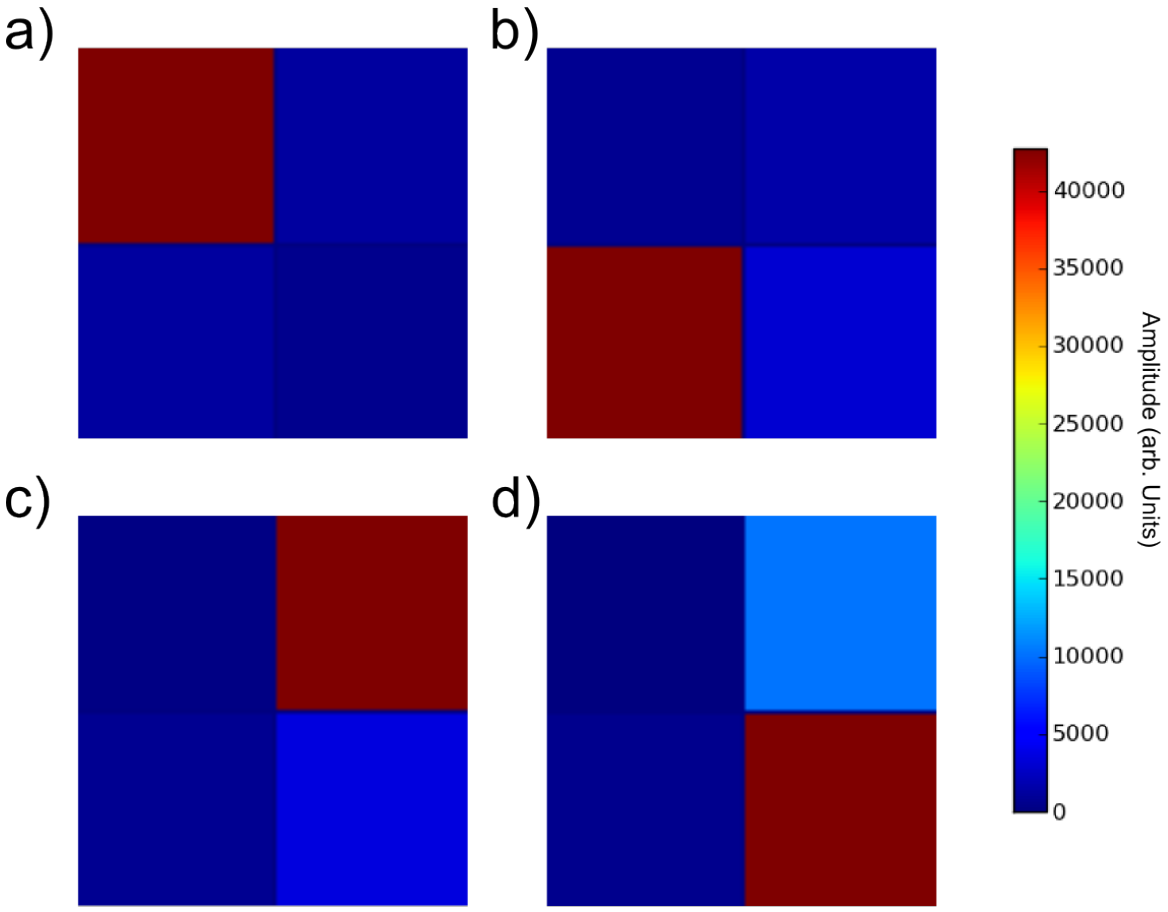

Fig. 3.9 Heatmaps showing the results of the 3D fft on the test piece. The testpiece consisted of a 100 pixel grid split into 4 squares which oscillated at 2, 5, 11 and 23Hz. The image stack was made up of 500 bmps with a 0.01s timestep between the images. Shown here are the resulting heatmaps for a)2Hz, b)5Hz, c)11Hz and d)23Hz drawn with a window of 0.1Hz. Show here is a colourbar which shows the values of the pixels.

This method can be refined in order to highlight weaker modes by calculating the natural log of each pixel however this method sacrifices spatial resolution as it brings the peak frequencies closer to the background level in the Fourier transformation.

3.10 Transport measurements

3.10.1 Transport method

In order to measure the effect of strain on the magneto-resistance of samples two Hall bars were mounted on a piezo transducer using an epoxy resin. The piezo electric transducer used are piezostacks PSt 150/5x5/7 devices from piezomechanik. The safe operating range of these devices lies between -30V and +150V (In order to prevent damage to the samples a maximum voltage of 50V is usually used) and is capable of producing a total tensile force of 1600N. Not all of this force is transmitted to the sample however, due to elasticity in the epoxy used to secure the sample to the stressor, meaning that the stress must be determined experimentally which is why the experiment requires two Hall bars. The alignment of the bars is shown in figure 3.10, the upper bar is aligned so that the strain (measured as a ratio of length with and without stress applied) is applied along the $\langle 100 \rangle$ axis meaning that it produces the largest possible magnetostrictive effect as discussed in section 1.4.

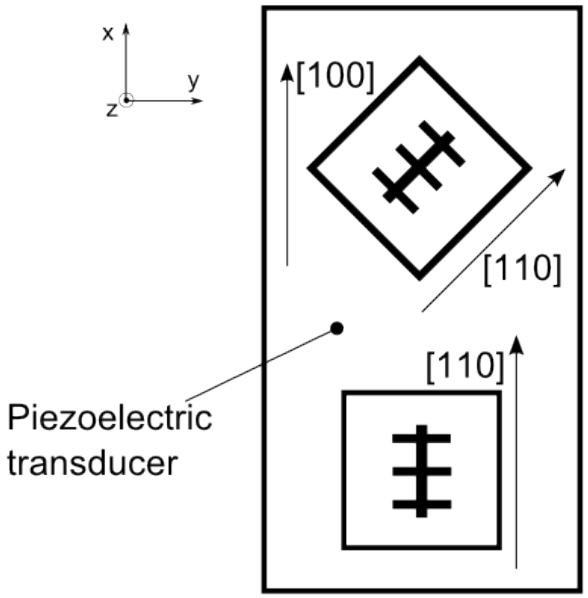

Fig. 3.10 Hall bar alignment on a piezoelectric transducer

The bar aligned so that the stress is applied along the $\langle 110 \rangle$ axis is used to gain a measure of the strain being experienced by the sample due to the piezoelectric transducer when a specific voltage is applied. This is done by first considering equation 3.8 which describes the relation between object length and applied strain. Poisson's ratio , ν, represents the ratio to which a material deforms in the y and z directions when a stress is applied in the x direction

and for our purposes we will assume it to be equal to 0.5 with deformation in the y and z planes of the sample being exactly equal. The strain is given by equation 3.8 in which x_0 is the initial length of the sample in the x direction, x_1 is the length of the sample in the x direction with a force applied in the x direction, x_0 is the length of the sample in the x direction with no force applied and ε_x is the strain in the x direction.

$$\varepsilon_x = \frac{x_1 - x_0}{x_0} \tag{3.8}$$

We will now define Poisson's ratio, ν as the ratio between the strain in the x axis and the strain in the y or z axes as we have done in equation 3.9 with the strain being denoted by ε_i.

$$\nu = -\frac{\varepsilon_y}{\varepsilon_x} = -\frac{\varepsilon_z}{\varepsilon_x} \tag{3.9}$$

In order to use this we first need to express the resistance, R, in terms of the length (x), width (y) and thickness (z) of the sample and its resistivity ρ as is done in equation 3.10

$$R = \frac{\rho x}{yz} \tag{3.10}$$

By partially differentiating R across x,y and z we find equation 3.11.

$$\Delta R = \frac{\rho \Delta x}{yz} - \frac{\rho x \Delta y}{y^2 z} - \frac{\rho x \Delta z}{y z^2} \tag{3.11}$$

Then dividing ΔR by R yields equation 3.12.

$$\frac{\Delta R}{R} = \frac{\Delta x}{x} - \frac{\Delta y}{y} - \frac{\Delta z}{z} \tag{3.12}$$

Equation 3.9 can then be substituted into equation 3.12 in order to produce the relation between resistance and strain given in equation 3.13 where we assume that Poisson's ratio is equal to 0.5.

$$\frac{R - R_0}{R} = (1 + 2\nu)\varepsilon_x = 2\varepsilon_x \tag{3.13}$$

The assumption of Poisson's ratio comes from the fact that the piezoelectric crystal the sample is mounted to has a Poisson's ratio of 0.5. However in reference [42] Clark et al. calculated values for the magnetoelastic energy constants, B_1 and B_2, (see section 2.5) for bulk galfenol which can be used to find a Poisson's ratio of 0.44 which would give our estimation of Poisson's ratio an error of 12% giving an error in our strain measurement of 6%. Since the relation between the resistance of a material and the strain on that material can be found using equation 3.13 the strain produced when the transducer is subject to different voltages using the bar aligned along the $\langle 100 \rangle$ axis can be found. By applying a saturating magnetic field in the $\langle 110 \rangle$ direction, in order to prevent the magnetisation from rotating in response to induced strain, we can ensure that any change in resistance is due to the strain on the sample only. We are unable to find the absolute strain applied to the sample since the curing process involves the glue expanding when setting in the oven and contracting when removed from the oven applying some unknown strain to the sample. We can however find the relative strain by taking the mean of the resistances at maximum and minimum strain as the zero strain resistance and then substituting it into equation 3.13 in order to find the relative strain for each resistance value.

The bar aligned with the [100] axis parallel to the stress is used to measure the effect of stress on the magnetoresistance of the sample. This bar is used for our measurements of the effects of a magnetic field because the $\langle 100 \rangle$ axis in Galfenol provides the strongest magnetostrictive response as described in section 1.4. We can identify the magnetically easy axis as the axis along which there is minimal change in the measured resistance as a magnetic field is swept between ± 0.01T along it and the hard axis is the axis in which large changes in resistance are observed. This is because the experiment measures the resistance of the sample rather than a direct measurement of the magnetisation. This means that when the magnetisation rotates away from the hard axes it does so gradually moving through an intermediate state which can be easily detected as a change in resistance of the sample. When the field is applied along the easy axis however the magnetisation reversal occurs over a small field range meaning it cannot be detected easily by measuring resistance at this resolution of field sweep.

The direction of the magnetisation was determined using measurements of the transverse and longitudinal components of AMR. This was done by first finding the angle of the magnetisation θ_{AMR} using equation 3.14.

$$\theta_{AMR} = \frac{1}{2} arcsin\left(\frac{\rho_{xy} - \rho_{av}}{\Delta\rho}\right) \tag{3.14}$$

The value of θ_{AMR} found from equation 3.14 is then used to find the magnetisation in the direction of R_{xy} using equation 3.7 (restated as equation 3.15) which is then used to produce a hysteresis loop for the sample at that level of applied stress.

$$M = M_s sin(\theta_{AMR}) \tag{3.15}$$

The angle, θ_{AMR}, in equation 3.15 is demonstrated by figure 2.4 which is repeated for the benefit of the reader in figure 3.11.

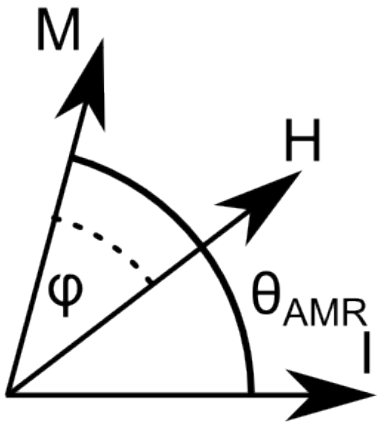

Fig. 3.11 Visual guide for the angles used in transport measurements.

The switching events in these hysteresis loops are then found as a function of field and then by comparing the position of the switching events in the actual data to the position of the switching events in simulated loops, as described in section 3.7, values for the strain anisotropy, K_s, and the pinning energy, E_{DW}, as a function of the strain can be determined. The field at which the switching event occurs is determined by first deciding where the start and end of the switching field occurs, the mean of these two values is considered as the location of the switching event. The errors on these measurements can be determined by finding the values for K_s and E_{DW} when the field for the switching event is set to the tops and bottoms of the switching events and then finding the mean difference between the K_s and E_{DW} which is used as the error bar for the found values.

3.10.2 Transport equipment

Transport measurements were performed using 2 Keithley 2000 multimeters, a Keithley 2400 source meter, a Keithley 196 multimeter, a Keithley 2600 combined source and multimeter, a

National Instruments DAQ card, a Kepco bipolar operational power supply, a small custom build iron core magnet and a large Newport Instruments electromagnet. The Keithley 196 multimeter was connected to a Hall probe held between the cores of the large electromagnet and was used to acquire a direct measurement of the field. This resistance value was calibrated to the field using a hand-held gauss meter to get a measure of the resistance/field conversion factor.

The Keithley 2000 multimeters were used to measure V_{xx} and V_{xy} of the samples by applying the probes to the positions on the Hall bars demonstrated in figure 3.12. The Keithley 2400 was used to supply a current down the spine of the bar (also shown in figure 3.12) and the Keithley 2600 was used to apply a voltage to the piezoelectric crystal the samples were mounted on.

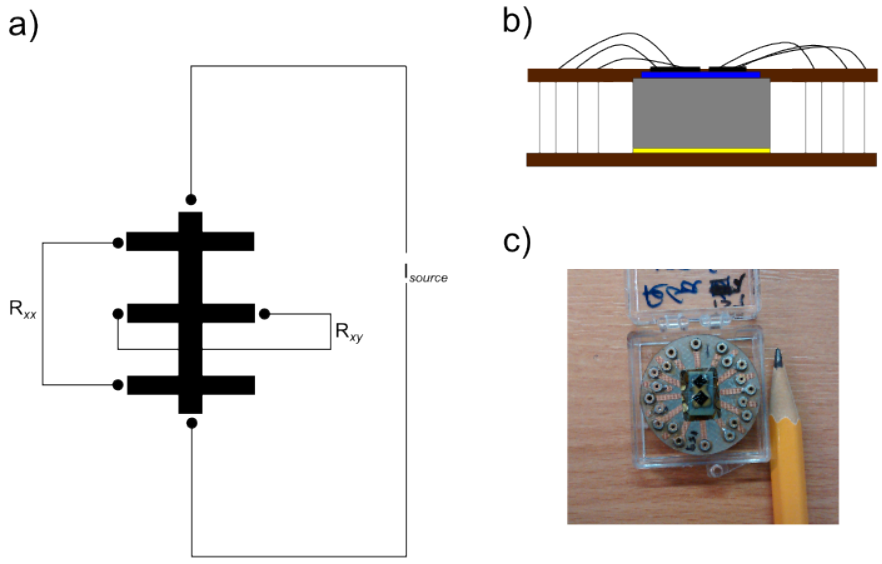

Fig. 3.12 Demonstration of the samples used to measure the transport properties of $Fe_{1-x}Ga_x$ thin films. A circuit diagram is shown in a) illustrating the terminals used for the R_{xy} and R_{xx} measurements as well as the terminals used to apply a current to measure the resistances. The samples were held onto the piezoelectric devices using HE-70 epoxy and the piezos were held in place using GE varnish as demonstrated in b) in which the piezo is represented in grey, the GE varnish in yellow and the epoxy in blue. The sample holder is brown and the bonding wires are shown as black lines. c) is the photo of an actual device used in these measurements. The device shown is the 10nm $Fe_{1-x}Ga_x$ sample used to gather the data on wafer S159 in chapter 4.

The bars were fabricated growing $Fe_{1-x}Ga_x$ with a 3nm aluminium capping layer, used to prevent oxidation, by sputter deposition. The samples were then patterned with photoresist as described in section 3.1 and milled into Hall bars as described in section 3.4. The bars were then mounted on the piezoelectric transducers using epo-tek HE-70 epoxy and then into a 20 pin header as shown in figure 3.12 c. The dimensions of the bars are demonstrated in figure 3.13.

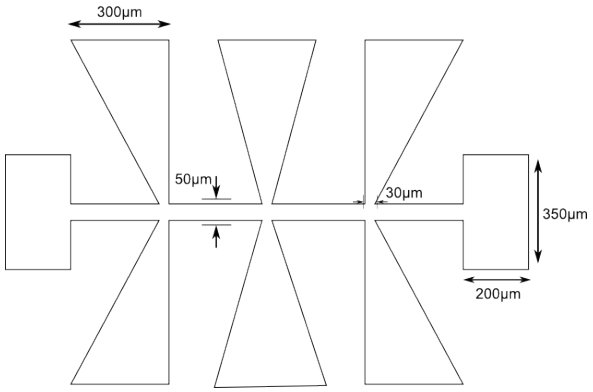

Fig. 3.13 Dimensions of the Hall bars used in transport measurements.

When the large magnet was used the DAQ card was used to send a voltage to the Kepco power supply in order to set the field and when the mini vector magnet, shown in figure 3.14, was used the DAQ card sent voltages to a Kepco bipolar operational amplifier power supply which supplied current to the coils of the magnet. The field to voltage ratio for the mini vector magnet was found using the handheld gauss meter and a direct transformation from supplied voltage to field produced was performed. When the mini vector was used in place of the large electromagnet the setup of the meters used for measuring the Hall bar was similar to the setup used for the large vector magnet however the Keithley 2400 was replaced with a battery box to supply a constant current. The current supplied by the battery box was monitored using a Keithley 196 in order to check for current spikes and to adjust for the batteries in the box running down. A photograph of the custom built mini vector magnet is shown in figure 3.14.

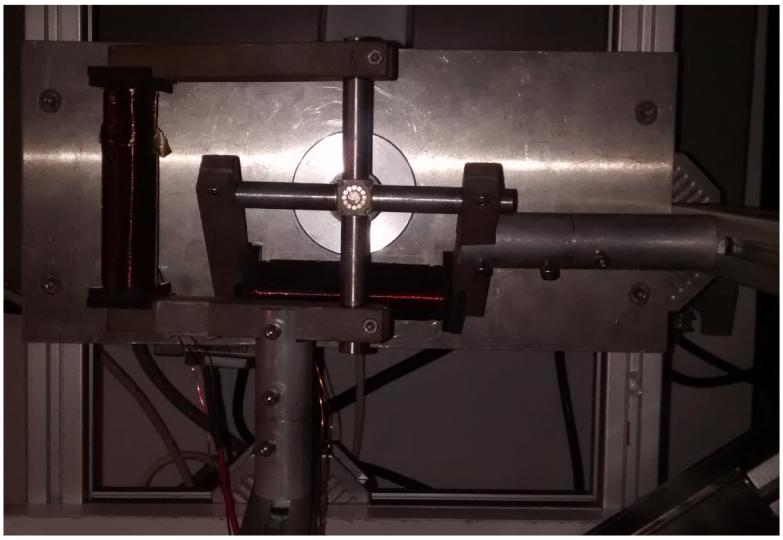

Fig. 3.14 Photo of the mini vector magnet used to collect some of the data presented in chapter 4.

3.11 X-ray diffraction

X-ray diffraction is a method of collecting information on the structural properties of a material. The method involves diffracting x-rays from a sample and measuring the angle of incidence of the x-rays, θ_{in}. The x-rays are diffracted from the sample at an angle determined by the Bragg condition given in equation 3.16 in which λ is the x-ray wavelength, d is the inter-planar spacing and n is the order of the diffraction.

$$n\lambda = 2dsin\theta_{in} \tag{3.16}$$

The inter-planar spacing and order of diffraction are demonstrated in figure 3.15.

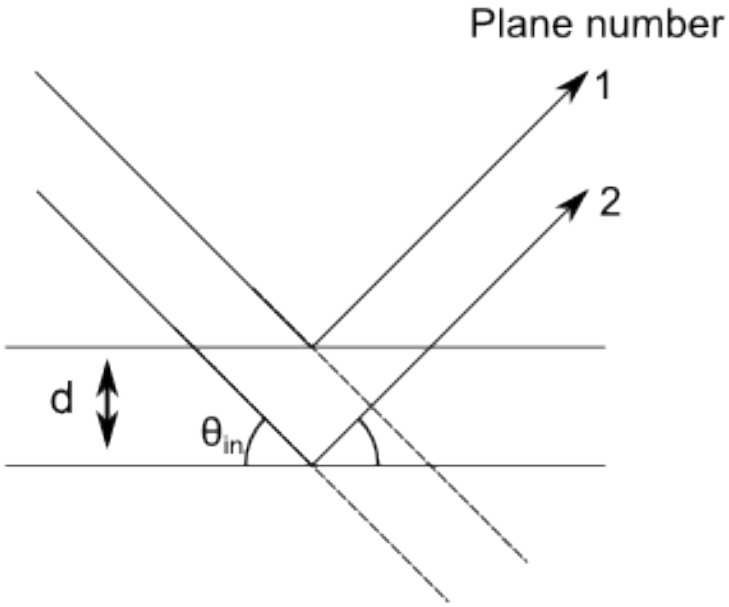

Fig. 3.15 Demonstration of Bragg diffraction. By looking at the distance between the fringes the distance between the layers can be determined using equation 3.16.

For this thesis triple axis diffractometry experiments were performed by Dr. P. Wadley. These measurements involved altering the angle of incidence of the x-rays to the sample, the rotation of the sample χ and the tilt of the sample, ψ as shown in figure 3.16 [118].

Measurements of the angle of intensity of x-rays detected versus the angle of incidence of the x-rays collected for this thesis were performed using a Phillips PANlytical X'Pert Materials Research Diffractometer (MRD) which has an angular resolution of 0.01^o for the tilt 0.0003^o for the angle of incidence. The detector and the sample are moved in order to set the crystallographic plane for investigation whilst the detector remained static in order to ensure a consistent supply of mono-chromatic x-rays with a wavelength of 0.154nm. The x-ray intensity as a function of the diffraction angle is then collected in order to investigate the regularity of the crystal structure in that plane. This data is then reconstructed by modelling the crystal as a series of ellipsoids. In a perfect mono-crystalline sample the result would be a single large sphere however in measured samples the result usually smaller, asymmetric ellipsoids misaligned to one another. The ellipsoids are a simplification of the actual structure made up of smaller crystals however the model is good enough to give a reasonable picture of the quality of the crystal and a rough idea of the size and orientation of the crystals in the mosaic.

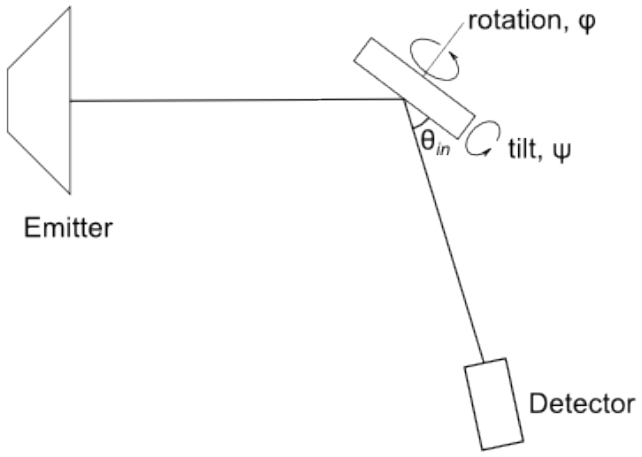

Fig. 3.16 Demonstration of the experimental equipment used to perform x-ray diffraction experiments. The emitter is stationary and the sample may be tilted or rotated in order to change the angle of incidence in order to measure how x-rays are diffracted and scattered by various planes of the sample. The detector can also be moved in order to find the intensity of the diffracted x-rays at different angles of incidence from the sample in order to measure the scattering of x-rays due to imperfections in the crystal lattice.

3.12 PEEM

It is possible to investigate the properties of a material by looking at the intensity of photoelectrons emitted from a sample using a PhotoEmission Electron Microscope (PEEM)[119–122]. An example of this is the PEEM used on the I06 beam-line at the Diamond synchrotron which uses circularly polarised x-rays to determine the magnetic domain structure and magnetisation dynamics of ferromagnetic materials. The design for this device, capable of performing Low Energy Electron Microscopy (LEEM), PEEM and X-ray Magnetic Circular Dichroism (XMCD) PEEM , is shown in figure 3.17.

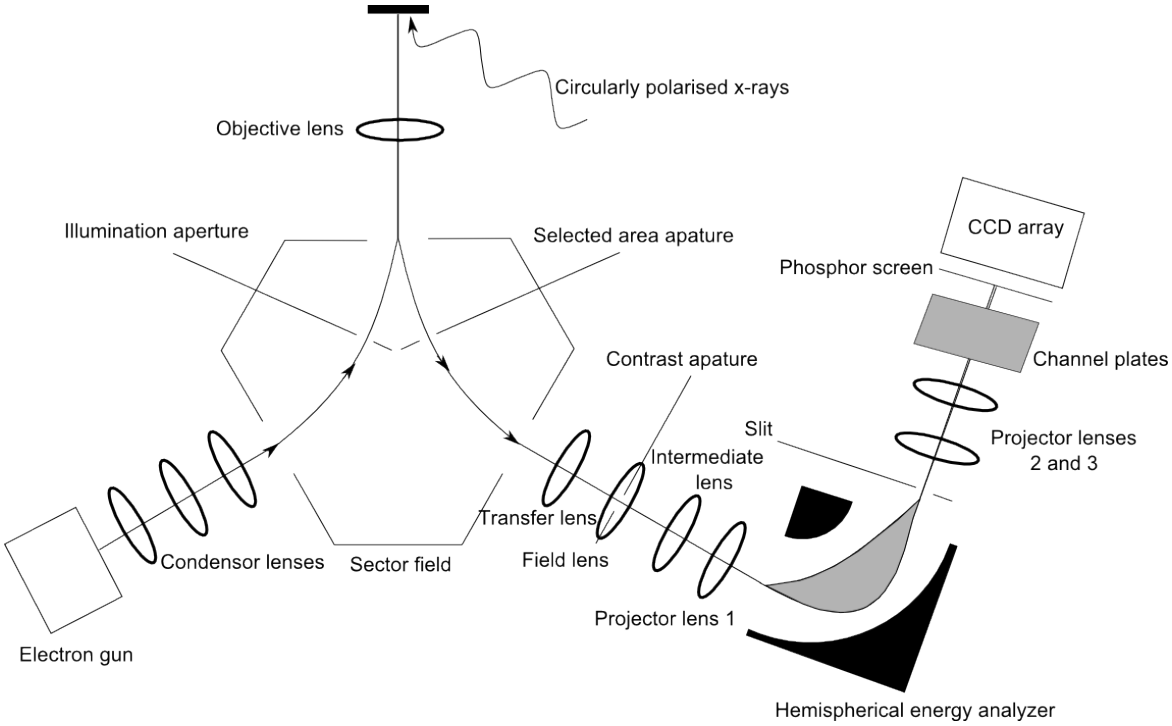

Fig. 3.17 Experimental set-up for the PEEM system at the Diamond synchrotron at Harwell Science Park, Oxford. This system may be used for LEEM, PEEM and both time resolved and non-time resolved XMCD PEEM experiments[123].

This design allows for image construction using either x-rays or electrons to produce the secondary electrons. However we will focus the discussion on the use of circularly polarised x-rays from the synchrotron to determine the magnetic domain structure of samples as discussed in section 3.12.1. The system uses a combination of magneto-static [124] and electrostatic [125] lenses to focus and refine the secondary electrons produced by the sample in a similar manner to optical lenses focusing light in a conventional microscope. The first set of these lenses are used to focus electrons from the electron gun when LEEM experiments are being performed and so are not covered in any detail here. When X-rays, with a photon energy greater than the workfuction of the sample, irradiate the surface, photoelectrons are liberated by the well known photoelectric effect. The escaping photoelectrons have a kinetic energy distribution shown in figure 3.18 [126].

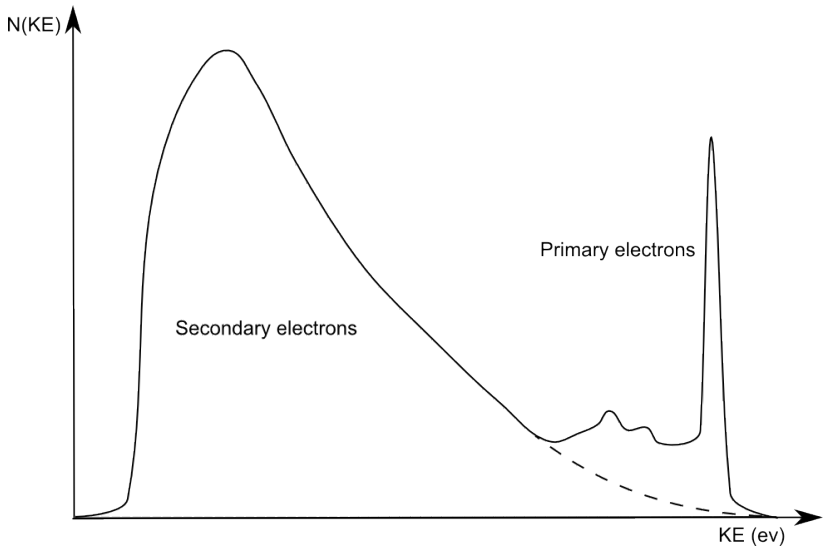

Fig. 3.18 Energy spectrum for photoelectrons excited from the surface of a sample with a skin depth greater than the mean free path of electrons. The number of photoelectrons produced (N(KE)) against the kinetic energy of those photoelectrons is shown demonstrating two main peaks representing primary and secondary electrons. The main peak in the primary electrons represents electrons excited from the highest occupied energy level with the smaller peaks representing core level electrons. The dotted line indicates the background due to secondary electrons[126].

Due to the penetration depth of x-rays in the material being greater than the mean free path of electrons moving through the sample the energy spectrum of photoelectrons has two main distinct peaks representing two types of photoelectrons, primary electrons and secondary electrons. The primary electrons are emitted due to the photoelectric effect in which the energy of the electrons is given by equation 3.17 where the kinetic energy of the electrons is given as E_{elec}, the frequency of the incident photon is given as ω_{inc} and the workfunction is given as χ_{work}.

$$E_{elec} = \hbar\omega_{inc} - e\chi_{work} \tag{3.17}$$

The primary electron peaks are due to electrons being excited from different energy levels providing a chemical finger print of the material. In addition by examining the angular dependence of the electrons emitted from the valence band the band structure of the material may be determined.

The second much larger peak represents the secondary electrons, these are photoelectrons produced due to x-rays interacting with electrons at a depth greater than the mean free path

of the electrons being liberated. In the absorption process a core hole is created which is then filled by Auger decay (dominant in the soft x-ray region over x-ray fluorescence). As the primary and Auger photoelectrons leave the sample, they create scattered secondary electrons from multiple several scattering events exciting near surface electrons into being emitted as secondary electrons. These secondary electrons form a much higher peak in intensity than primary electrons and show a much wider range of energies. This peak in the secondary electrons' intensity is proportional to the absorption coefficient of x-rays in the material. This, combined with the increased intensity means that it is preferable to image objects in an electron microscope using secondary electrons.

The system is designed to image electrons with an energy of 20keV±0.6eV electrons. A voltage of -20kV is placed between the sample and ground in order to accelerate electrons away from the sample. In order to image electrons with a non-zero kinetic energy gained from the photoemission process a start voltage is used in order to offset the additional kinetic energy.

A key feature of the Elmitec PEEM is the energy analyser which consists of two curved charged plates which radially deflect electrons moving between them causing electrons with energy too high or too low to disperse. The exit slit is then used to select a narrow (0.7eV) energy bandwidth of these dispersed electrons allowing for the effects of chromatic aberation to be severely reduced improving the resolution of the final image and reducing the number of photoelectrons. The projector lenses magnify the final image until it hits the final target, the channel plate detector. This is a ceramic plate with a number of $\sim 10 \mu$m bored holes in its surface uniformly spread. A voltage applied across the plate accelerates electrons entering any given channel and produce further secondary electrons due to collisions with the edges of the channel meaning that the channel plates act as an amplifier. These accelerated electrons then hit a phosphor screen which emits photons according to the number of electrons hitting it. The photons are then detected by the charge coupled device (CCD) camera producing an image.

3.12.1 XMCD

XMCD was used as a contrast mechanism to produce images of the magnetisation profile of various magnetic nanostructures. The PEEM on the I06 beamline at the Diamond synchrotron was adapted to perform time resolved measurements and was used to collect the data described in this thesis. In order to produce the circularly polarised x-rays the I06 beamline at the Diamond synchrotron is used which is shown in figure 3.19 which was taken from the Diamond website.

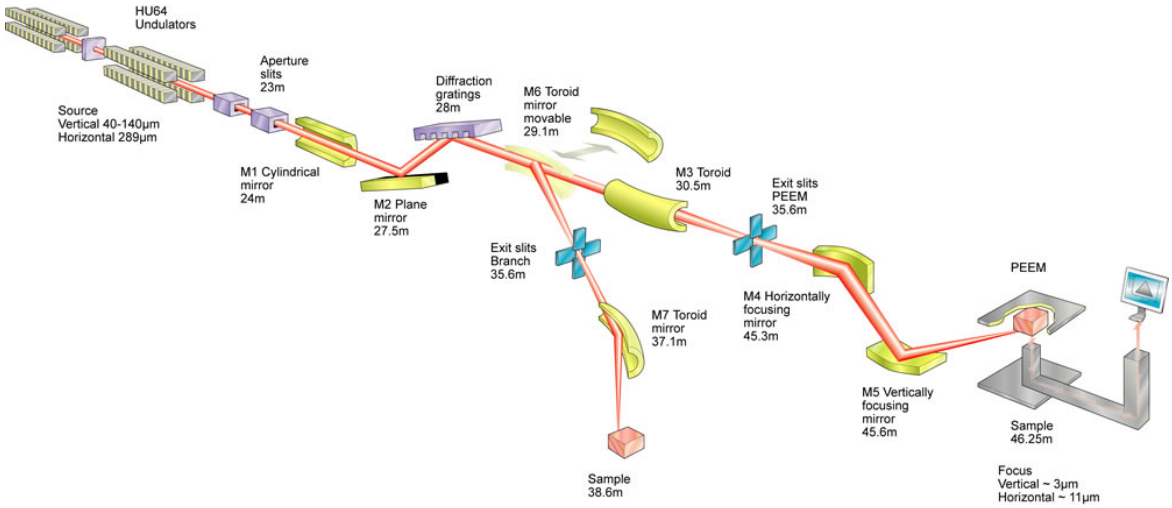

Fig. 3.19 Schematic of the I06 beamline at Diamond synchrotron in Harwell UK [127]

Figure 3.19 shows how the undulators, which consist of four magnet arrays, are used to cause electrons in the synchrotron ring to corkscrew creating circularly polarised light. These x-rays are then focused and monochromated using a plane grating monochromator and set of exit slits to select the desired wavelength of light. The monochromator allows photon energies between 106 and 1300eV for circularly polarised light with an energy resolution of less than 300meV. The beam is then focused onto the sample using a Kirkpatric Baez pair of mirrors in order to produce a circular spot approximately 30 microns in diameter. The selection of x-ray energy in PEEM is used to access the $L_{2,3}$ absorption edges for the material being tested as shown in figure 3.20.

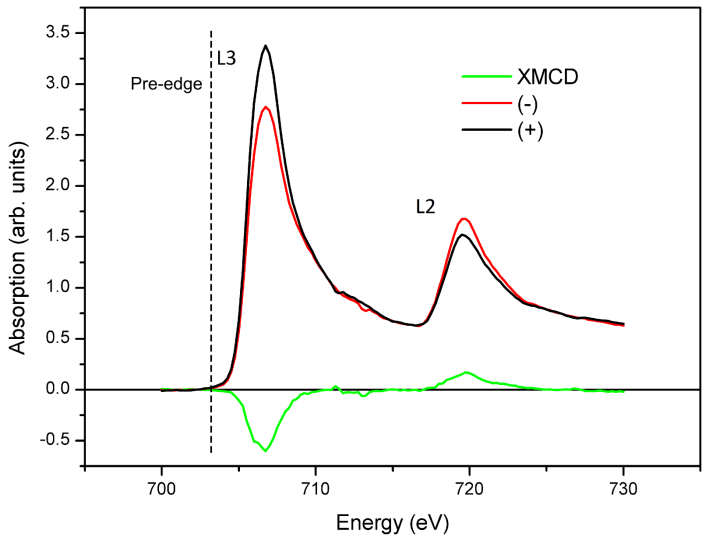

Fig. 3.20 Demonstration of the difference in x-ray absorption for σ_+ and σ_- circularly polarised x-rays with RCP light being represented by the black curve and LCP light being represented by the red curve. Also shown here is the pre-edge energy used to normalise the images. This graph was taken from reference [128] and represents an x-ray scan of iron in a $Fe_{81}Ga_{19}$ sample.

To produce each magnetic contrast image 40 images need to be taken. 10 of these images are taken with RCP x-rays at the L_3 peak energy and then 10 are taken with the x-ray energy tuned to the pre-edge. Next 10 are taken with LCP x-rays at L_3 peak energy and finally 10 images are taken with LCP x-rays energy tuned to the pre-edge energy. These images are then used to find X_+ and X_- calculated either equations 3.18 or 3.19.

$$X_+ = \frac{I_{L3+}}{I_{pre-edge}} \tag{3.18}$$

$$X_- = \frac{I_{L3-}}{I_{pre-edge}} \tag{3.19}$$

Where I_{L3+} and I_{L3-} is the intensity of each pixel at the L_3 peak when RCP and LCP x-rays are used respectively, $I_{pre-edge}$ is the intensity of each pixel at the pre-edge used to normalise the image in order to counter the effects of variations in x-ray beam intensity due to the position of the sample. The images are then constructed using either the difference method described in equation 3.20 or the asymmetry method described in equation 3.21.

$$D = X_+ - X_- \tag{3.20}$$

$$A_{sym} = \frac{X_+ - X_-}{X_+ + X_-} \tag{3.21}$$

These two methods of producing the image of the magnetisation both have their advantages and disadvantages. Images produced using the difference method tend to display high magnetic contrast but low resolution as to the direction of the magnetisation. Images produced using the asymmetry method demonstrate the magnetisation as a function of the absorption coefficient. In the asymmetry images there is also a offset applied to avoid dividing by zero however this can lead to loss of information and reduced quality in the image. Examples of images of a FeGa L bar collected by these methods are shown in figure 3.21.

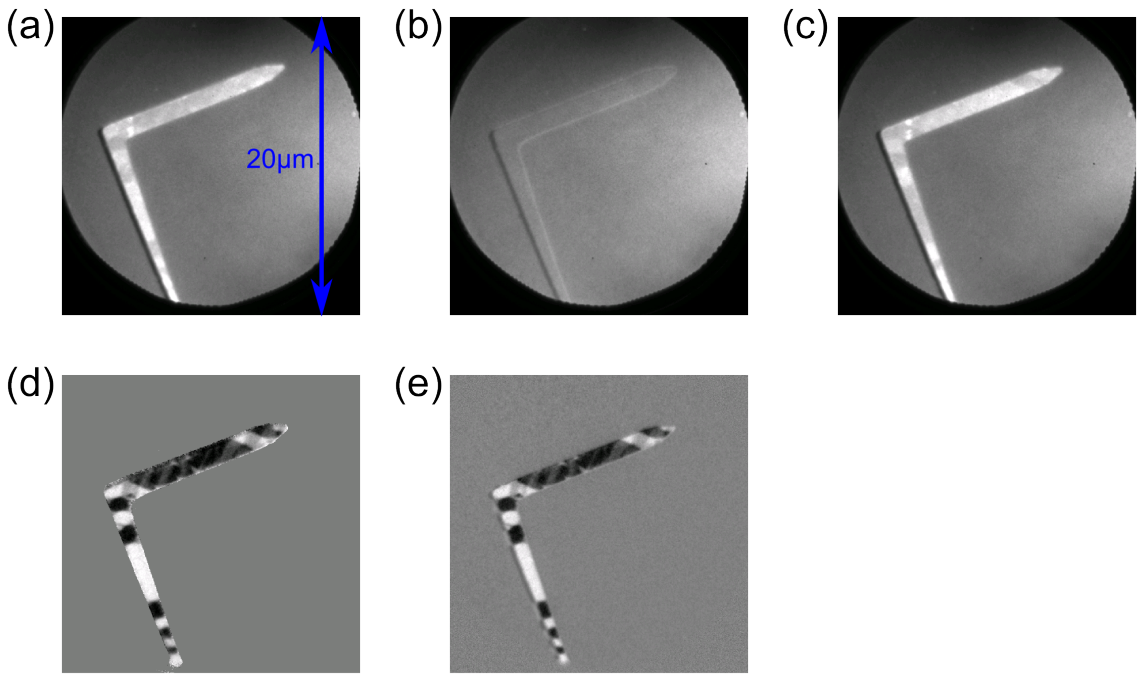

Fig. 3.21 Images collected via XMCD PEEM with a 20μm aperture. a) shows an image collected with RCP x-rays aligned to the the L3 edge, b)shows the same object imaged with the x-ray energy aligned to the pre-edge, c) shows the object imaged with LCP x-rays aligned to the L3 edge, d) shows an image produced using the difference method and e) shows an image produced using the asymmetry method.

This process was used to collect the data presented in reference [21] and was adjusted to observe the evolution of a micromagnetic system over time as will be described in chapter 5.

3.13 Time resolved XMCD

In order to resolve these issues time resolved XMCD PEEM was developed at the Diamond light source in Harwell Oxfordshire using an electronic delay stage in combination with a cam shaft electron fill in the synchrotron. In order to understand how the time resolved images were produced we first have to examine the samples used. The samples were grown onto a 50Ω waveguide which was made from a tantalum/gold multilayer sputter grown on a GaAs substrate. After the waveguide was formed the GaAs substrate was thinned to $150\mu m$ using the backthinning method described in section 3.5 before being epoxy glued to a piezo stressor. The full multilayer structure is shown in figure 3.22.

Fig. 3.22 Drawing of the multilayer structure used in the construction of waveguides. The waveguide is made up of Ta (blue) and gold (yellow). The waveguide is made with a 5nm base layer of tantalum on the surface of the GaAs (gray) followed by three identical bilayers of 25nm of gold followed by 3nm of tantalum. The whole structure is then capped with 25nm of gold. The GaAs is epoxied to the surface of the PZT piezoelectric transducer (black).

Electron beam lithography was performed by Dr. Christopher Reardon at the University of York allowing for the samples to be sputter grown onto the active region of the waveguide as shown in figure 3.23.

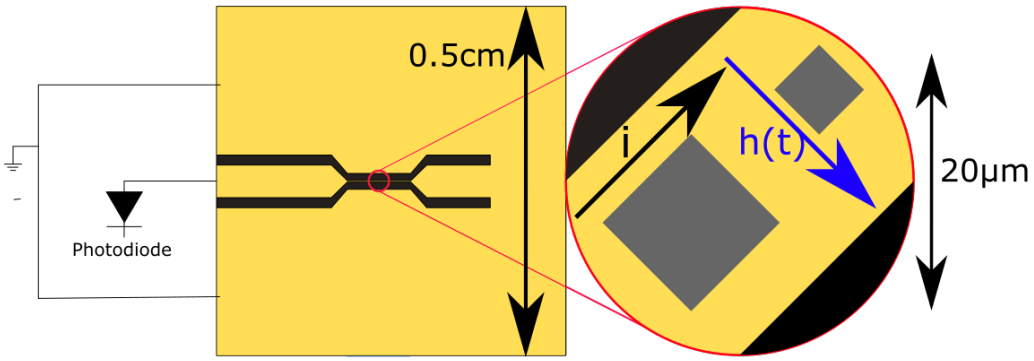

Fig. 3.23 Diagram of a waveguide used in time resolved XMCD PEEM. The surface of the chip is gold with trenches in the gold forming the wave guide (black area). The grey squares represent ferromagnetic microstructures mounted on top of the waveguide. The Points A and B show the location of the contacts used to pass a current through the waveguide. A current is generated by the photodiode when irradiated by a short laser pulse. This current pulse travels through the waveguide producing a magnetic field h(t) which applies a torque to the magnetisation within the sample

The samples were mounted into cartridges designed to slot into the XMCD PEEM system and bond wires were attached at the points marked A and B in figure 3.23 in order to apply a voltage across the waveguide. A voltage was placed across a photodiode so that when the photodiode was illuminated by a pulsed RegA 9000 titanium sapphire laser current could flow through the waveguide inducing a magnetic field exerting a torque on the magnetisation of the samples. This process is demonstrated in figure 3.24 which shows the laser being synchronised to the synchrotron. It then shows the laser pulse hitting a photodiode allowing for current to flow through the waveguide resulting in a magnetic field pulse being applied to the magnetic microstructures grown on the surface of the waveguide.

The synchrotron contains 936 electron bunches with a time of 2ns between bunches. The bunches rotate the synchrotron at a frequency of 533.8kHz. The synchrotron may be run in a number of different ways depending on the fill pattern of these bunches. The ways these bunches may be filled are demonstrated by the graphs shown in figure 3.25 which show the bunch charge against the bunch number when the synchrotron is running in different modes. These graphs were taken from the Diamond Light Source website [129].

Figure 3.25 a) shows the fill pattern of the synchrotron when the system is run in standard mode.In this mode every bunch is filled providing high x-ray flux but zero time resolution. Figure 3.25 b) shows the fill pattern of the synchrotron when the system is run in hybrid mode. In this mode there are 686 contiguous bunches with a spacing of 2ns followed by a single bunch which is spaced 250ns away from the contiguous bunches. This mode allows

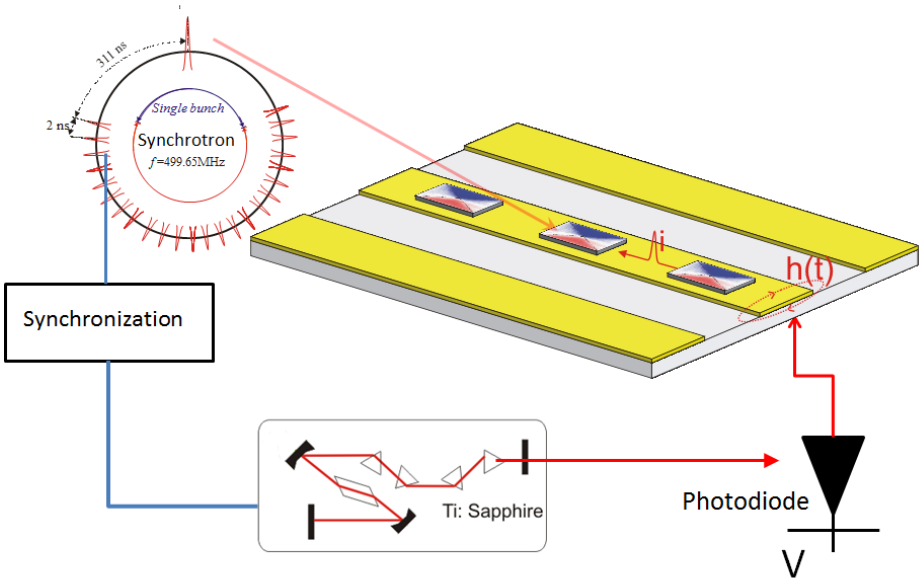

Fig. 3.24 Time Resolved XMCD PEEM (TRXMCDPEEM) is performed using the circuit shown. The Titanium:Sapphire laser synchronised to the synchrotron hits the photodiode allowing a current,i, to run through the waveguide from A to B producing a magnetic field, h(t). Also demonstrated here is single and multi-bunch electron packets in the synchrotron.

time resolved measurements to be performed using the single isolated bunch. However, since there is only one single bunch time resolved measurements become time consuming due to the infrequency of suitable x-ray bursts. The final mode synchrotron described here is shown in figure 3.25 c). In this mode there are no contiguous bunches and the system is filled with 156 electron bunches 12ns apart. This fill mode allows for time resolved measurements to be take quickly due to the high frequency of suitable x-ray bursts however the x-ray flux is comparatively low for non-time resolved experiments.

In order to construct time resolved image sequences using the hybrid and 156 fill patterns a delay is manufactured between the excitation of the system and the x-ray burst used to image the system. When the laser hits the photo diode it allows an electric current to flow through the waveguide applying a magnetic torque to the devices on the waveguide causing a shift in the domain structure. The x-rays hitting the sample at time Δt after the electric pulse will then produce an image of the sample at a time Δt. By repeating this process for a range of Δt a video can be built up showing the time evolution of the system. Then by performing spatial frequency analysis of the video the frequency of oscillation of the magnetic spins in various areas of the sample can be found. This allows the response time of the micro structures to be determined and how strain and shape anisotropy affect the response times

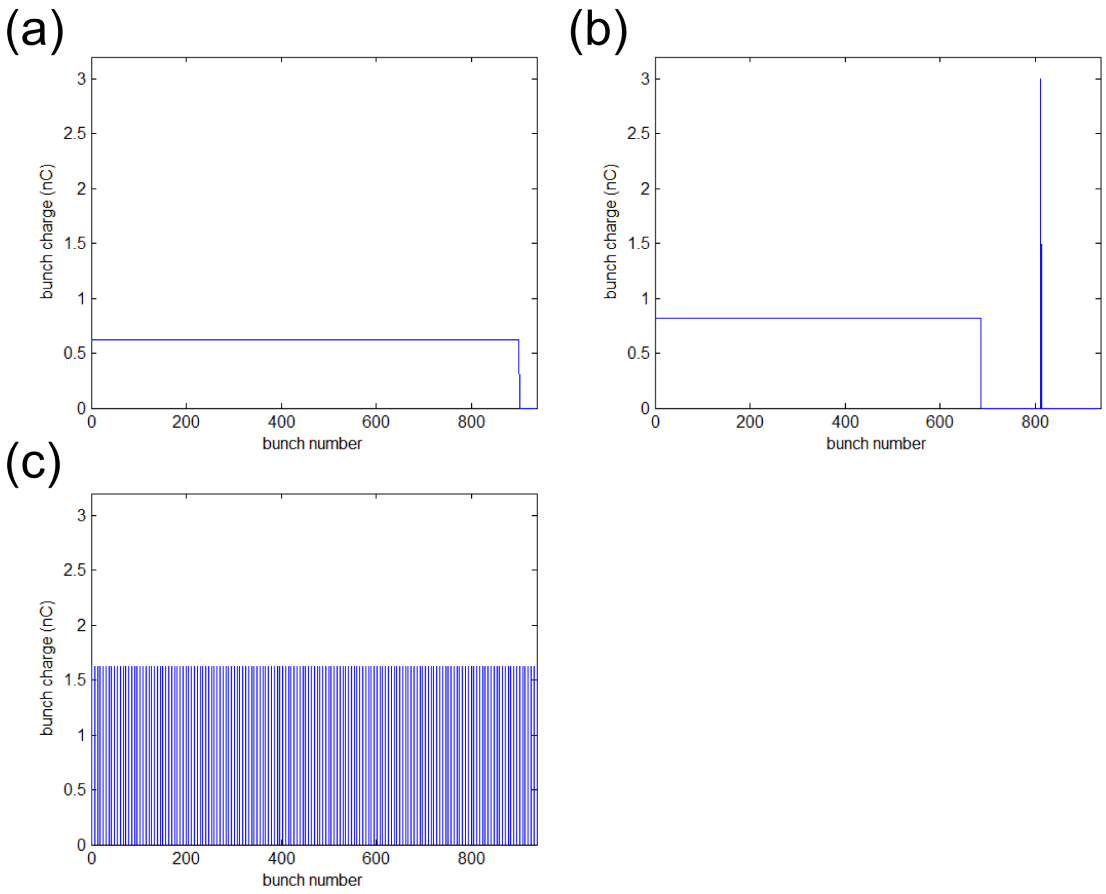

Fig. 3.25 Plots of bunch number against bunch charge for various operation modes of the Diamond Light Source synchrotron. Shown here are fill patterns for a)standard mode, b)Hybrid mode and c)156 bunch mode. All graphs were taken from the Diamond Light Source website [129].

and characteristic spatial frequencies within ferromagnetic samples. A laser is used in place of a high frequency pulse generator since the PEEM vacuum chamber is not capable of accommodating high vacuum cables capable of carrying a RF pulse on top of a 20kV system voltage.

3.13.1 Running time resolved experiments in hybrid mode

In order to run time resolved XMCD experiments when the synchrotron was run in hybrid mode the laser system used to irradiate the photodiode was configured as shown in figure 3.26.

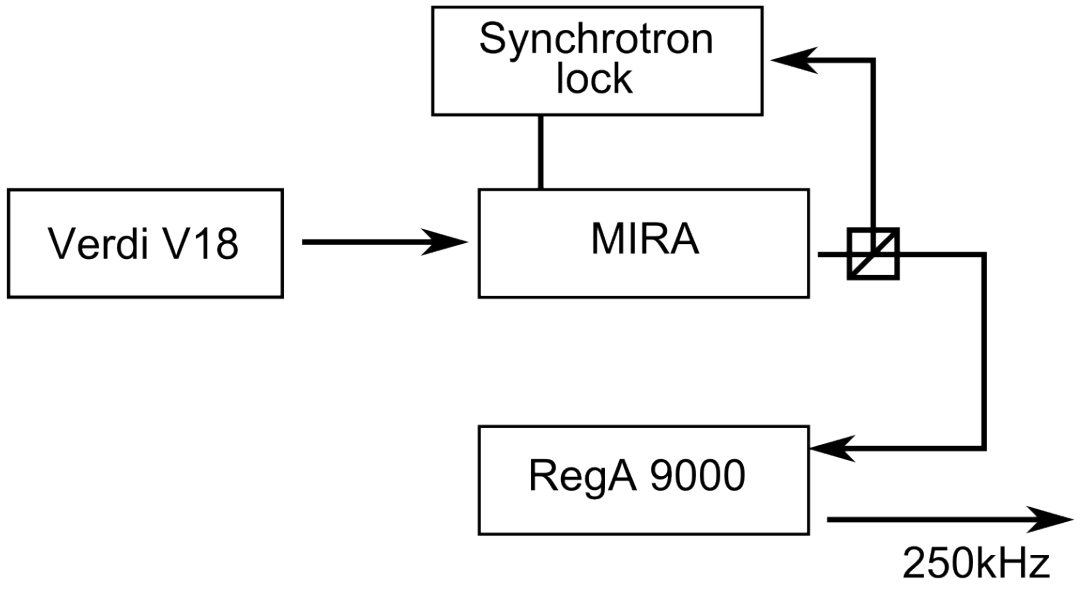

Fig. 3.26 Laser set up for time resolved measurements using x-rays produced by the synchrotron when run in hybrid mode. The MIRA pulsed laser is driven by Verdi V18 continuous diode laser. A section of the output from the MIRA laser is then split off to be used for synchronisation between the laser and the synchrotron. The main part of the output from the MIRA laser is sent to a RegA 9000 pulse picker and amplifier which reduces the frequency of the pulse train to match the synchrotron.

Figure 3.26 shows a laser set-up designed to produce a laser pulse every 3.7μs. This works by first driving the MIRA pulsed laser using a Verdi V18 continuous diode laser. The MIRA produces a pulse train at a frequency of 83.3MHz. This pulse train is then moved into the Reg A 9000 pulse picker and amplifier which reduces the frequency of the pulses to 266.9kHz. The synchrotron produces single bunch X-rays at a frequency of 533.8kHz and produces multi-bunch x-rays as well. In order to produce time resolved images the voltage supplied to the channel plates, which allows the detector to be turned on and off, is controlled by a function generator running at a frequency of 266.9kHz. This means that images are collected only when the pulsed laser and the synchrotron are phase locked to one another. This principal is demonstrated in figure 3.27.

In order to alter the delay between the laser pulse exciting the system and the x-ray pulse an electronic delay line is added to the output of the laser system. This involves changing the frequency of the pulse train of the MIRA pulsed laser in order to alter the phase difference between the synchrotron and the MIRA. The length of the laser cavity within the MIRA is changed slightly so that the frequency of the pulse train and the frequency of the synchrotron

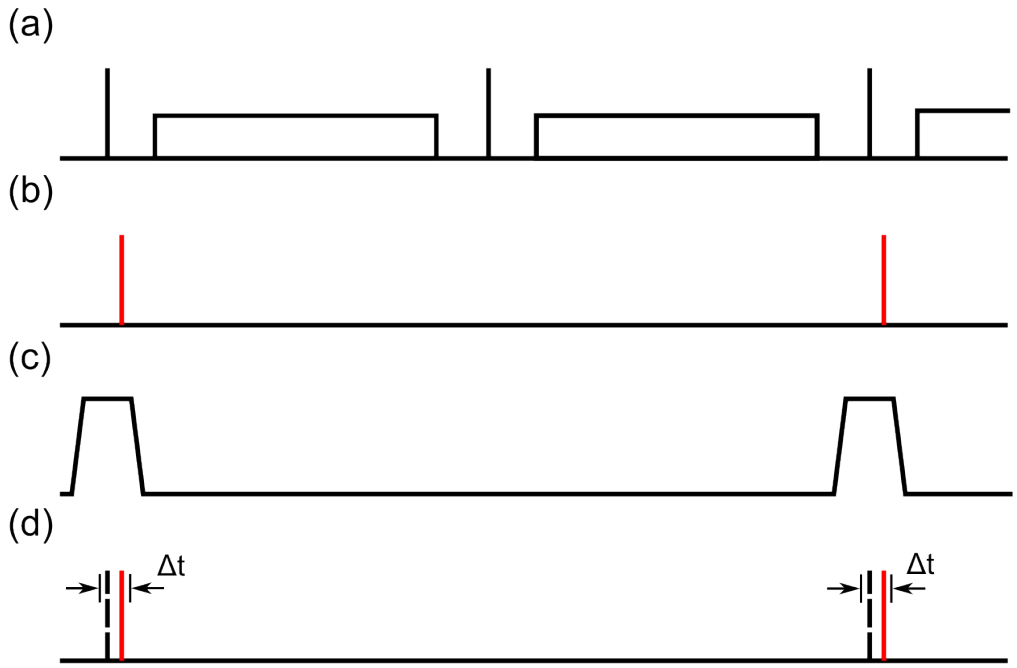

Fig. 3.27 Pulse trains from a) the synchrotron running in hybrid mode, b) the output from the RegA 9000 pulse picker, c) the function generator sending a voltage to the channel plates and d) shows the delay between the excitation by the laser pulse and imaging by the x-ray pulse.

differ slightly. This causes the phase between the two pulse trains to drift. Once the desired phase difference has been achieved the laser cavity is returned to its original length and the laser pulse train and the x-ray pulse train become phase locked once again, now with a new phase difference between the two pulse trains.

3.13.2 Running time resolved experiments in 156 bunch mode

When the synchrotron is run in 156 bunch mode the laser set-up is altered as shown in figure 3.28.

Comparing figure 3.28 with figure 3.26 the major change is the removal of the RegA 9000 pulse picker and amplifier. This means that the laser pulse train will be of frequency 83.3MHz since the laser pulse train is produced directly by the MIRA. This frequency matches that of the x-ray pulses from the synchrotron meaning that the laser pulse train is phase locked to the pulse train from the synchrotron. This means that time resolved images may be collected much more quickly than when the system is run in hybrid mode however the potential length of time delays is much shorter.

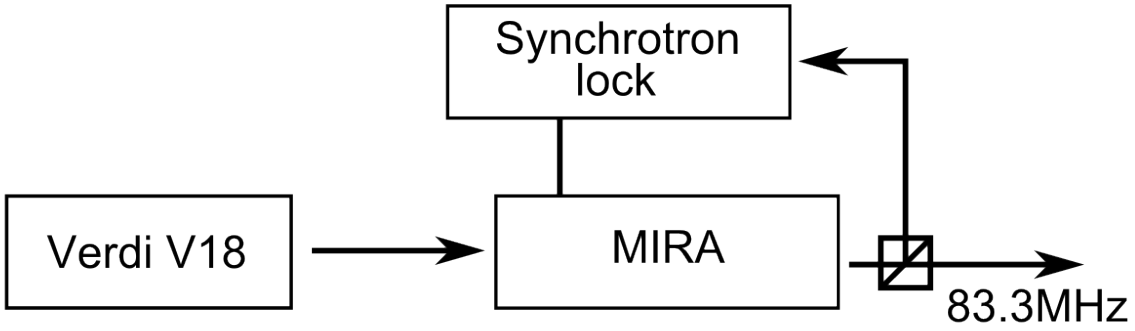

Fig. 3.28 Laser set up for performing time resolved experiments when the synchrotron is run in 156 bunch mode. The MIRA pulsed laser is driven by the continuous Verdi V18 diode laser. Part of the output from the MIRA laser is used to ensure phase locking between the laser pulse train and the synchrotron and the main part of the beam is directed onto the photodiode to excite the sample.

3.13.3 Experimental difficulties

Arcing

Since the objective lens had to be held at a potential difference of 20kV from the surface of the sample in order to accelerate electrons from the surface of the sample into the PEEM there was a significant problem with arcs forming between the objective lens and the sample. This would often alter the magnetisation of the sample or damage the surface of the waveguide. Damage to the surface of the waveguide would alter its impedance meaning that the ac current could no longer flow to produce the exciting magnetic pulse rendering the sample useless for time resolved measurements. The result of an arc is shown in figure 3.29.

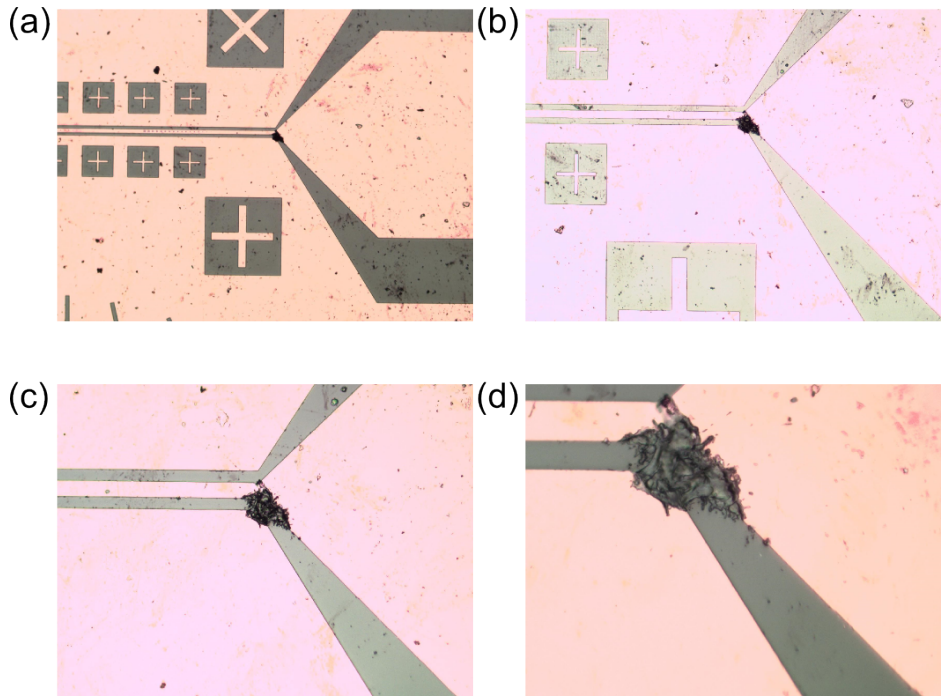

Fig. 3.29 Photos of waveguides with magnetisation of a)5X, b) 10X, c)20X and d)50X on the secondary lens following an arc.

Impedance mismatches

The waveguides had to be grown to a high level of precision to match the desired impedance. The value of the impedance could be altered if the thickness of the layers were calculated incorrectly or if the surface of the waveguide was damaged. Damage to the surface of the waveguide may occur due to arcs, described in section 3.13.3, whilst the backthinning operation was being performed, see section 3.5 or due to failures in the optical lift off procedure. Any of these problems could lead to reflection of the current, reducing the amplitude of the exciting pulse and causing the exciting pulse to become chaotic.

Chapter 4

Material characterisation of sputter deposited $Fe_{1-x}Ga_x$ films

In this section the effects of film thickness on the magnetic properties of sputter grown $Fe_{1-x}Ga_x$ thin films grown on GaAs substrates were studied using SQUID magnetometry and DC transport measurements. The effects of thickness on the crystal structure of the films was also studied using x-ray diffraction experiments. DC transport measurements were carried out on devices under controlled uniaxial strain to determine the magnetostriction constant, using the technique developed by Parkes et al. [61].

4.1 Sample growth

The samples were grown on $350\mu m$ thick GaAs substrates using the sputter technique described in section 3.3. In order to prepare the surface the substrate was first submerged in a 50:50 HCl to water solution in order to remove organic contaminants and the native oxide. This substrate was then moved into the vacuum chamber of the sputter machine where it was annealed at 550^oC for 1 hour and allowed to cool to room temperature. Preparing the surface in this way has been shown to result in a larger grain size in the films produced as described in reference [130]. $Fe_{1-x}Ga_x$ films were grown by co-sputtering a FeGa target alongside a pure Fe target, in order to grow Fe films only the Fe target was used.

Six $Fe_{1-x}Ga_x$ films were grown and six Fe films were grown. Four of the $Fe_{1-x}Ga_x$ films were grown by Dr. M. Wang and all other films were grown by myself. The nominal thicknesses of these films, the nominal composition and the person responsible for their growth are demonstrated in table 4.1.

Sample name	Sample thickness (nm)	Material	Grower	Argon pressure (Pa)	Growth rate (nms^{-1})
S159	10 ±2.1	$Fe_{1-x}Ga_x$	MW	0.21	0.48±0.03
S219	20 ±4.3	$Fe_{1-x}Ga_x$	MW	0.23	0.48±0.03
S221	30 ±6.4	$Fe_{1-x}Ga_x$	MW	0.21	0.48±0.03
S227	100 ±21.4	$Fe_{1-x}Ga_x$	MW	0.21	0.48±0.03
S366	10 ±2.1	Fe	SB	0.21	0.15±0.03
S367	20 ±4.3	Fe	SB	0.21	0.15±0.03
S368	30 ±6.42	Fe	SB	0.21	0.15±0.03
S406	1 ±0.2	Fe	SB	0.21	0.18±0.04
S407	3 ±0.6	Fe	SB	0.21	0.18±0.04
S408	5 ±1.1	Fe	SB	0.21	0.18±0.04
S410	30 ±6.4	$Fe_{1-x}Ga_x$	SB	0.19	0.46±0.10
S411	20 ±4.3	$Fe_{1-x}Ga_x$	SB	0.19	0.46±0.10

Table 4.1 Samples grown for the thickness study. The nominal value for x in this table is 0.19.

The thicknesses of these samples were measured using the quartz crystal monitor (QCM) in the sputter machine. This device was regularly calibrated by growing test films and then measuring the thickness of these films using an x-ray reflectivity experiment performed by Dr. Mu Wang. The result of this measurement was used to set a tooling factor when using the sputter machine. This tooling factor would change over time however meaning that the tooling factor needed to be regularly recalibrated. The system was calibrated after the growth of the samples S159, S219, S221 and S227 demonstrating an error of 6% in the tooling factor of the QCM. No recalibration was done after the growth of the other samples examined so the mean change in this recalibration factor across the lifetime of the sputter machine was used to find the error for these samples leading to an error of 21.4% in the tooling factor of the QCM. This value for the error in the tooling factor is likely to be an overestimate however the lack of good calibration data means that the large error bounds must be used. These errors in the tooling factors lead to the errors in the sample thickness and growth rate in table 4.1.

4.2 SQUID measurements of $Fe_{1-x}Ga_x$ grown on GaAs

SQUID magnetometry measurements were performed on $Fe_{1-x}Ga_x$ grown on GaAs substrates by sputter deposition in order to investigate the effects of film thickness on the uniaxial and cubic magnetocrystalline anisotropy constants. Magnetic hysteresis loops were measured while sweeping the external magnetic field back and forth from -200mT to +200mT at

temperatures of 2K and 300K. The field was applied in the [110], [1$\bar{1}$0] and [010] directions. The magnetic hysteresis loops produced in this way for the 10nm $Fe_{1-x}Ga_x$ sample, S159, at a temperature of 2K are shown in figure 4.1.

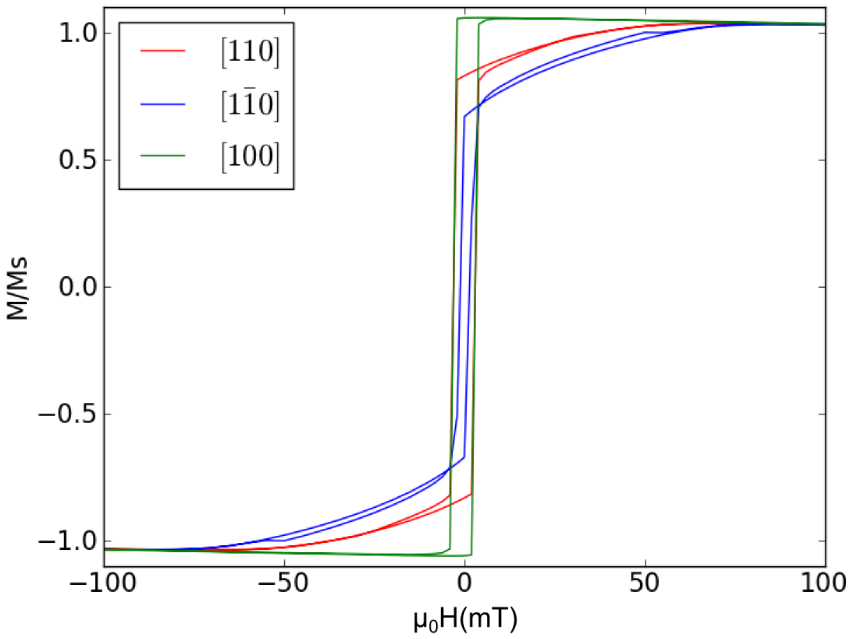

Fig. 4.1 Hysteresis loops for a 10nm $Fe_{1-x}Ga_x$ film grown on GaAs, S159, normalised by the saturation magnetisation as a function of magnetic field. The initial loops were taken by sweeping the field from 200mT to -200mT and back again however the data is shown in the range -100mT to + 100mT to focus on the region of interest.

From these loops we can see that the relatively easy axis is the [100] direction that the [110] and [1$\bar{1}$0] directions are relatively hard,with the [110] direction an easier axis than the [1$\bar{1}$0]. This indicates that there is a strong cubic anisotropy in the [100]/[010] directions and a weaker uniaxial anisotropy in the [110] direction, corresponding to the anisotropies typically observed in iron films on GaAs as described in section 1.4. This means that the [1$\bar{1}$0] direction is the relatively hard axis and will therefore magnetic hysteresis collected with the field applied in this direction will be used for fitting to the data. The effects of the diamagnetic background due to the GaAs substrate the samples were grown on can be seen causing the magnetisation to begin to decrease once the saturation magnetisation has been exceeded. This diamagneic background also explains why the value of M/M_s appears greater than one once switching occurs since the value for the saturation magnetisation was chosen for the value of magnetisation with 200mT of field applied. The [1$\bar{1}$0] loop demonstrates

an asymmetry in the 10mT to 50mT region depending on the direction in which the field was swept. This asymmetry is due to the formation of domains within the sample and is the reason that the fitting regions described in figure 4.3 were used. The measured magnetisation in the $[1\bar{1}0]$ direction, normalised by the saturation magnetisation for samples S159, S219, S221 and S227, thicknesses 10nm,20nm,30nm and 100nm respectively are shown in figure 4.2.

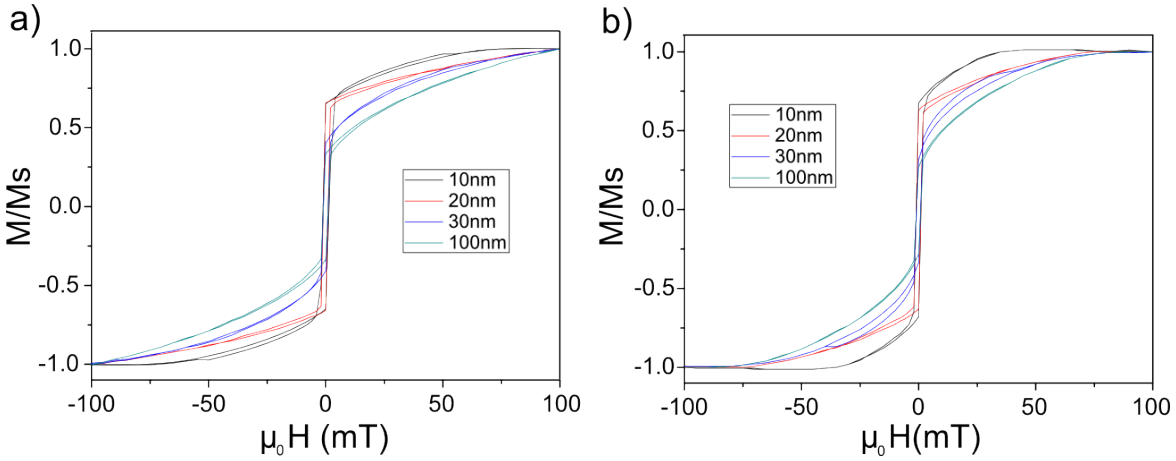

Fig. 4.2 Hysteresis loops for $Fe_{1-x}Ga_x$ grown on GaAs, normalised by the saturation magnetisation as a function of magnetic field applied along the $[1\bar{1}0]$ direction. The initial loops were taken by sweeping the field from 200mT to -200mT and back again however the data is shown in the range -100mT to + 100mT to focus on the region of interest. a) shows the measurements at 2K and b) shows the measurements at 300K.

From these loops we can see that as the thickness increases the remnant magnetisation decreases indicating that the uniaxial anisotropy increases with thickness. As the thickness increases the magnetisation rotation at which the switching event occurs moves more towards the [110] axis. The 20nm sample, S219, also shows a more uniform curvature than the other samples indicating that the cubic anisotropy may be higher in this sample. The cubic anisotropy causes the magnetisation to rotate more uniformly as it makes the magnetisation directions between the two hard axis easier allowing for a more uniform transition.

Before determining the uniaxial and cubic anisotropy of the samples the Ga concentration of the samples may be determined using the saturation magnetisation found using the SQUID magnetometery measurements. This is done by assuming the magnetic component comes entirely from the iron within the sample and that the estimated thickness of the films, with the associated errors, may be calculated from the readings from quartz crystal monitor (QCM) in the sputter machine. This was calibrated by growing test films and then measuring the thickness of these films by x-ray reflectivity in order to find a tooling factor for the QCM, a

task completed by Dr. Mu Wang. This value changes over time however, due to build up of material on the surface of the QCM device. The ratio of Fe to Ga may also change over time as the Fe in a FeGa target sputters at a faster rate meaning an older FeGa target may be Ga rich. This means that the thicknesses and compositions reported are nominal as the growth rates read from the QCM may contain a systematic error. This is taken into account by the error value calculated from the mean change in the QCM tooling factor between calibration growths. The surface area of the samples was found using an office scanner to take an image of the samples and then counting the number of pixels the sample occupied. This method was used to estimate the composition of the samples as is shown in table 4.2.

Sample no.	Sample (nm)	Measured area (mm^2)	Volume (m^3 ($\times 10^{-13}$))	M_s (Am^{-1})	Iron content (%)
S159	10±2	18.6±0.2	1.9±0.1	1.51×10^6	88.8 ± 4.7
S219	20±4	21.2±0.2	4.3±0.3	1.52×10^6	89.4 ± 5.3
S221	30±6	17.9±0.2	5.4±0.3	1.38×10^6	81.2 ± 4.7
S227	100±21	17.1±0.2	17.1±1.1	1.48×10^6	87.1 ± 5.1

Table 4.2 Iron concentration in $Fe_{1-x}Ga_x$ samples, measured at 300K.

This study of the iron concentration in the samples indicates that the level of iron in the sample is not an adequate explanation for the high cubic anisotropy in the 20nm sample since the concentration of iron only dips in the 30nm sample and remains consistent to within the estimated uncertainty for the other samples. The error in these measurements is not sufficiently large that it is likely that the $Fe_{1-x}Ga_x$ may differ from A2 structure.

The uniaxial and cubic anisotropies of these samples were then extracted from the hysteresis loops measured at 300K using the fitting program described in section 3.7. An example of this fitting is shown in figure 4.3 where the magnetic hysteresis loop collected from the 10nm $Fe_{1-x}Ga_x$ sample, S159, at a temperature of 300K is shown in black with the results of the fitting procedure shown in blue.

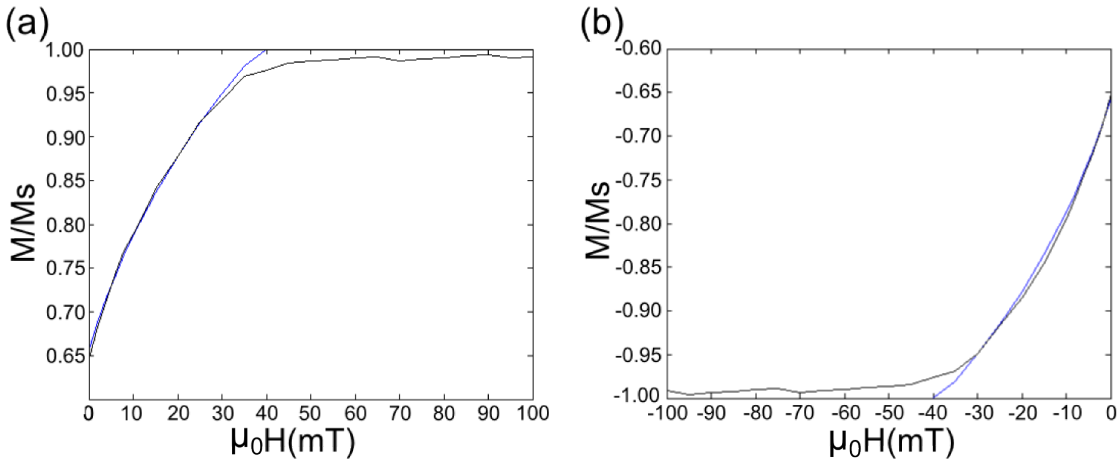

Fig. 4.3 Demonstration of fitting to the magnetic hysteresis loop for S159 at a temperature of 300K. The blue line is the simulated data and the black line is the magnetic hysteresis loop collected by SQUID magnetometery.

The blue line in figure 4.3 shows the simulated loop which has been fitted to the regions of the magnetic hysteresis loop in the regions where the magnetisation in the material was rotating towards the [110] axis. The fit was focused on this region in order to ensure that the effects of domain wall nucleation were not included in the fitting procedure. The cost function of the fit was found using the least squares method and the uniaxial and cubic anisotropy values for the lowest cost fit were used as the results of the fitting procedure. A full set of all the fits to SQUID magnetometry data performed in this thesis can be found in Appendix A.

In order to find the error in K_c a procedure using a windowing function was used. This involved plotting simulated loops with a K_c value which differed from the best fit value calculated from the raw data by a respective error. If the number of data points between these two curves was greater than 66% of the total number of points the supposed error was said to be too low and then increased. This process was repeated until less than 66% of the data points were contained within the window and then the error was assumed to be the largest window containing 66% of the data points. This meant that the number of points inside the window drawn by our error value was approximately 2σ from the actual data. An example of the windows drawn in this way is shown in figure 4.4 which represents the window used to fit K_c for the 10nm sample, S159, at a temperature of 300K.

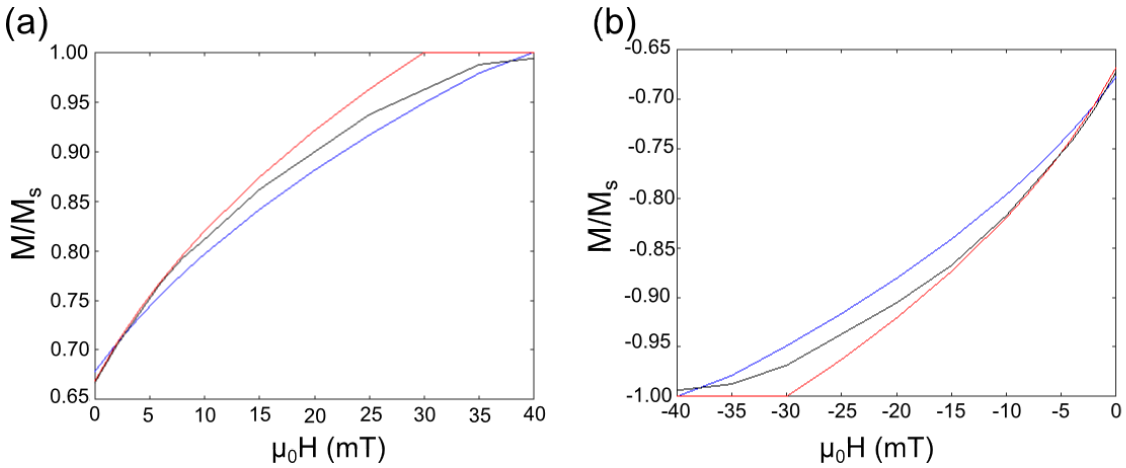

Fig. 4.4 Demonstration of the method used to find errors in the results from fitting to a magnetic hysteresis loop produced from SQUID magnetometry. Shown here are windows used to find the error in the K_c value found for the 10nm $Fe_{1-x}Ga_x$ sample at a temperature of 300K. The windows are represented by the blue and red lines and the experimental data is represented by the black line.

The error in the K_u value was found by repeating this process substituting K_u for K_c.

This process was performed in order to find K_c and K_u values with associated errors for all the loops shown in figure 4.2 resulting in the graph shown in figure 4.5 which gives K_c and K_u values for samples S159, S219, S221 and S227.

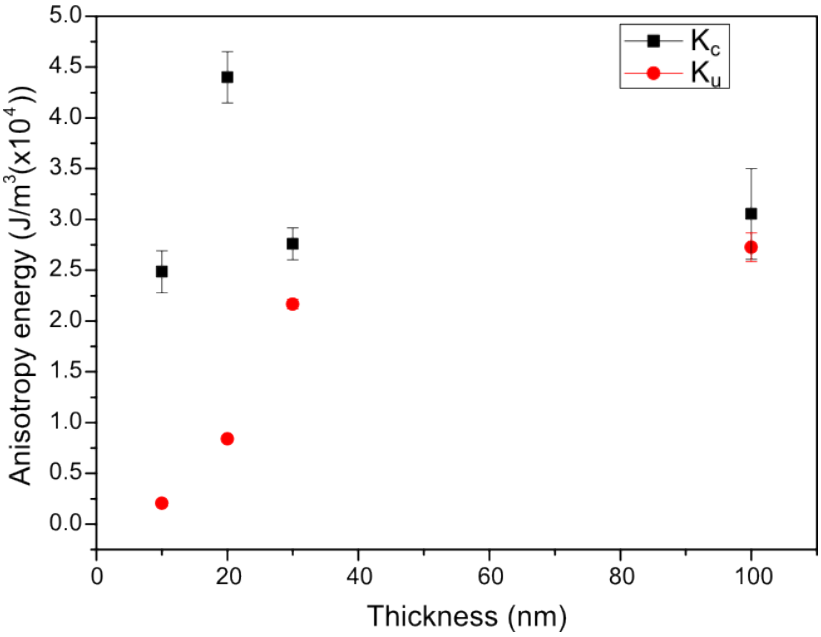

Fig. 4.5 Values for the uniaxial, K_u, and cubic anisotropy, K_c, constants in $Fe_{1-x}Ga_x$ at 300K. K_c is represented by the black points and K_u by the red. Values were determined by fitting numerically calculated magnetic hysteresis loops to the experimental SQUID magnetometry data.

Figure 4.5 shows that at room temperature the uniaxial anisotropy grows with the thickness of the sample and then saturates at around 30nm. The cubic anisotropy however remains relatively constant, except for a spike in the 20nm sample. This pattern repeats itself when the samples are cooled to 2K, producing the anisotropy results shown in figure 4.6.

When the samples are cooled to 2K the cubic anisotropy shows the same behaviour. The uniaxial anisotropy remains low until the thickness hits 30nm at which point it rises abruptly. The errors on these measurements are reasonably small indicating that this pattern is not a product of either noise in the measurement or imprecision in the fitting method. In order to confirm the validity of the fitting procedure the process of finding the anisotropy values was the repeated for pure Fe grown on GaAs in imitation of reference [78], in order to test the efficacy of the fitting methods employed. This resulted in the hysteresis loops shown in figure 4.7.

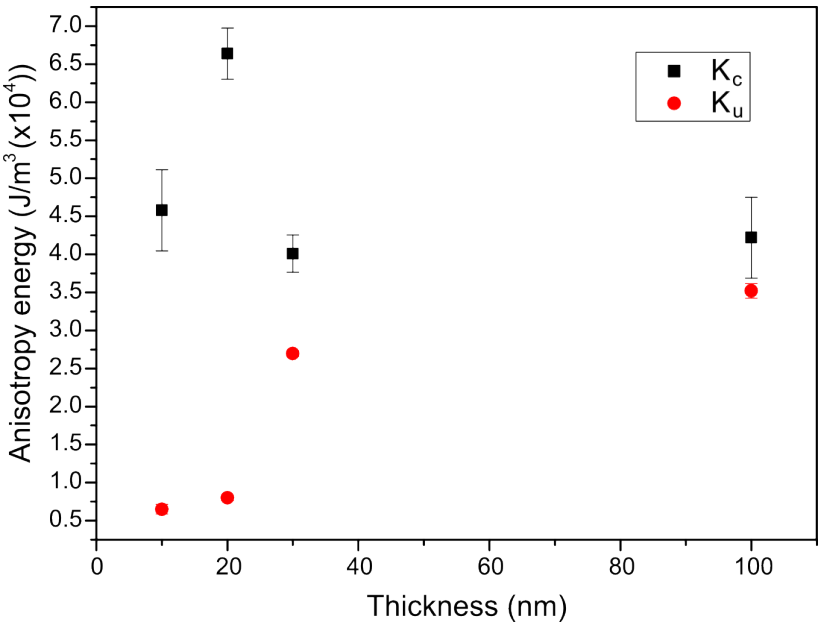

Fig. 4.6 Values for the uniaxial, K_u, and cubic anisotropy, K_c, constants in $Fe_{1-x}Ga_x$ at 2K. K_c is represented by the black points and K_u by the red. Values were calculated from SQUID magnetometer data.

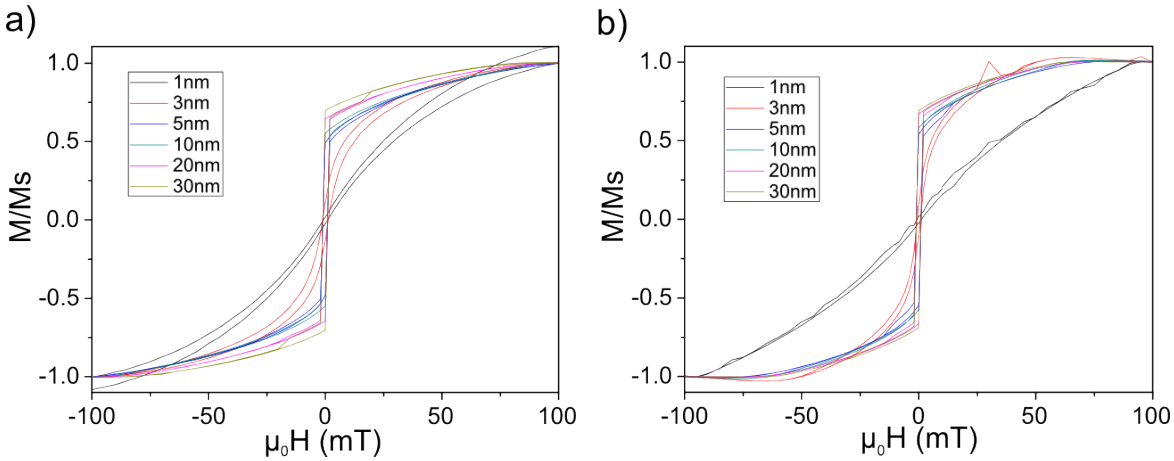

Fig. 4.7 Hysteresis loops for Fe grown on GaAs, normalised by the saturation magnetisation with the field applied along the $[1\bar{1}0]$ direction. The initial loops were taken by sweeping the field from 200mT to -200mT and back again however the data is shown in the range -100mT to + 100mT to focus on the region of interest. a) shows the measurements at 2K and b) shows the measurements at 300K.

The anisotropy analysis for these curves was then repeated resulting in the anisotropy relations at 300K shown in figure 4.5.

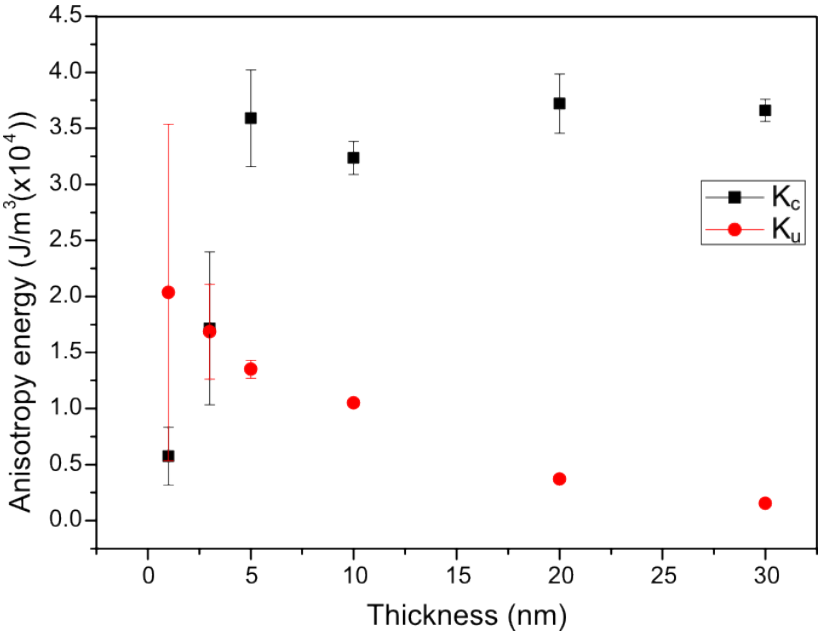

Fig. 4.8 Values for the uniaxial and cubic anisotropy constants in iron at 300K. K_c is represented by the black points and K_u by the red. Values were calculated from SQUID magnetometer data.

We can see that the uncertainty in the K_u value in the 1nm sample is relatively large. This can be understood by looking at references [78] and [85] in which films of this thickness were studied and it was found that when the film thickness dropped below ∼4.8ML (0.72nm) the iron formed islands on the surface of the substrate rather than a continuous film. These islands were also found to be super paramagnetic meaning that whilst they form a single magnetic domain due to their small size, the domain they form can be changed purely by fluctuations in temperature when no field is applied to the sample. The magnetic response of our 1nm Fe sample shown in figure 4.7 indicates that this is indeed the case and is what has happened to our 1nm Fe film even if the thickness is slightly above the thickness at which we would expect this transition to occur. The early emergence of superparamagnetism may be due to the material being sputter grown rather than MBE grown, the thickness being lower than expected or due to variation in the growth temperature. Indeed thicknesses at which the superparamagnetism to ferromagnetism transition occurs have been observed at thicknesses as much as ∼10ML (1.5nm) in reference [131]. If we look at the anisotropy results for the same samples at 2K we find the results shown in figure 4.6.

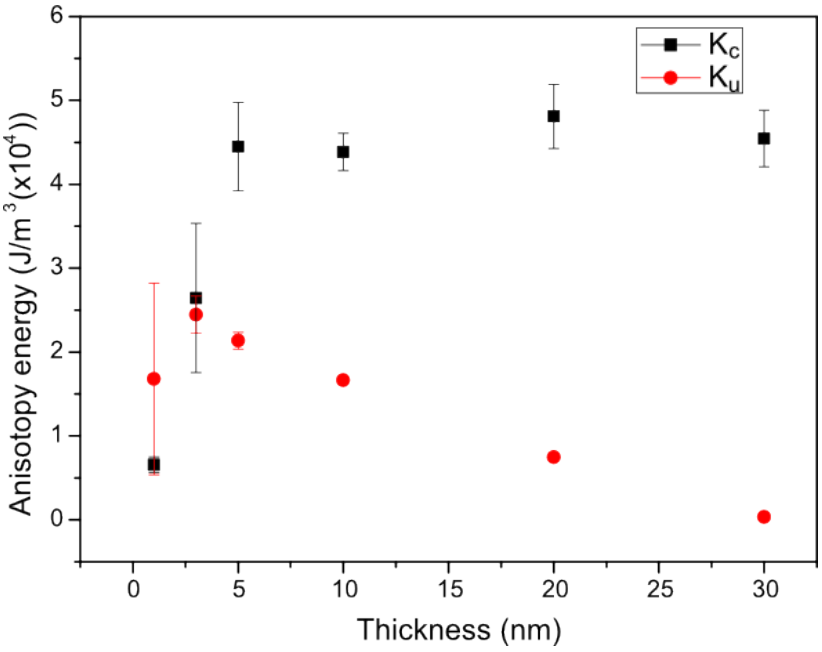

Fig. 4.9 Values for the uniaxial and cubic anisotropy constants in iron at 2K. K_c is represented by the black points and K_u by the red. Values were calculated from SQUID magnetometer data.

Here we see a similar pattern as in figure 4.8 however, the uniaxial anisotropy for the sample at 1nm does not follow the trend that the rest of the samples adhere to. This can again be explained by the extremely low thickness of the sample possibly not creating a continuous film on the surface of the substrate.

By comparing the results in figures 4.8 and 4.9 we can see that the anisotropy of iron grown on GaAs gives the same anisotropy relation as found in [78] shown in figure 2.5. The unaxial anisotropy constant decreases and the cubic anisotropy constant increases as the thickness of the film increases.

The anisotropy results found using least squares fit analysis were checked according to the relation described in reference [132]. This involved finding the ratio of the remnant magnetisation of the sample to the saturation magnetisation which is related to the ratio between the constants of uniaxial and cubic anisotropy according to the relation in equation 4.1.

$$\frac{K_u}{K_c} = 2(\frac{M_{res}}{M_s})^2 - 1 \tag{4.1}$$

The results of this consistency check for $Fe_{1-x}Ga_x$ are shown in table 4.3.

Sample no.	Sample thickness (nm)	$\frac{K_u}{K_c}$	$\delta(\frac{K_u}{K_c})$	M_s $[1\bar{1}0]$ $Am^{-1}(\times 10^6)$	M_{rem} $[1\bar{1}0]$ $Am^{-1}(\times 10^6)$	$1-2(\frac{M_{res}}{M_s})^2$ $[1\bar{1}0]$
S159	10	0.08	0.01	1.57	1.07	0.07 $\pm$0.02
S219	20	0.19	0.01	1.54	0.97	0.20 $\pm$0.00
S221	30	0.78	0.05	1.52	0.51	0.77 $\pm$0.02
S227	100	0.89	0.13	1.47	0.41	0.84 $\pm$0.01

Table 4.3 Consistency check results for $Fe_{1-x}Ga_x$ at 300K. The sample thickness is a nominal value.

The error in the value of $\frac{K_u}{K_c}$ was calculated using equation 4.2 in which the error in K_c is given by δK_c and the error in K_u is given by δK_u.

$$\delta\frac{K_u}{K_c} = \sqrt{(\frac{\delta K_u}{K_c})^2 + (\frac{-K_u \delta K_c}{K_c^2})^2} \tag{4.2}$$

The error in $1-2(\frac{M_{res}}{M_s})^2$ was found as the difference in the value of $1-2(\frac{M_{res}}{M_s})^2$ when calculated from the up and the down loop with the value given being the mean of the two values. This consistency check was then repeated for the data measured at 2K and is shown in table 4.4.

Sample no.	Sample thickness (nm)	$\frac{K_u}{K_c}$	$\delta(\frac{K_u}{K_c})$	M_s $[1\bar{1}0]$ $Am^{-1}(\times 10^6)$	M_{rem} $[1\bar{1}0]$ $Am^{-1}(\times 10^6)$	$1-2(\frac{M_{res}}{M_s})^2$ $[1\bar{1}0]$
S159	10	0.14	0.02	1.60	1.04	0.16 $\pm$0.01
S219	20	0.12	0.01	1.55	1.02	0.13 $\pm$0.00
S221	30	0.67	0.04	1.50	0.61	0.67 $\pm$0.01
S227	100	0.83	0.10	1.47	0.49	0.78 $\pm$0.00

Table 4.4 Consistency check results for $Fe_{1-x}Ga_x$ at 2K. The sample thickness is a nominal value.

In these tables we see that the values of $\frac{K_u}{K_c}$ and $1-2(\frac{M_{res}}{M_s}^2)$ are roughly equal, with the differences in values being well within the boundaries of reasonable error. This further indicates that the results generated by fitting to the SQUID data are accurate. Then the results of the check for the iron sample at 300K are shown in table 4.5 and the results for 2K are shown in table 4.6.

Sample no.	Sample thickness (nm)	$\frac{K_u}{K_c}$	$\delta(\frac{K_u}{K_c})$	M_s $[1\bar{1}0]$ $Am^{-1}(\times 10^6)$	M_{rem} $[1\bar{1}0]$ $Am^{-1}(\times 10^6)$	$1-2(\frac{M_{res}}{M_s})^2$ $[1\bar{1}0]$
S406	1	3.54	3.05	1.49	1.13	1.00 $\pm$0.00
S407	3	0.98	0.46	1.39	0.12	0.98 $\pm$0.01
S408	5	0.38	0.05	1.50	0.81	0.41 $\pm$0.02
S366	10	0.32	0.02	1.31	0.75	0.34 $\pm$0.02
S367	20	0.10	0.01	1.31	0.88	0.11 $\pm$0.00
S368	30	0.04	0.01	1.31	0.90	0.05 $\pm$0.01

Table 4.5 Consistency check results for iron at 300K. The sample thickness is a nominal value.

Sample no.	Sample thickness (nm)	$\frac{K_u}{K_c}$	$\delta(\frac{K_u}{K_c})$	M_s $[1\bar{1}0]$ $Am^{-1}(\times 10^6)$	M_{rem} $[1\bar{1}0]$ $Am^{-1}(\times 10^6)$	$1-2(\frac{M_{res}}{M_s})^2$ $[1\bar{1}0]$
S406	1	2.56	1.79	0.38	0.00	1.00 $\pm$0.00
S407	3	0.92	0.33	1.43	0.18	0.97 $\pm$0.01
S408	5	0.48	0.06	1.49	0.73	0.54 $\pm$0.03
S366	10	0.38	0.02	1.35	0.74	0.40 $\pm$0.01
S367	20	0.15	0.01	1.35	0.87	0.18 $\pm$0.00
S368	30	0.01	0.01	1.19	0.83	0.02 $\pm$0.00

Table 4.6 Consistency check results for iron at 2K. The sample thickness is a nominal value.

The similarity in results for $\frac{K_u}{K_c}$ and $1-2(\frac{M_{res}}{M_s})^2$ of most of the iron consistency checks indicate that the fitting results for iron are also accurate. In the 1nm samples however the difference in $\frac{K_u}{K_c}$ and $1-2(\frac{M_{res}}{M_s})^2$ is much larger.

This can be explained by remembering that the 1nm samples exhibited super paramagnetism meaning that the model used to fit to the data is not valid for this sample.

In order to further investigate the anomalous measurements of the uniaxial anisotropy in the 20nm film, S219, a second batch of $Fe_{1-x}Ga_x$ wafers were prepared with film thickneses of 20nm and 30nm, the wafer numbers being S411 and S410 respectively. These wafers were then cut up and SQUID magnetometer measurements were performed on samples of the wafer in the same manner as was performed in section 4.2 resulting in the loops shown in figures 4.10 and 4.11 representing SQUID loops for the 20nm sample at 300K and 2K.

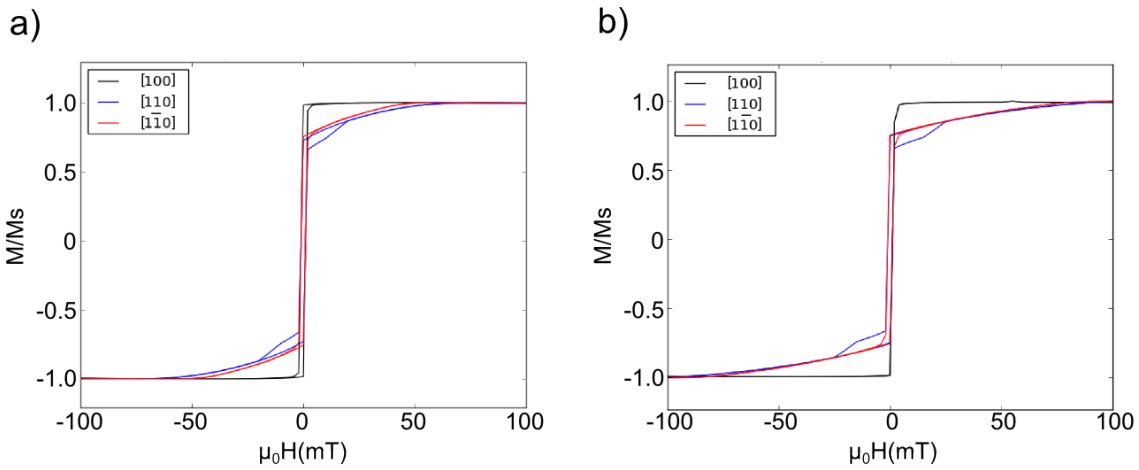

Fig. 4.10 Hysteresis loops collected by SQUID magnetometry for S411 at a) 300K and b) 2K. The loops were collected with the field aligned to three different directions, the [110] direction, the [1$\bar{1}$0] direction and the [100] direction. The field was swept from -200mT to +200mT and back again, shown here are the results within the -100mT to +100mT window.

In figure 4.11 we can see that the [110] and [1$\bar{1}$0] axes are roughly equivalent hard axes and the [100] axis is the relative easy axis. This would indicate a lack of uniaxial anisotropy since in S219, the 20nm sample, the uniaxial anisotropy led to the [1$\bar{1}$0] axis being the hard axis. The fitting will still be performed on the magnetic hysteresis loop collected with the magnetic field aligned along the [1$\bar{1}$0] since the relatively hard axes are roughly equivalent. This behaviour is evidenced in the SQUID loops at both 300K and 2K. Next we look at the SQUID loops for data collected on the secondary 30nm sample which are shown in figure 4.11.

Figure 4.11b) shows that the [1$\bar{1}$0] and [110] loops are once again roughly equally hard meaning that either the [1$\bar{1}$0] or the [110] could be used to determine the values of K_c and K_u. The [1$\bar{1}$0] loop is the loop used for fitting however, for the sake of consistency with previously measured samples. The loops shown in figures 4.10 and 4.11 were then subjected to the same analysis procedure as the loops tested in 4.2. The results of this analysis for the two secondary samples at 300K are shown plotted alongside the results for the primary samples in figure 4.12.

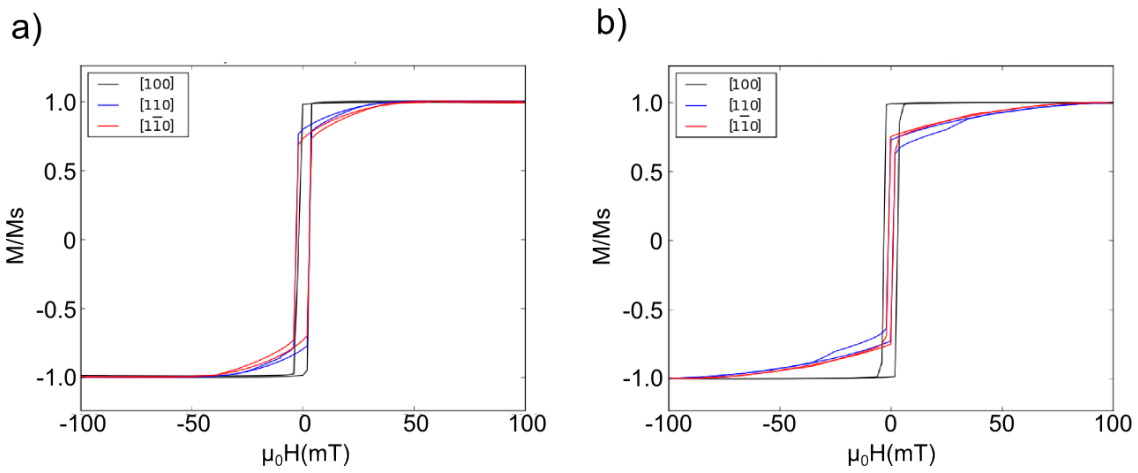

Fig. 4.11 Hysteresis loops collected by SQUID magnetometry for the S410 at a)300K and b)2K. The loops were collected with the field aligned to three different directions, the [110] direction, the [1$\bar{1}$0] direction and the [100] direction. The field was swept from -200mT to +200mT and back again, shown here are the results within the -100mT to +100mT window.

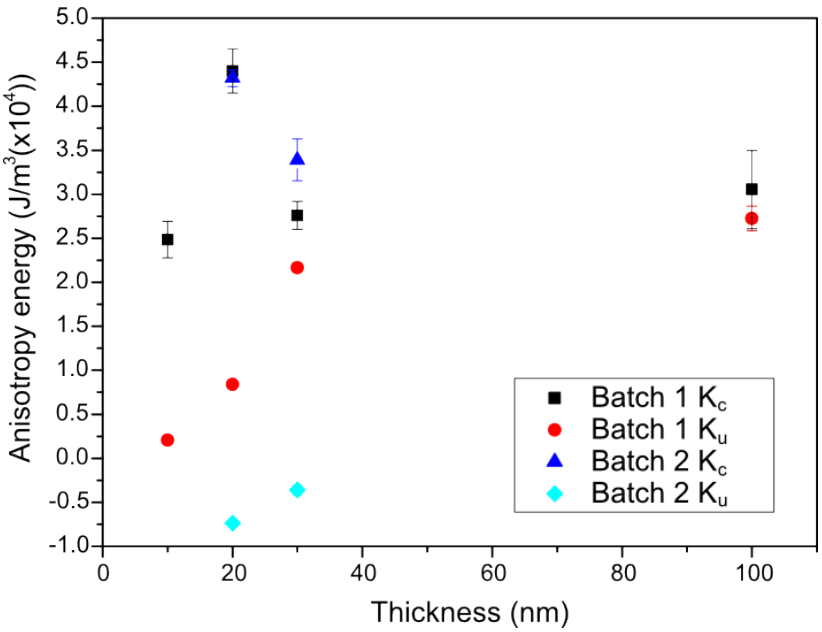

Fig. 4.12 Anisotropy at 300K with the films from the second batch included. Error bars are shown for all measurements however many of the error bars are smaller than the markers.

This shows that whilst the uniaxial anisotropy for the secondary loops is negative, the cubic anisotropy in the samples is roughly equal to the anisotropy values found for the primary samples. This indicates that even with some change in internal structure, altering the uniaxial anisotropy, the cubic anisotropy retains a strong thickness relation. Further evidence supporting this is provided by figure 4.13 where the loops for these samples at 2K are analysed.

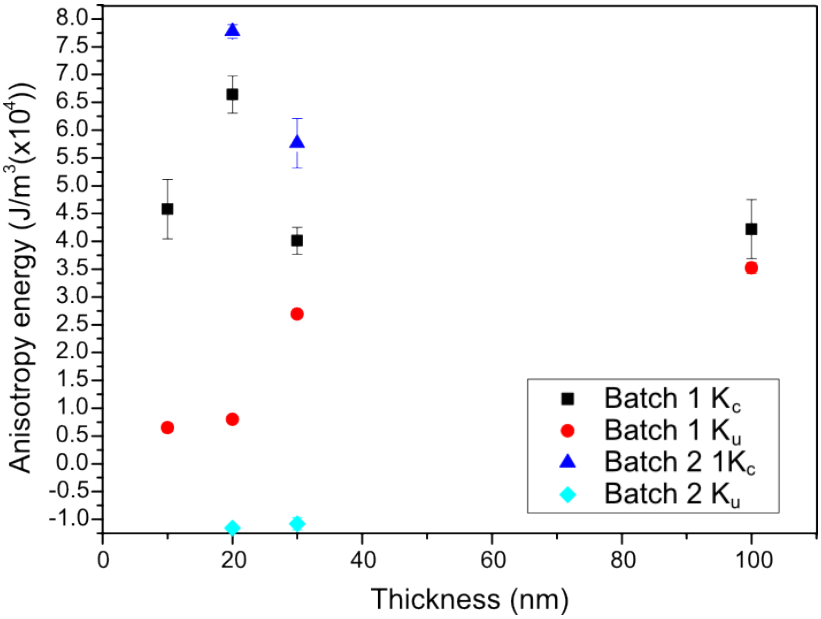

Fig. 4.13 Anisotropy at 2K with the films from the second batch included. Error bars are shown for all measurements however many of the error bars are smaller than the markers.

This shows the same relation as in measurements at 300K however the change in the uniaxial anisotropy is smaller and the anisotropy constant has a negative value. The experiment was repeated with chips taken from a different region of the wafer. The SQUID loops produced in this way are shown in figure 4.14.

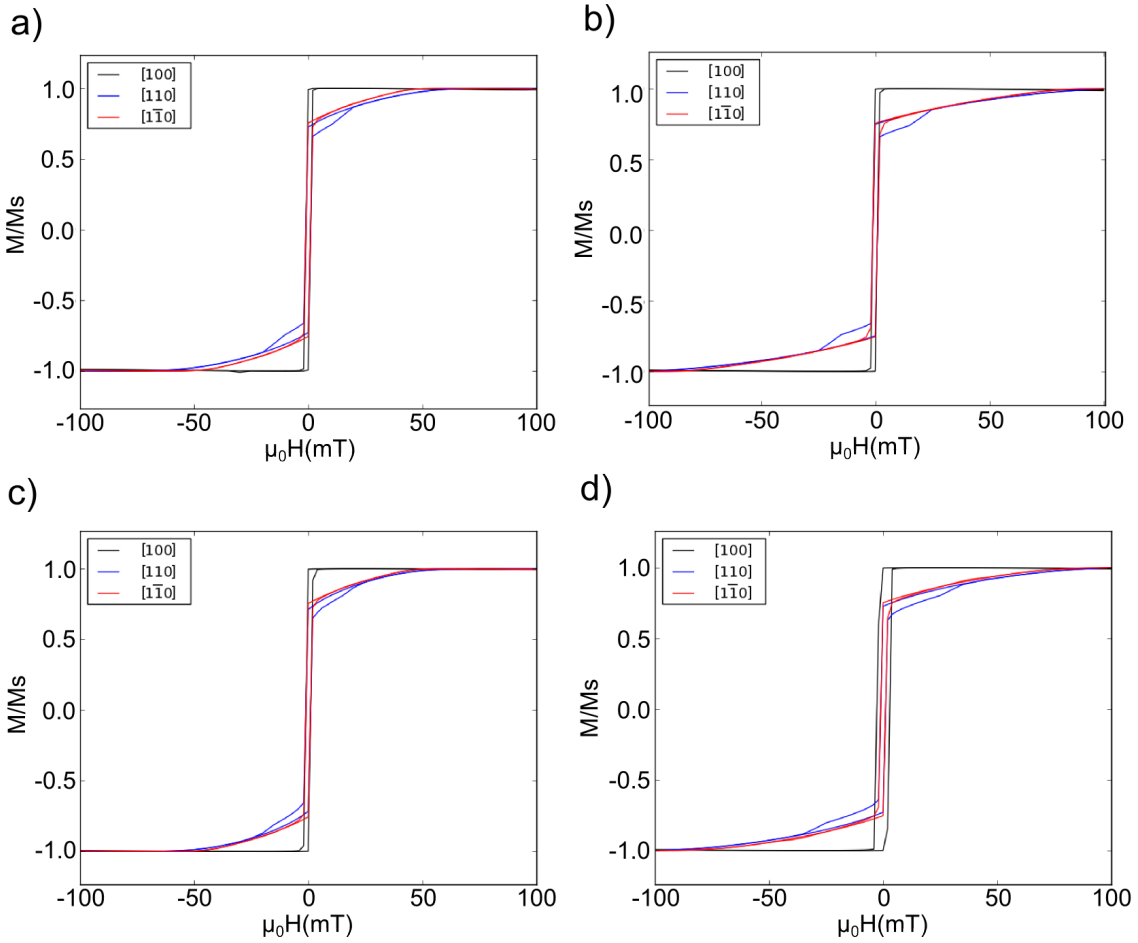

Fig. 4.14 Hysteresis loops collected by SQUID magnetometry for the second chips collected taken from the secondary samples. The loops were collected with the field aligned to three different directions, the [110] direction, the [1$\bar{1}$0] direction and the [100] direction. The field was swept from -200mT to +200mT and back again, shown here are the results within the -100mT to +100mT window. The loops represent S411, the 20nm sample, a) and b), and S410, the 30nm sample, c) and d). The loops were collected at 300K, a) and c), and 2K b) and d).

These loops bear a striking resemblance to the loops collected in figures 4.10 and 4.11 and when analysed resulted in similar values of K_c and K_u as shown at 300K in figure 4.15.

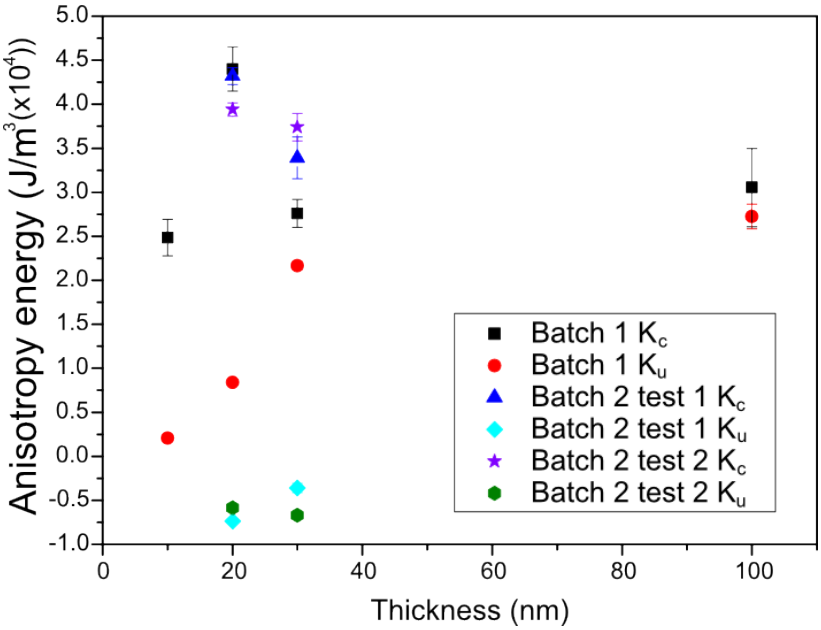

Fig. 4.15 Anisotropy at 300K with the films from the second batch included. Error bars are shown for all measurements however many of the error bars are smaller than the markers.

The similarities continue when we look at the results collected when the wafers were cooled to 2K as shown in figure 4.16.

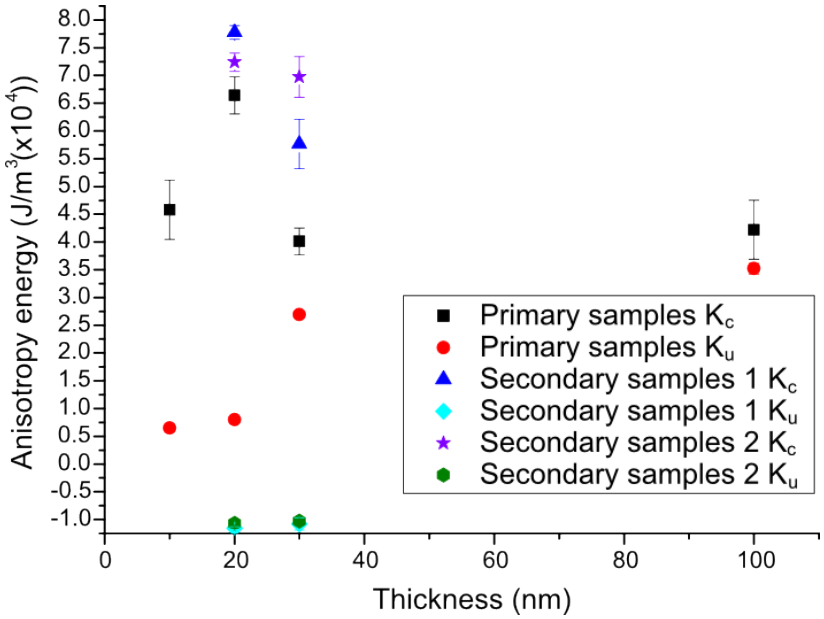

Fig. 4.16 Anisotropy at 2K with the films from the second batch included. Error bars are shown for all measurements however many of the error bars are smaller than the markers.

From figure 4.15 and figure 4.16 it can be observed that the anisotropy constants for the samples S411 and S410 follow the same trend both times they were measured. It can also be seen that whilst the uniaxial anisotropy values differ between the first and second batch of samples the cubic anisotropy retains the same trend with film thickness.

These anisotropy values were tested in the same way as was done for the iron and the first set of $Fe_{1-x}Ga_x$ wafers and the values found from the collected loops are consistent as shown in table 4.7 which represents the loops at 300K and table 4.8 which represents the loops at 2K.

Sample -	Sample thickness (nm)	$\frac{K_u}{K_c}$	$\delta(\frac{K_u}{K_c})$ $[1\bar{1}0]$	M_s $[1\bar{1}0]$ $Am^{-1} \times 10^6$	M_{rem} $[1\bar{1}0]$ $Am^{-1} \times 10^6$	$1-2(\frac{M_{res}}{M_s})^2$
S411	20nm sample 1	-0.17	0.01	1.65	1.26	-0.17 $\pm$0.01
S410	30nm sample 1	-0.11	0.02	1.60	1.18	-0.09 $\pm$0.00
S411	20nm sample 2	-0.15	0.01	1.49	1.13	-0.15 $\pm$0.01
S410	30nm sample 2	-0.18	0.01	1.58	1.21	-0.17 $\pm$0.02

Table 4.7 Consistency check results for the second batch of $Fe_{1-x}Ga_x$ films at 300K The sample thickness is a nominal value.

Sample no.	Sample thickness (nm)	$\frac{K_u}{K_c}$	$\delta(\frac{K_u}{K_c})$ $[1\bar{1}0]$	M_s $[1\bar{1}0]$ $Am^{-1} \times 10^6$	M_{rem} $[1\bar{1}0]$ $Am^{-1} \times 10^6$	$1-2(\frac{M_{res}}{M_s})^2$
S411	20nm sample 1	-0.15	0.01	1.66	1.25	-0.14±0.02
S410	30nm sample 1	-0.19	0.02	1.62	1.22	-0.13±0.01
S411	20nm sample 2	-0.15	0.01	1.52	1.15	-0.14±0.00
S410	30nm sample 2	-0.15	0.01	1.62	1.22	-0.13±0.01

Table 4.8 Consistency check results for the $Fe_{1-x}Ga_x$ films from the second batch at 2K. The sample thickness is a nominal value.

The concentration of iron in the samples was found using the same method as described previously which yielded the results shown in table 4.9.

Sample no.	Sample	Measured area (mm^2)	Volume (m^3 ($\times 10^{-13}$))	M_s (Am^{-1})	Iron content (%)
S411	20nm test 1	22.1±0.2	4.4±1.0	1.47×10^6	86.5 ± 16.0
S410	30nm test 1	20.3±0.2	6.1±1.5	1.55×10^6	91.2 ± 18.2
S410	20nm test 2	19.6±0.2	3.9±1.0	1.49×10^6	87.7 ± 17.7
S411	30nm test 2	20.8±0.2	6.2±1.5	1.55×10^6	91.2 ± 17.7

Table 4.9 Iron concentration in the $Fe_{1-x}Ga_x$ samples from the second batch at 300K.

This table shows that the iron concentration in the secondary samples is generally higher than in the primary films however this does not give any indication as to why the uniaxial anisotropy is so much lower in these samples as compared to the primary films. Body centred cubic structure is the most probable structure of these sputter grown films as the gallium concentration is typically below $\sim 20\%$ and studies have found that a body centred cubic structure for $Fe_{1-x}Ga_x$ to be the most likely structure for epitaxially grown $Fe_{1-x}Ga_x$ films grown on GaAs substrates in reference [133] and in sputter grown films in reference [49]. The large error in the percentage of iron in these samples indicates that there may be some instances of B2 structure mixed into the A2 structure however further calibration growths may reveal that these errors are an overestimate and that the structure is purely A2.

The results from the iron samples demonstrates that the fitting and measurement procedure is reliable however the anisotropy results found from the $Fe_{1-x}Ga_x$ samples is somewhat perplexing. The results of the measurement of K_c and K_u show that the cubic anisotropy spikes in the 20nm sample but rises gradually in all other samples.

4.3 X-ray analysis of the $Fe_{1-x}Ga_x$ samples

Triple axis diffractometery experiments were performed on the samples S159(10nm), S219(20nm), S221(30nm) and S227(100nm) by Dr. P. Wadley. These experiments involved measuring the diffraction of x-rays from the surface of the sample at various angles in order to construct 2D reciprocal space maps. By altering the position of the sample relative to the x-ray source different planes of the sample could be investigated. By analysing multiple 2D reciprocal space maps the mean size and misorientation of the mosaic blocks which made up the sample could be determined using the fitting processes performed by Prof. V. Holý at Charles University, Prague. Unfortunately the 10nm sample (S159) was found to be too thin for effective x-ray analysis of the sample however 2D reciprocal space maps were constructed for S219, S221 and S227. These maps are shown in figure 4.17.

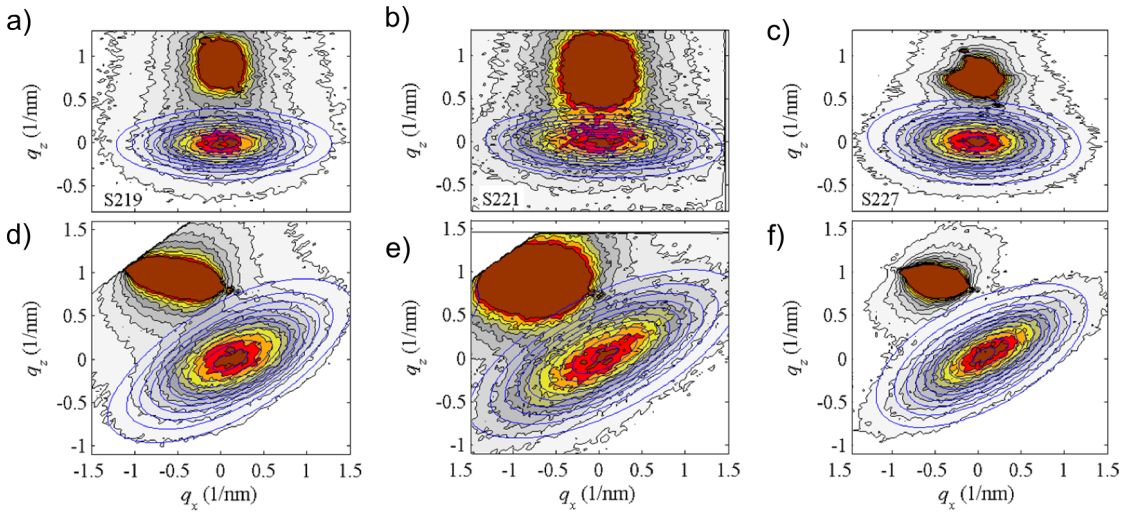

Fig. 4.17 Reciprocal space maps collected by triple axis diffractometry by Dr. P. Wadley. The data is shown in red whilst the fit is demonstrated by the blue lines. a), b) and c) show diffractometry data when x-rays were diffracted from the (002) plane and d), e) and f) show data diffracted from the (112) plane. a) and d) represent data collected on wafer S219, b) and e) represent data taken on wafer S221 and c) and f) represent data taken on wafer S227.

Looking at the reciprocal space maps we can see that there are two dots in each image, one centred roughly on (0, 0) and one centred on (0,1) in a), b) and c) but (-0.5, 1) in d), e) and f). This is because the dot centred around (0, 0) represents diffraction from the $Fe_{1-x}Ga_x$ and the dot centred around either (0, 1) or (-0.5, 1) represents x-ray diffraction from the GaAs substrate.

By looking at the separation between these dots lattice constants for the $Fe_{1-x}Ga_x$ films may be extracted. This was done by Prof. V. Holý at Charles University, Prague yielding the lattice constants in and out of the plane of the film shown in figure 4.18.

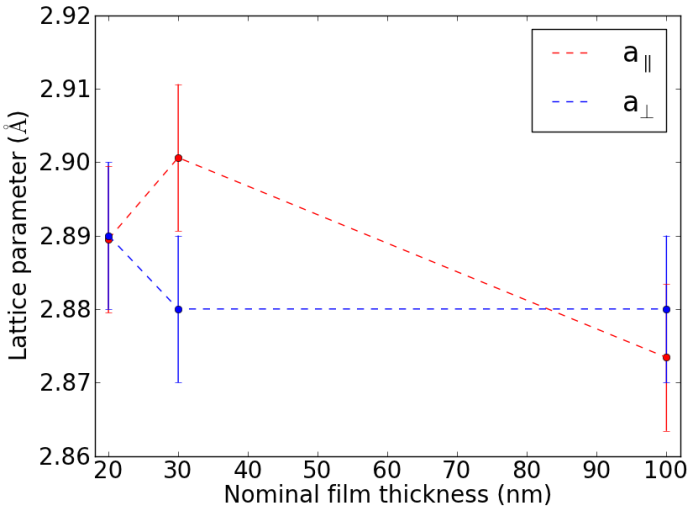

Fig. 4.18 Plots of the lattice constants of the material in the plane of the film,$a_{\parallel}$, and out of the plane of the film, $a_{\perp}$.

From these lattice constants the in-plane lattice mismatch between the film and the substrate , η_{miss} may be calculated using equation 4.3 in which a_0 is half the lattice parameter of the GaAs substrate, 2.83nm[78, 85]. This value represents the lattice parameter of $Fe_{1-x}Ga_x$ when perfectly matched to the GaAs substrate resulting in zero strain.

$$\eta_{miss} = \frac{a_{\parallel} - a_0}{a_0} \tag{4.3}$$

Applying equation 4.3 to the in plane lattice constants given in figure 4.18 we can find the percentage lattice mismatch which is given in figure 4.19.

Figures 4.18 and 4.19 show no clear correlation between the lattice parameters of the films and their thickness. This most likely indicates that the large uniaxial anisotropy observed in the 20nm film was not due to a unusually high strain induced by the mismatch between the $Fe_{1-x}Ga_x$ film and the GaAs substrate. The strain observed in these samples is slightly lower than the strain observed in MBE grown material of 4.6% [128].

For further information to be gathered from the reciprocal space maps we must look at the results of the fitting procedure performed by Prof. V. Holý. This fitting procedure involves

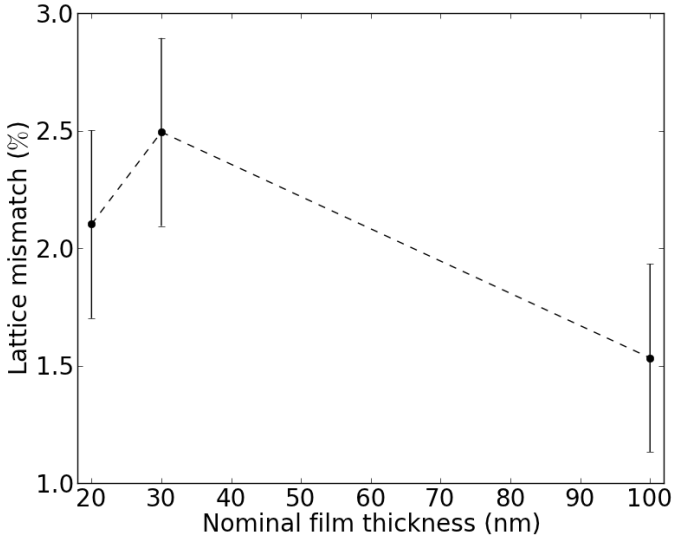

Fig. 4.19 In-plane lattice mismatch between the $Fe_{1-x}Ga_x$ film and the GaAs substrate calculated using the data shown in figure 4.18.

simulating the lattice as a mosaic of ellipsoidal crystals with the fitting parameters being the crystal axis dimensions in the in and out of the plane directions. The fitting procedure also provides information as to the average misorientation of the crystals, the mean angle of rotation required to move two crystals onto the same frame as one another. This process is not described in detail in this thesis as all analysis of the reciprocal space maps was done at Charles University. This fitting procedure is demonstrated by the blue lines on the reciprocal space maps and yielded the results shown in figure 4.20.

Here we can see that whilst the block size in the x plane does change slightly the alteration is within the bounds of error and could therefore be entirely down to noise within the measurement leading us to state that there is no evidence for a thickness dependence on the size of the mosaic blocks in the plane of the sample. The same is true of the angle of misorientation which indicates that the misalignment of the blocks is also independent of the thickness of the material. The change in the z-radius of the ellipses indicates a relation to the thickness of the sample. We see that as the thickness of the sample increases the mean block size decreases in the z direction. This in itself is not sufficient to provide a concrete understanding of the causes of the anisotropy results presented in section 4.2 or the high magnetostrictive energy observed in section 4.5. The grain size observed in these samples is much lower than was observed in $Fe_{1-x}Ga_x$ films sputter grown on Si substrates by Dean et al. [54] in which grain sizes between 40 and 80 nm were observed depending on thickness.

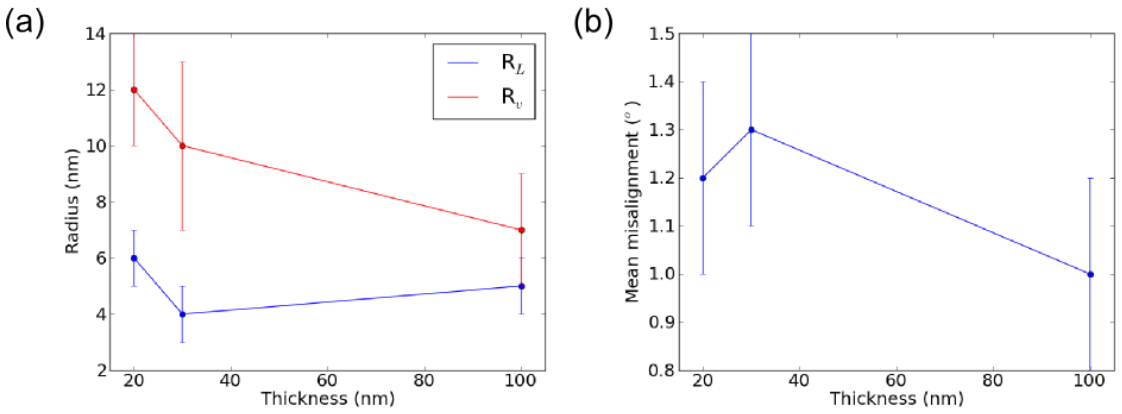

Fig. 4.20 Plot of results of fitting to triple axis diffractometry data done by Václav Holý at Charles University in Prague. Figure a) shows the mean block size in the x, R_L, and z, R_v, directions in nm and b) shows the mean disorientation of the blocks.

The grain size observed here is also much lower than the grain size observed in MBE grown material by Parkes et al. [61] where the film was observed to be roughly mono-crystalline. Whilst the mean grain size was small the mean misalignment between the grains was also very small which may explain the high magnetostriction as the magnetostriction constant is largest along the [100] direction. Large misorientations would lead to the magnetostriction constant being reduced due to many crystallites being aligned away from this direction whilst the mosaic structure suggested by these data would mean a large number of crystallites aligned to this direction.

In order to continue this work rocking curves should be collected and analysed in order to give insights into the sample thickness, the substrate film interface and the number of defects within the films. This would hopefully provide further insight into the polycrystallinity of the samples as well as the gallium content which in turn might explain the high magnetostriction and cubic anisotropy found in the 20nm galfenol film from the first batch of samples, S219, as well as the general trend of increasing cubic anisotropy and decreasing uniaxial anisotropy. Performing x-ray measurements on the samples from the second batch could also hopefully provide some insight into the strange uniaxial anisotropy values found for those samples and the apparent lack of differentiation between the film's [110] and [1$\bar{1}$0] crystal axes.

4.4 Discussion of magnetometry and x-ray results

We have used SQUID magnetometry and X-ray triple axis diffractometery to study the magnetic anisotropies and the crystal structure in $Fe_{1-x}Ga_x$ thin films grown by sputter

deposition onto GaAs substrates. We have observed that $Fe_{1-x}Ga_x$ films grown in this way exhibit both uniaxial and cubic anisotropy. We have observed that the trend between thickness and anisotropy is the opposite of that observed in iron samples. We have also observed an unusually high cubic anisotropy in the 20nm $Fe_{1-x}Ga_x$ films studied. This unusually high cubic anisotropy was repeatedly observed across both batches of 20nm $Fe_{1-x}Ga_x$ films, S219 and S411, indicating that films of thicknesses between 10nm and 30nm may be an interesting avenue for further study to discover at what thickness the cubic anisotropy is at a maximum thereby providing a further insight which may help to explain this unusual result.

The hysteresis loops collected from samples S411 and S410 were identical regardless as to whether the loops were collected with the magnetic field applied in the $[1\bar{1}0]$ or the [100] direction indicating no uniaxial anisotropy due to the $Fe_{1-x}Ga_x$ film not growing epitaxially on the GaAs surface[63, 78]. Despite this the result of fitting to the hysteresis loop produced by sweeping the field in the $[1\bar{1}0]$ direction yielded a non-zero negative uniaxial anisotropy. Normally this would indicate a uniaxial anisotropy at 90^o to the applied field however in this instance it most likely indicates that the model is not capable of producing a zero value for the uniaxial anisotropy instead producing a non-zero negative result.

We have also performed studies of iron thin films which were sputter grown onto GaAs substrates. These films demonstrated uniaxial and cubic anisotropy in the $[1\bar{1}0]$ and [100] directions similar to previously described iron films grown on GaAs substrates [63]. The trend in the relation between the thickness and the strength of these anisotropies also matches that of previously described iron films grown on GaAs [78].

This study was followed up with an x-ray study of the devices examined by SQUID magnetometery. This analysis produced no explanations as to the strange behaviour of either the cubic or uniaxial anisotropy of the batch of samples studied due to the lack of a significant variation in the lattice constants of the $Fe_{1-x}Ga_x$ films studied. No x-ray analysis of the second batch of samples, S411 and S410, was performed however. X-ray analysis of these samples may give a greater insight into the causes of the unusual behaviour of the uniaxial anisotropy.

4.5 Transport measurements for $Fe_{1-x}Ga_x$ grown on GaAs

Hall bars were fabricated from the $Fe_{1-x}Ga_x$ wafers and then mounted on a piezoelectric crystal as described in section 3.10. The alignment of these hall bars is repeated in figure 4.21 for the benefit of the reader showing the hall bar used for the measurement of the magnetoelastic constant in figure 4.21a) and the hall bar used as the strain guage in 4.21b).

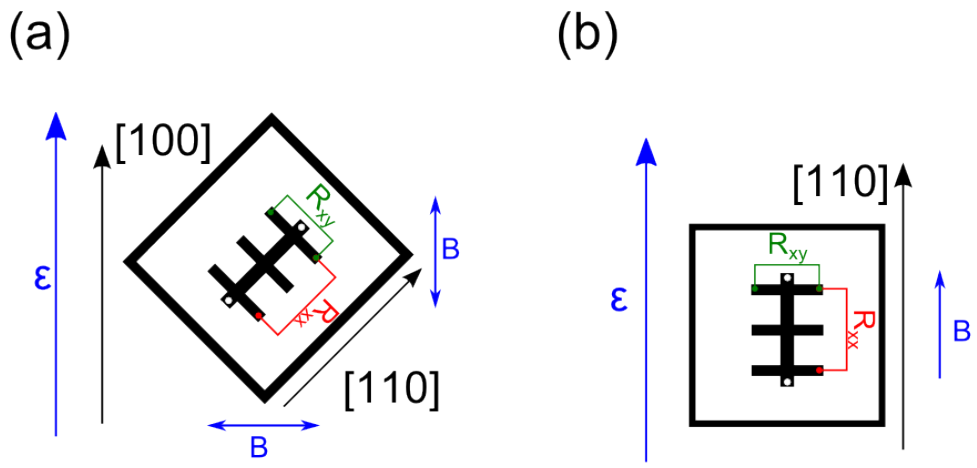

Fig. 4.21 Hall bar alignment used for transport measurements. a) shows the orientation of the hall bar used for measurements used to determine the magnetoelastic constant of galfenol hall bars. b) shows the alignment of the hall bar used as the strain gauge. In both diagrams the direction of the strain and the applied magnetic field are shown by the blue arrows. The two white dots on the bar indicate the arms used to apply voltage across the bar and the terminals used to measure R_{xx} and R_{xy} are shown in red and green respectively. Crystallographic axes of the bars are indicated by the black arrows.

The first data collected on these samples was a measurement of the longitudinal and transverse resistance as a function of the angle of a saturating magnetic field applied in the plane of the film with no applied strain in order to determine the orientation of the bar relative to the magnet. The angle between the external magnetic field and the current may be determined from the resistivity ρ_{xx} and ρ_{xy} using equations 4.4 and 4.5 which were described in full in section 2.6. In equations 4.4 and 4.5 ρ_{av} is the mean resistivity of the sample, $\Delta\rho$ is the change in resistivity due to AMR and θ_{AMR} is the angle between the current and the magnetisation.

$$\rho_{xx} = \rho_{av} + \Delta\rho cos(2\theta_{AMR}) \tag{4.4}$$

$$\rho_{xy} = \Delta\rho sin(2\theta_{AMR}) \tag{4.5}$$

The results of these measurements on the 10 and 20nm samples, S159 and S219 are shown in figure 4.22. The curve for R_{xy} was collected for sample S159 because this is the

resistance measure which will be used to determine the switching fields of the samples (see field sweep measurements presented later in this section), however there was a problem with the cables during the R_{xy} measurement on S219 so the R_{xx} value was used instead.

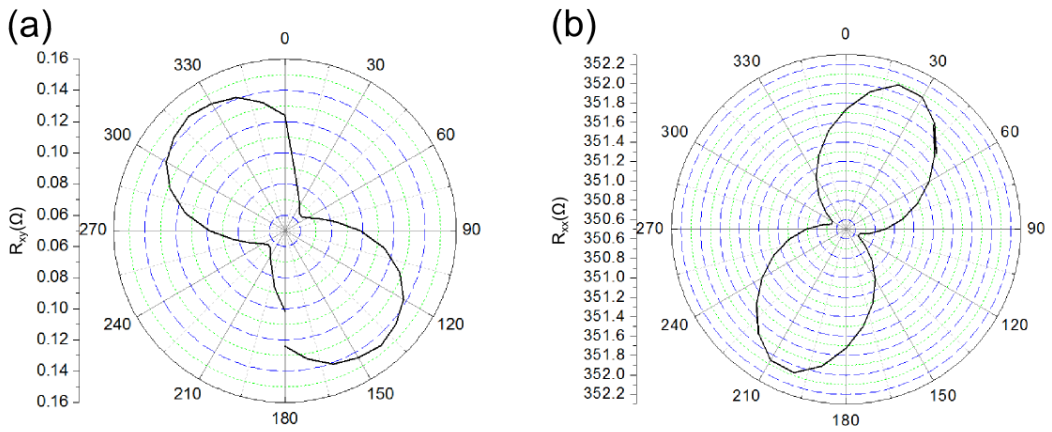

Fig. 4.22 AMR curves for selected $Fe_{1-x}Ga_x$ samples. a) shows the dependency of R_{xy} of the 10nm sample on the angle of applied field and b) shows the dependency of R_{xx} on the angle of applied field for the 20nm sample. No voltage was applied to the piezo-electric transducer for these measurements. A 0.14T magnetic field was used to magnetically saturate the samples.

The AMR curves shown in figure 4.22 were used to determine the position of the samples relative to the magnetic coils used to provide a magnetic field so that the field could be correctly aligned to the crystallographic axis of the devices.

The first sample to be examined was the 10nm sample. The first step in measuring this sample was to measure the relation between the voltage applied to the piezoelectric the sample was mounted on and the strain produced by that voltage. This was done by placing the sample in a saturating magnetic field and then sweeping the voltage on the transducer from -30V to +50V and back again twice in order to find the relation between strain and applied voltage. The saturating magnetic field ensured that any change in resistance was due to the strain on the Hall bar used as the strain gauge which in turn meant we could use the R_{xx} data to determine the strain on the bar when the transducer was subjected to a given voltage. When sweeping the voltage on the transducer steps of 0.1V were used and every time the voltage was stepped up or down the source meter paused until the current required to achieve the desired voltage dropped below $10\mu A$. This was done in order to ensure the transducer was not charging when the measurement was taken. The result of this

measurement performed on a Hall bar used as a strain gauge as described in section 3.10.1 from wafer S159, a 10nm $Fe_{1-x}Ga_x$ film, is shown in figure 4.23.

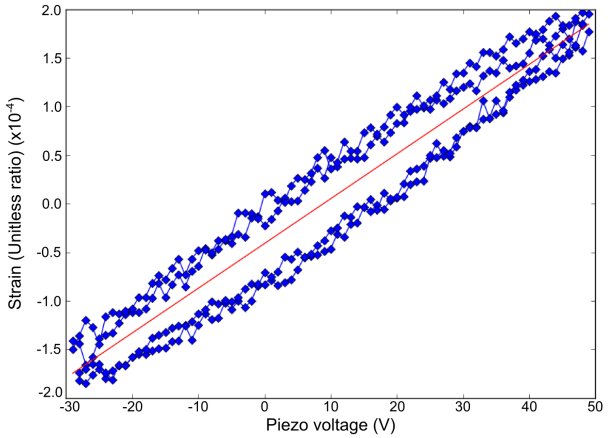

Fig. 4.23 Strain loop for the 10nm $Fe_{1-x}Ga_x$ sample. The voltage applied to the piezoelectric crystal was swept from -30V to +50V and back again twice. The strain was then found from the value of R_{xx} as described in equation 3.13 to produce the relation between voltage on the piezoelectic and strain indicated by the blue data points. This data was then averaged and the result fitted to with a linear polynomial indicated by the red line. This fit gave a strain to voltage ratio of $(4.6 \pm 0.0) \times 10^{-6} V^{-1}$.

This data was fit to in order to find the change in strain as the voltage was applied to the transducer, yielding a strain to voltage ratio of $(4.6 \pm 0.0) \times 10^{-6} V^{-1}$. The error in the measurement was found as the standard error of the fit.

The up and the down sweeps were fitted to simultaneously in order to find a value for the relative strain. Whilst all the data collected within this chapter were collected using an increasing voltage applied to the piezoelectric transducer this relative measurement of strain was used since there is no practical way to determine the absolute strain as a function of voltage applied to the stressor due to strain induced by the curing of the epoxy.

The next step in the measurement was to sweep the field along the magnetic hard axis in order to find the field required to cause magnetic switching in the sample. The raw R_{xy} data collected from the 10nm $Fe_{1-x}Ga_x$ sample, S159, with $(2.3 \pm 0.0) \times 10^{-4}$ strain is shown in figure 4.24a). This data was subject to a number of callibration requirements in order to account for sample heating, the sample lying at a canted angle and mixing of the longitudinal resistance into the transverse resistance. The effects of heating were removed by removing a constant gradient from the data, the sample cant was adjusted for using a process known as symmetrisation and the mixing of the longitudinal and transverse resistances was accounted

for by a process known as a V_{xx} correction. The full details of these corrections may be found in appendix B however the results of these corrections are shown in figure 4.24b).

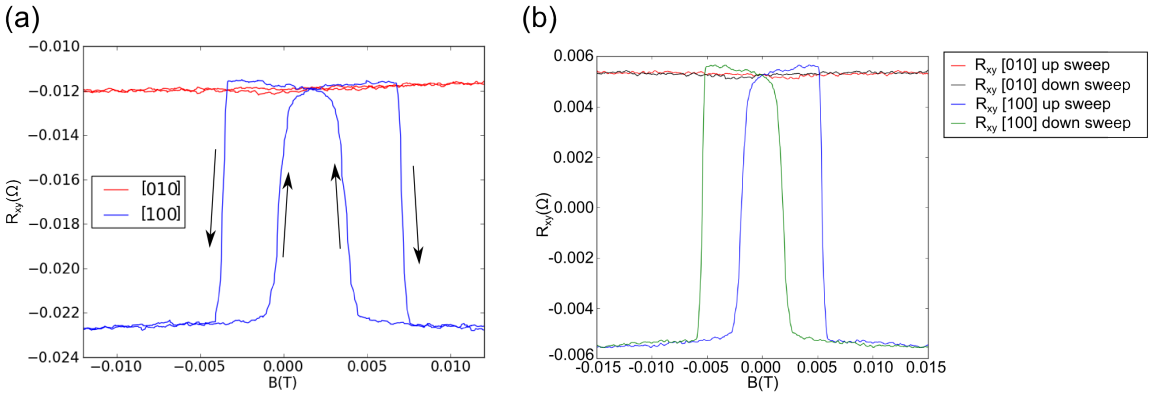

Fig. 4.24 Raw and corrected R_{xy} field sweep data for the 10nm $Fe_{1-x}Ga_x$ sample, S159, with $(2.3 \pm 0.0) \times 10^{-4}$ strain. In a) the raw field sweeps when the field was swept along the [100] direction are shown in blue whilst the measurement of R_{xy} when the field was swept along the [010] direction is shown in red. The black arrows show the sweep directions. b) shows the R_{xy} measurement after the data has been corrected. The results when field was swept along the [100] axis, are shown in blue for the up sweep and green for the down sweep. Results taken when the field was swept the the [010] axis are shown in black for the up sweep and red for the down sweep.

Figure 4.24 demonstrates that when a strain of $(2.3 \pm 0.0) \times 10^{-4}$ is applied, changes in the value of R_{xy} can be seen when the field is applied along the [100] axis indicating that the [100] axis is the hard axis. This change in resistance occurs since the magnetisation of the sample rotates 90^o from the [100] direction and a large field is required to return the magnetisation to lying along the [100] axis. Conversely we can see that the [010] axis is the magnetically easy axis since the magnetisation does not rotate 90^0 to the [010] direction as the field is reduced.

This process was repeated on all the field sweeps in order to produce the field sweeps shown in figure 4.25.

By looking at the change in resistance in these field sweeps we can a strong effect due to applied strain resulting in a change from the hard axis being along the [010] axis when the strain is negative to the [100] direction when the strain is positive. We can also see spikes in the data in figure 4.25b) at $\sim \pm 12$mT and $\sim \pm 9$mT. These are an artefact of the symeterisation procedure amplifying and distorting noise in the measurement.

The switching fields lie in the range of $3 - 5 \times 10^{-3}$T after the switch in hard axis direction. We can demonstrate the switching these loops represent more clearly by using

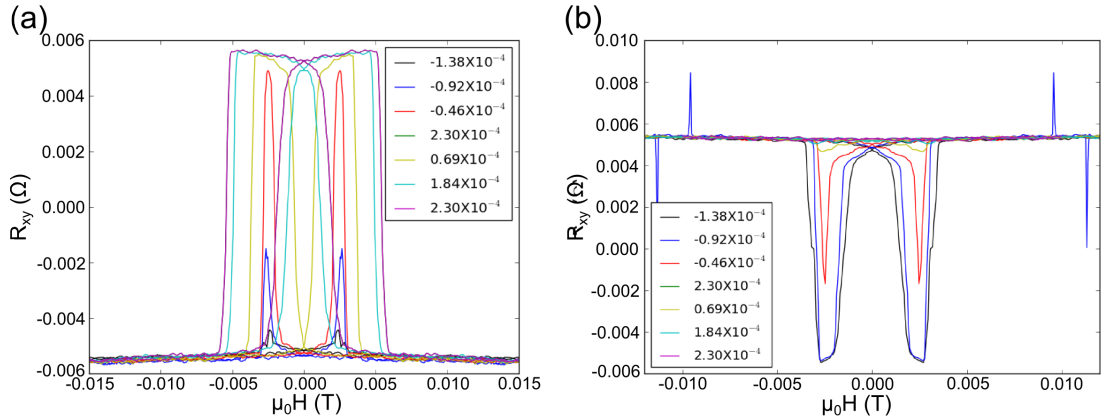

Fig. 4.25 Field sweep loops for 10nm sample, S159, with different levels of stress applied via the transducer. a) shows the effect of applied strain on the field sweeps collected with the field aligned to the [100] direction and b) shows the effects of strain on field sweeps collected with the field aligned along the [010] direction.

them to construct magnetic hysteresis loops. This is done by considering each switching event as a 90 degree switch as demonstrated in figure 4.26. The resistance measurement is converted into an angle as described in equation 3.14. This angle is then adjusted by 180^o in order to take into account the resistance measurement's lack of sensitivity to antiparallel measurements and converted into a magnetisation using equation 3.15. In figure 4.26a) the switching events when the field is increasing are numbered 1 and 2. The change in angle these events represent is demonstrated in figure 4.26b). This can then be used to produce the hysteresis loops shown in figures 4.26c) and 4.26d)which demonstrate hysteresis loops for the 10nm film with 2.3×10^{-4} and -1.4×10^{-4} of strain applied by the transducer respectively. The magnetic hysteresis loop shown in 4.26c) demonstrates the magnetisation rotation when the field is applied along the [100] axis and figure 4.26 d) demonstrates the magnetisation rotation when the field is applied along the [010] axis. This shows the magnetic hysteresis loop produced when the magnetic hard axis lies along the [100] and the [010] axis respectively.

The location of these switching events can extracted with the associated error as described in section 3.10. The extracted switching events are plotted as a function of the strain applied to the sample as has been done in figure 4.27.

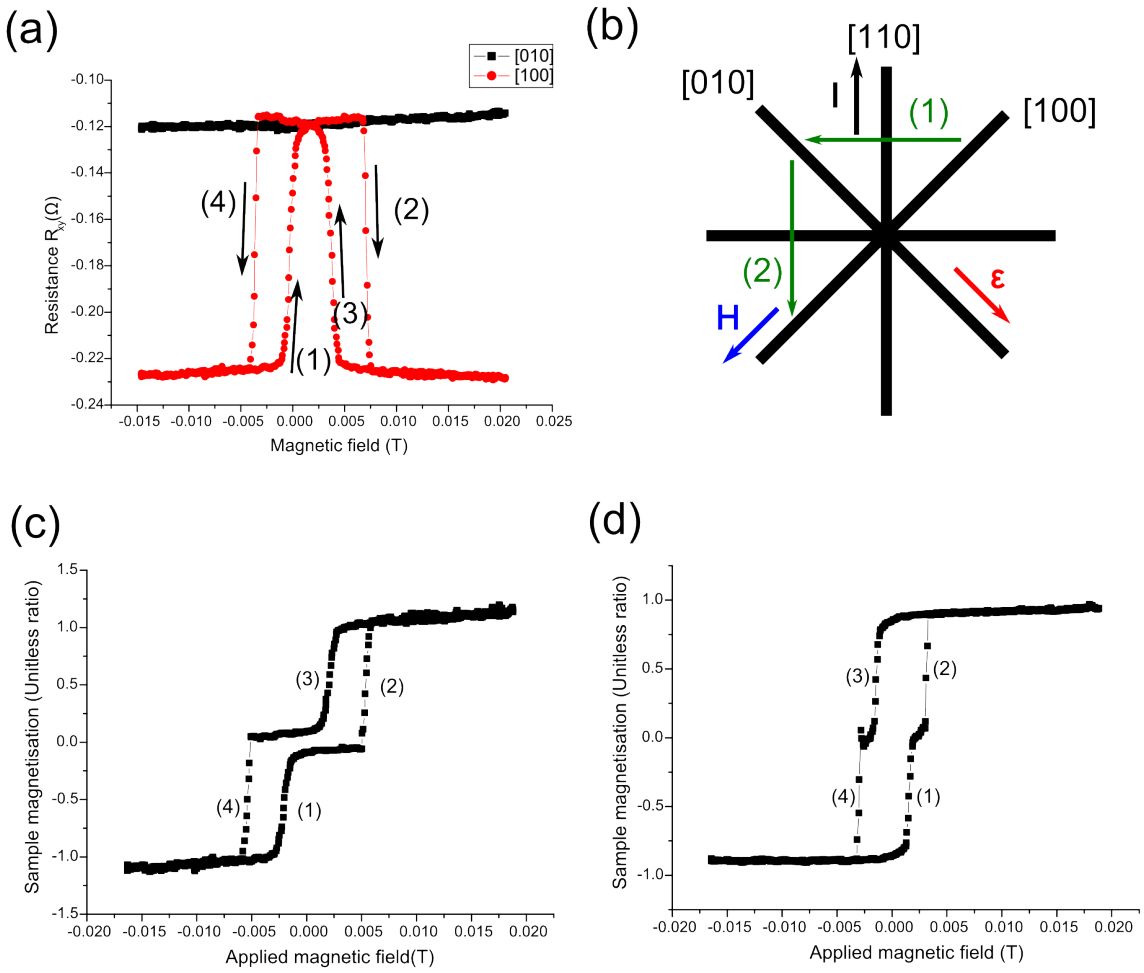

Fig. 4.26 Demonstration of the construction of a hysteresis loop from raw data from S159 with 50V applied to the transducer (corresponding to a strain of 2.3×10^{-4} applied to the Hall bar). a) shows the change in R_{xy} as the field is swept from -0.018T to +0.018T. Also shown in a) are the locations of switching events 1,2,3, and 4. The change in the direction of magnetisation is demonstrated in b) which shows the direction of the magnetisation after switching events 1 and 2, switching events 3 and 4 reverse this. Also shown in b) are the directions of the applied field, H, demonstrated by the blue arrow, the direction of the applied current, I, represented by the black arrow and the applied strain, ε, demonstrated by the red arrow. c) shows the hysteresis loop constructed from a). d) shows a hysteresis loop constructed from R_{xy} data from the same sample as a) but with a voltage of -30V applied to the transducer (corresponding to a strain of -1.4×10^{-4}). In c) the field was applied in the [100] direction and in d) the field was applied in the [010] direction.

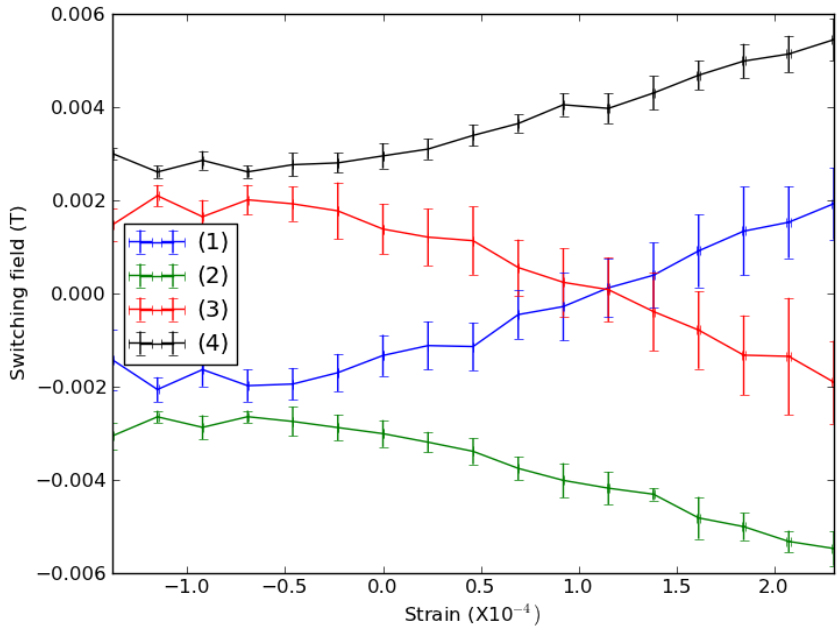

Fig. 4.27 Switching events vs strain for S159. The switching event labelling corresponds with the labels used in figure 4.26a) with event 1 being shown in blue, event 2 shown in green, 3 in red and 4 in black.

This measure of the switching events shows what we would have expected by visual inspection of the field sweep data shown in figure 4.25, that is to say that events 1 and 4 move to more positive fields as 2 and 3 move to more negative fields as the strain becomes more positive. The switching event pairs, the first switching event in the up and down sweep and the second switching event in the up and down sweep, move with roughly the same difference in field whilst the field at which the first and second switching events occur diverges. The domain wall pinning energy increases the switching fields increase due to the jump to the global minima occurring due to a lower applied magnetic field.

In order to determine the value of the strain anisotropy constant, K_s, and domain wall energy for the sample a modified version of the fitting program described in section 3.7 was used. Here the K_c and K_u values found in section 4.2 were used to fit a hysteresis loop to the switching events by varying the K_s and domain wall depinning energy as the free parameters. This was done using a cost function which was defined as the mean difference in field between the switching events in the simulated loops and the switching events in the collected R_{xy} data.

Then, by fitting to these switching events, we find the relation between strain and K_s shown in figure 4.29a) and the relation between the strain and the domain wall pinning energy is shown in figure 4.29b).

The fitting procedure used K_s and the domain wall energy as the fitting parameters with K_u and K_c being set by the values found in section 4.2. A cost function for the fit was found as the mean difference in field between the switching events in the simulated loops and the switching events in the collected R_{xy} data and the best fit was established as the fit with the lowest cost function.

An example of a fit for the 10nm $Fe_{1-x}Ga_x$ film, S159, with a strain of 2.31×10^{-4} present is shown in figure 4.28.

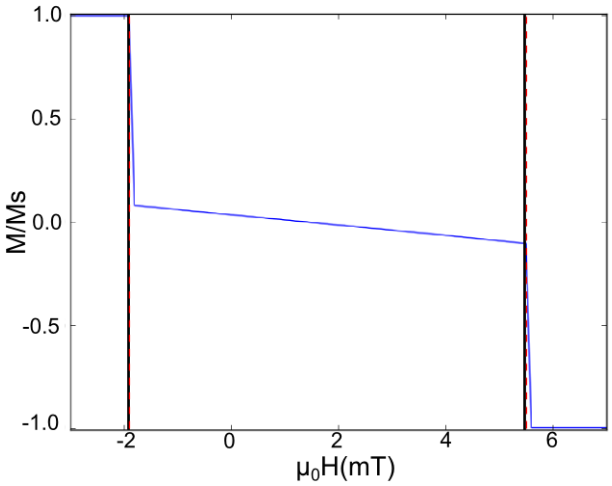

Fig. 4.28 Fitting of a simulated loop to the switching events collected from the 10nm $Fe_{1-x}Ga_x$ film with a strain of 2.3×10^{-4} applied. The switching events extracted from the experimental data are represented as black lines and the simulated loop is represented by the blue lines. The switching events extracted from the simulated data is represented by dotted red lines.

By performing this process on the switching events shown in figure 4.27 we find the relation between K_s and strain shown in figure 4.29a) and the relation between the domain wall energy and strain shown in figure 4.29b). The errors in the domain wall pinning energy are exceptionally large due to the effects of the domain wall pinning energy being much weaker than that of the strain induced anisotropy. This means that a large change in the domain wall pinning energy only produces a slight change in the switching field. The cost functions for the fits used to find these relations can be seen in 4.29c) with the fits themselves

being found in appendix C. The error bars were found by applying the same fitting procedure to the start of the switching event which was found using the method described in 3.10.1

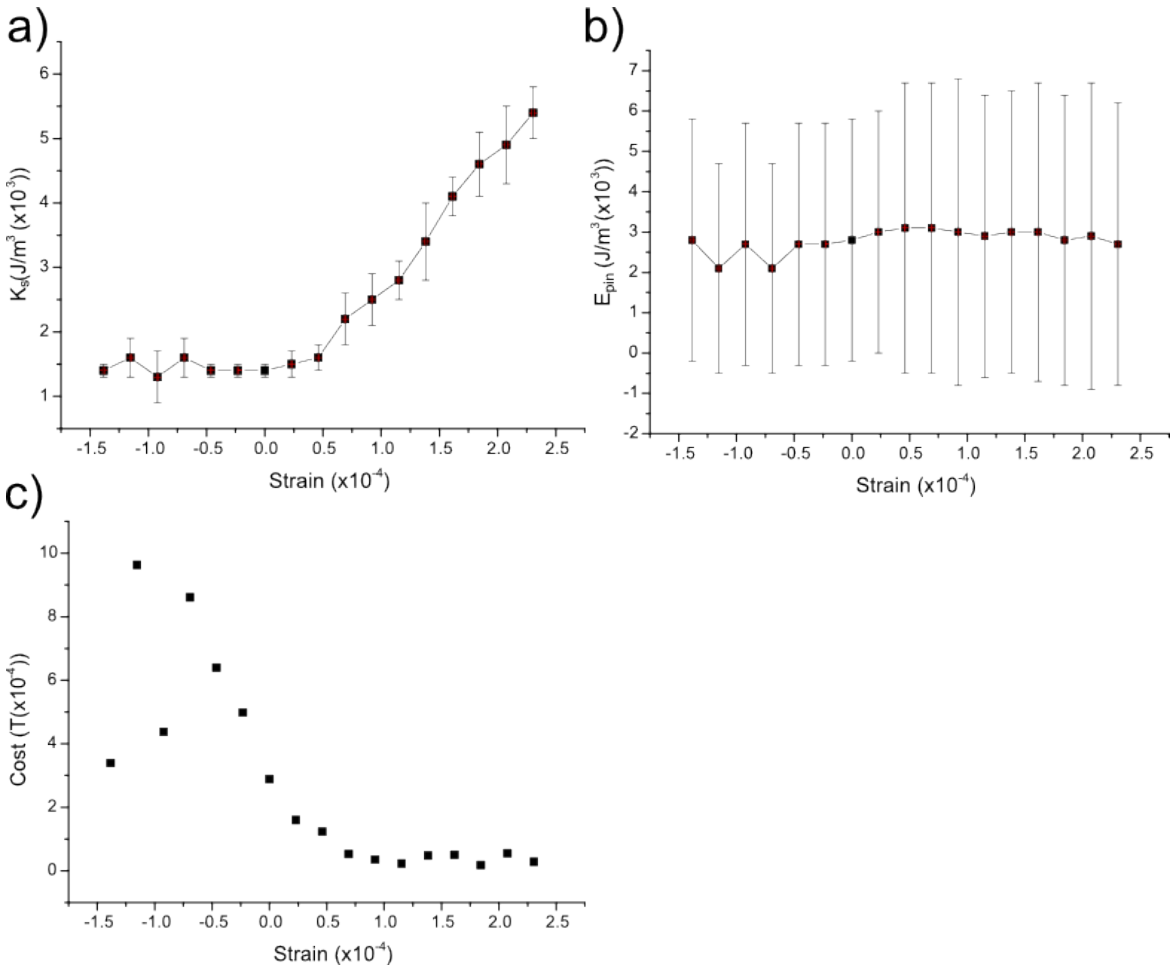

Fig. 4.29 Fitting results for the switching events for S159. a) shows the resulting K_s values, b) shows the domain wall energy values and c) shows the cost function for each fit. The red errors bars in a) and b) show the error in the strain for each fit, please note that these error bars are smaller than the markers for most data points.

The cost functions shown in figure 4.29c) demonstrates that the cost function is high when the strain is below 5×10^{-5} indicating that the model used to simulate the data breaks down at lower strain. This is most likely due to the hard axis transitioning from the [100] direction to the [010] direction meaning that instead of two clearly defined switching events as can be seen in figure 4.26b) we begin to see the two switching events being sufficiently close that it becomes difficult to differentiate where one switching event begins and one ends as demonstrated in 4.26d). This means that when we numerically model the hysteresis loop the two switches collapse into one switching event and the best result which can be

found is, by necessity the lowest set of values of K_s and domain wall energy for which two switching events can be successfully modelled. The domain wall depinning energy is roughly equivalent to that found in MBE grown $Fe_{1-x}Ga_x$ thin films. Parkes et. al found a value of $\sim 2\times 10^3 \mathrm{Jm}^{-3}$ in reference [61] which is within error the values of $\sim 3\times 10^3 \mathrm{Jm}^{-3}$ given in figure 4.29. The lack of a meaningful change in the domain wall pinning energy despite the increase in applied strain is due to the fact that the domain wall pining energy primarily results from the magnetic interaction energy and shape anisotropy of the material and has a weak dependence on the magnetic anisotropy of the material [133, 134].

The magnetoelastic constant was then found from the K_s data using a linear fit of the K_s values as a function of the strain. The numerical model used to determine K_s and the domain wall pining energy from the switching events tends to breakdown when the value of K_s is sufficiently low, resulting in the plateau seen in figure 4.29a). In order to determine which modelling results could be considered valid for a particular fit the cost function for that fit was used. If the cost function was lower than 1mT for that particular fit, indicating that the difference between the simulation and the collected data was less than the step size of the simulation the fit was not used as a data point for the calculation of the magnetoelastic constant. This left the points shown in figure 4.30 to which a linear fit was performed.

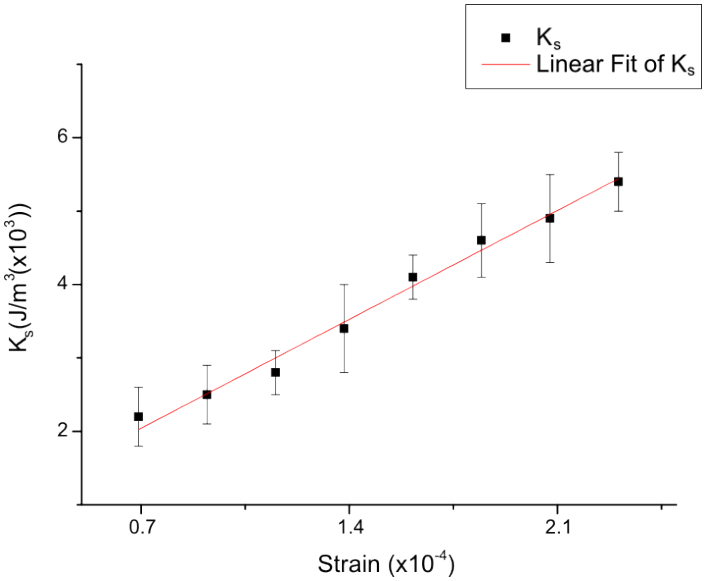

Fig. 4.30 Linear fit expressing the relation between the strain anisotropy value, K_s and the strain applied to the 10nm $Fe_{1-x}Ga_x$ sample, S159. The result of this fit was a ratio of strain anisotropy to strain of $(2.1 \pm 0.1) \times 10^4$ kJm^{-3}

The ratio of induced anisotropy to the strain found from this fit is $(2.11 \pm 0.11) \times 10^4 kJm^{-3}$ which may be interpreted as the magnetoelastic constant, B_1, in accordance with equation 4.6 which was described in full in section 2.5.

$$K_s = B_1(\varepsilon_{xx} - \varepsilon_{xx}) \tag{4.6}$$

This value for the magnetoelastic constant is similar to that found by Parkes et al. [61] of $(2.1 \pm 0.2) \times 10^4$ Jm^{-3} for a $Fe_{1-x}Ga_x$ film grown by MBE on a GaAs substrate.

The next sample to be tested was the 20nm $Fe_{1-x}Ga_x$ film, S219. The strain to voltage ratio on this sample was found using the strain gauge as was done for the 10nm sample. A strain sweep was performed as was done for S159 yielding the strain relation of $(2.9 \pm 0.0) \times 10^{-6} V^{-1}$. This value was then used to determine the strain on samples as a voltage was applied to the transducer in order to collect data on the effect of the strain on the R_{xy} measurement when sweeping a field across the [100] and [010] directions. This data was then symmetrised as was done to the field sweeps collected on S159 resulting on the field sweeps shown in figure 4.31.

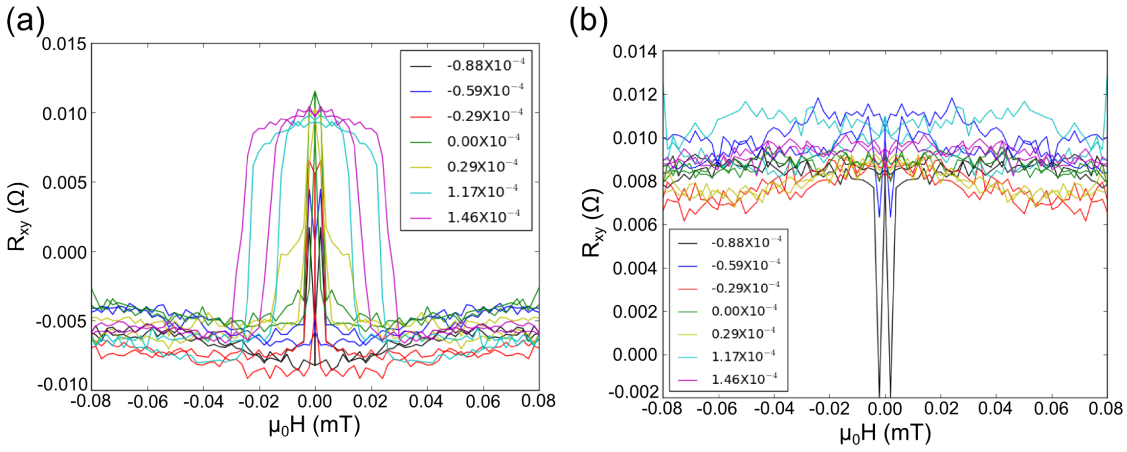

Fig. 4.31 Field sweep loops for secondary 20nm sample with different levels of stress applied via the transducer. a) shows the field sweeps in the [010] direction and b) shows the field sweeps with the field in the [100] direction.

These field sweeps show the switching events occurring at more than twice the field at which the switching events for the 10nm sample occurred. The switching events are plotted as a function of strain in figure 4.32.

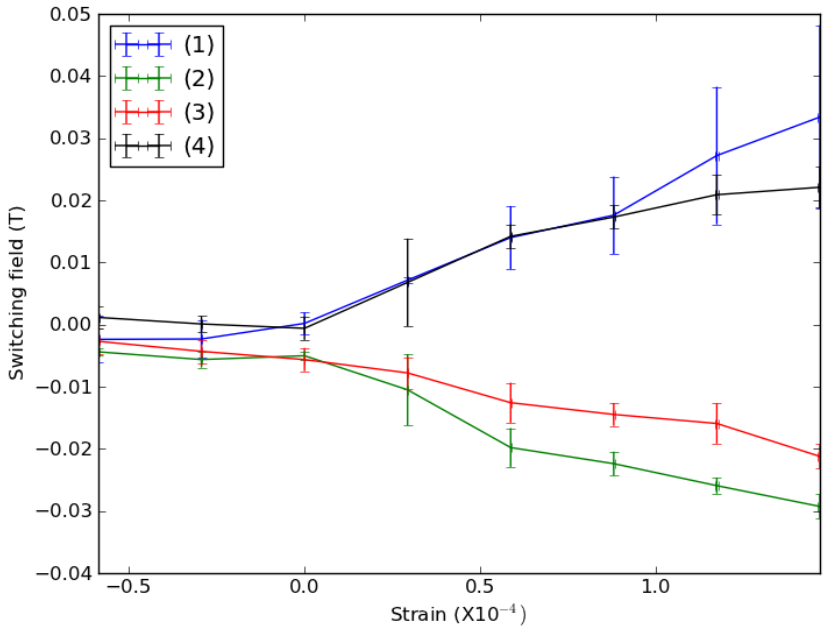

Fig. 4.32 Switching events vs strain for the 20nm $Fe_{1-x}Ga_x$ sample, S219. The switching event labelling corresponds with the labels used in figure 4.26a) with event 1 being shown in blue, event 2 shown in green, 3 in red and 4 in black.

Looking at the switching fields for S219 we can see that the effect of strain becomes significant only when the strain is positive. These switching events were analysed by fitting to simulated loops as was done with the switching events for S159 yielding the relationship between the K_s and the strain shown in figure 4.33.

The change in the domain wall pinning energy observed in figure 4.33b) is unusual since it would be expected that the domain wall energy would remain approximately constant regardless of the strain applied to the device. This may indicate a rotational asymmetry in the grain structure of the device, or else an issue with the calibration of the applied magnetic field. These results were then used to find the constant of proportionality between the value of K_s and the strain by fitting a line to all the data points for which the cost function was less than 1. This fit is shown in figure 4.34.

Figure 4.34 shows the linear fit to S219 giving an unusually high magnetoelastic constant of $(22.8 \pm 0.6) \times 10^4 Jm^{-3}$. It also shows an increase in the domain wall nucleation energy as a function of strain. This indicates that as the strain increases the energy required to move a domain wall increases. The domain wall pinning energy starts out at zero but increases to $\sim 7 \times 10^3 \mathrm{Jm}^{-3}$, more than double the domain wall pinning energy in S159, the 10nm sample.

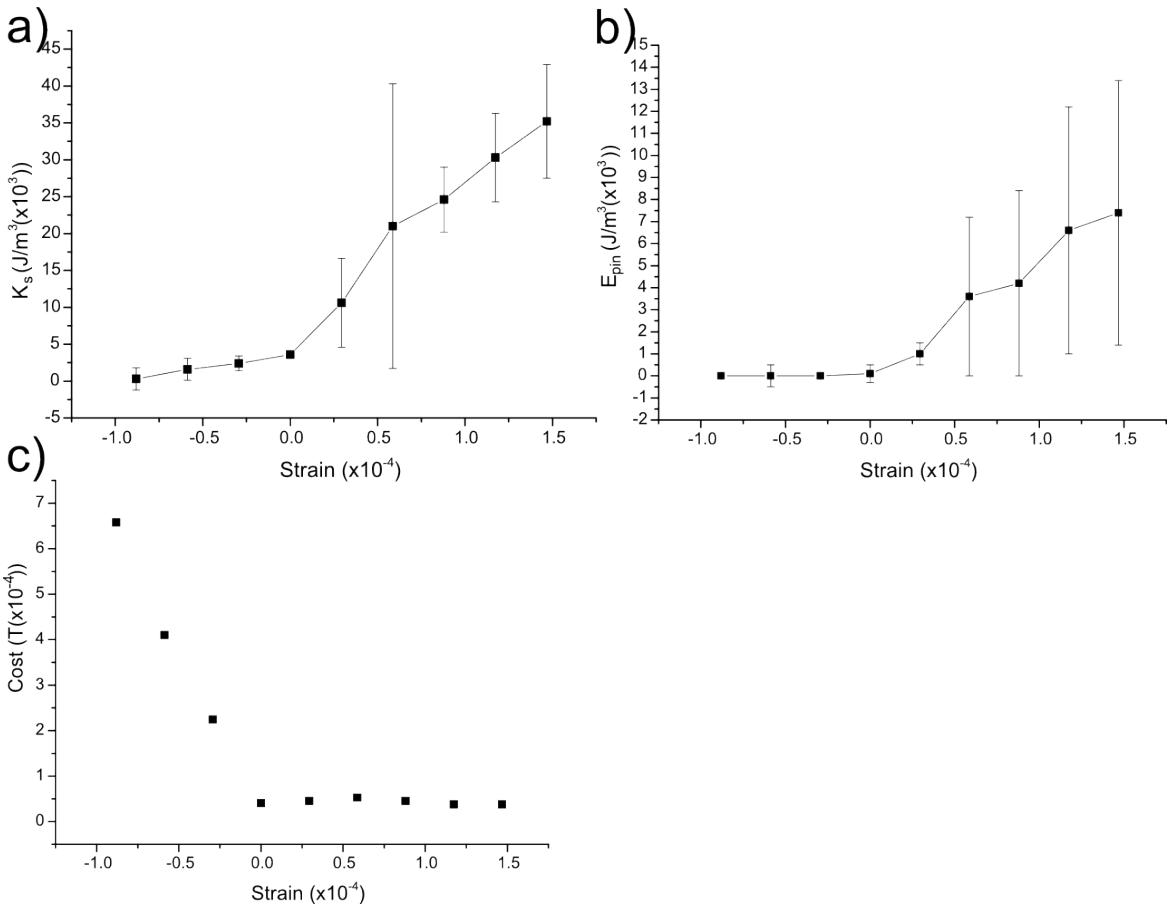

Fig. 4.33 Fitting results for the switching events for the 20nm sample, S219. a) shows the resulting K_s values, b) shows the domain wall energy values and c) shows the cost function for each fit. The red errors bars, which are often smaller than the markers, in a) and b) show the error in the strain value for each fit.

This unusually high magnetoelastic constant combined with the unusuall behaviour of the domain wall pinning energy may indicate one of two things. The first is that the calibration of the electro magnetic used to produce the applied magnetic field was inaccurate due to some problem with the gauss meter used. The second possibility is that there was some rotational asymmetry in the grain boundaries in the $Fe_{1-x}Ga_x$ film. This would explain both the unusually high response to an externally applied strain and the increase in the domain wall pinning energy with strain as the strain may alter the separation between the grains thereby altering the magnetic interaction between grains across the lattice.

The analysis of these two results shows an increase in strain response of an order of magnitude for sample S219, as compared to S159. This might suggest that the effect of strain is greatly amplified by the thickness of the film. In order to test this further the second batch

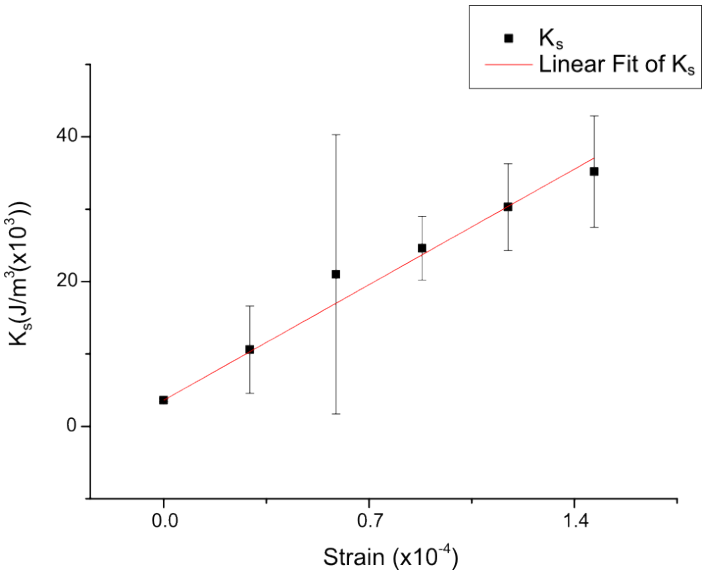

Fig. 4.34 Linear fit expressing the relation between the strain anisotropy value, K_s and the strain applied to the 20nm sample, S219. The result of this fit was a ratio of strain anisotropy to strain of $(22.8 \pm 0.6) \times 10^4$ kJm^{-3}.

of samples were subjected to the same tests as S159 and S219. Magnetoelastic constants for samples S221 and S227 were not extracted due to a lack of material. The transport data for the second batch was collected using the mini vector magnet, described in section 3.10.2. Measurements of longitudinal and transverse resistance as a function of the angle of a saturating magnetic field applied in the plane of the film for S411 and S410, thicknesses 20 and 30nm, are shown in figure 4.35.

The strain applied to S411 as a function of the voltage applied to the piezo-electric crystal was measured using the large electromagnet to produce a field of 0.4T which was used to saturate the magnetisation within the sample. Once the magnetisation was saturated the strain measurement was performed in exactly the same way as it was performed on S159 and S219 yielding a strain to voltage ratio of $(8.5 \pm 0.0) \times 10^{-6} V^{-1}$. This is an unusually high strain to voltage ratio however it is still within the expected range and the error is still very low so we shall assume the result to be broadly accurate. The next step of the K_s measurement was the R_{xy} measurement for which the field was applied along the [100] and [010] directions as was done for the primary samples and as with the primary samples the results were symmetrised in order to produce the field sweeps shown in figure 4.36.

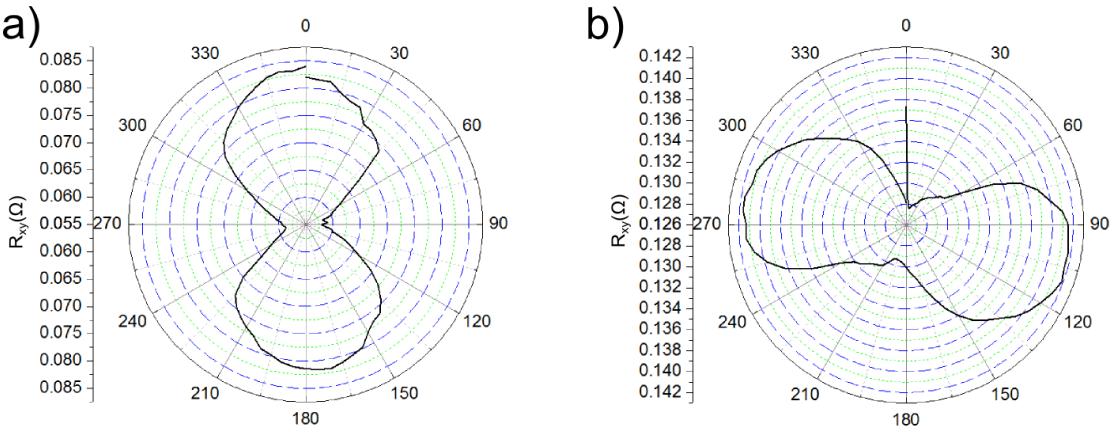

Fig. 4.35 AMR curves for secondary $Fe_{1-x}Ga_x$ samples. a) shows the dependency of R_{xy} of S411 (20nm) on the angle of applied field, b) shows the dependency of R_{xy} on the angle of applied field for S410 (30nm). A magnetic field of 0.05T was used to magnetically saturate the samples.

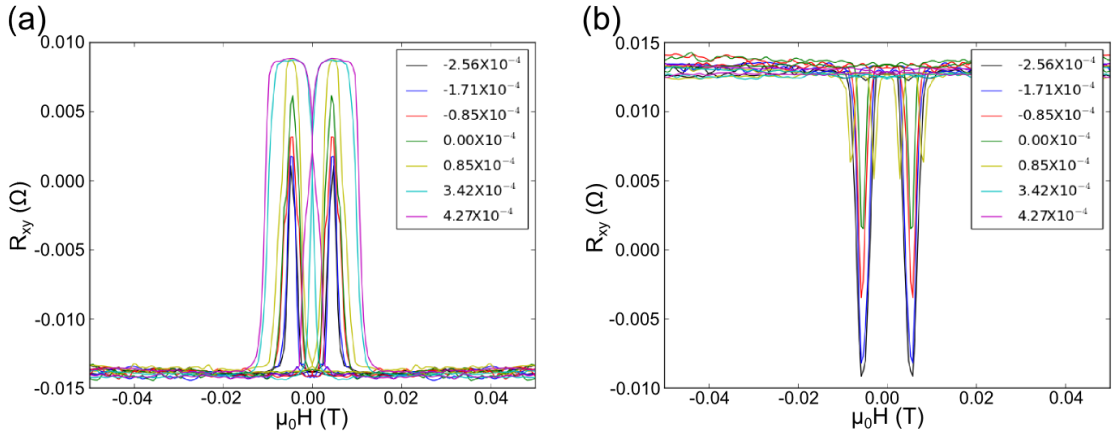

Fig. 4.36 Field sweep loops for S219 sample with different levels of stress applied via the transducer.a) shows the result when the field is applied along the [100] direction and b) shows field sweeps produced with the field aligned along the [010] direction.

The general pattern remains the same as in the primary 10nm sample as demonstrated by the switching fields which were extracted and shown in figure 4.37.

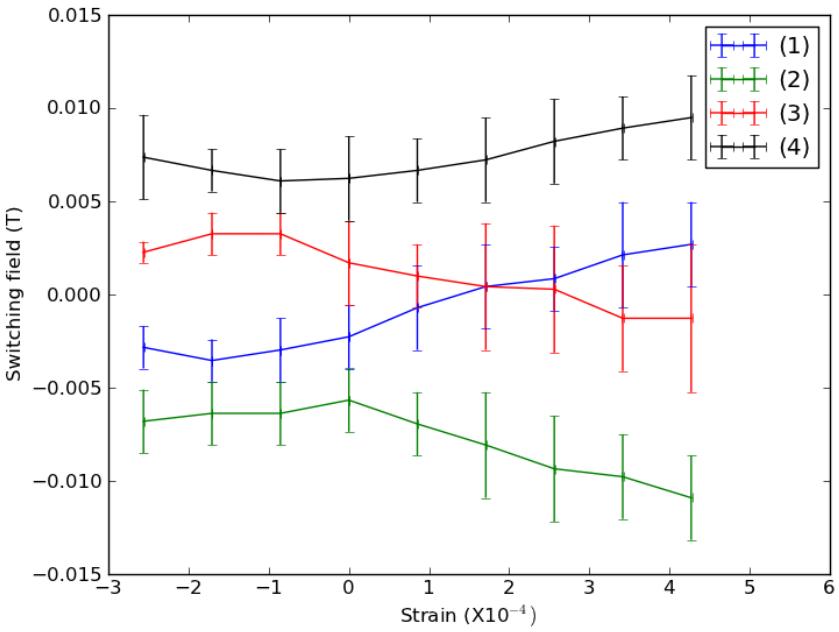

Fig. 4.37 Switching events vs strain for S411. The switching event labelling corresponds with the labels used in figure 4.26a) with event 1 being shown in blue, event 2 shown in green, 3 in red and 4 in black.

These switching events indicate that the effects of strain become significant when the strain is positive which is similar to the effect of strain seen in the primary samples. By fitting to these switching events we produce the results shown in figure 4.38.

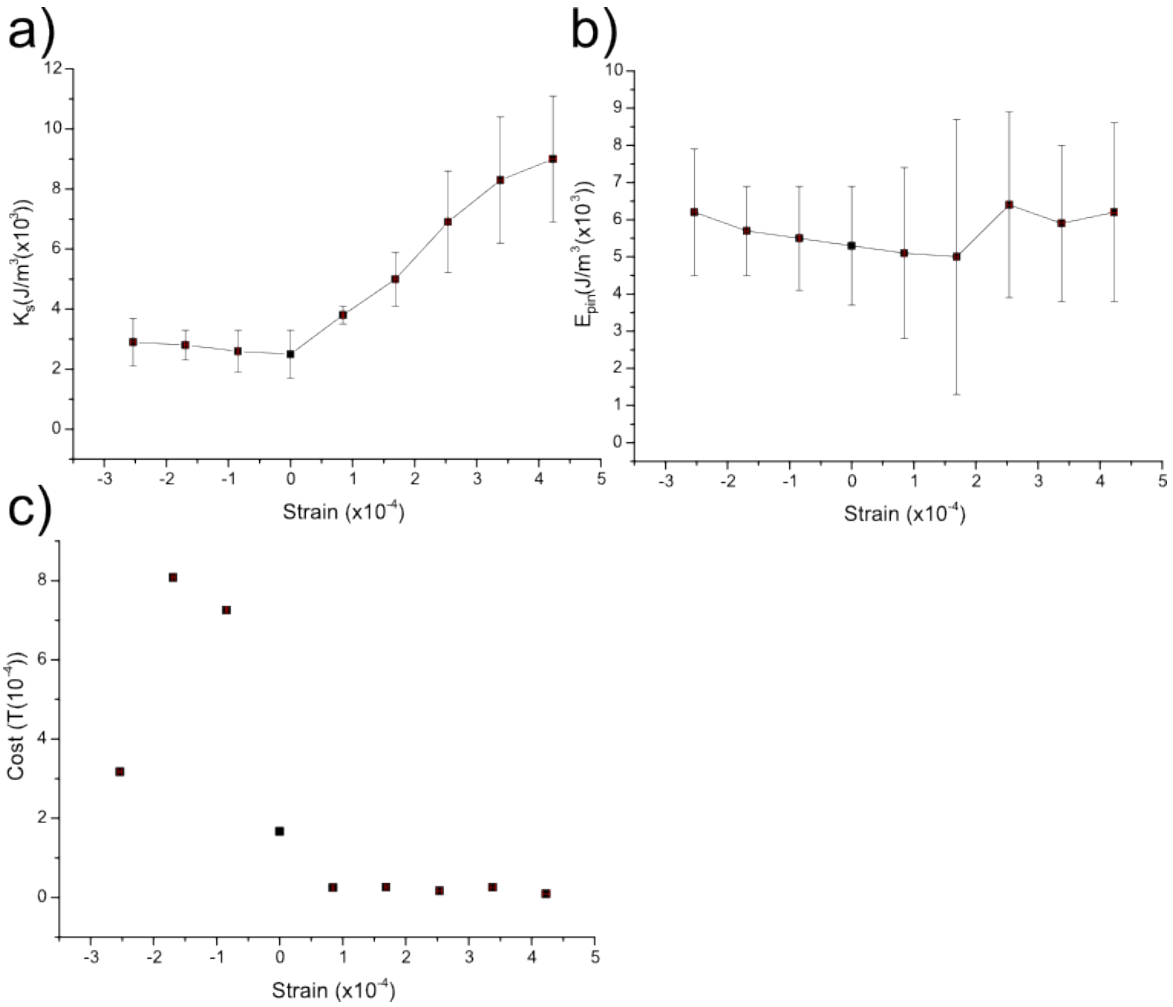

Fig. 4.38 Fitting results for the switching events for S411. a) shows the resulting K_s values, b) shows the domain wall energy values and c) shows the cost function for each fit. The red errors bars in a) and b) show the error in the strain value for each fit.

As with the primary samples the fits with a cost greater than one were discounted leaving a linear relationship between the applied strain and the strain anisotropy. Also consistent is that the domain wall depinning energy remains roughly constant at all levels of strain with a magnitude of $\sim 6 \times 10^3$ Jm^{-3}. This value is large compared to S159 however it is within the bounds of error for the magnitude of the pinning energy found in sample S159. Once again the fitting results for which the cost function was less than one were plotted and linearly fit to in order to find the magnetoelastic constant for the sample as was done in figure 4.39 which yielded a magnetoelastic constant of $(1.6 \pm 0.1) \times 10^4 kJm^{-3}$.

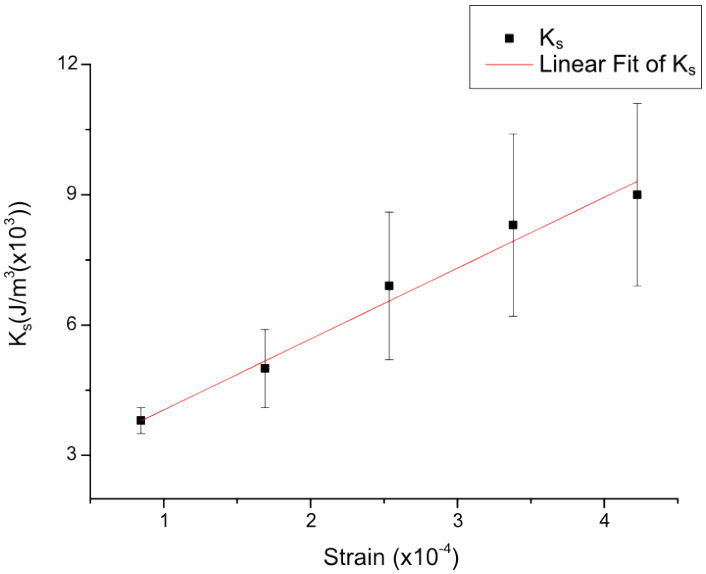

Fig. 4.39 Linear fit expressing the relation between the strain anisotropy value, K_s and the strain applied to the sample for S411. The result of this fit was a magnetoelastic constant of $(1.6 \pm 0.1) \times 10^4 kJm^{-3}$.

The final set of transport data to be collected was that for S410, the 30nm sample from the second batch. However when it came time to find the voltage/strain relation for this sample it was found that the strain produced by the transducer had dropped significantly. This was probably due to a current spike damaging the PZT since the capacitance of the device dropped from $20\mu F$ during the measurements of R_{xy} to $0.7\mu F$ during the measurement of the strain. A strain sweep was performed as before however the results demonstrated a low level of strain as shown in figure 4.40.

For this reason the voltage to strain conversion factor used for S410 was the mean of previously collected values with an error decided by the standard deviation of the previously collected values. This resulted in a strain conversion factor of $(5.1 \pm 2.0) \times 10^{-6}$.

The measurement of the voltage to strain ratio was done after the main experiment however during which the field was swept up and down in order to collect the R_{xy} loops which were then symmetrised in order to produce the loops shown in figure 4.41

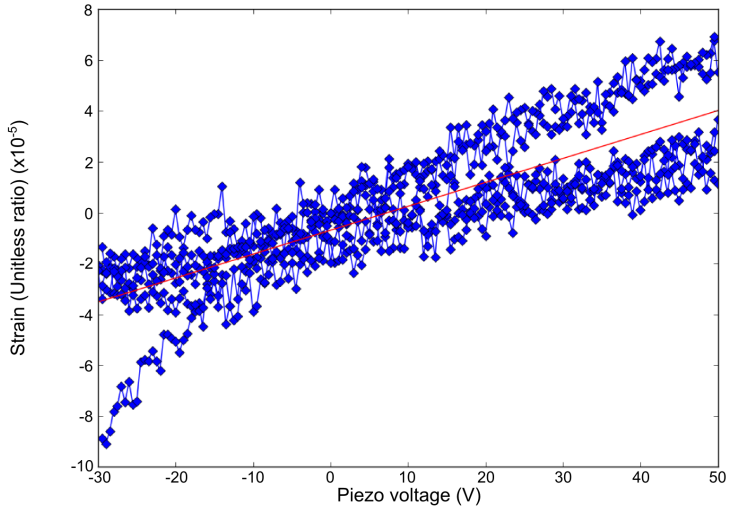

Fig. 4.40 Strain loop for S410. The voltage applied to the piezoelectric crystal was swept from -30V to +50V and back again twice. The strain was then found from the value of R_{xx} as described in equation 3.13 to produce the relation between voltage on the piezoelectic and strain indicated by the blue line. This data was then averaged and the result fitted to with a linear polynomial indicated by the red line. This fit gave a strain to voltage ratio of $(9.4 \pm 0.1) \times 10^{-7} V^{-1}$.

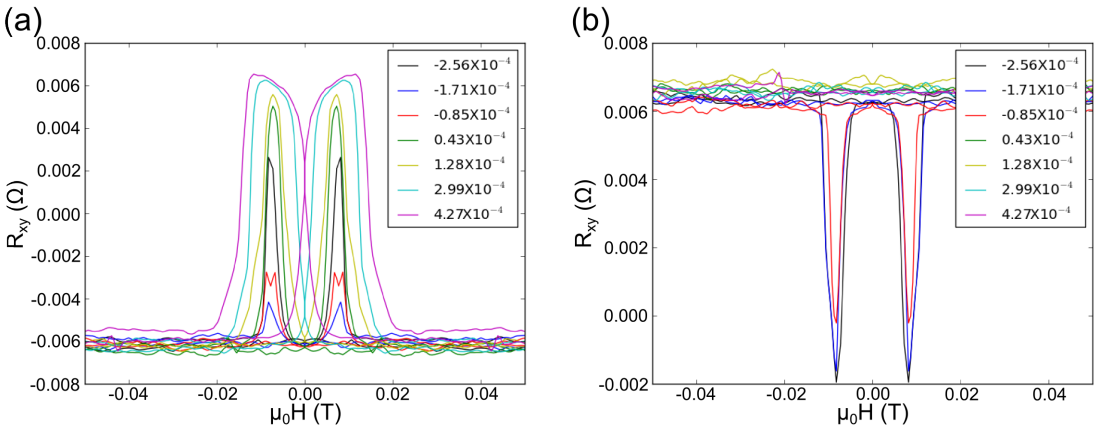

Fig. 4.41 Field sweep loops for S410 with different levels of stress applied via the transducer. a) shows the result when the field is applied along the [100] direction and b) shows field sweeps produced with the field aligned along the [010] direction.

Here we can see the same general pattern as before and that the switching occurs at fields around 5mT. The switching fields for S410 are plotted in figure 4.42.

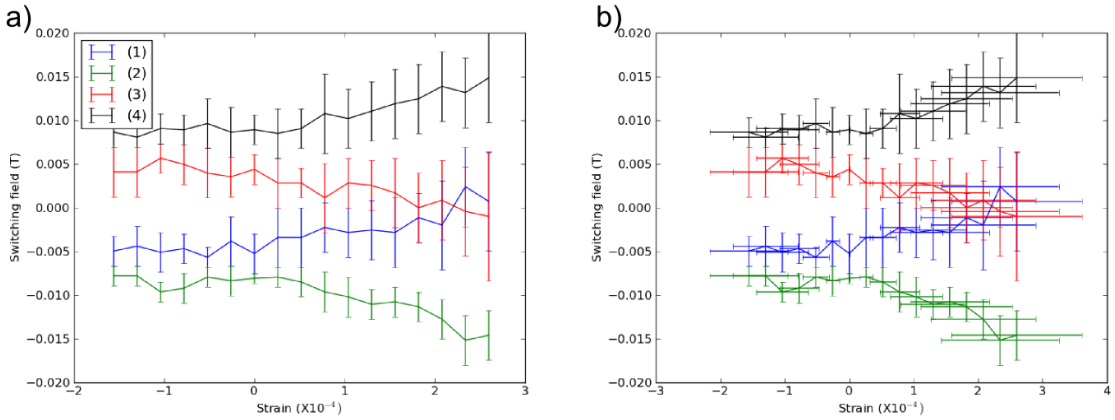

Fig. 4.42 Switching events vs strain for S410. The switching event labelling corresponds to the labels used in figure 4.26a) with event 1 being shown in blue, event 2 shown in green, 3 in red and 4 in black. The plot in a) shows the data without the error on the strain measurement and the plot in b) shows the result with the error in the strain measurement.

Once again we see that the strain only really begins to have an effect when positive. The value of the strain anisotropy was then extracted by fitting to the data, the results of this fitting are shown in figure 4.43.

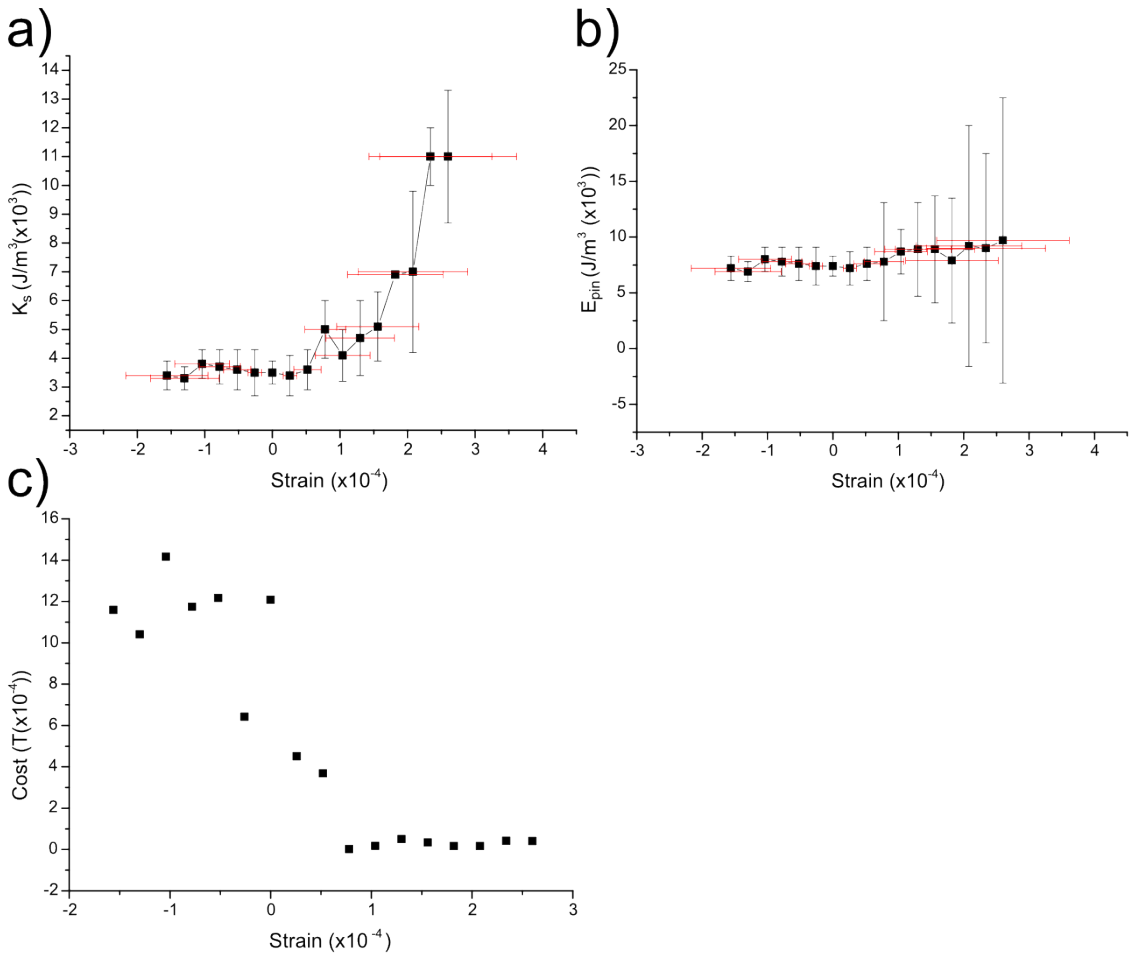

Fig. 4.43 Fitting results for the switching events for S410. a) shows the resulting K_s values, b) shows the domain wall energy values and c) shows the cost function for each fit. The red errors bars in a) and b) show the error in the strain value for each fit.

Once more we see a fairly constant domain wall pinning energy, here with a value similar to that found in sample S411 of $\sim 6\times 10^3 \mathrm{Jm}^{-3}$. The strain anisotropy increases once the level of strain is greater than zero again in a similar manner to S411. By fitting to the K_s values for which the cost is less than 1×10^{-4} we can find the constant of proportionality for S410 using the fitting shown in figure 4.44, yielding a magnetoelastic constant of $(3.9\pm 0.8)\times 10^4 Jm^{-3}$.

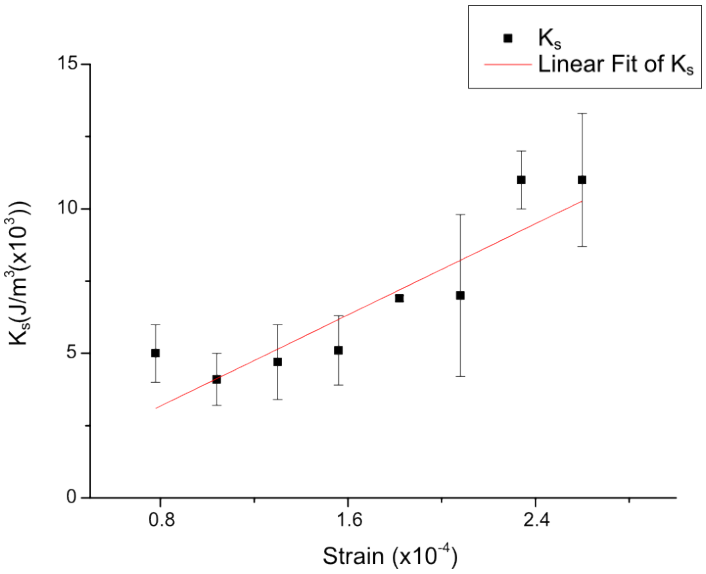

Fig. 4.44 Linear fit expressing the relation between the strain anisotropy value, K_s and the strain applied to the sample for S410. The result of this fit was a magnetoelastic constant of $(3.9 \pm 0.8) \times 10^4 kJm^{-3}$.

This data was then used to extract the magnetoelastic constants for the second batch of samples. The results of which are shown alongside the magnetoelastic constants for the primary films in figure 4.45.

We can see here that sputter grown material exhibits a similar response to strain as the bulk or MBE grown material. The sample S219 produced an unusually strong response to strain however the cause of this may either be a miscalibration of the applied magnetic field or a structural asymmetry within the $Fe_{1-x}Ga_x$ film. If either of these explanations are correct then reproducing the high magnetoelastic constant observed may prove almost impossible however, therefore no meaningful conclusions may be made from this result. A trend of an increase in magnetoelastic constant with thickness was observed in the two sets of samples however this trend is not observed continuously across the two sets of samples and if the results found from S219 are to be discounted this trend is only observed in the secondary samples S411 and S410. The magnetoelastic constants observed in samples S159, S411 and S410 are comparable to those observed in bulk material and those observed previously in $Fe_{1-x}Ga_x$ films grown on Si with thicknesses greater than 100nm [54].The $Fe_{1-x}Ga_x$ films grown on GaAs were capable of exhibiting high magnetostriction at much lower thickness films than those grown on Si however indicating advantages in growing $Fe_{1-x}Ga_x$ films on GaAs over Si.

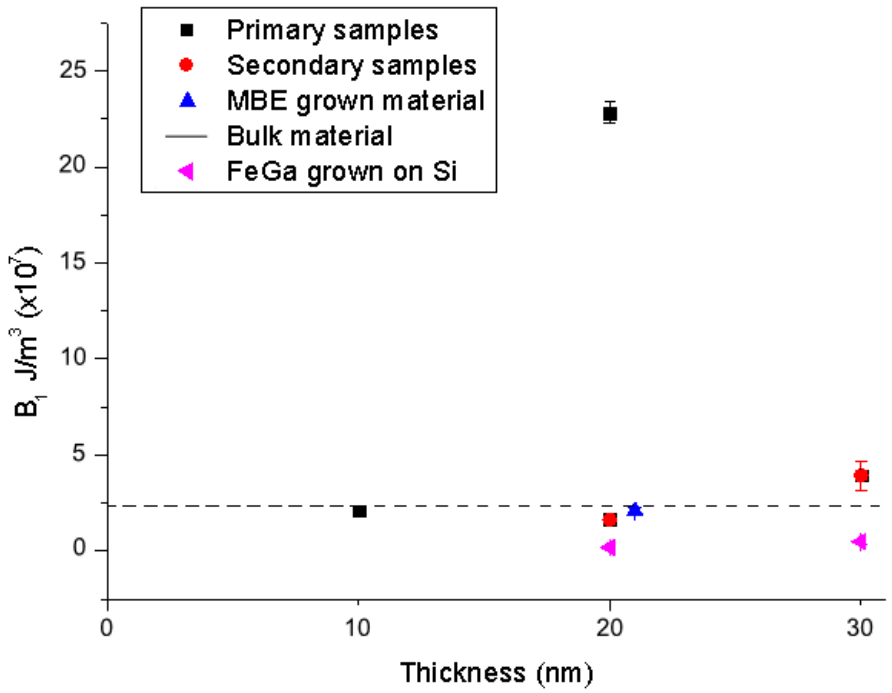

Fig. 4.45 Demonstration of the relation between the thickness of a sample and the resulting magnetoelastic constants. The magnetoelastic constants for the primary samples are represented by the black squares and the magnetoelastic constants for the secondary samples are represented by the red circles. The magnetoelastic constant for the MBE grown sample was taken from reference [61], the magnetoelastic constant for bulk $Fe_{0.81}Ga_{0.19}$ was taken from reference [42] and the values for $Fe_{1-x}Ga_x$ grown on Si were taken from reference [54].

The relationship between sample thickness and the strength of the magnetostrictive effect demonstrated in reference [54] also indicates a contribution to the magnetostriction in a thin film due to the interface between the film and the substrate. This effect appears to be present in the films measured here however the number of measured films from each batch is not sufficient to provide strong evidence for this conclusion.

4.6 Conclusions of the study of $Fe_{1-x}Ga_x$ thin films

This chapter examined the properties of $Fe_{1-x}Ga_x$ films grown on GaAs substrates by sputter deposition. Measurements using SQUID magnetometry were performed which revealed that the cubic and uniaxial anisotropy constants of these films demonstrated the opposite relation to thickness seen in iron in previous studies. These measurements were repeated with a second batch of $Fe_{1-x}Ga_x$ thin films with thicknesses of 20nm and 30nm and the trend

in the cubic anisotropy values was repeated. The results of fitting to the second batch of $Fe_{1-x}Ga_x$ samples also exhibited unusual values for the uniaxial anisotropy. This was most likely due to the model used breaking down when applied to samples which exhibited zero uniaxial anisotropy. This is the most likely explanation as the hysteresis loops collected by sweeping the magnetic field in the [110] and [1$\bar{1}$0] directions were almost identical indicating zero, or very low uniaxial anisotropy due to poor epitaxial matching between the $Fe_{1-x}Ga_x$ film and the GaAs substrate. Tests were done on pure iron films using the same methods used on the $Fe_{1-x}Ga_x$ films. This resulted in the same relation between anisotropy and thickness observed in previously published experiments, lending credence to the methods and mathematical models used to study galfenol films.

The magnetoelastic response of these samples was demonstrated to be roughly equivalent to similar films formed by MBE and bulk material. The magneostriction was observed to increase as a function of the film thickness however this effect was not observed continuously over two sets of samples. The magnetoelastic constant found for S219 was much larger than that found for the other samples however this is likely to be an experimental artefact caused either by a bad calibration of the applied field or an unusual growth artefact which may prove difficult to reproduce. This indicates that sputter grown $Fe_{1-x}Ga_x$ films on GaAs substrates may be used to produce the high magnetoelastic constants observed in bulk $Fe_{1-x}Ga_x$ materials at much lower thicknesses than equivalent films grown on Si substrates.

Lattice constants for S219,S221 and S227 were determined however no clear relation between thickness or anisotropy and the lattice parameters could be established. Triple axis diffractometery experiments revealed that the 20nm sample, S219, had a smaller in-plane grain size than S221 and S227 which may lead to a greater number of grain boundaries inducing its unusually large response to strain but a great deal of further study into the mosaic structure of the films is required to confirm or deny this hypothesis. These experiments also demonstrated a low average misalignment between the grains which may explain the high magnetostriction despite the low grain size. These experiments also demonstrated a similar level of strain due to a lattice mismatch between the substrate and the film as that seen in MBE grown films. Further x-ray diffractometer experiments could be used to study the grain size of mosaic blocks in the secondary samples S410 and S411 in order to find whether the grain size in the S219 sample was the cause of the high response to strain. Further X-ray diffraction experiments could be performed in order to determine the thickness and density of defects within the lattice which could also give insights into the causes of the high magnetostriction and cubic anisotropy in the 20nm $Fe_{1-x}Ga_x$ samples.

Chapter 5

Static and time-resolved PEEM measurements of ferromagnetic microstructures

This chapter describes the results of time resolved XMCD-PEEM measurements of micron sized square ferromagnetic structures. The structures were stimulated using magnetic field pulses produced by a pulsed current passing through a coplanar waveguide (CPW) underneath the structures. The magnetisation dynamics of the system were recorded as a function of time using the method outlined in section 3.13. Initial studies were focused on $Fe_{1-x}Ga_x$ structures grown by sputter deposition, however measurements were also performed on nickel structures. The measurements of the nickel structures were focused on the effect on domain structure resulting from a strain-induced anisotropy. We were unable to perform time resolved measurements on strained devices for reasons which are explored in this chapter.

5.1 Time resolved measurements of $Fe_{1-x}Ga_x$ squares

Circular and square planar $Fe_{1-x}Ga_x$ polycrystalline structures were grown by sputter deposition on gold/tantalum CPWs to study the confined spin wave modes in magnetostictive materials. Full details of the structure of the devices can be found in section 3.13. Imaging XAS scans were performed to clearly find the location of the Fe L_3 peak and evidence of XMCD. These scans were also used to check the samples for oxidation. The energies for the L_2 and L_3 edges in iron taken from reference [135] are 706eV and 719eV respectively. In order to detect the L_3 and L_2 edges the X-ray energy was scanned from 700eV to 730eV

in 0.2eV steps. At each energy an image was collected and saved as an energy scan. The images collected are demonstrated in figure 5.1.

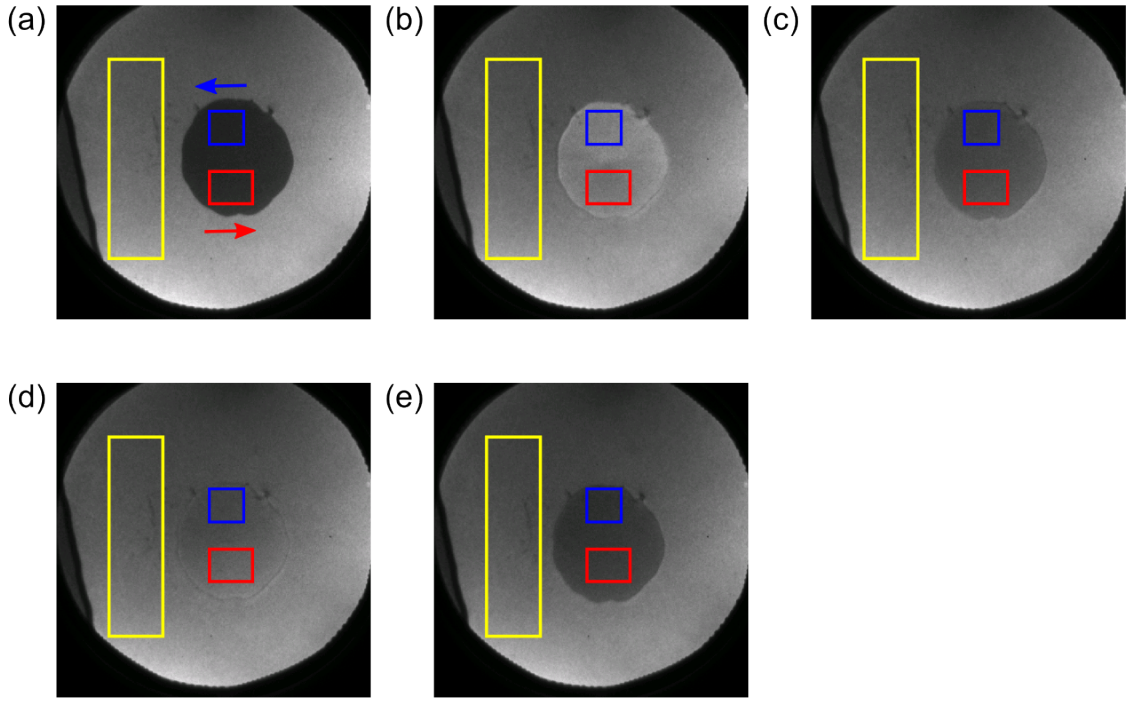

Fig. 5.1 Images taken from an energy scan used to find the Fe L_2 and L_3 edges of the galfenol samples. The red square represents the area with magnetisation in the direction indicated by the red arrow, the blue square represents the area with net magnetisation in the direction of the blue arrow. The yellow square represents the area used to determine the background which was subtracted from the red and blue area region of interest (ROI) scans. The images shown here were taken at energies of a)700eV, b)707.4eV, c)714.4eV, d)720.6eV and d)730eV. The field of view in these images is $20\mu m$.

Figure 5.1 shows a 7μm $Fe_{1-x}Ga_x$ circle on a 20μm CPW. The light gray background of the image shows the gold CPW and the dark grey at the edge of the image is the GaAs substrate. The circular object was chosen for energy scans since it has large areas with inverse magnetisation to one another. Squares were used for measurements of the time resolved dynamics and the effects of a strain induced anisotropy since the domain walls allow for high magnetic contrast in the collected images.

Shown on figure 5.1 are 3 regions of interest, demonstrated by the red, blue and yellow squares. These regions were selected to represent areas with inverted magnetisation (red and blue) and the background variation image intensity (the yellow area).

The mean pixel value of each of these areas was calculated in order to find how the mean intensity varied as a function of energy. Then the background scan was subtracted from both the red and blue regions in order to remove the effects of variation in the image intensity due to incident beam fluctuations. Finally, the energy profiles of the red and blue areas were plotted in figure 5.2 as red and blue lines alongside the result of the difference of the two profiles represented by the green line.

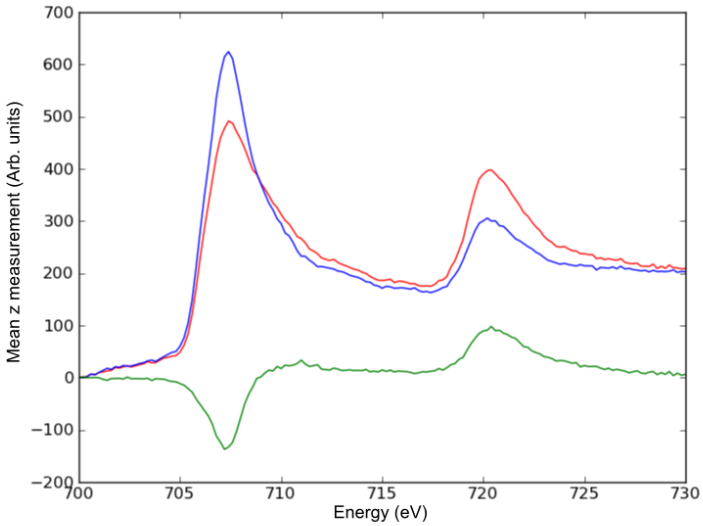

Fig. 5.2 Plots of the mean pixel intensity in the regions of interest indicated in figure 5.1. The red line indicates the red ROI and the blue line indicates the blue ROI, in both cases the background value from the yellow ROI has been subtracted. The green line indicates the difference between the two measurements.

Once the location of the edges had been determined squares were found in which the magnetisation formed a Landau flux closure state, discussed in section 2.8. Overall three squares were studied in which a Landau flux closure state was observed. These squares were found across two separate visits to the Diamond light source where the system was run in hybrid mode and 156 mode as described in section 3.13. The squares studied, their sizes and the operational mode of the synchrotron used to study them are given in table 5.1.

The photodiodes used in the experiments, centronic AEPX65 diodes [136], had rise times in the range of 100-200ps and the magnetic field pulse resulting from the current moving through the waveguide had a magnitude of between 5mT and 8mT. The amplitude of the magnetic pulse would vary depending on the impedance of the waveguide being used This leads to a theoretical magnetic pulse profile of the devises shown in figure 5.3.

Sample name	Sample width (μm)	Synchrotron filling pattern
A5	10	Hybrid
D6	3	156 bunch
D7	3.5	156 bunch

Table 5.1 Details of $Fe_{1-x}Ga_x$ square objects studied using time resolved XMCD PEEM experiments.

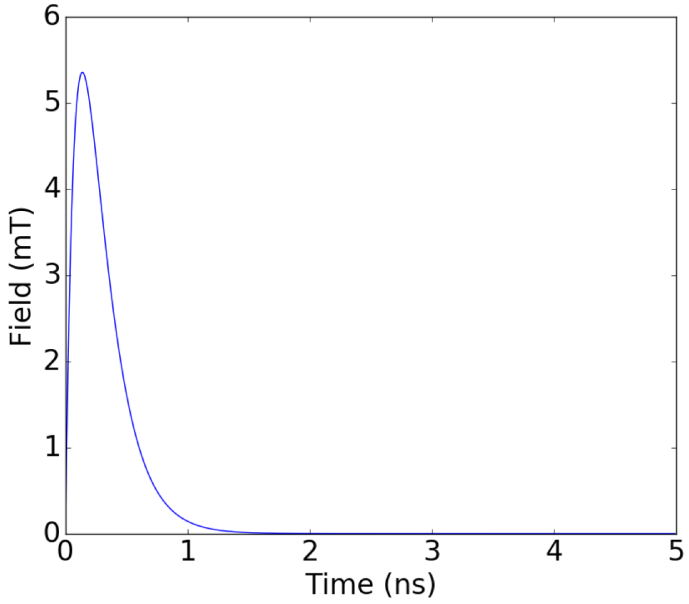

Fig. 5.3 Theoretical profile of the magnetic pulse produced by current moving through a waveguide when a laser is incident on the photodiode.

The largest square found in a flux closure state was the $10\mu m$ square, square A5, and a sequence of time resolved images was collected with the synchrotron running in hybrid mode. The resulting sequence of time resolved images is demonstrated in figure 5.4.

Figure 5.4 shows some core motion indicated by the expansion and contraction of the blue domain and reverse behaviour in the red domain. This demonstrates core movement at 90^o to the magnetic field pulse in contrast to observations of vortex core motion induced in cobalt [137] but agreement with observations of vortex core motion in permalloy [138]. There is also evidence in figure 5.4 of precessional dynamics within the domains perpendicular to the direction of the incident x-rays.

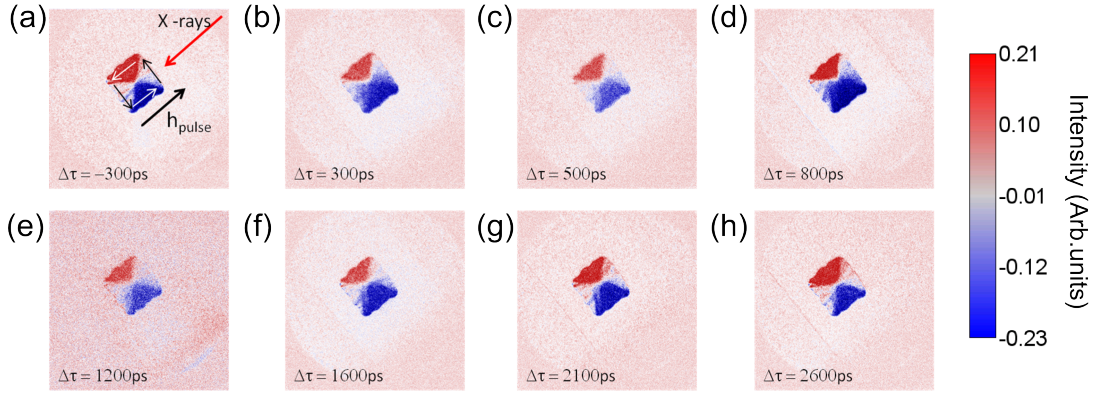

Fig. 5.4 Images taken from the image sequence collected from square A5, a 10μm galfenol square. The time between the field pulse and the image is indicated on each image. Figure a) shows the direction of the magnetisation, field pulse and angle of incidence of the x-rays on the square with the magnetisation of the square in its ground state.

In order to examine the change in the domain structure of square A5 resulting from the magnetic field pulse the first image in the sequence was subtracted from all subsequent images. This was done to show the change in the magnetisation within square A5 as a function of time. The result of this subtraction can be seen in figure 5.5.

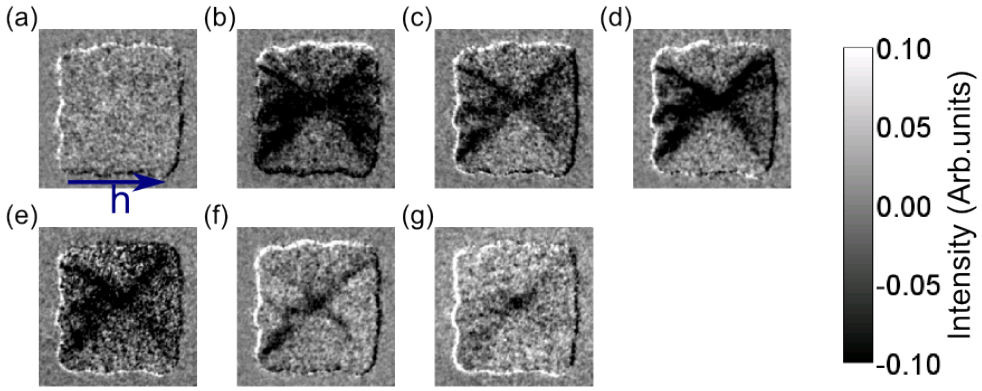

Fig. 5.5 10μm galfenol square with the first image, t=-0.4ns, subtracted from all subsequent images. The images here were taken at times of t= a) -0.3ns, b) 0.3ns, c) 0.5ns, d) 0.8ns, e) 1.2ns, f) 2.1 and g) 3.4ns after the magnetic field pulse. The blue arrow indicates the direction of the magnetic field pulse.

Figure 5.5 shows the magnetisation in the areas of uniform domains aligned perpendicular to the magnetisation oscillating at a frequency of ∼2GHz with the absolute change in magnetisation being at a maximum 0.3ns after the field pulse decaying across the next 0.2ns

before reaching a second, lower maximum 0.8ns after the magnetic field pulse indicating a damped spin wave mode oscillating at ∼2GHz in the regions of the square with magnetisation perpendicular to the incident x-rays. Also visible in figure 5.5 are changes in magnetisation along the domain walls as seen 2.1 ns after the magnetic field pulse which are caused by the displacement of the vortex core due to the magnetic field pulse. The oscillations in the domains aligned at 90^o to the magnetic field pulse also appear to take the form of oscillations observed in simulations of $Fe_{1-x}Ga_x$ squares with no uniaxial anisotropy in section 6.5 and in simulations of permalloy squares performed in reference [104]. These spin waves appear to oscillate at much lower frequencies in square A5 than in the simulations however this may be due to square A5 being much larger than the simulated objects with larger objects being shown to exhibit lower frequency spin wave modes in section 6.4. In order to investigate the oscillation within these domains further region of interest (ROI) scans were performed across the image sequence as shown in figure 5.6.

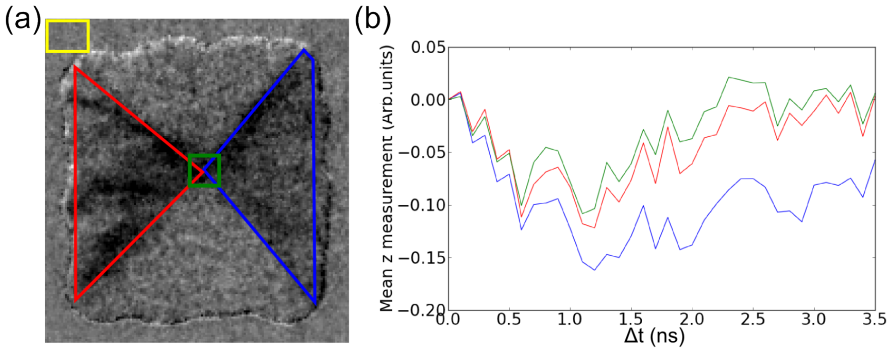

Fig. 5.6 ROI scans of the subtracted images of a 10 μm galfenol square. Shown in a) is the square at t=3.3ns after the magnetic field pulse with the regions of interest highlighted in blue, green and red with the background shown in yellow. The ROI profiles with the background subtracted are shown in b).

Figure 5.6 demonstrates that the magnetic field pulse is applied the effective field causing a torque. In the areas where the magnetisation is perpendicular to the incident x-rays this causes the magnetisation to perform damped precessional motion as shown by the magnetisation within the areas covered by the ROI scan continuing to deviate from its ground configuration reaching maximum displacement after the magnetic field pulse has decayed.

The movement of the core was investigated by setting up a simple program to display an image and then store the x and y co-ordinates of the mouse pointer when the user clicked on the image. The program would display the next image in the sequence and repeat the process until the core's position had been tracked throughout the video. The core's position was found manually rather than programmatically, as was done extensively in chapter 6, due

to the contrast of the XMCD PEEM images rendering core finding using images produced using the Sobel transformation, described in section 6.6, ineffective.

The manual extraction of the core's position as a function of time resulted in figure 5.7 showing the core's position in x and y as dots and a guide to the eye as a solid line.

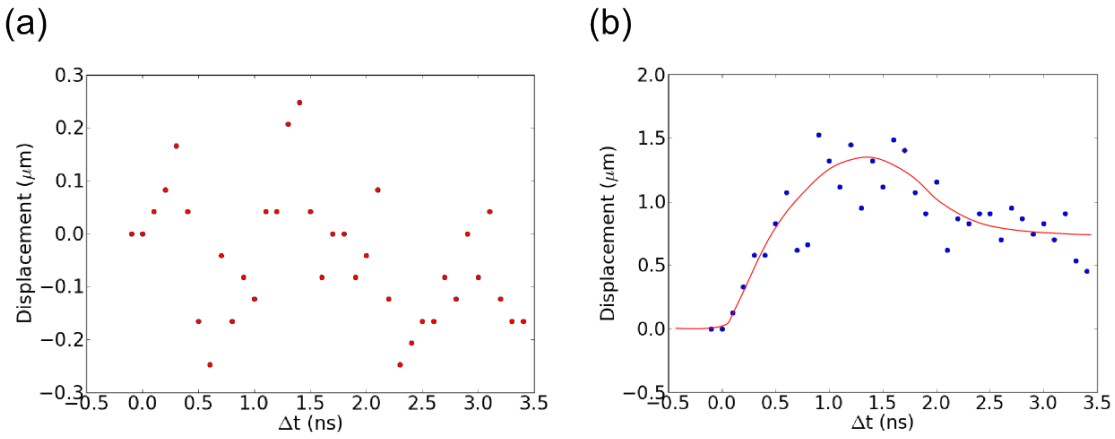

Fig. 5.7 Plot of the core position in a $10\mu m$ galfenol square. The core's position in x, the direction of the magnetic field pulse, is shown in a) and the core's position in y, at 90^o to the field pulse, is shown in b). The red line in b) acts as a guide to the eye to show the core's movement.

By examination of the core's position as a function of time it can be observed that the core becomes displaced by a distance of $\sim$1.4 μm over $\sim$1.3ns and then slowly begins to return to its equilibrium position. This means that the core moves with a velocity of $\sim 1076\pm150 ms^{-1}$ during its initial displacement. This movement persists after the magnetic field pulse has decayed indicating that it is due to the energy deposited within the domains by the field pulse.

The next set of time resolved experiments were performed whilst the synchrotron was run in 156 bunch mode. The first object to be imaged was a $3\mu m$ $Fe_{1-x}Ga_x$ square, designated D6, the ground state of which is shown in figure 5.8.

An image sequence lasting 6.2ns was collected from square D6, snapshots from which are shown in figure 5.9.

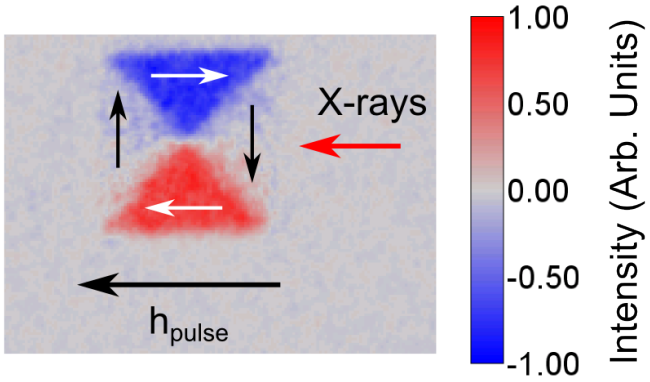

Fig. 5.8 Landau flux closure state in square D6, a 3μm $Fe_{1-x}Ga_x$ square. The polarisation of the x-rays, the magnetisation of the sample and the direction of the magnetic field pulse are indicated by the arrows.

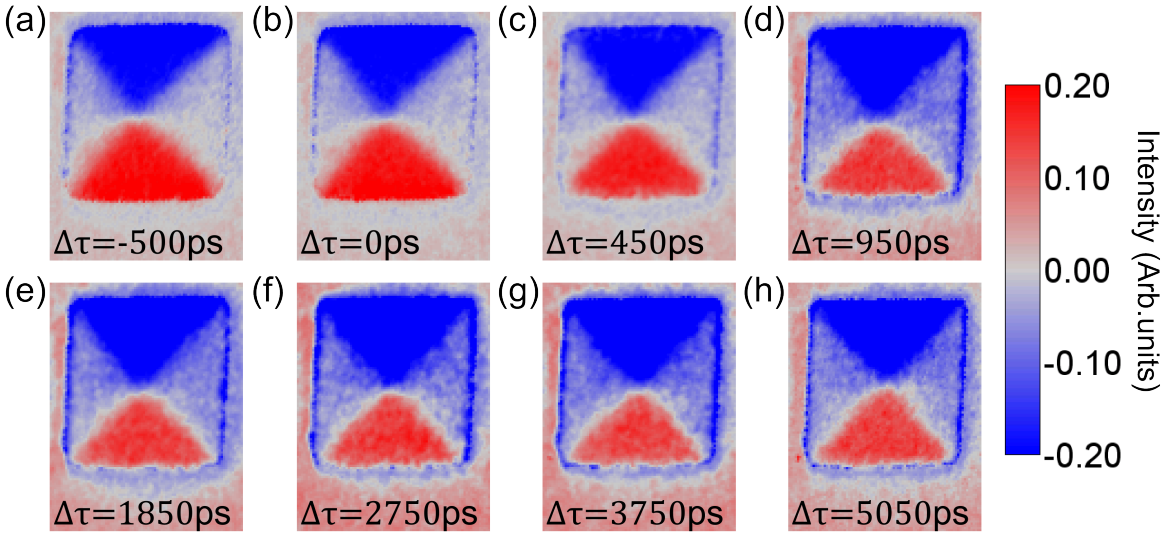

Fig. 5.9 Images taken from a video of a 3μm galfenol square at times after the magnetic field pulse of Δt=a)-0.5ns, b)0ns, c)0.45ns, d)0.95ns, e)1.85ns, f)2.75ns, g)3.75ns and h)5.05ns. These images have been cropped and rotated in order to demonstrate the changes in the magnetic domains of the sample.

In this video we can see clearly see core movement in both the x and y directions within the sample. The core's position was then measured as before and the position of the core in x and y as a function of time was plotted as shown in figure 5.10.

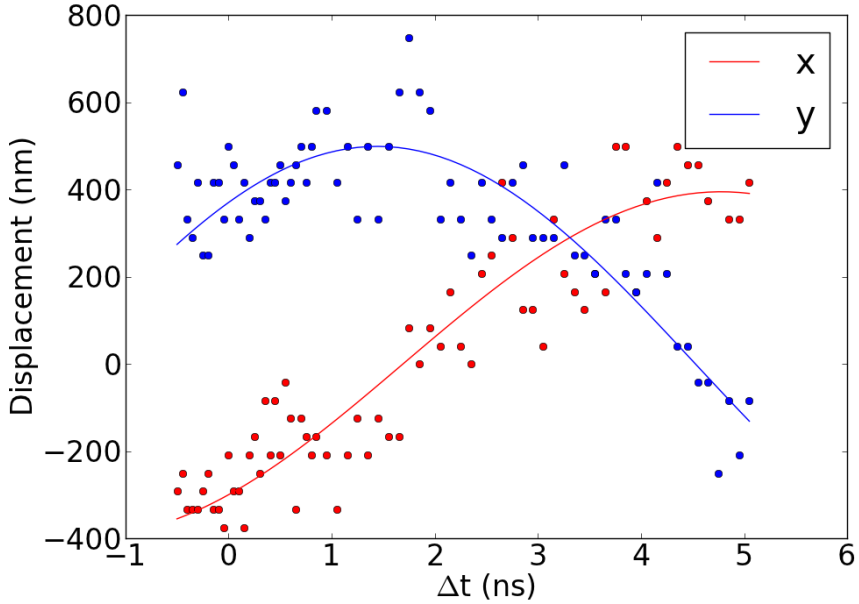

Fig. 5.10 Plot of the position of the vortex core in a $3\mu m$ galfenol square as a function of time when excited with a magnetic pulse. The data for the x position of the core is shown in red and the core's position in y is shown in blue. The x direction is defined as the axis of the field pulse and the y axis is defined as 90^o to the field pulse. The dots indicate the position of the core as found from experimental data and the solid lines are a sinusoidal function with a frequency of 80±20MHz which has been fitted to the experimental data.

By tracking the movement of the vortex core as a function of time using the same method as before and fitting to the data using the non-linear curve fitting function in origin 8 we found the frequency of oscillation to be $\sim$ 80±20MHz. The core's movements in x and y had phases of $1.54\pi\pm0.13\pi$ and $1.08\pi\pm 0.13\pi$ which were roughly $\frac{\pi}{2}$ out of phase with one another due to the core moving in a circular motion. The errors here were calculated by the origin 8 fitting procedure. This data yields a core velocity of $\sim 201\pm50\text{ms}^{-1}$ which was calculated by multiplying the radius of the area described by the core by the angular frequency. Calculating the core's velocity using the difference in time between the core reaching the positions of its extremes yields a core velocity of $\sim 220\pm19\text{ms}^{-1}$. The error in this value was found by finding the standard deviation from the fit and then assuming this was the error in the position of the core which was used to calculate the error in the velocity.

The large circular motion observed in this sample was most likely due to the pulse rate being 83MHz, a close match to the natural frequency of oscillation of the sample. The frequency of oscillation found by OOMMF simulation of the system was 90±40MHz. This value was found using a standard python peak finding program and the error was found as the width of the peak at half maximum as described in detail in section 6.2. This frequency differs slightly from the experimentally measured frequency however the difference is within the bound of the error in the simulation.

In order to show changes in the magnetic domains of the sample due to spin wave modes the first image in the image sequence was subtracted from all subsequent images. The effects of variation in beam intensity across the image sequence were removed by producing a gaussian blur of the subtracted images and then subtracting this from the subtracted images. The results of this transformation are shown in figure 5.11.

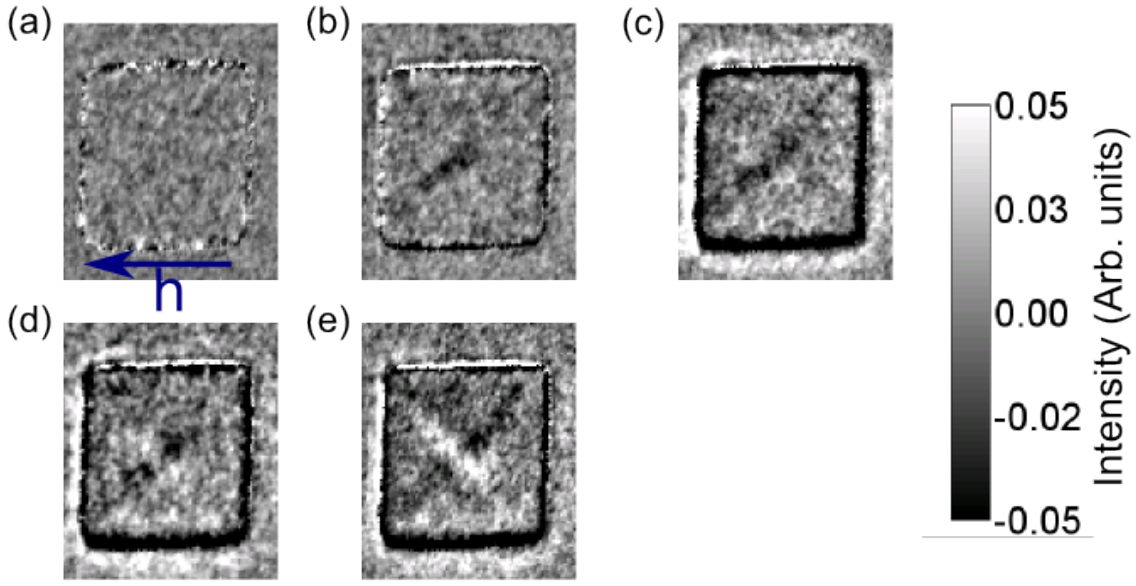

Fig. 5.11 3μm galfenol square with the first image, t=-0.5ns, subtracted from all subsequent images. Images are taken with the delay line set to t=a)-0.45ns, b)0.5ns, c)1.55ns, d)2.85ns, e)5.05ns. The blue arrow indicates the direction of the magnetic field pulse.

In this subtracted image we can see the two domain walls appearing in the image due to the motion of the core. The change in intensity can be observed by performing ROI scans of the sample as have been done in figure 5.12.

Figure 5.12 shows the magnetisation along the domain walls changing due to the motion of the vortex core however the image sequence is not long enough to fit a frequency of

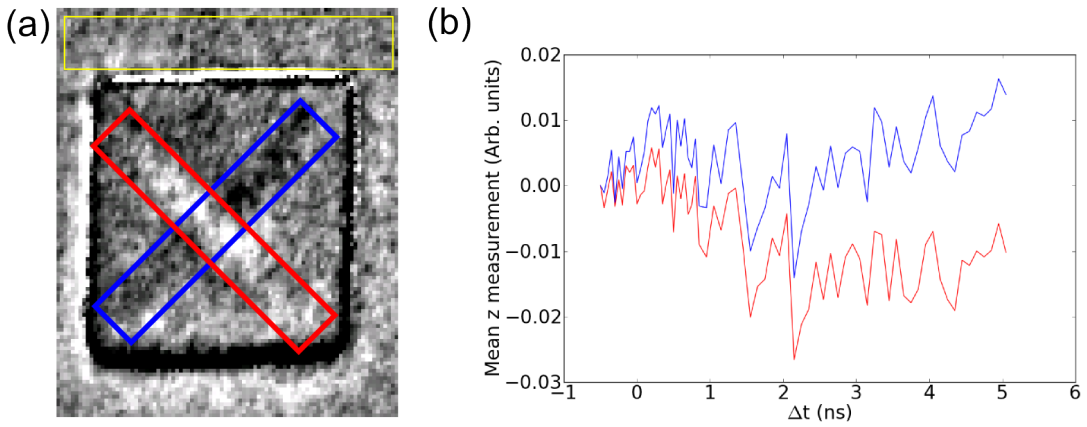

Fig. 5.12 ROI scans for the subtracted images from the video for the $3\mu m$ galfenol square. The areas scanned are indicated on the image taken at t=6.2ns in a) by the blue, green and red squares with the black rectangle being the background used to adjust for image brightness being demonstrated by the black rectangle at the top of the image. The results of the ROI scans are shown in the graph shown in b).

oscillation to this motion. If the experiment had continued it is possible the two profiles would converge 12ns after the magnetic field pulse as the core returned to its initial position.

The fact that the core movement was so strong and the frequency of oscillation is so close to the frequency of the pulse train driving the core motion may indicate that the natural frequency of oscillation of the vortex core within this square is in fact 83MHz and that the resonant mode of the system is being excited by the magnetic pulse.

Before more images could be taken to extend the length of the image sequence the system unfortunately experienced an arc whilst collecting data with a delay of 6.3ns in the delay line resulting in the magnetic configuration of this square being altered so that no further data could be collected. The experiment was therefore moved to a slightly larger object, a 3.5 μm galfenol square which was found in a Landau flux closure state as shown in figure 5.13.

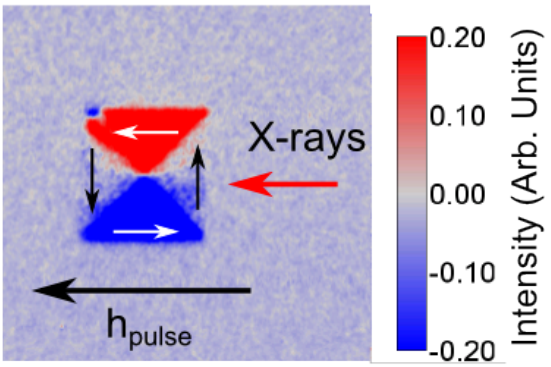

Fig. 5.13 Landau flux closure state in square D7, a 3.5μm $Fe_{1-x}Ga_x$ square. The polarisation of the x-rays, the magnetisation of the sample and the direction of the magnetic field pulse are indicated by the arrows.

An image sequence consisting of over 200 images was collected from this object, some of which are demonstrated in figure 5.14.

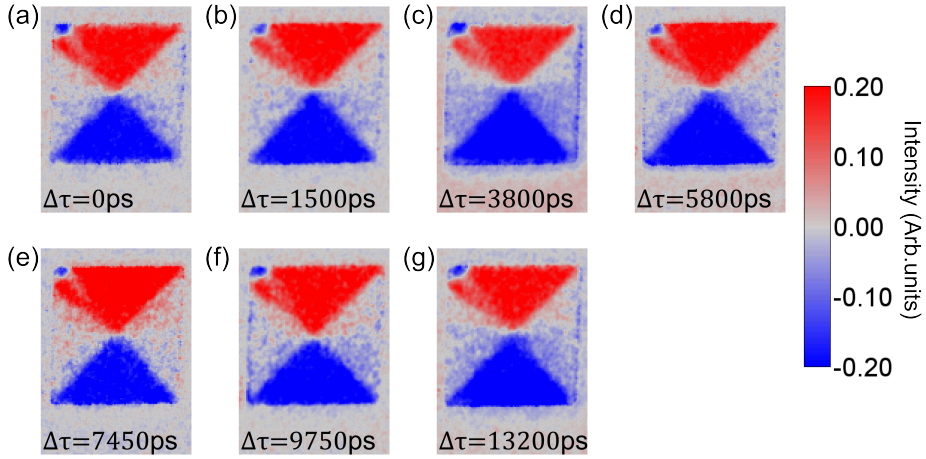

Fig. 5.14 Images taken from a video of a 3.5 μm galfenol square with times from the delay line being t = a)0ns, b)1.5ns, c)3.8ns, d)5.8ns, e)7.45ns, f)9.75ns, g)13.2ns. The images have been rotated, cropped, and re-coloured to show the core dynamics more clearly.

In this video we can also see that the vortex core no longer oscillates in a clean circle which can be further confirmed by looking at the core's position as a function of time in figure 5.15.

When we look at the fit to this data we see that the frequency of oscillation is 83 $\pm$ 20MHz with a core velocity of $\sim$ 136 $\pm$ 12ms^{-1}.

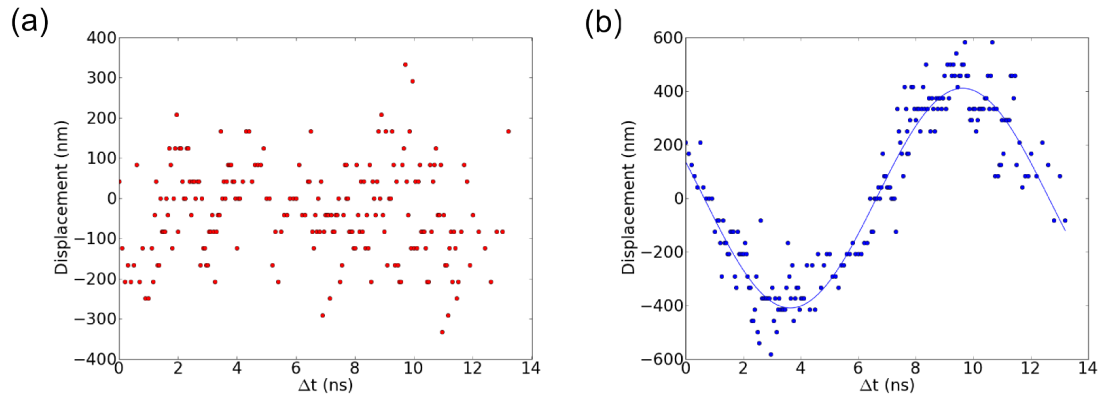

Fig. 5.15 Plots of the core's position as a function of time. a) shows the core's displacement from its starting position in x and b) shows the core's displacement in y. The solid line in b) demonstrates the fit to the oscillation consisting of sinusoid with a frequency of 83MHz.

In order to investigate the frequency of oscillation further the first image in the sequence was subtracted from all subsequent images as done previously. The results of this subtraction are shown in figure 5.16.

Looking at the subtracted images we can see that in the $3.5\mu m$ sample we can only see the movement of the vortex core indicating that the oscillations in the vortex core do not extend further into the object. In order to test the frequency of oscillation seen when the core's movement was tracked visually the core was examined with a z-axis profile as shown in figure 5.17.

The fit shown in figure 5.17 b) yields a frequency of oscillation of 85.5 $\pm$2.2MHz. This value is slightly higher than the value found by fitting to the core's position in figure 5.15 of 83 $\pm$ 20MHz however the large error values in the earlier fit mean that the value is within the error values of the previous measurement. Simulation of this device found a resonant frequency for the core of 90$\pm$40MHz which, whilst higher than the frequencies observed experimentally is within error of the experimentally observed results. This value was found by fft analysis of a simulation of a 3.5μm device as described in section 6.2.

The time resolved data shows that the core in D7 does not perform the same movements as were observed in sample D6. The core moves only in the y direction, 90^o to the direction of the pulse, and does not move significantly in the x-direction oscillating only in the y-direction. This is the inverse of what would be expected in a larger object due to the reduced shape anisotropy. The displacement of the core in the larger object is the same as the displacement observed in the smaller object however this indicates weaker oscillation since the core would be expected to move more in the larger object due to the reduced shape anisotropy. A

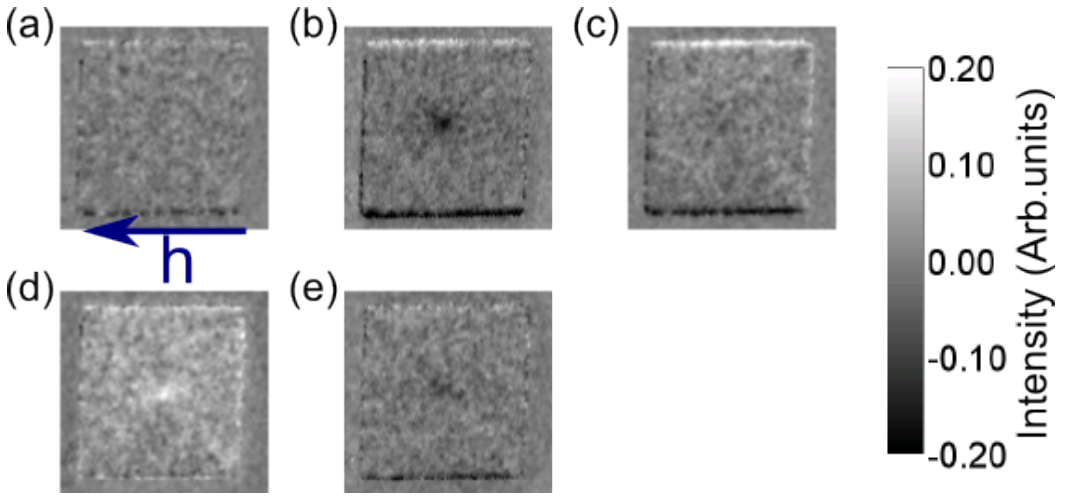

Fig. 5.16 3.5μm galfenol square with the first image subtracted from all subsequent images. Images are taken with the delay line set to t = a) 0ns, b) 3.6ns, c) 6.9ns, d) 9.45ns, e) 13.2ns. The blue arrow indicates the direction of the magnetic field pulse.

probable cause for the difference in core motion may be that the difference in the size of the object has caused the resonant frequency of the vortex core to move away from 83MHz so that it is no longer being driven at its resonant frequency. The sample size available here is too small to confirm that the difference in size is the cause of the change in the character of the vortex core motion meaning that further experimentation should be directed towards exploring vortex core motion in square objects with various widths in order to experimentally investigate the relation between object size and the resonant oscillation frequency of the vortex core.

Attempts to study the effects of a strain induced anisotropy on the frequency of oscillation were not successful as the strain was not sufficiently transmitted through the epoxy, the GaAs and the waveguide to induce any detectable change in the magnetic configuration. Future work may include the design of a waveguide capable of carrying a high frequency pulse train when grown on a substrate made from a piezoelectric material such as PMN-PT in order to improve the transmission of strain to the sample.

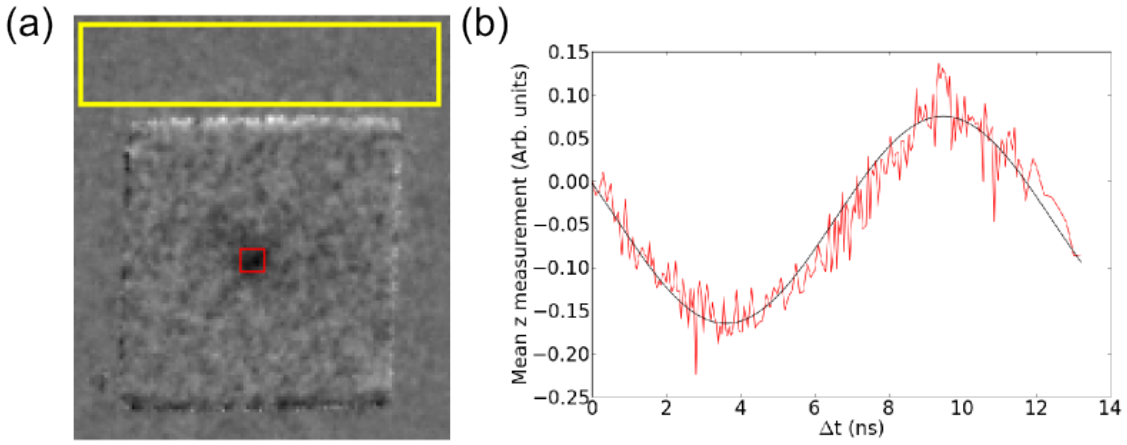

Fig. 5.17 ROI scan for the subtracted images from the 3.5 μm galfenol square. The areas scanned are indicated by the red and yellow enclosures in a). The yellow enclosure represents the background from the image which was subtracted from the result from the red ROI. The result of this scan is shown in b). The zero point in b) has been set to the value of the measurement at t=0.

5.2 Static measurements of Ni squares

The magnetoelastic coefficient of polycrystalline $Fe_{1-x}Ga_x$ was insufficient to respond strongly enough to the effects of applied strain. As both nickel and cobalt have larger magnetoelastic coefficients these were considered next. Ni and Co squares were fabricated upon waveguides similar to those used in order to study the behaviour of the $Fe_{1-x}Ga_x$ samples. However, due to the lower magnetisation for nickel and cobalt the weaker shape anisotropy reduced the probability for the structures to form flux closure states in the optimal object size range for imaging (2-10μm). A few nickel squares were found in the flux closure state and were therefore singled out for further experimentation. Imaging XAS was used to confirm the location of the L_3 edge as shown in figure 5.18.

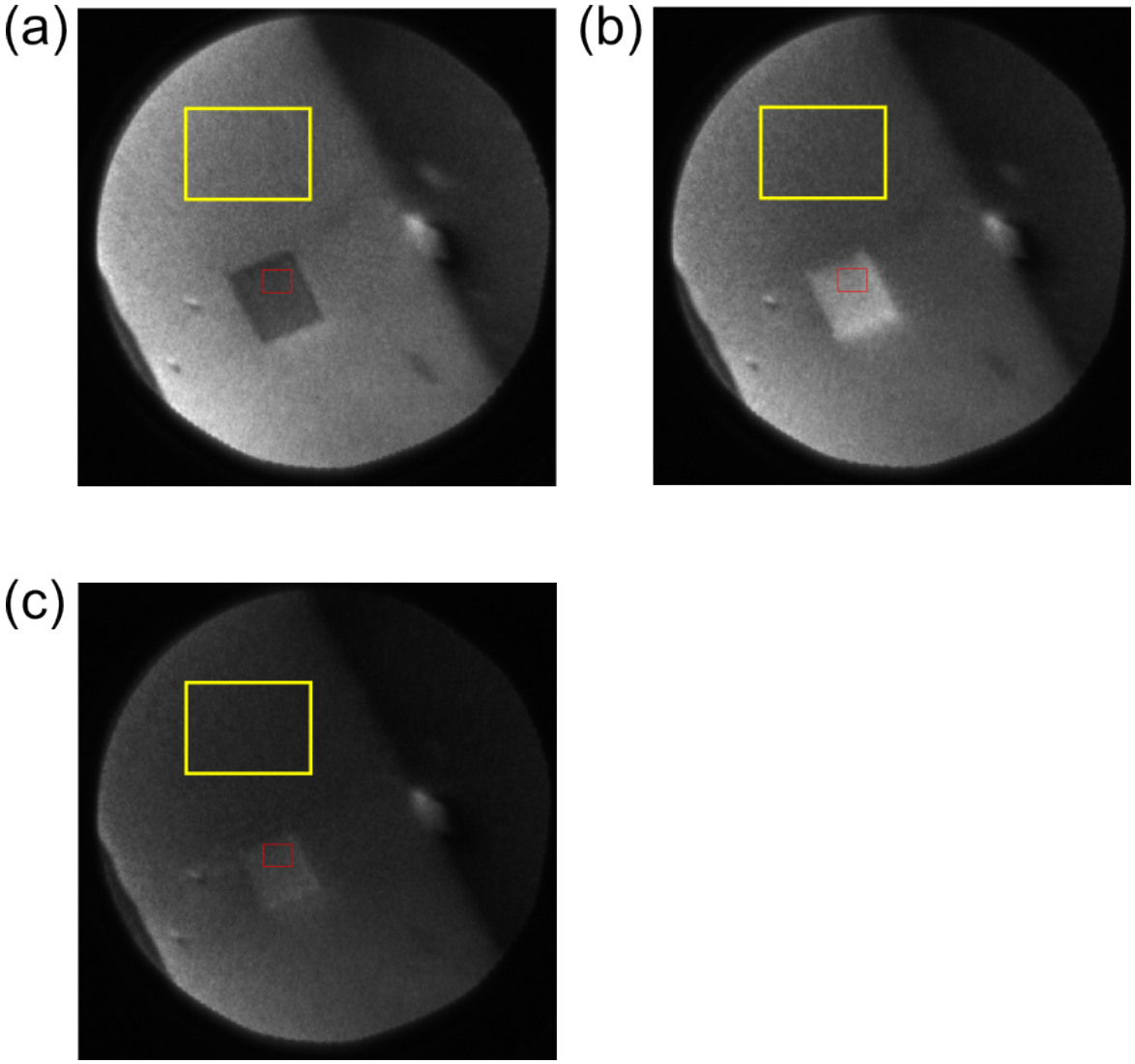

Fig. 5.18 Images from the energy scan used to determine the L_3 edge of the nickel squares. The energies shown are a)848ev, b)852.5eV and 860eV. The red square represents the ROI for the energy scan and the yellow square indicates the ROI for the background used to determine variations in image intensity. The field of view in these images is 20 μm

From this sequence of images, we can see that the L_3 edge is indeed present at around $852 \pm 0.25eV$ however in order to confirm this the result of an ROI scan is plotted in figure 5.19 which shows the mean pixel intensity for the red ROI with the mean pixel intensity from the yellow ROI subtracted as background.

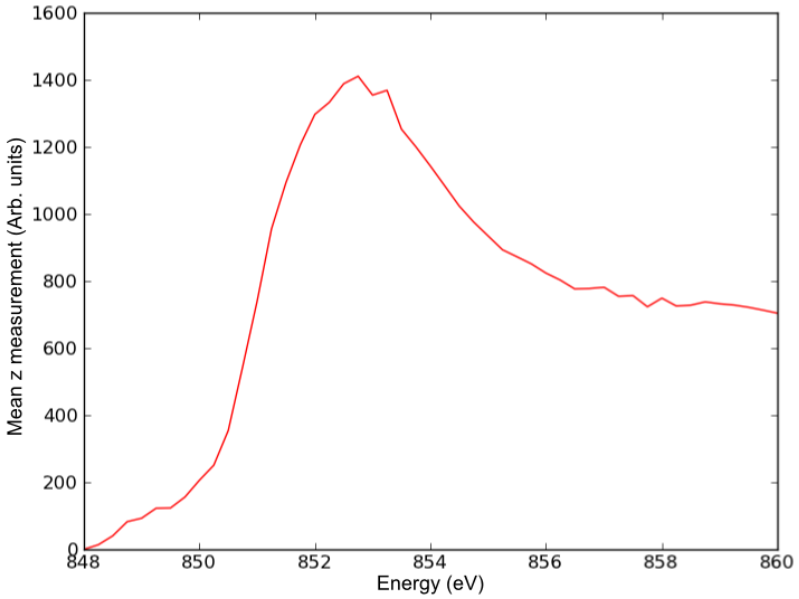

Fig. 5.19 Plot of the energy scan used to determine the L_3 edge of nickel squares. The data plotted here represents the mean pixel intensity of the red ROI in figure 5.18 with the mean intensity of the yellow square subtracted to remove background variations in image intensity.

Here we can see that the L_3 edge is at 852.7±0.25eV which is exactly the same as value for the L_3 edge in reference [135]. The square used for the energy scan was also found to be in a Landau flux closure pattern and was therefore used to test the effects of strain on the magnetic domain structure of the sample. The results of this test are shown in figure 5.20.

Looking at these domains we can see that strain induced pinching of the magnetic domains does indeed occur in the nickel square with the strain being transmitted through the waveguide. Figures 5.20 b) and 5.20 f) demonstrate that the process of strain-induced pinching is not entirely reproducible however since the pinching observed in b) is much stronger than that in f). In b) a system with only two domains is achieved however in f) the system is a highly pinched flux closure state. Despite the lower constant of magnetostriction in nickel the increased elastic coefficients and lower magnetisation allows the strain to have a greater effect on the polycrystalline nickel structures than on the polycrystalline $Fe_{1-x}Ga_x$

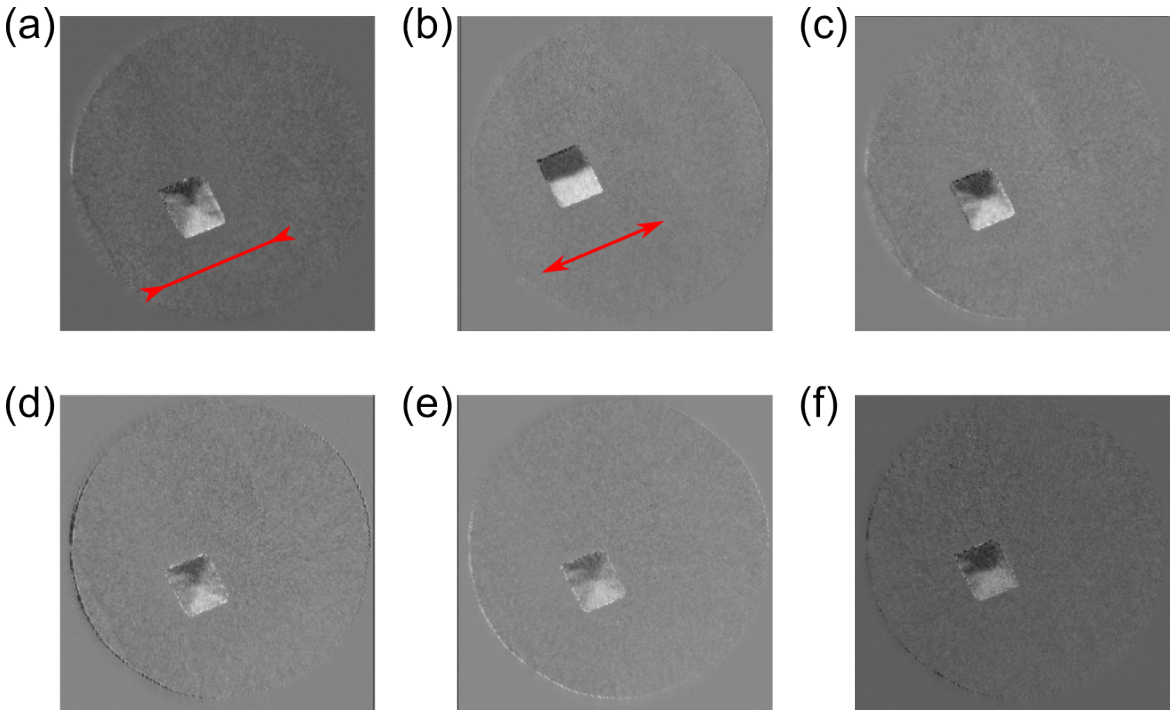

Fig. 5.20 XMCD PEEM images of a nickel square with various levels of strain applied to the sample. The voltage applied to the piezo electric was swept from -25V to +40V. A nickel square is shown with a)-25V, b)+40V, c)0V, d)-25V, e)0V and f)+40V applied to the piezo-electric transducer. The red arrows indicate the direction of the strain with the arrows in a) indicating the compressive strain resulting from the negative voltage on the piezoelectric transducer and the arrows in b) indicating tensile strain due to the positive voltage on the piezoelectric transducer.

structures. Unfortunately when time resolved measurement were performed on the nickel squares no core movement was observed.

The reason for this was investigated by FMR analysis of a Ni token at an oscillation frequency of 10GHz performed by Mr. Christopher Love and fitted to by Dr. S. A. Cavill. The result of this measurement is shown in figure 5.21.

This fitting produced a Gilbert damping parameter of 0.12, a factor of ten higher than the value of 0.017 previously reported for $Fe_{1-x}Ga_x$ [61]. This explains the low response to the magnetic field pulse exhibited by the Ni samples as compared to the $Fe_{1-x}Ga_x$ samples.

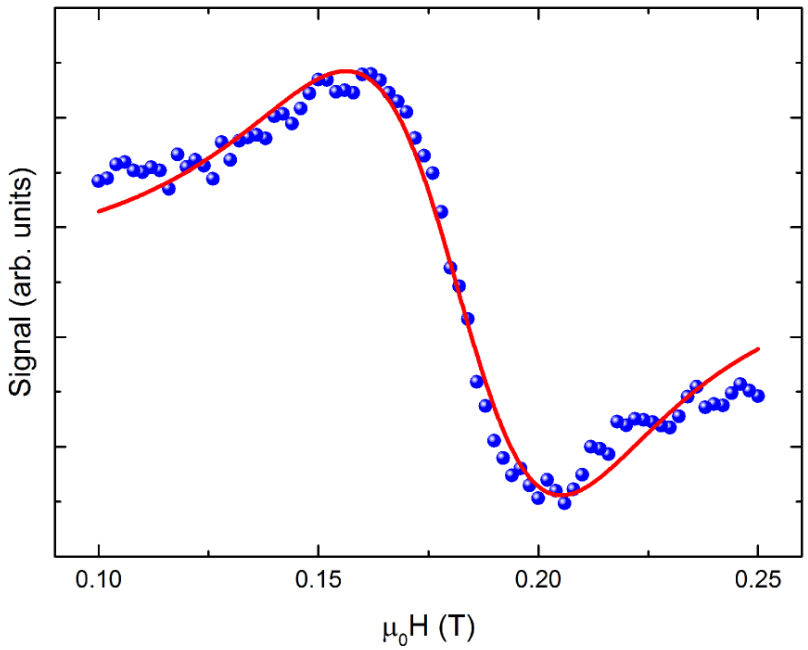

Fig. 5.21 FMR data collected by Mr. Christopher Love and fitted by Dr. S. A. Cavill. The blue dots indicate the experimental data and the red line indicates the fit to the data.

5.3 Conclusions from XMCD PEEM measurements

We have successfully demonstrated time resolved measurement of vortex core gyration in galfenol microstructures using time resolved XMCD PEEM at the Diamond Light Source at Harwell, Oxford. Damped spin wave modes were observed at a frequency of 2GHz in a 10 μm square. Core gyration in both the x and y directions was observed in a 3.5μm square with a frequency of 80$\pm$ 20MHz however an arc occurred in the system meaning that the experiment had to be moved to a 3 μm square which exhibited an oscillation frequency of 83$\pm$15MHz. These large osculations are likely to have been due to the natural frequency of oscillation of the vortex core in the 3μm square, D6, being a close match to the frequency of the pulse train, 83MHz. The smaller oscillations in the larger 3.5μm square, D7, were most likely due to the natural frequency of oscillation of the vortex core in the larger object not being as close a match to the frequency of the pulse train. This indicates a relation between object size and oscillation frequency however investigations into the oscillation frequency of differently sized square objects must be performed in order to gain a full understanding of the effects of object size on vortex core oscillation frequency. These samples were unresponsive

to an applied stress however due to an inability to transmit stress through the epoxy, the sample substrate and the waveguide.

This could be corrected by using a piezoelectric substrate such as PMN-PT however the waveguide would need to be redesigned for this experiment to work as intended. This is due to the dielectric constant of the PMN-PT substrate being different to that for the GaAs substrate. In order to correct for this first the dielectric constant of PMN-PT with different strengths of electric field applied across the device would need to be determined by capacitance measurements. The results of these measurements would then need to be used to redesign the waveguide using a piece of mathematical modelling software such as FIMMWAVE [139]. The width and length of the central channel as well as the width of the troughs to either side of the central channel would need to be customised in order to produce a waveguide with the desired impedance to allow the pulse train to pass through the waveguide regardless of the voltage applied to the piezoelectric substrate. Experiments were also performed on 35nm thick nickel squares. These samples responded strongly to stress exhibiting clear changes in the domain structure of the devices however no gyroscopic motion was observed due to the high damping parameter of the devices, as determined by FMR measurements performed by Mr. Christopher Love.

Chapter 6

Micromagnetic simulations of nanoscale magnetic structures.

A series of micromagnetic simulations were performed using the Object Oriented Micromagnetic Framework (OOMMF) [51] in order to investigate the effect of strain induced anisotropy and object size on spin waves and vortex core motion in a Landau flux closure state.

This was done by first investigating the effects of shape and strain induced anisotropy on the Landau flux closure states of square and circular systems in order to identify the sizes and shapes of objects which may prove interesting for further study. The objects which were chosen were then subjected to a short magnetic field pulse in order to excite the resonant modes so that they may be determined. The effects of a strain induced anisotropy on these modes within 500nm squares were determined revealing both a reduction in the frequency of oscillation of the spin wave modes and an increase in the amplitude of the magnetic field pulse required to induce switching of the vortex cores' polarisation as the strain induced anisotropy increased. Next, the effects of increasing the size of the objects on the frequency of oscillation of the modes were determined. Increasing the size of the objects was shown to reduce the frequency at which the oscillatory modes occurred. Also observed in larger samples was a breakdown of the central vortex core once the magnetic field pulse used to induce oscillations was sufficiently large. The higher frequency modes were then studied in more detail and an s-wave was discovered along the domain wall in the direction of the uniaxial anisotropy. The effects of the core breakdown event were then studied in more detail and the core breakdown event is shown to lead to much greater vortex core displacement than when no vortex core breakdown was observed. Finally experiments were performed on samples with no strain induced anisotropy in the presence of realistic damping and it was found that key observations made on the oscillatory modes in the undamped samples remain

once realistic damping is returned to the system and therefore are expected in real world devices.

6.1 Effects of size anisotropy on strain induced pinching

The first set of simulations was designed to determine the effects of shape anisotropy on the ground state of magnetic circles and squares. These simulations were set up with parameters suitable for epitaxial $Fe_{0.81}Ga_{0.19}$ films. They include a uniaxial anisotropy, K_u, in the [110] direction of 12.4×10^3 Jm^{-3}, and a cubic anisotropy, K_c, in the [100] and [010] directions of 18.9×10^3 Jm^{-3} as given by reference [21]. The exchange constant used was 1.4×10^{-11} Jm^{-1} [54] and the saturation magnetisation used was 1378×10^3 Am^{-1} [79]. The damping parameter, α, was set to 0.0001 in order provide sufficient oscillations to identify spin waves of the simulation. The effects of strain were simulated by a uniaxial anisotropy applied along the [010] direction. The objects were divided into grids of cell size 2nm $\times$ 2nm $\times$ 10nm and the initial state of the system was loaded in using the images shown in figure 6.1. Also indicated on figure 6.1 are the directions of the cubic, uniaxial and strain induced anisotropies.

The system was then allowed to evolve in the presence of a strain induced anisotropy until the change in magnetisation between iterations had dropped below the arbitrary value of $1Am^{-1}$ at which point the magnetic configuration was output to a .omf file. By simulating 100nm, 500nm and 1000nm squares at $0kJm^{-3}$, $10kJm^{-3}$, $20kJm^{-3}$, $30kJm^{-3}$ and $40kJm^{-3}$ of strain induced anisotropy the results shown in figure 6.2 were obtained. These sizes were chosen to represent the fabricated structures and the strain induced anisotropies were chosen in order to slightly exceed the experimentally achievable range.

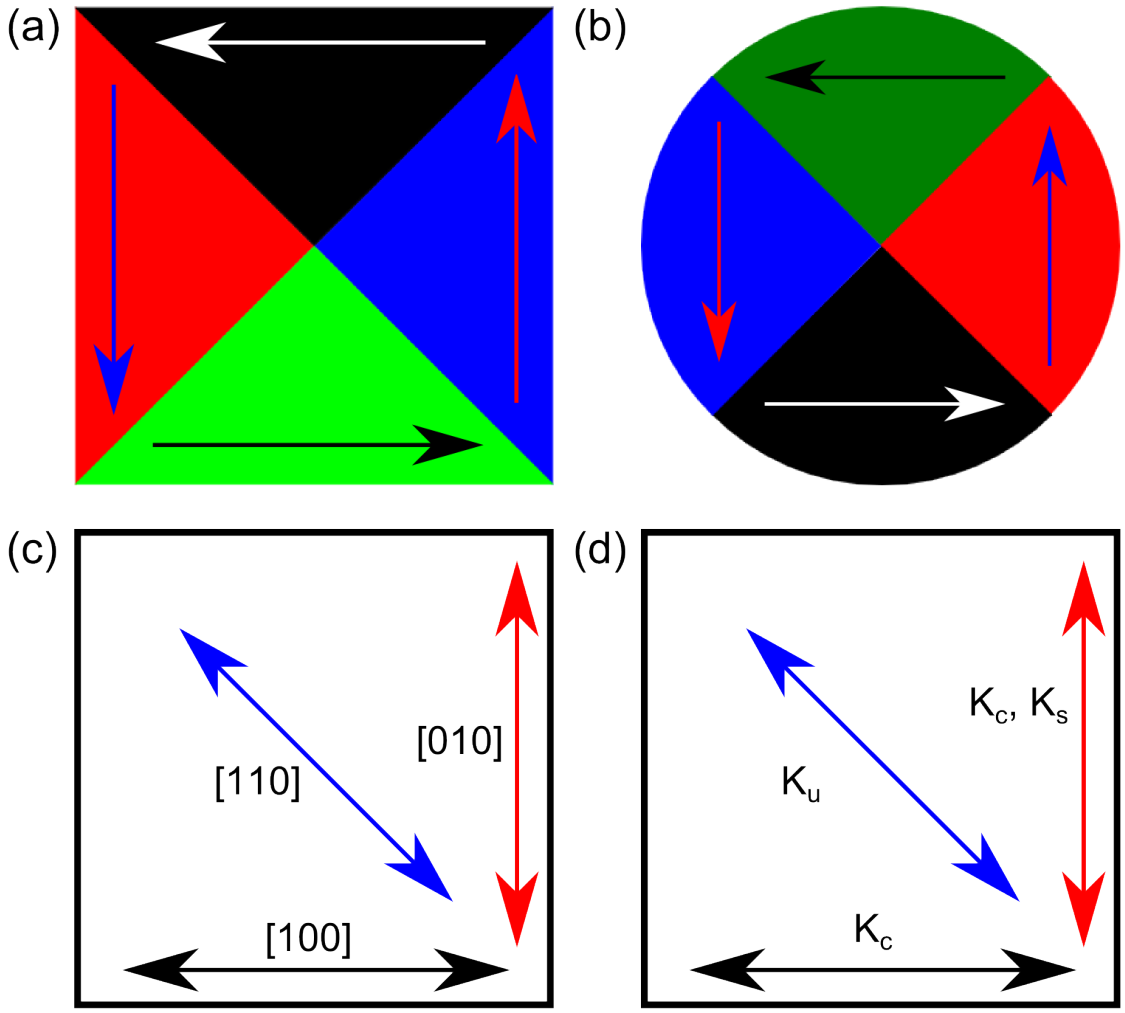

Fig. 6.1 Images used to initialise calculations of the ground states of a) a square and b) a circle. The arrows in a) and b) indicate the direction of the magnetisation in the regions they are superimposed upon. The colour of these arrows was chosen to maximise viability. The arrows in c) indicate the directions of the anisotropy terms used in the simulation with the cubic easy axes lying along the red and black arrows, the strain induced anisotropy being applied along the red arrow and the uniaxial anisotropy lying along the blue arrow. This is shown explicitly in d) where the arrows are labelled with the anisotropy terms lying along them rather than the crystallographic direction which they represent.

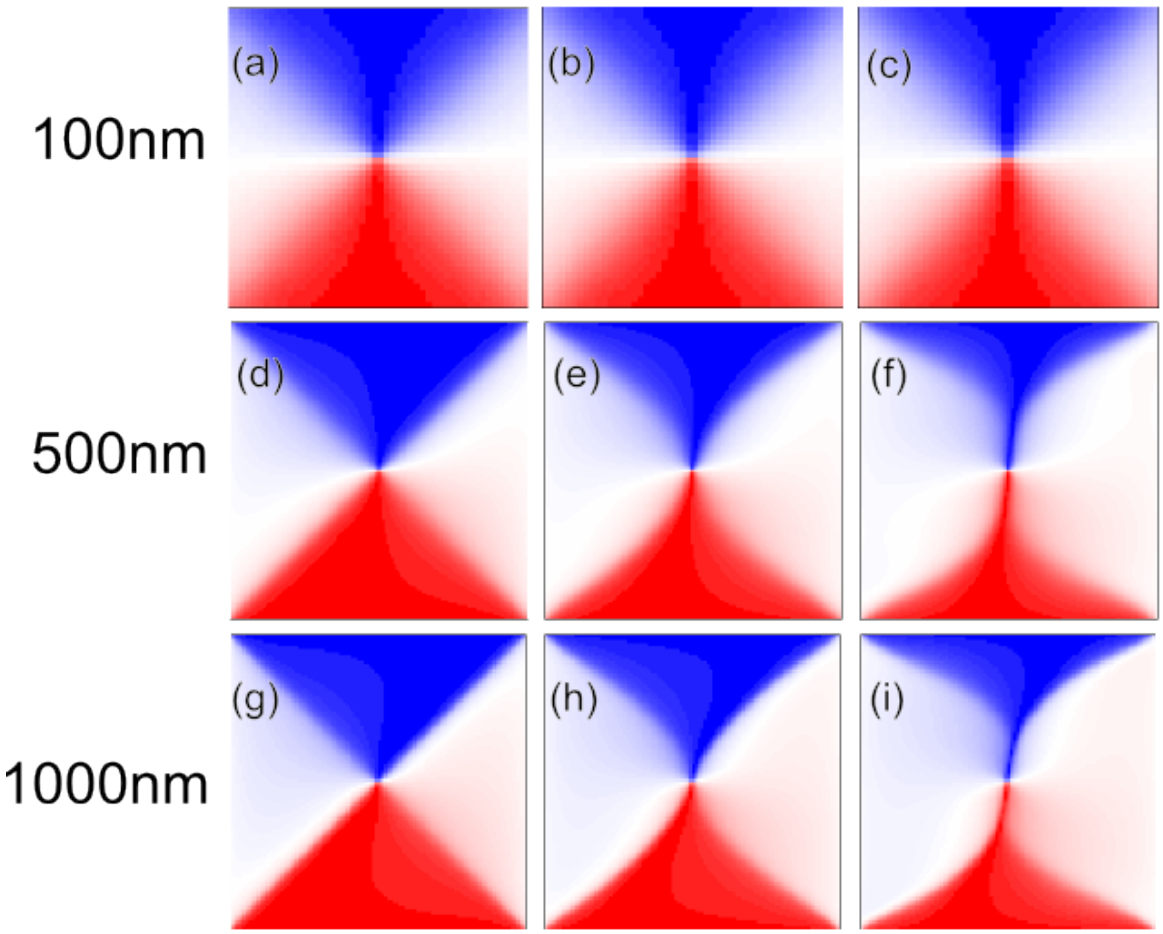

Fig. 6.2 Results of OOMMF simulations of squares of a series of sizes with a series of strain induced anisotropies. (a)-(c) demonstrate a 100nm square with 0,20 and 40kJm^{-3} of strain induced anisotropy applied respectively. (d)-(f) illustrate a 500nm square with 0,20 and 40kJm^{-3} of strain induced anisotropy and (g)-(i) demonstrate 0,10 and 20kJm^{-3} of strain induced anisotropy in a 1000nm square.

Figure 6.2 demonstrates that the shape anisotropy dominates over the strain induced anisotropy in the smaller squares requiring a much greater level of strain induced anisotropy to achieve pinching of the Landau flux closure state described in section 2.8. The pinching occurs because the strain induced anisotropy makes it energetically favourable for the magnetisation in the sample to align itself along the direction of the induced anisotropy. These simulations were also performed on a series of circles to see how the shape of the object affects the amount of strain required to produce a pinched state. The results of this study can be seen in figure 6.3 in which it can be seen that the level of pinching in circular objects is similar to that seen in square objects.

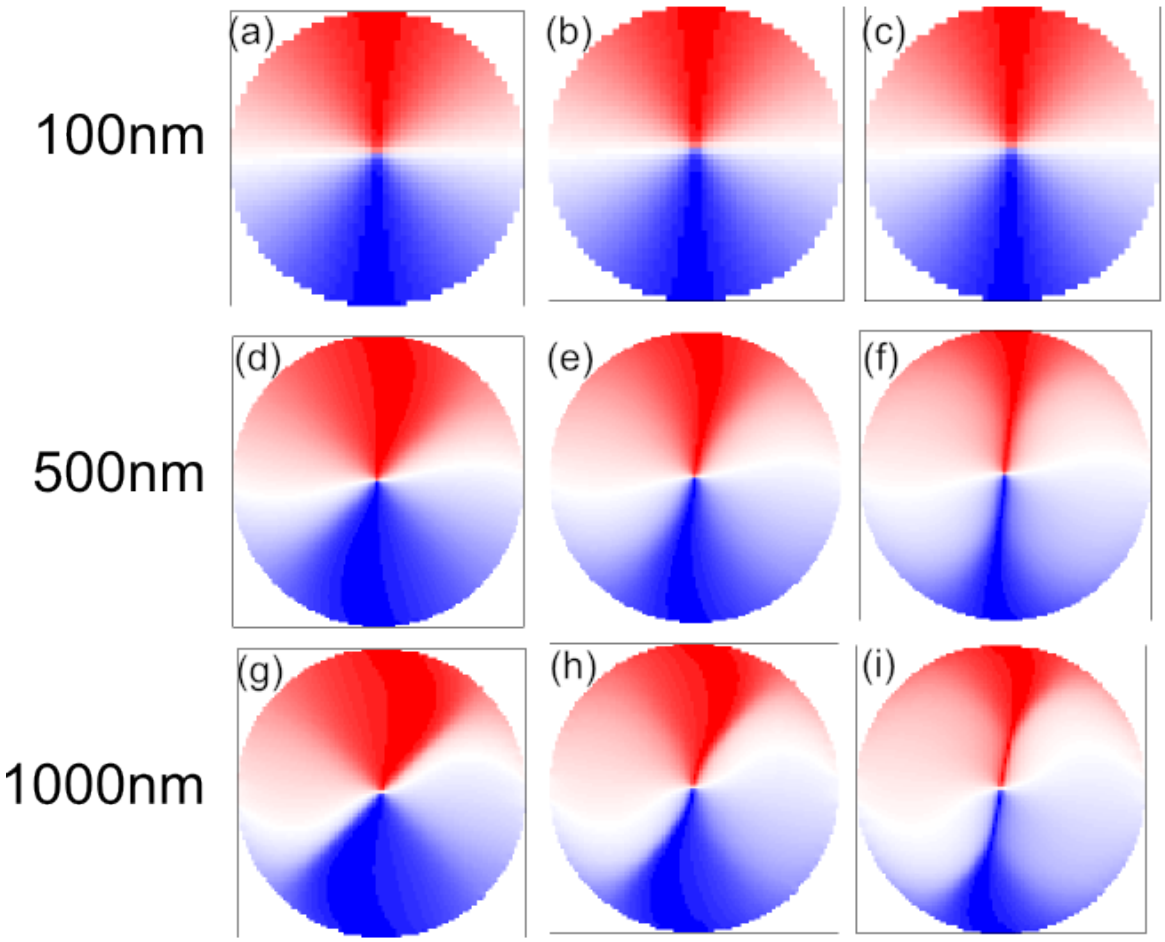

Fig. 6.3 Results of OOMMF simulations of circles of a series of sizes with a series of strains applied. (a)-(c) demonstrate a 100nm square with 0,20 and 40kJm^{-3} of strain applied respectively. (d)-(f) illustrate a 500nm square with 0,20 and 40kJm^{-3} of strain and (g)-(i) demonstrate 0,10 and 20kJm^{-3} of strain in a 1000nm square.

Here again we see that the size of the object significantly affects the effectiveness of applying a strain induced anisotropy to the sample. After examining this data we decided to focus on square objects of 500nm, 1000nm, 1500nm and 2000nm as objects of these sizes exhibited a strong response to strain and were small enough to be simulated in time resolved simulations. Square objects were chosen over circular objects since the measurements performed in chapter 5 were performed on square objects.

The width of the domain walls in the objects chosen for further study were measured using linescans across the upper left domain wall as demonstrated in figure 6.4.

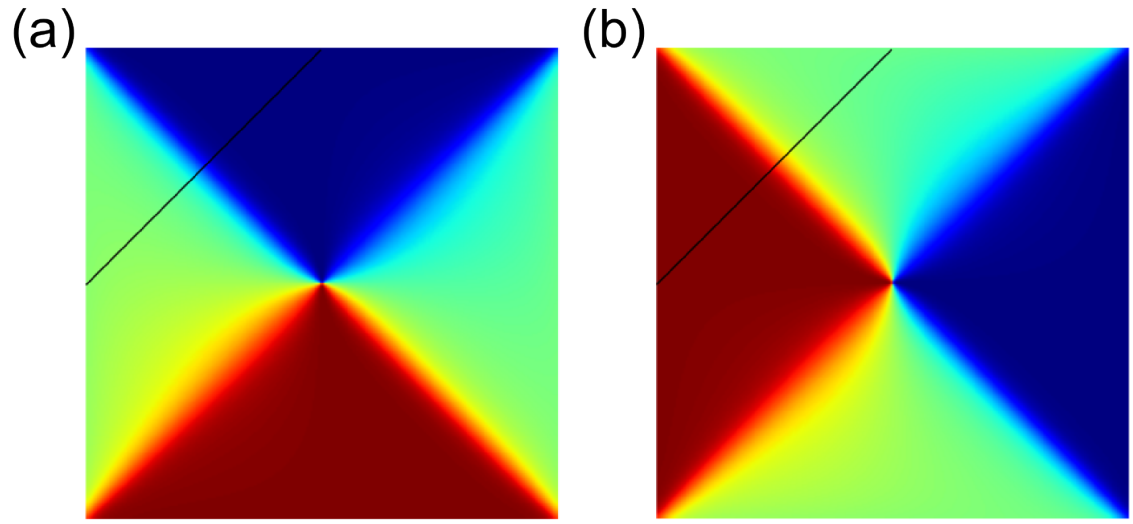

Fig. 6.4 Demonstration of the linescan used to determine the domain wall width in the ground state in a 500nm square. The magnetisation in the x direction is shown in a) and the magnetisation in the y direction is shown in b). The line used for the scan is shown in black.

The profiles produced by performing this linescan on the 500nm square are shown in figure 6.5a) and b). The edges of the domain wall were then determined by applying the standard peak finding program included with the scipy python package to the double differential of the linescan as shown in figure 6.5 c). The peak finding program uses continuous wavelet transformation in order to find peaks, a full description of this algorithm can be found in reference [140].

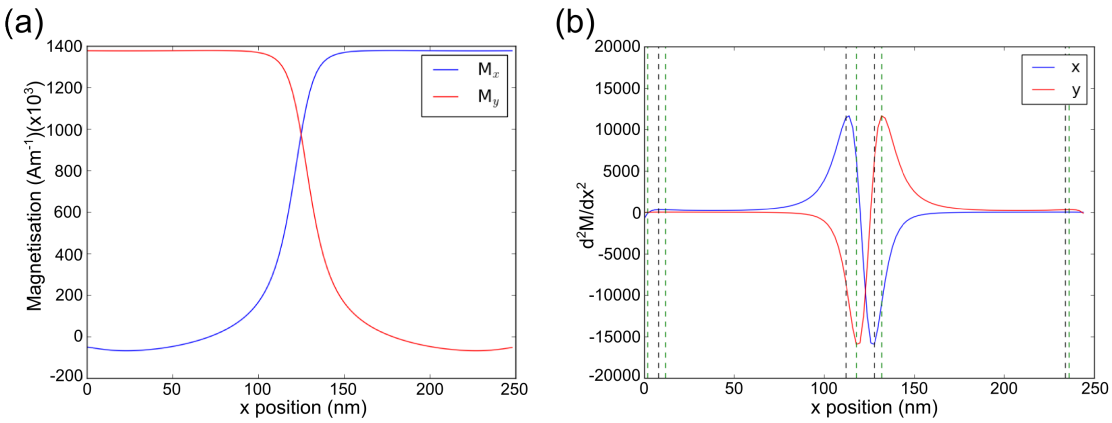

Fig. 6.5 Data produced by linescans of a simulated 500nm galfenol square. a) shows the result of the linescan with positive magnetisation defined so that the linescans for x and y can be shown on the same axes. b) shows the double differential of the linescan data with the peaks found in the data demonstrated by the black dotted line for the linescan of the x magnetisation and the green dotted line for the y magnetisation.

This process was repeated for the ground states of all the squares chosen for further study yielding the domain wall widths shown in figure 6.6.

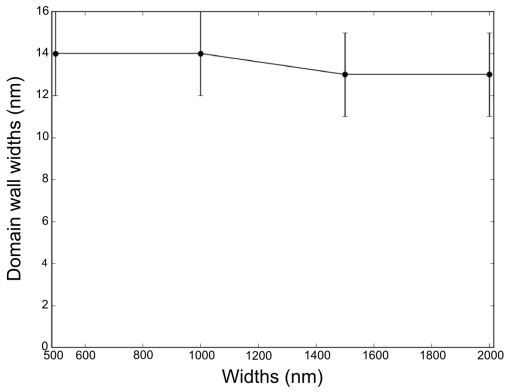

Fig. 6.6 Domain wall widths in simulated galfenol squares of varying sizes. The errors were found using the sizes of the elements used in the simulations.

It can be seen in figure 6.6 that the size of the object does not significantly affect the width of the domain walls with the variation in domain wall widths being lower than the error in the measurement, found as the element size within the simulation. This indicates that the domain wall width is not product of the object's size but rather its material properties.

6.2 Time resolved magnetisation dynamics

The 500nm squares shown in figure 6.2 were subjected to a magnetic field pulse with a duration of 70ps. The peak strength of the pulse was calculated by multiplying $0.815\mathrm{Am}^{-1}$ (approximately 1mT) by an amplitude factor which was altered for different simulations. The pulse was applied in the [010] direction and was described using equation 6.1 in which H is the pulse form, t is the time and A is the amplitude. The constants represent values of $p_1 = 50 \times 10^{-12}$s, $p_2 = 70 \times 10^{-12}$s and $p_3 = 40 \times 10^{-12}$s.

$$H = A * \left(1 - e^{-\frac{t}{(p_1)}}\right) * e^{-\frac{t-(p_2)}{(p_3)}} \tag{6.1}$$

This pulse profile was chosen in order to emulate the magnetic pulse resulting from the current through the waveguide as described in section 3.13 however the pulse was made shorter for the simulations in order to excite a greater range of frequencies. The values of p_1, p_2 and p_3 were chosen in order to emulate the response of the diodes used in the XMCD experiments detailed in chapter 5 [136]. The amplitudes of the pulses were arbitrarily chosen to exceed the values used in reference [104] by 10mT. The pulse profile resulting from equation 6.1 is shown in figure 6.7.

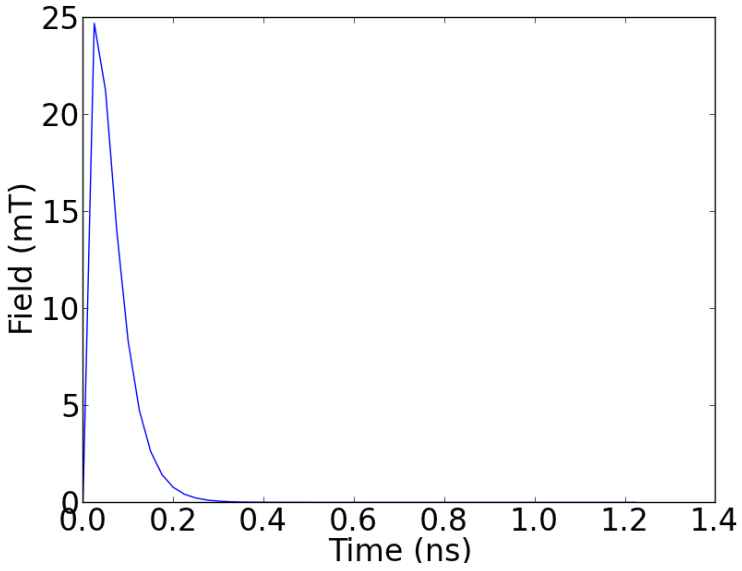

Fig. 6.7 Profile of the pulse used to excite movement in the vortex core. The pulse demonstrated on the figure has an amplitude of 25mT. The pulse length is always 70ps regardless of the pulse amplitude.

The Fourier transformation profile of this pulse profile (figure 6.8) shows the frequencies excited by the pulse.

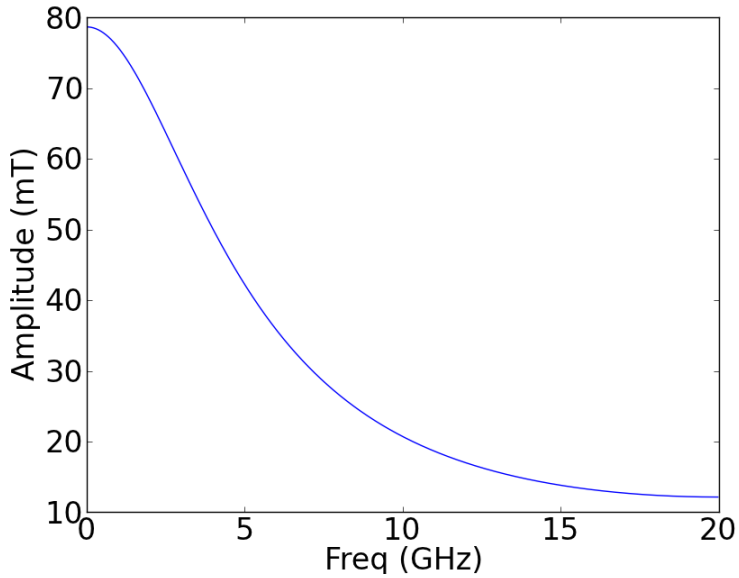

Fig. 6.8 Fourier transform of the magnetic pulse used to excite vortex core movement. This shows the frequencies excited by the pulse and the intensity with which it excites those particular frequencies.

OOMMF outputted an image of the simulation every 25ps. By using the sequence of images the vortex core motion was analysed and the spectral components of the magnetisation dynamics as a function of position in each structure were determined. The core's motion was tracked using the core tracking algorithm described in appendix E. It was found that the core of the system would oscillate around the centre of the object similar to the movement described in reference [32]. This is demonstrated in figure 6.9 which shows the trajectory of the vortex core of the system with a strain induced anisotropy of 0kJm^{-3} when excited by a pulse of strength 25mT.

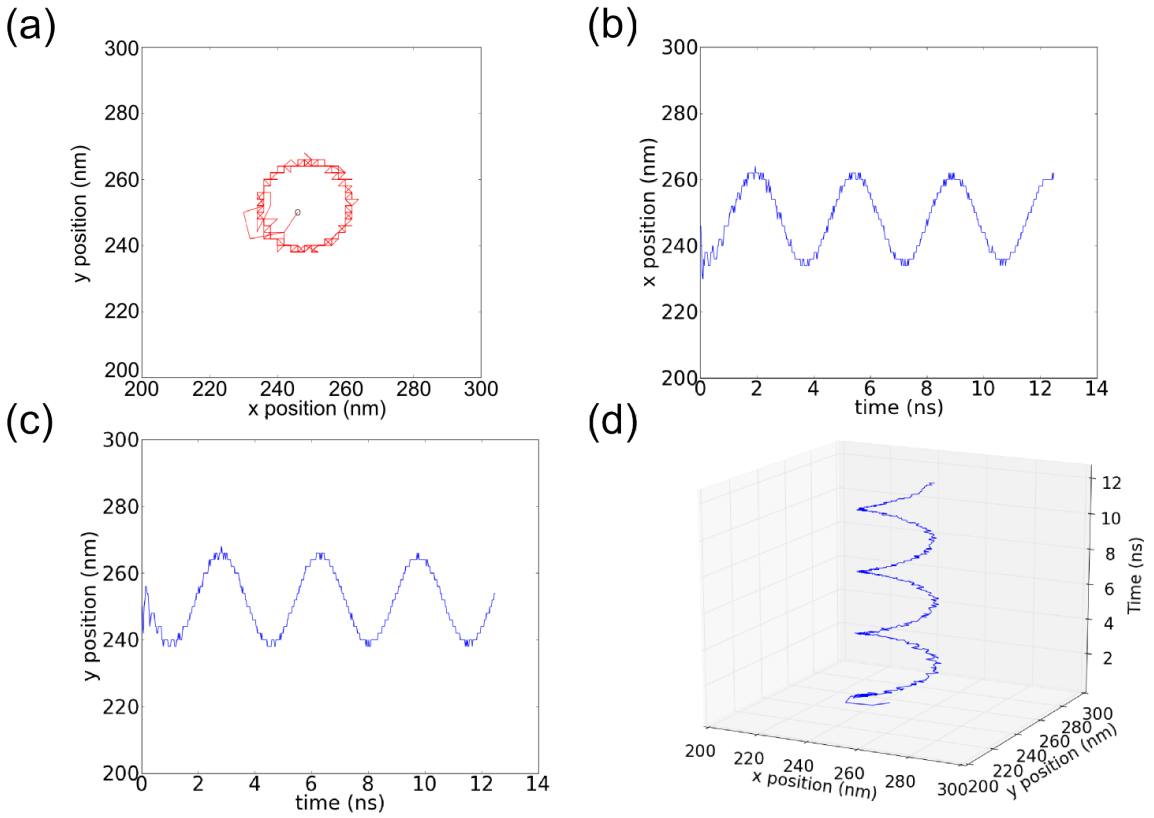

Fig. 6.9 Tracking results for a 500nm sample with 0kJm^{-3} of strain induced anisotropy applied to the sample and a 25mT magnitude magnetic field pulse was used to excite core movement. In a) we can see a phase diagram of the core's movement with the starting point indicated in the centre by a black circle, in b) we can see the x-component of the core's position as a function of time and in c) we can see the y-component of the core's position as a function of time. Finally in d) the core's position in x and y is shown as a function of time in a 3D line plot.

Figure 6.9 shows that the core describes a circular motion which did not decay over the simulation time. The fact that the area described by each oscillation of the core's motion does not change over the duration of the simulation is due to the lack of damping in the system and the circle described in a real sample would decay as shown in reference [141]. The next step of this analysis was to look at the magnetisation dynamics across the whole shape. Examples of these profiles for a sample with no strain induced anisotropy and a field pulse of amplitude 10mT are shown in figure 6.10.

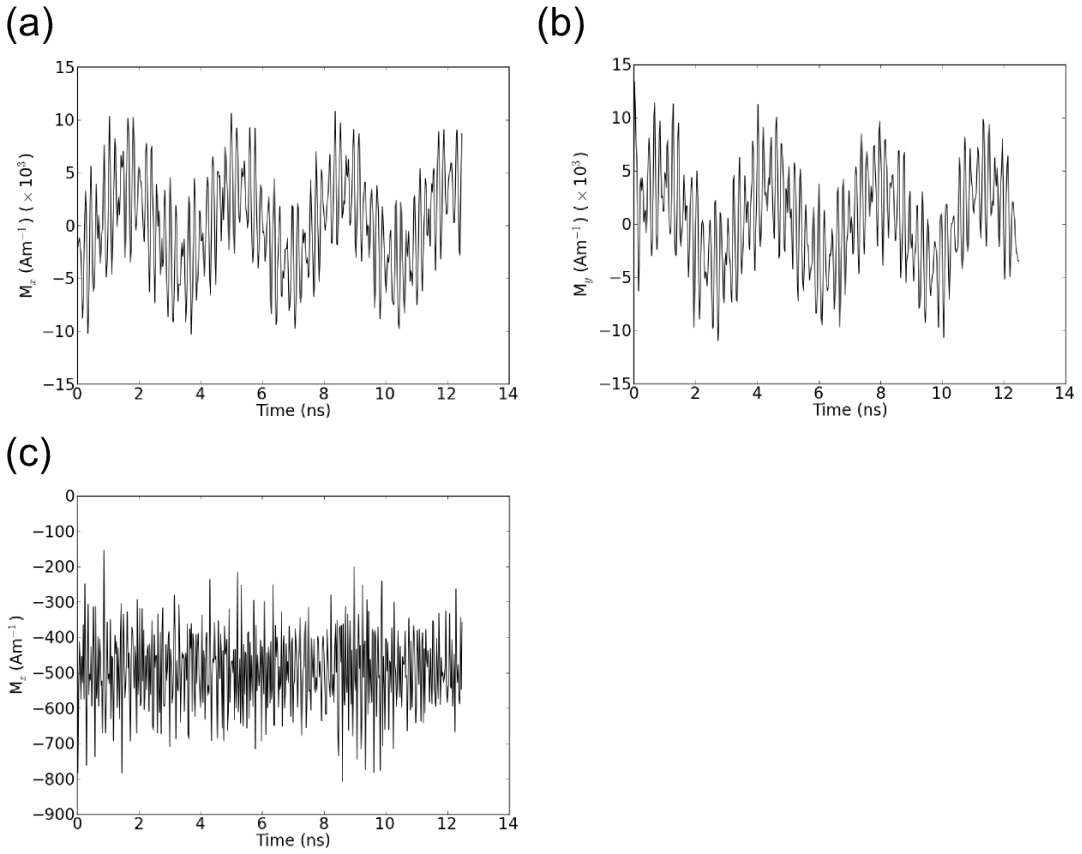

Fig. 6.10 Magnetisation profile for the 500nm sample with 0kJm^{-3} of strain. The sample was excited with a 10mT magnetic pulse and then allowed to evolve. Shown in a) is the x-component of the magnetisation as a function of time, b) is the y-component of the magnetisation as a function of time and c) shows the z-component of the magnetisation as a function of time.

Figure 6.10 shows that whilst there is a single strong oscillation moving slowly throughout the simulation there are also secondary oscillations which persist throughout the simulation. The principal oscillation corresponds to the vortex core motion shown in figure 6.9 and the

smaller modes correspond to spin wave modes within the confined structure. In order to determine the frequency of these oscillations the data was subjected to a one dimensional Fourier transform in order to produce the frequency amplitude graphs shown in figure 6.11 in which the frequency amplitude profile for the 1mT and 25mT simulations are shown at 0kJm^{-3} of strain.

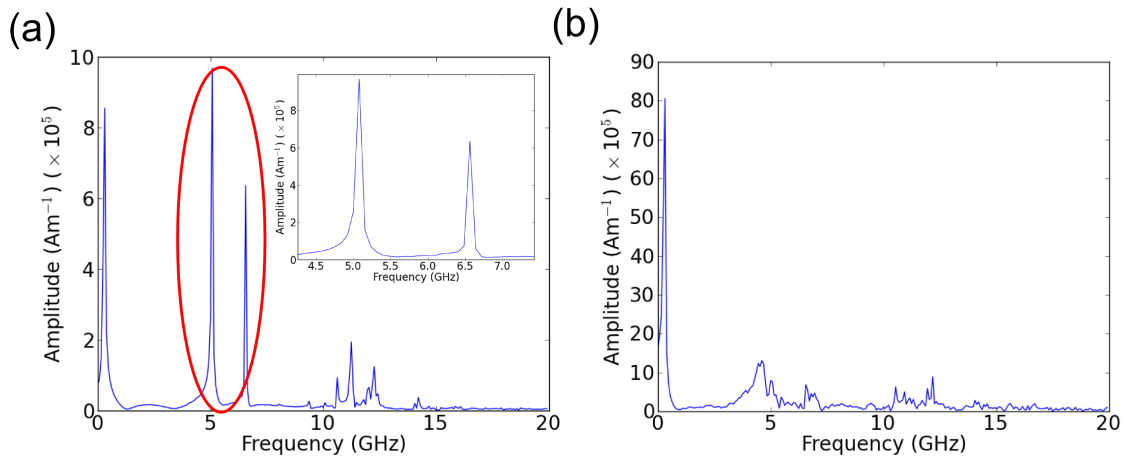

Fig. 6.11 Results of a Fourier transformation of the M_x component of time resolved simulations of 500nm square subjected to magnetic pulses of strength a) 1mT and b) 25mT. The inset in a) is a zoomed in view of the secondary modes highlighted with a red circle.

In figure 6.11 we can see the primary frequency mode centred on 300MHz but we can also see that there are secondary modes centred on 5GHz and 6.5GHz as well as a series of tertiary modes centred around 12.3GHz. These modes appear in both figures 6.11a) and 6.11b) however the amplitude of the primary mode is much larger in figure 6.11b) with the amplitude of the higher frequency spin wave modes remaining constant. The linewidth of the higher frequency spin wave modes appears to broaden at higher pulse amplitudes.

The vortex core's motion will now be studied by further examination of the data presented in figure 6.9 showing the core's position as a function of time.

If we calculate the Fourier transformation of the core's movements in the x and y directions we obtain the result in figure 6.12.

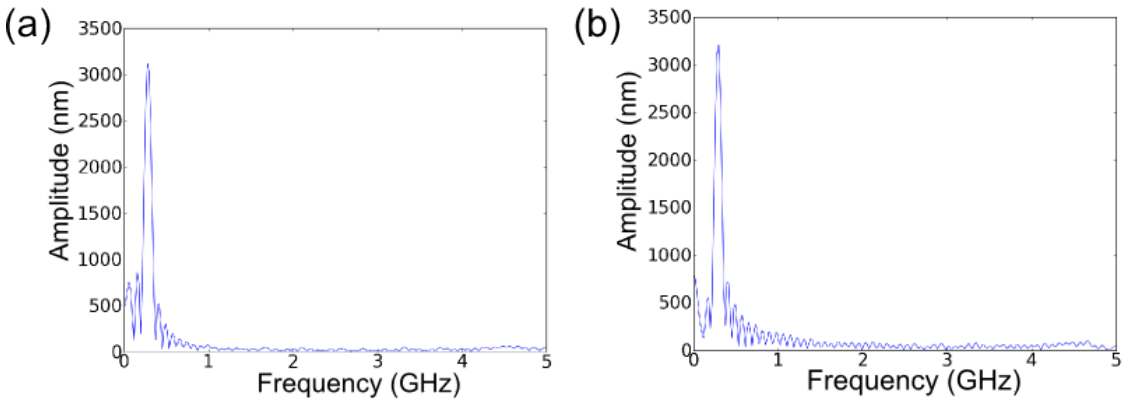

Fig. 6.12 Fourier transform of the movement of the core in a 500nm square sample with zero strain applied when excited by a 25mT magnetic pulse. In a) the Fourier transform of the movement of the core in the x direction is shown and the Fourier transformation profile of the core's movement in the y direction is shown in b).

Figure 6.12 shows that the frequency of oscillation of the cores matches that of the primary oscillation of the magnetisation. This confirms indicates that the primary frequency of the oscillation in the magnetisation is a result of the oscillation of the vortex core. The movement of the core as a function of the amplitude of the pulse used to excite its movement can be studied a number of ways. Firstly, the area of the circle that the core describes, ζ_{core}, as a function of the amplitude of the exciting pulse can be examined. The vortex core was forced to form with positive polarisation by the means of a static external magnetic field of amplitude 100mT applied in the [001] (z) direction whilst the system settled into its ground state. The results of this calculation are shown in figure 6.13.

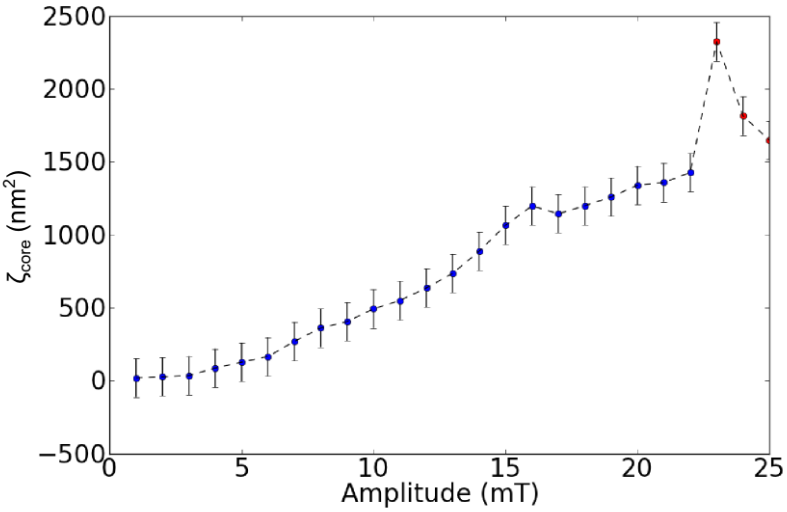

Fig. 6.13 Plot of the area traced out by the central core, ζ_{core}, as it moves in a circle in a 500nm square with zero strain applied to the sample as a function of the amplitude of the exciting magnetic field pulse. The blue dots indicate that the polarisation of the core remained constant throughout the simulation whereas the red dots indicate that the core's polarisation reversed when a magnetic field pulse was applied.

As can be seen in figure 6.13 the area of the circle traced out by the core's motion increases as the amplitude of the exciting magnetic field pulse increases however once the amplitude of the magnetic field pulse exceeds 22mT it becomes sufficient to induce vortex core switching in the sample. This switching event is accompanied by a sharp rise in the area described by the vortex core's motion which then begins to decrease as the amplitude of the magnetic field pulse continues to increase. This indicates that once the vortex core switching event occurs, the core's behaviour as a function of the magnetic field pulse becomes non-linear.

In order to investigate the change in the core's velocity as a function of the amplitude of the exciting magnetic pulse, the speed with which the core moved was found as described in reference [31].

First the core's speed of rotation was found by plotting the core's displacement in radians from its starting position, θ. A line was fitted to this measurement in order to find the core's angular velocity, $\dot{\theta}$ as shown in figure 6.14 which shows the result of this fitting for a 500nm square when excited with a pulse with a peak amplitude of 5mT. The error in the calculation of the core's velocity is given as an output of the fitting function used.

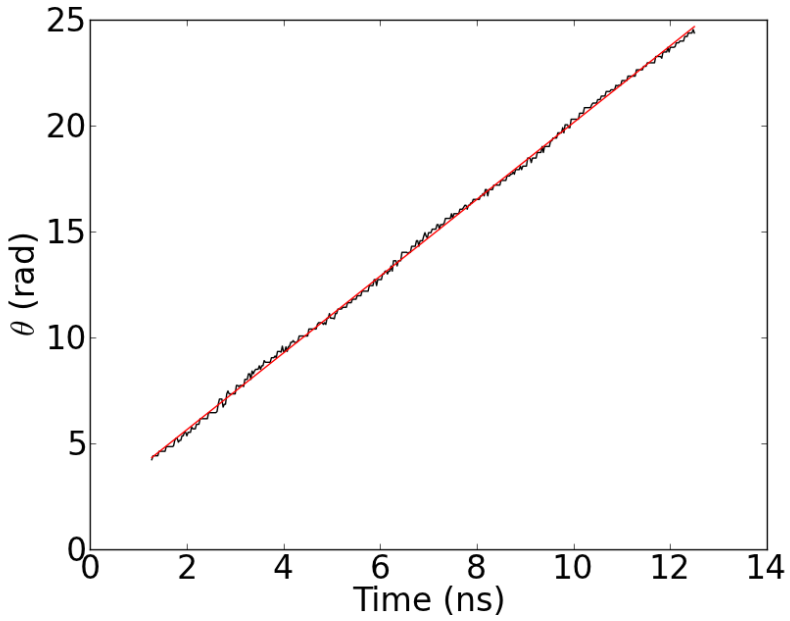

Fig. 6.14 Plot of core displacement in radians as a function of time. The black line represents core displacement in a 500nm FeGa square with low damping and no strain induced anisotropy when excited with a 5mT pulse. The red line represents a linear fit to the data used to extract the core's angular velocity, $\dot{\theta}$ in rad/s.

This value is then multiplied by the core's radius at a particular point in order to find the velocity of the core at that particular time, $\dot{S}$ as demonstrated by equation 6.2

$$\dot{S} = r \cdot \dot{\theta} \tag{6.2}$$

A flip in the core's chirality not only leads to a drop in the area which the core describes but also leads to a change in the direction of the core's movement as can be seen in figure 6.15 which shows the core's velocity $\dot{\theta}$ as a function of the amplitude of the magnetic field pulse with the core's polarisation after the magnetic field pulse being shown in blue for negative polarisation and red for positive polarisation.

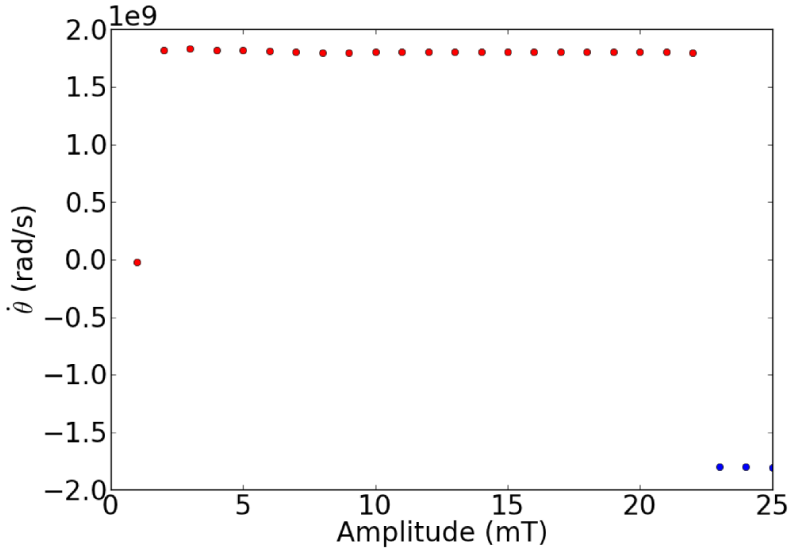

Fig. 6.15 Plot of $\dot{\theta}$ as a function of the amplitude of the exciting pulse for a 500nm square. The colour of the dots indicates the polarisation of the core with red dots indicating the core has positive polarisation at the end of the simulation and blue dots indicating a negative polarisation. Error bars are smaller than the markers.

In figure 6.15 we can see that the direction of the core's movement is directly tied to its polarisation in agreement with reference [31]. The values of $\dot{\theta}$ when the pulse amplitude is below 2mT are unreliable since the movement in the core is too small to gain a good measure of θ. When the core's movement becomes large enough for a reasonable measurement of its velocity we see that $\dot{\theta}$ remains constant regardless of the pulse amplitude or even direction of motion as the core oscillates at its resonant frequency which is dependent on the properties of the material and not the amplitude of the exciting pulse. This can be seen in equation 2.34 which describes the frequency of oscillation of the core as a function of the saturation magnetisation, the gyromagnetic ratio and the magnetic susceptibility with no dependence on the driving force. The value of $\dot{S}$ for the core as a function of amplitude was therefore investigated and it was found that the velocity of the core closely matches the behaviour of the amplitude of the core's oscillation as demonstrated in figure 6.16. $\dot{S}$ was found by taking the values of $\dot{\theta}$ shown in figure 6.15 and then multiplying this value by the radius of the orbit in accordance with equation 6.2. The final value of $\dot{S}$ was found as the mean value of $\dot{S}$ across the simulation by multiplying the value of $\dot{\theta}$ by r, the distance from the core to the center of the simulation, at each point in the simulation and then finding the mean of this value. The standard deviation of this value was used as the error in the result.

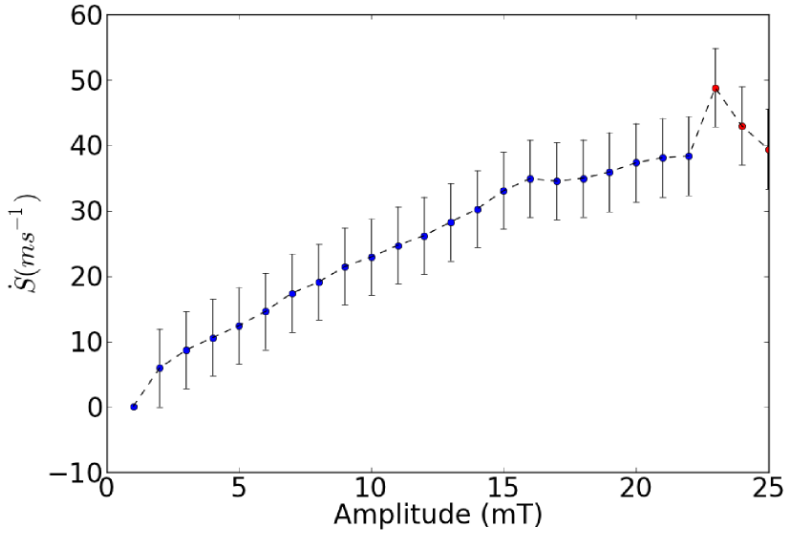

Fig. 6.16 Plot of the average value of $\dot{S}$ as a function of the amplitude of the exciting pulse for a 500nm square. The blue dots indicate that the polarisation of the core remained constant throughout the simulation whereas the red dots indicate that the core's polarisation reversed when a field was applied.

The core's velocity rises steadily as the amplitude of the exciting magnetic field pulse increases until the core switching event takes place at which point there is a sharp rise in the core velocity before it begins to fall. Studying the behaviour of the core with simulations with higher time resolution may reveal why it is that the core appears to gain speed when the field required to induce vortex core switching is only slightly exceeded but begins to drop as the magnetic field continues to increase. This behaviour is most likely due to the system exhibiting non-linear behaviour similar to that observed in a 2000nm square in section 6.6. The core's maximum velocity is reached immediately after it is excited by the magnetic field pulse. Using equation 2.32 and taking the value of η for iron, 1.72 ± 0.09, a critical velocity of $358\pm19\text{ms}^{-1}$ for the simulation can be found. When a switching event occurs this critical velocity is exceeded during the initial displacement of the core. It should be noted that the value of η used for this calculation is the value found for iron and not galfenol. The values for $\dot{S}$ shown in figure 6.16 are lowe than the critical velocity as would be expected for steady procession.

The effect of the amplitude of the magnetic field pulse on the frequency of the oscillation is shown in figure 6.17. This examines the one dimensional frequency profiles of the samples with zero strain induced anisotropy and various amplitudes of exciting field.

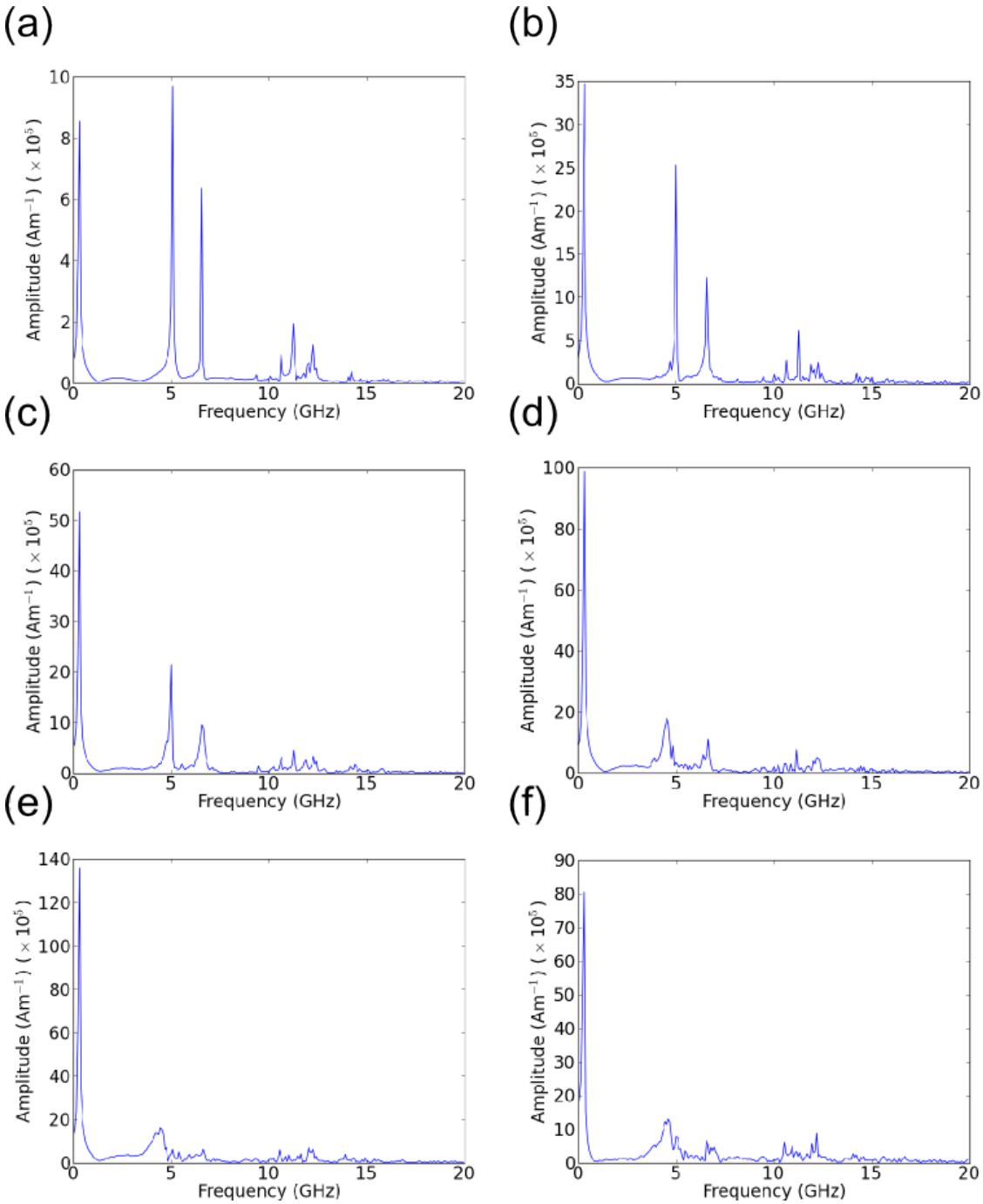

Fig. 6.17 M_x frequency analysis for a 500nm square with a)1mT, b) 4mT, c) 6mT, d) 12mT, e) 18mT and f)25mT magnitude magnetic field pulse applied to the sample.

Figure 6.17 demonstrates that the frequencies of the oscillations remain roughly constant with magnetic field pulse amplitude. However, the amplitude of the oscillations in the secondary modes appears to reduce compared to the amplitude of the primary mode as the amplitude of the exciting magnetic field pulse gets stronger.

As the amplitude of the magnetic field pulse increases we can make two observations. The first is that the amplitude of the primary mode increases as the amplitude of the magnetic field pulse increases, due to the increase in vortex core motion seen in figure 6.13. The primary mode is diminished when the pulse amplitude is 25mT in comparison to 18mT due to the reduction in the area described by the motion of the core, which can also be seen in figure 6.13. The second observation we make is linewidth broadening as the amplitude of the pulse increases and a increase in the amplitude of the primary mode as the amplitude of the exciting pulse increases. In order to examine how much the oscillation modes change as a function of the amplitude of the exciting field the frequencies of the primary and two secondary modes were plotted as a function of the pulse amplitude in figure 6.18.

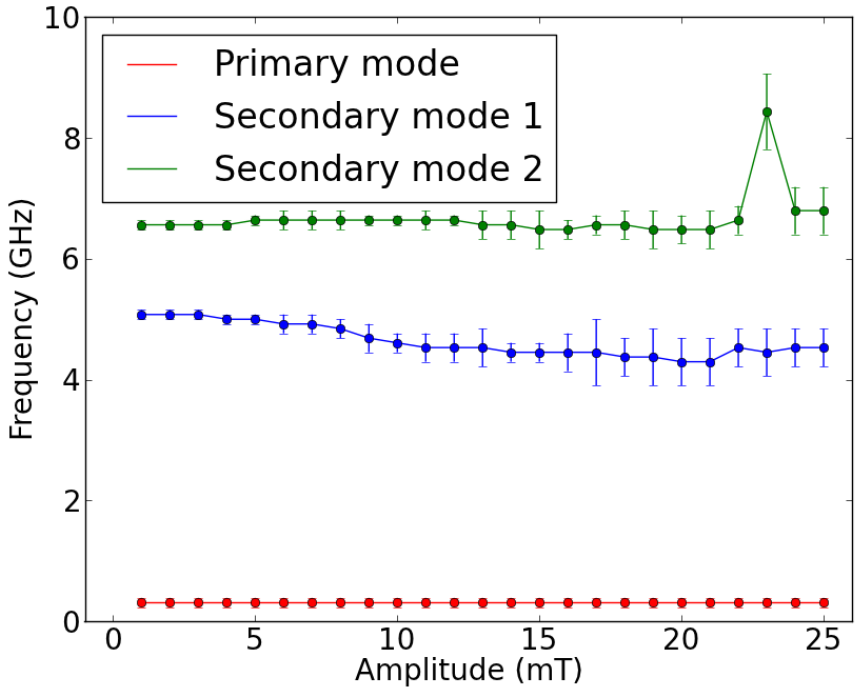

Fig. 6.18 Plot of the detected frequency modes found in the Fourier transform of the x component of the magnetisation of a 500nm square with the exciting magnetic field pulse set to various amplitudes. Shown in blue is the oscillation frequency of the primary mode with the secondary modes shown in green and blue.

The frequency of the primary oscillation, that of the core, remains constant regardless of the amplitude of the exciting field indicating as we would expect since the oscillation frequency of the core is dependant on the anisotropies of the material due to the effect of the magnetic anisotropies on the effective mass of the core, as shown in equations 2.33 and 2.34 and described in reference [111]. The errors in the measurement of the frequency of oscillation of the primary core are also very small being smaller than the markers used to denote them. The change in the secondary modes is also sufficiently small to be discounted as an effect of the large errors in the measurement. The frequency of oscillation of the second secondary mode at a pulse amplitude of 23mT differs from the frequency of oscillation of the second secondary modes at other amplitudes by more than the error in the measurement. This discrepancy is most likely due to the peak finding program incorrectly identifying the peak corresponding to this oscillatory mode. The peaks were found using the same standard peak finding program included in the scipy python library used to find the domain wall widths in section 6.1. Visual inspection yielded a value of 6.64 ± 0.04GHz however only the value found by the peak finding algorithm was plotted for the sake of consistency.

In order to investigate these secondary and tertiary modes the three dimensional time resolved frequency analysis program described in section 3.9 was used to produce the heat maps shown in figure 6.19 which show where in the sample the frequency modes manifest themselves when the sample was excited with a 1mT magnetic field pulse with no strain induced anisotropy.

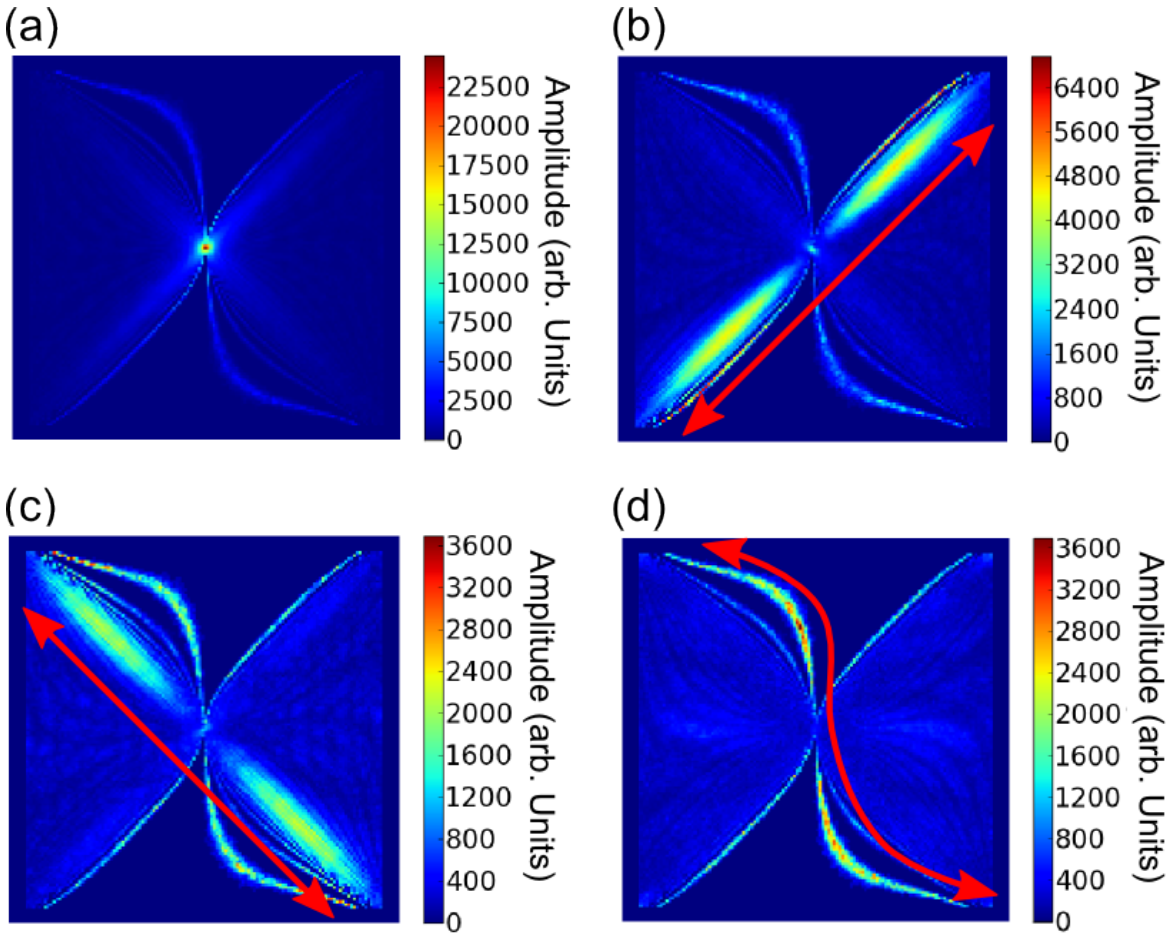

Fig. 6.19 Fourier transformation heat maps for the magnetisation of a 500nm square in the x direction when a magnetic field pulse of 1mT was used to excite the system. Shown are the heatmaps with windows of 200MHz and central frequencies of a) 300MHz, b)5GHz, c)6.5GHz and d)12.3GHz. The red arrows indicate the directions of the wavevectors of the detected modes.

The first critical observation that can be made from figure 6.19 is confirmation that the primary frequency mode is clearly the motion of the vortex core as shown in figure 6.19a). It can also be seen in figure 6.19 b) and 6.19 c) that the secondary modes take the form of standing waves oscillating along the domain walls of the flux closure state with stationary points at the corners of the sample and at the vortex core. This means the secondary modes resemble Damon-Eshbach modes due to their wavevectors being approximately 90^o to the direction of the magnetisation. This analysis offers an explanation as to why the secondary modes were both diminished and broadened at higher pulse amplitudes since the increased core motion means that the domain walls regions represent a less uniform effective field.

To put it another way the area over which the effective field is uniform reduces as the pulse amplitude increases. The result is a reduction in the amplitude and broadening of the features in the spectral response corresponding to these Damon-Eshbach like modes. These modes were described in detail in reference [104] where the frequency was described as being dependant on the length and shape of the domain wall. For these simulations, this would imply that the frequency will be dependant on the magnetic anisotropy which alters the shape for the domain walls, as observed in figure 6.1.

An interesting feature of the secondary modes is that there are two modes localised along different domain walls in figures 6.19b) and 6.19c). To investigate the origin of this observation the simulation of the 500nm square with zero strain induced anisotropy and a pulse amplitude of 1 mT was repeated with no intrinsic uniaxial anisotropy present along the [110] direction. This gave the one dimensional frequency profile for the x component of the magnetisation shown in figure 6.20.

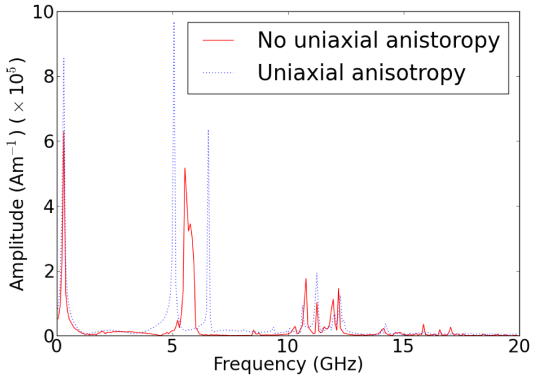

Fig. 6.20 Fourier transform profile for the x component of the magnetisation for a 500nm square with no uniaxial anisotropy in the [110] direction when subjected to a 1mT magnetic field pulse. Also shown for comparison is the Fourier transformation profile for the x component of the magnetisation in a 500nm square with uniaxial anisotropy present.

As we can see the frequency of oscillation of the domain walls merge when the uniaxial anisotropy is removed, an effect which is shown explicitly in figure 6.21 in which the standing waves can be clearly seen forming symmetrically within the same frequency window.

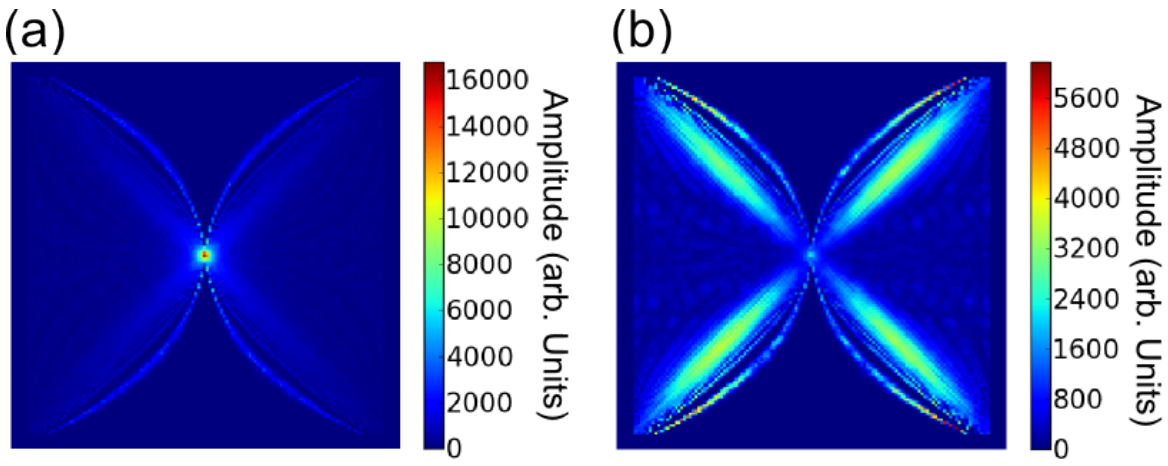

Fig. 6.21 Fourier transformation heat maps for the magnetisation of a 500nm square in the x direction when a magnetic field pulse of 1mT was used to excite the system. The uniaxial anisotropy along the [110] direction was set to zero for this simulation. Shown are the heatmaps with windows of 200MHz and central frequencies of a) 300MHz and b)5.7GHz.

We can see that removing the uniaxial anisotropy removes the asymmetry from the frequency of oscillation of the domain walls. This indicates that the asymmetry is a result of the uniaxial anisotropy altering the effective field along the domain walls. This is consistent with the findings in references [104] and [111] in which it was shown that the core oscillation frequency and domain wall frequencies are dependant on the anisotropies of the system.

In order to check for further asymmetries due to the direction of the magnetisation being studied, the direction of the incoming magnetic field pulse and the chirality of the magnetic vortex, a number of simulations were performed. None of these results showed any significant change in the frequency modes within the objects studied, as can be seen in appendix D.

In order to check that the amplitude of the exciting field pulse had no effect on the positions of the secondary modes we also did a 3D Fourier transformation of the x component of the magnetisation in a sample which was excited with a 25mT magnetic pulse, the results of which are shown in figure 6.22.

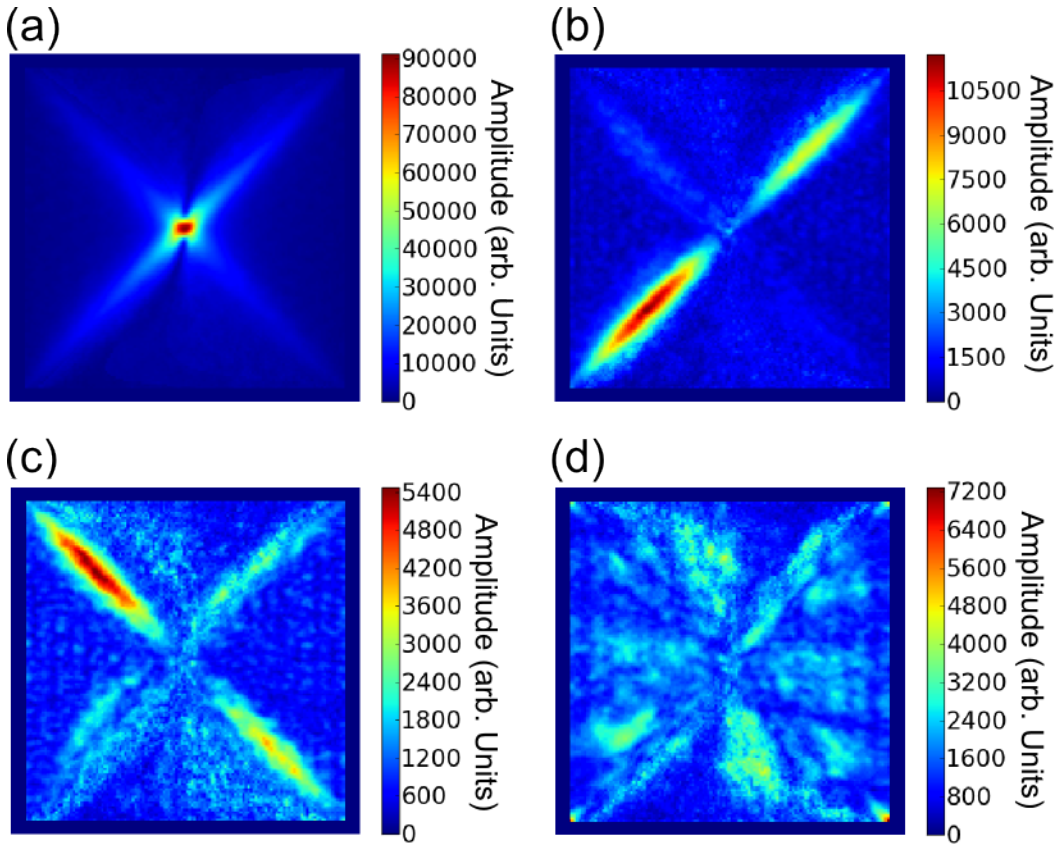

Fig. 6.22 Fourier transformation heat maps for the magnetisation of a 500nm square in the x direction when a pulse of 25mT was used to excite the system. Shown are the heatmaps with windows of 200MHz and central frequencies of a) 300MHz, b) 5GHz, c) 6.5GHz and d) 12.3GHz.

The domain walls oscillate at the same frequency however the reduction in the intensity of the oscillations leads to a greater noise level in the spatial Fourier map. The domain wall modes still occur in the same space however which indicates that the domain wall oscillation modes do not change position as a consequence of the increased vortex core movement. Also worth noting is the asymmetry in the domain wall modes. It is unclear why this asymmetry occurs since the system is symmetrical along the domain walls however it may be a result of direction of the exciting magnetic field pulse. This may be investigated further by repeating the tests for symmetry in figures D.3, D.4 and D.6 with a higher amplitude of exciting magnetic field pulse. The map centred around 12.3GHz shows an absence of the tertiary modes which were observed in figure 6.19. This indicates that the effective field in the areas of uniform magnetisation is not sufficiently uniform to allow for tertiary modes to form once the motion of the core becomes too large.

6.3 Effect of strain induced anisotropy on core movement

The effect of a strain induced anisotropy on the orbit of the vortex core was then studied by repeating the simulation with strain induced anisotropies of 0kJm^{-3}, 10kJm^{-3}, 20kJm^{-3}, 30kJm^{-3} and 40kJm^{-3}. These amplitudes of strain induced anisotropy were chosen since they were believed to slightly exceed the achievable range of strain induced anisotropies using a piezoelectric transducer. The amplitudes of the pulses used were the same as before. In order to demonstrate the effect of the strain induced anisotropy core tracking was performed on a 500nm square with 40kJm^{-3} of strain induced anisotropy applied in the [010] axis, corresponding to the y-direction in the simulation, and the results are shown in figure 6.23.

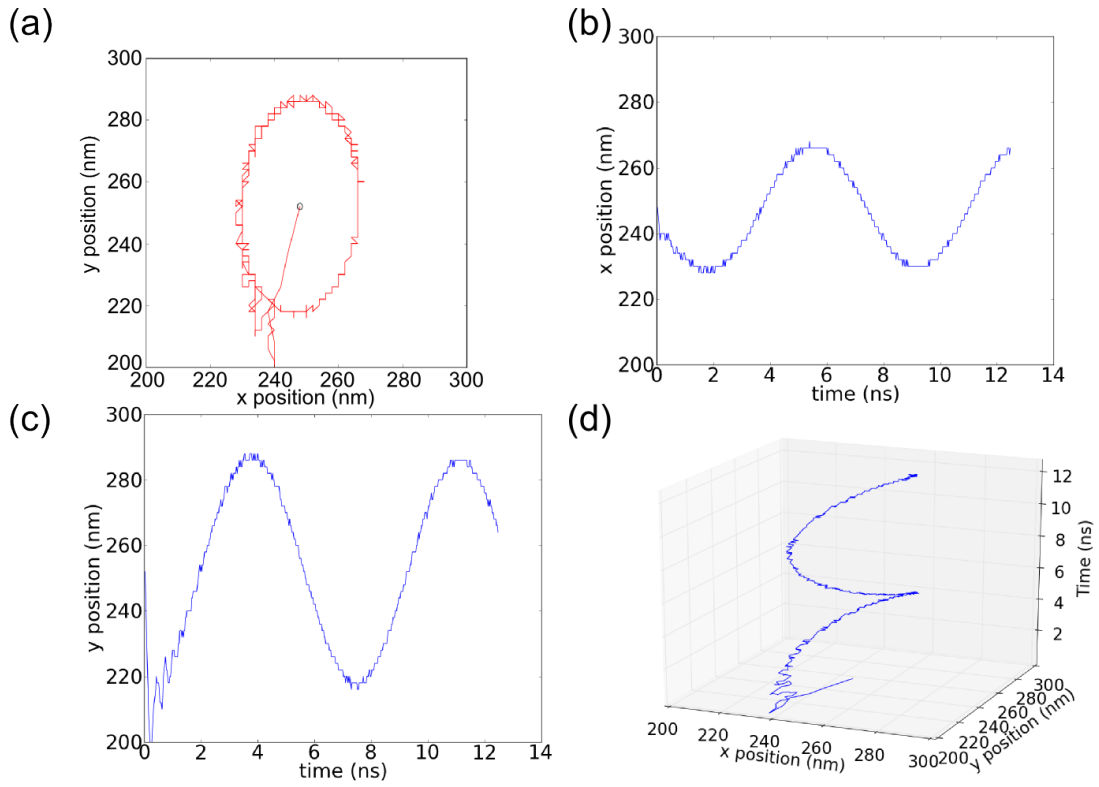

Fig. 6.23 Tracking results for a 500nm sample with 40kJm^{-3} of strain induced anisotropy applied to the sample and a 25mT magnitude magnetic field pulse was used to excite core movement. In a) we can see a phase diagram of the core's movement with the starting position of the core being indicated by the black circle at (250, 250), in b) we can see the core's position as a function of time and in c) we can see the core's position in y as a function of time. Finally, in d) the core's position in x and y is shown as a function of time in a 3D line plot.

Comparing the results shown in figure 6.23 with those shown in figure 6.9 we see that the strain induced anisotropy alters the trajectory of the core causing it to precess in an elliptical manner as opposed to the circle described without the strain induced anisotropy. This eccentricity was investigated by measuring the movement of the core as a function of the strain induced anisotropy in a method similar to that used in reference [21]. Figure 6.24 shows the eccentricity of the ellipse described by the vortex cores' movement as a function of the strain induced anisotropy.

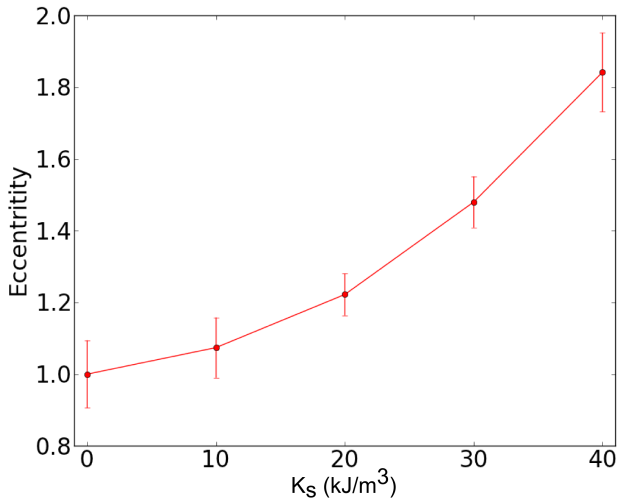

Fig. 6.24 Eccentricity (y radius/x radius) vs strain induced anisotropy for magnetic vortex core rotations in a 500nm square excited by a 22mT magnetic pulse. Error bars are determined from the width of the vortex core.

Figure 6.24 shows the eccentricity of the orbit of the vortex core increasing as the strain induced anisotropy increases almost doubling the eccentricity of the orbit when 40kJ/m^3 of strain induced anisotropy is applied to the system. In order to understand why the strain induced anisotropy alters the eccentricity we must examine the effect of strain induced anisotropy on the frequency of oscillation of the vortex core. The effect of strain induced anisotropy on the frequency modes of the samples was then investigated by performing one dimensional frequency analysis on the x-component of the magnetisation as the simulation progressed once the system was excited with a 1mT pulse. The results of this can be seen in figure 6.25 which shows the frequency profiles for the 500nm sample with various levels of strain induced anisotropy being applied along the [010] direction.

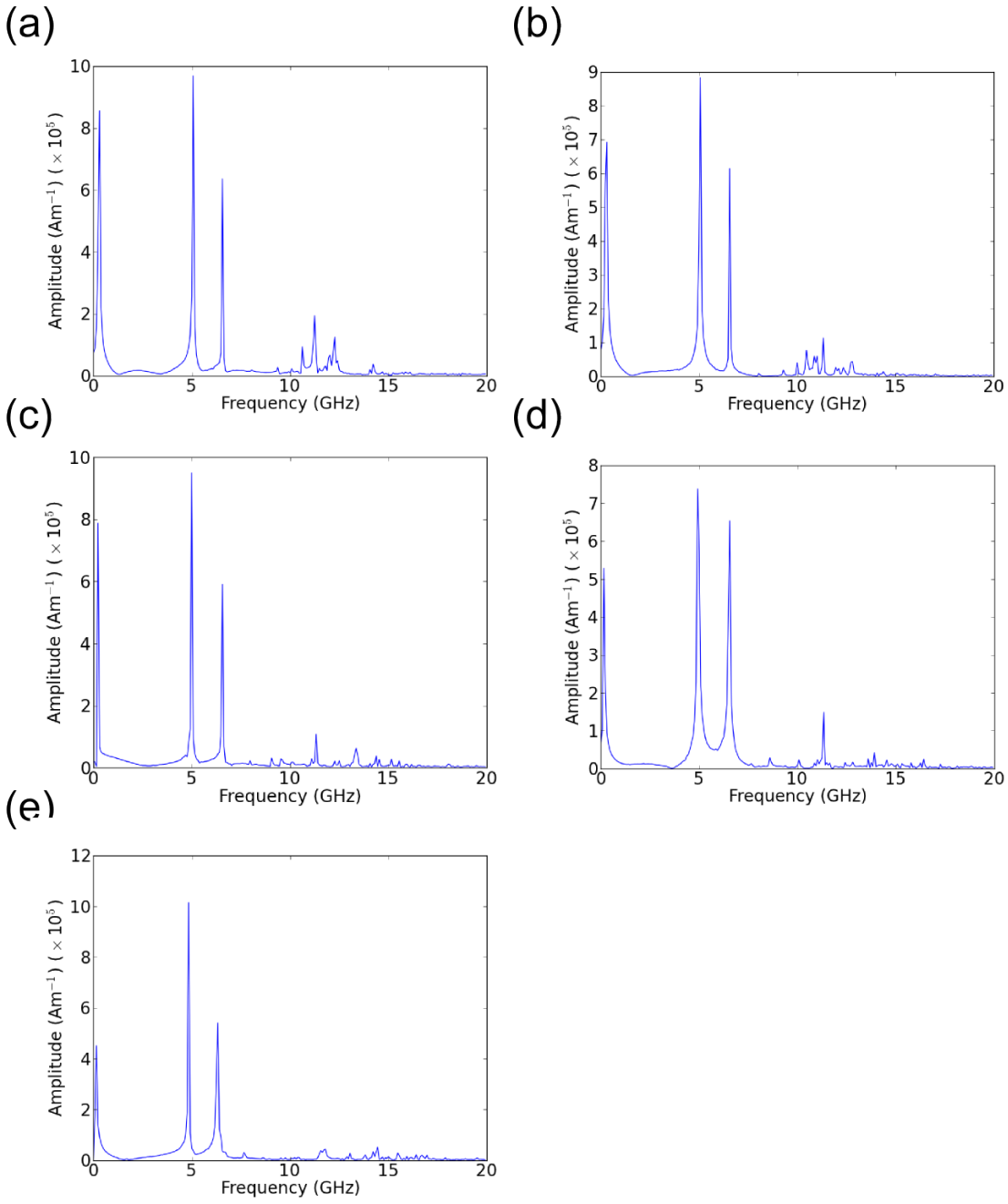

Fig. 6.25 Fourier transformation profiles for the magnetisation of a 500nm square in the x direction with a)0kJm^{-3}, b) 10kJm^{-3}, c)20kJm^{-3}, d)30kJm^{-3} and e)40kJm^{-3} once excited with a 1mT magnetic pulse.

Figure 6.25 shows that as the strain induced anisotropy increases the frequency of the resonant modes decreases and that the intensity of the secondary modes in relation to the primary modes increases. In order to understand the relative increase in the intensity of the secondary modes the shape of the modes must be investigated however first we shall investigate the change in the frequency of the modes as a function of the strain induced anisotropy.

The change in frequency as a function of strain induced anisotropy can be illustrated by plotting the frequency of oscillation of the core as a function of strain induced anisotropy as is shown in figure 6.26. The errors are the full widths at half maximum of the peaks in the frequency spectrum used to find the frequencies.

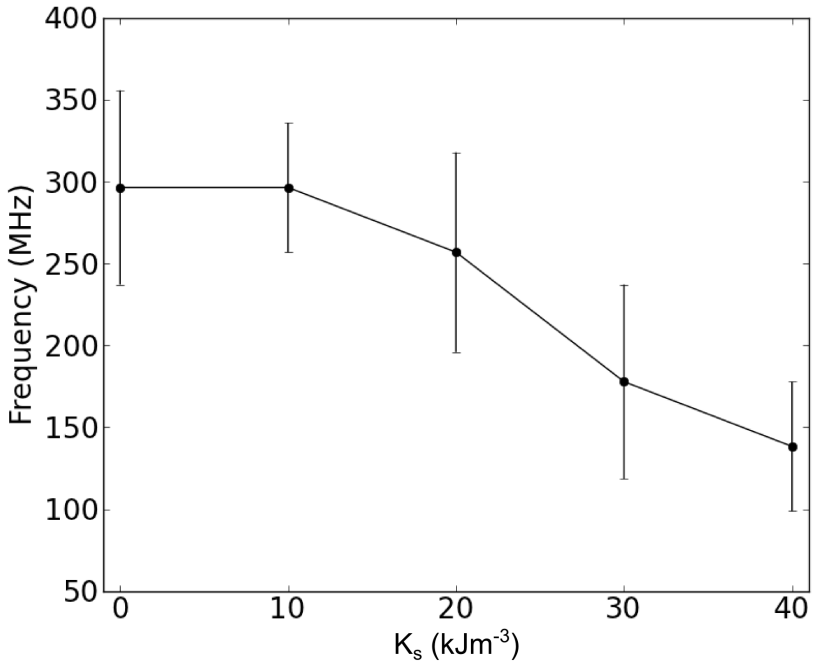

Fig. 6.26 Plot of the frequency found for the primary mode of oscillation from the Fourier transformation profiles shown in figure 6.25 as a function of the strain induced anisotropy.

This is as we would expect from equation 2.33 as applying a strain induced anisotropy alters the magnetic susceptibility of the sample in a particular direction, thereby altering the effective mass of the vortex core. This anisotropy in the susceptibility tensor also explains the increase in ellipticity as a function of strain induced anisotropy shown in figure 6.24.

The frequency of oscillation for the secondary modes as a function of strain induced anisotropy was extracted and is shown in figure 6.27.

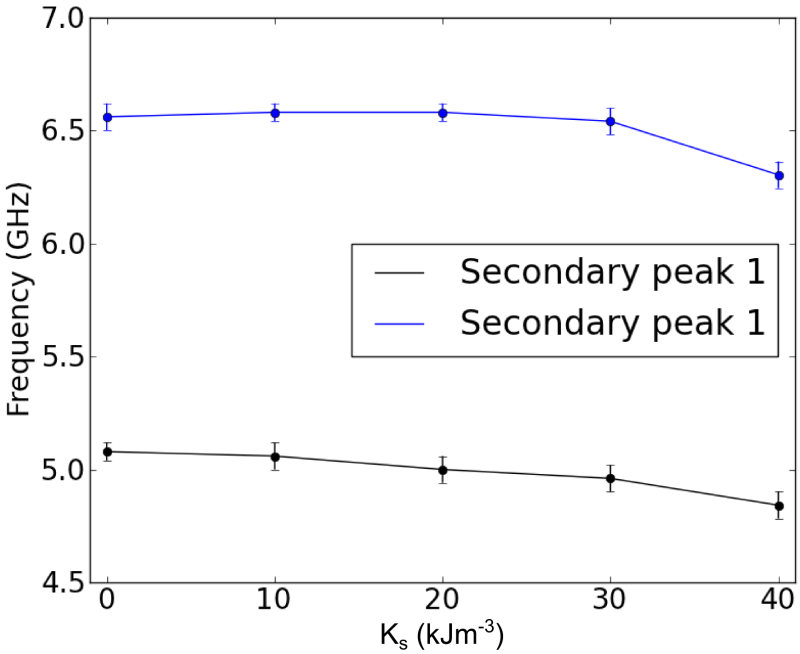

Fig. 6.27 Plot of the frequency found for the secondary modes of oscillation from the Fourier transformation profiles shown in figure 6.25 as a function of the strain induced anisotropy.

Figure 6.27 shows that the frequency of oscillation of the secondary modes is also reduced as the strain induced anisotropy increases. The change in frequency is roughly the same as the change in frequency in the primary mode meaning it represents a much lower percentage change in frequency.

To investigate this further the 3D Fourier transformation program was used on the simulations in order to produce heatmaps showing the location of the domain wall modes in the strained simulations for the 500nm square. The results of this are shown in figure 6.28.

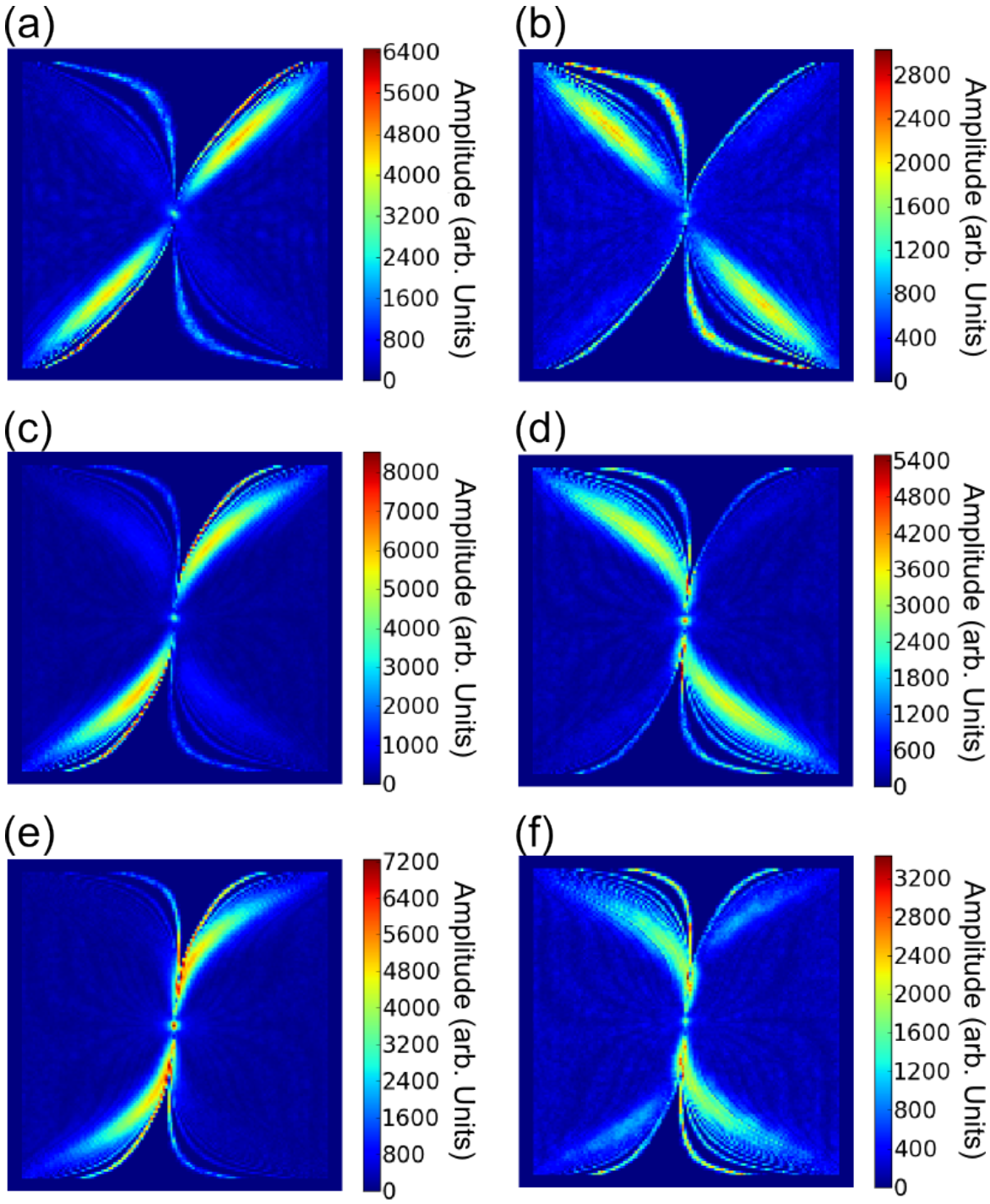

Fig. 6.28 Fourier transformation heat maps for 500nm square with various levels of strain induced anisotropy applied to the sample. The maps in a),c), e) and g) are centred around 5GHz while b), d), f) and h) are centred around 6.5GHz. The strain induced anisotropy on the samples in a),b) was 10kJm^{-3}, 30kJm^{-3} in c) and d) and 40kJm^{-3} in e) and f). The window in all of these images is 200MHz.

In figure 6.28 we can see that the secondary modes follow the distorted domain walls indicating that the standing waves which form on the domain walls remain regardless of the strain induced anisotropy. The shape of the secondary modes also indicates that the standing waves form with stationary points at the corners of the sample and at the central core even with a strain induced anisotropy present. The reduction in frequency of oscillation is most likely to be due to the distortion of the domain walls by the strain induced anisotropy, increasing the domain wall modes' length which reduces their frequency of oscillation as described in reference [104].

The effects of the strain induced anisotropy on the area of the ellipses described by the vortex core motion was then investigated by plotting the area described by the core motion as a function of the amplitude of the exciting field pulse, shown in figure 6.29. Also shown in figure 6.29 is whether or not the polarisation of the core was reversed by the application of the field pulse with a red dot indicating polarisation reversal and a blue dot indicating the lack thereof. The area described by the core motion was found by calculating the distance between the centre of the core and the centre of the simulation in each frame and then using that value to find the maximum and minimum radius of the ellipse described so that the area could be calculated.

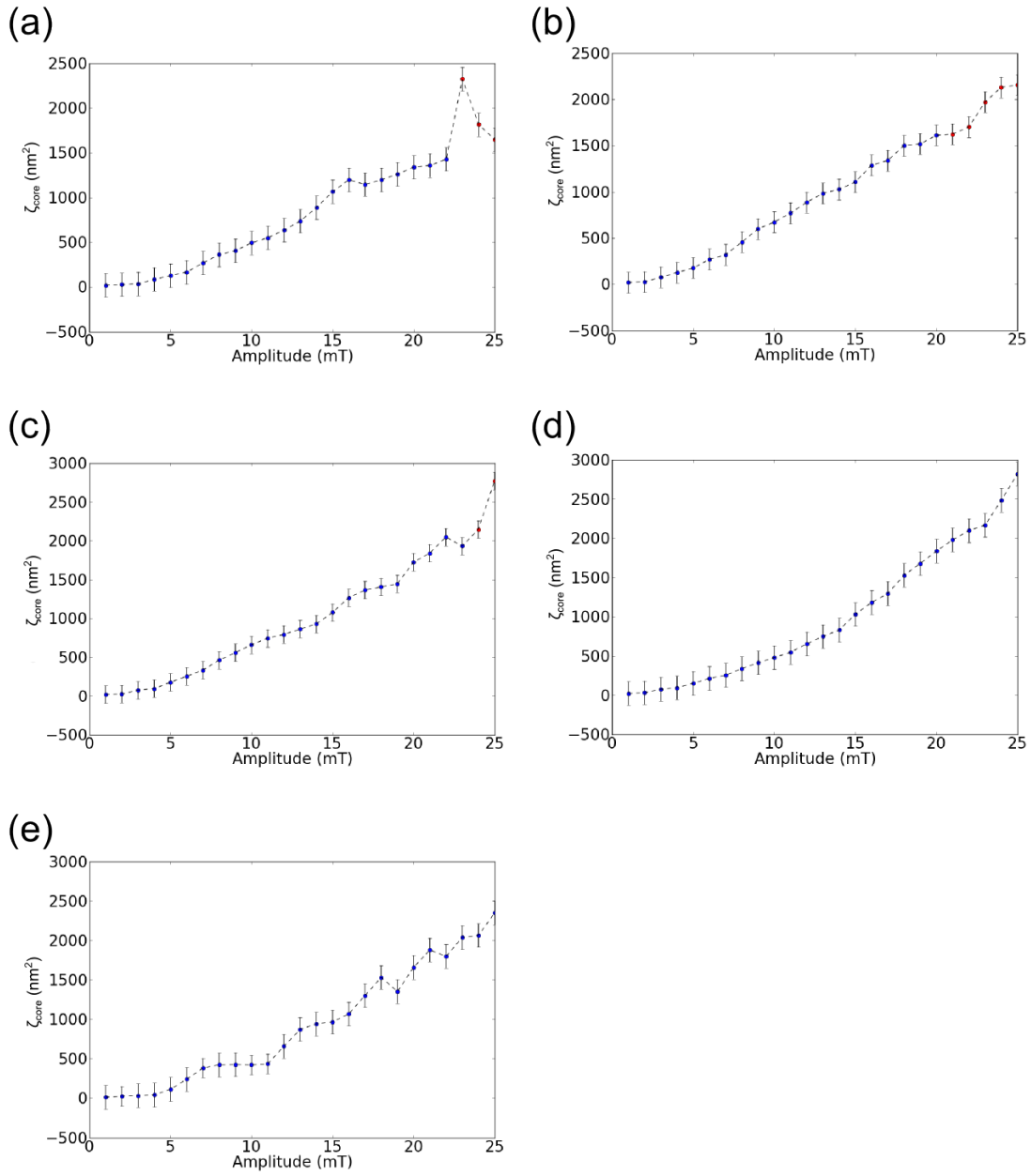

Fig. 6.29 Plots of the area described by core motion against amplitude of exciting pulse for a 500nm square at various levels of strain induced anisotropy. The strain induced anisotropies are a)0kJm^{-3}, b)10kJm^{-3}, c)20kJm^{-3}, d)30kJm^{-3} and e)40kJm^{-3}. The blue dots indicate that the polarisation of the core remained constant throughout the simulation whereas the red dots indicate that the core's polarisation reversed when a magnetic field pulse was applied.

In figure 6.29 it can be seen that once the amplitude of the magnetic field pulse is large enough to induce vortex core switching the area described by the core's motion does not immediately decrease. Indeed it can be seen that the area the core describes in b), when the sample experiences a strain induced anisotropy of 10kJm^{-3}, increases after the switching event. This strain anisotropy is of similar amplitude to the uniaxial and cubic anisotropies indicating that these anisotropies act to increase the switching field in the zero strain and that the presence of strain anisotropy along the [010] direction counteracts the effects of these anisotropies thereby reducing the switching field.

Figure 6.29 also indicates that the application of a strain induced anisotropy increases the amplitude of magnetic field pulse required to induce vortex core switching. Whilst the field required to induce switching seems to decrease when 10kJm^{-3} of strain induced anisotropy is applied compared to the case of no strain induced anisotropy the highest switching field is observed when 20kJm^{-3} of strain induced anisotropy is applied to the sample. At values of strain induced anisotropy of greater than 20kJm^{-3} the switching field is not observed within the range of pulse amplitudes from 1mT-25mT indicating that the switching field has exceeded 25mT.

Before investigating the relation between the switching field and the strain induced anisotropy further the effects of the strain induced anisotropy on the core's velocity are determined.

First it was determined whether or not the reversal in the polarisation of the core also resulted in a reversal of the direction in which the core propagated, as it did in the sample with no strain induced anisotropy. The plots in figure 6.30 show the dependence of $\dot{\theta}$ on the amplitude of the pulse applied to the sample. $\dot{\theta}$ being found by a linear line fit as described in section 6.2.

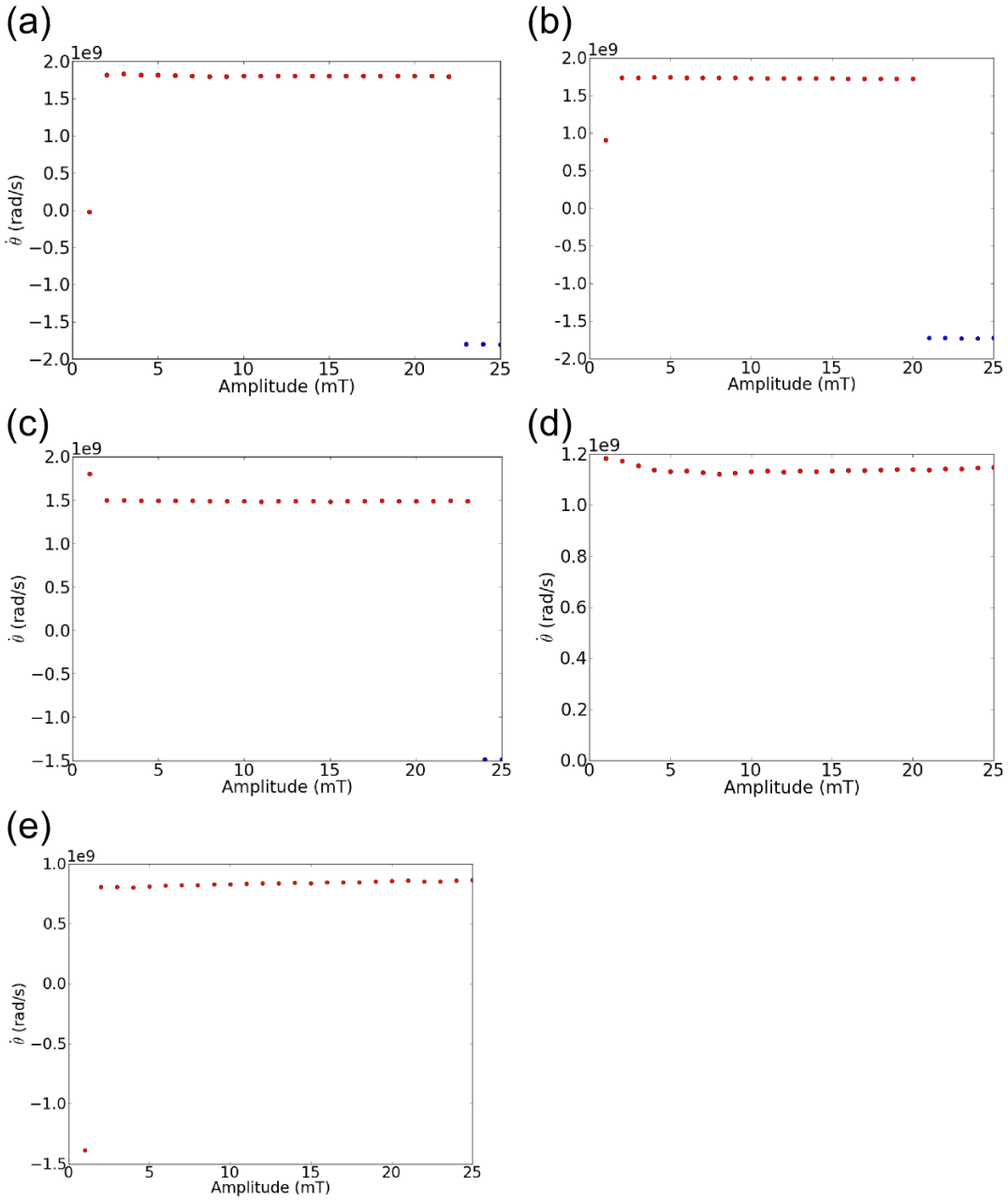

Fig. 6.30 Plots of $\dot{\theta}$ against amplitude of exciting pulse for a 500nm square at various levels of strain induced anisotropy. The strain induced anisotropies are a)0kJm^{-3}, b)10kJm^{-3}, c)20kJm^{-3}, d)30kJm^{-3} and e)40kJm^{-3}. The colour of the dots indicates the polarisation of the core at the end of the simulation with a red dot indicating a positive polarisation and a blue dot indicating a negative polarisation. The error bars in these plots are smaller than the markers.

In figure 6.30 a negative $\dot{\theta}$ indicates that the core moved in a clockwise motion and a positive $\dot{\theta}$ indicates that the core moved in an anti-clockwise motion. As can be seen from figure 6.30 the direction in which the core moves is dependant on its polarity, just as discussed in section 1.3 and seen when investigating the core's chirality as a function of its polarisation with no strain induced anisotropy. We also see that as the strain induced anisotropy increases the absolute value of $\dot{\theta}$ decreases due to the decrease in oscillation frequency observed in figure 6.26.

In order to investigate whether the strain induced anisotropy has an effect on the velocity of the core we next investigate the value of $\dot{S}$ as a function of amplitude in samples with various strain induced anisotropies as shown in figure 6.31. These were calculated in the same manner as the value of $\dot{S}$ in section 6.2, with the value of $\dot{\theta}$ being calculated from $\dot{\theta}$ and the value of r. This means that the value of $\dot{\theta}$ will vary as a function of time however for the purpose of this investigation this variation will be represented by the error in the measurement of the value of $\dot{S}$.

Figure 6.31 shows that the highest velocity which the core achieves during gyroscopic motion is found when 20kJm^{-3} of strain induced anisotropy was applied to the system. The core velocity increases as a function of the pulse amplitude however the results in the samples with greater strain induced anisotropy do not exhibit a higher mean core velocity than the samples with a lower strain induced anisotropy. This may be due to the eccentricity of the core orbits as demonstrated in figure 6.24 which cause the core to move at different velocities over the course of the simulation.

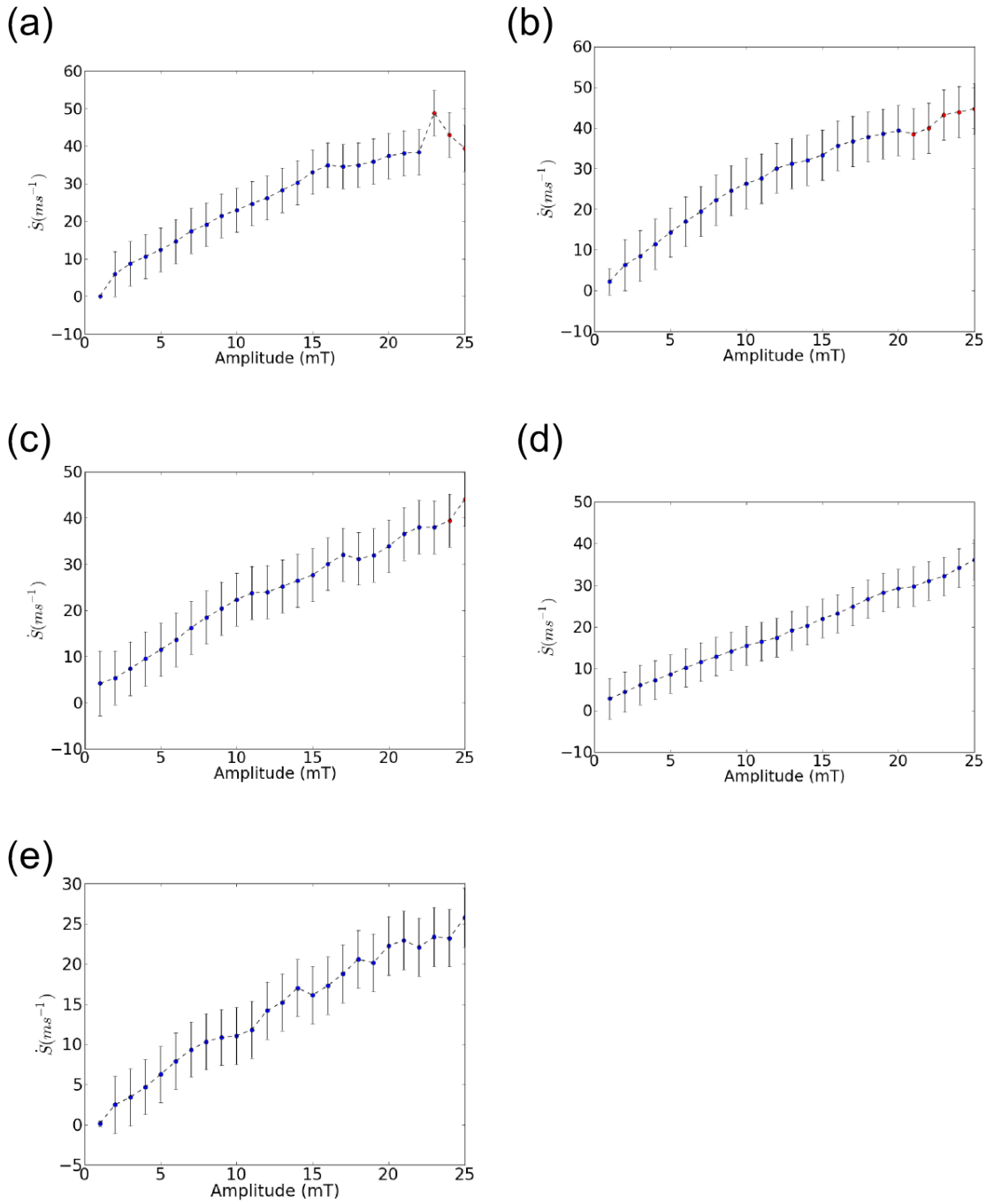

Fig. 6.31 Plots of the average value of $\dot{S}$ against amplitude of exciting pulse for a 500nm square at various levels of strain induced anisotropy. The strain induced anisotropies are a)0kJm^{-3}, b)10kJm^{-3}, c)20kJm^{-3}, d)30kJm^{-3} and e)40kJm^{-3}. The blue dots indicate that the polarisation of the core remained constant throughout the simulation whereas the red dots indicate that the core's polarisation reversed when a field was applied.

It can also be seen that as the strain induced anisotropy increases the switching field also increases. This increase in switching field as a function of strain induced anisotropy was investigated using a two step process.

The first step was to generate two ground states for the 500nm square with the vortex core having a positive polarisation in the first ground state and negative polarisation in the second. This was accomplished using a static 100mT magnetic field applied in the z-direction whilst the system settled into its ground state in order to force the vortex core to form with the desired polarisation.

The static magnetic field was then removed and these ground states were excited using a magnetic field pulse as before, however the simulation was only continued for 2.5ns rather than 12.5ns as used previously. This was done in order to save computation time in determining whether or not the vortex core would switch its polarisation due to the magnetic field pulse. If no switching event occurred the amplitude of the exciting magnetic field pulse was increased by 1mT and the simulation was repeated until the switching event was observed. The switching fields determined by these simulations are shown in figure 6.32.

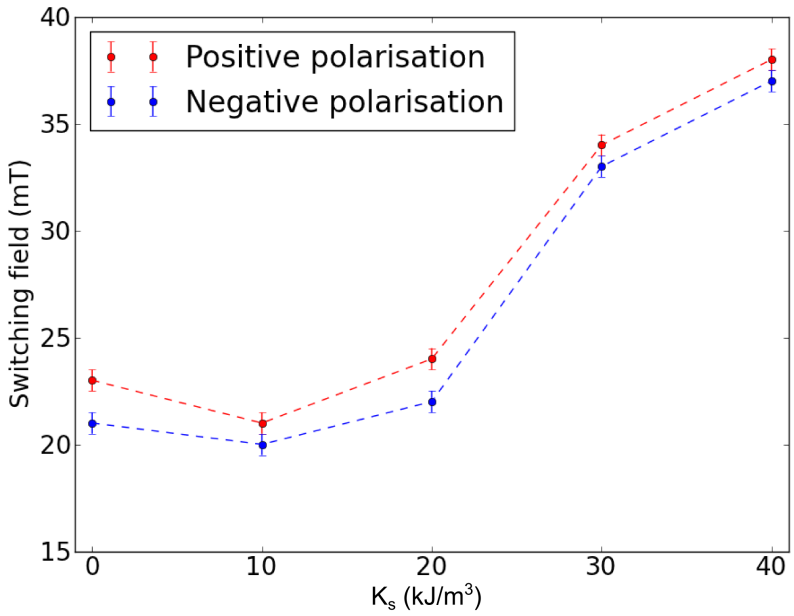

Fig. 6.32 Amplitude of magnetic field pulse required to induce vortex core switching as a function of the strain induced anisotropy when the magnetic field pulse was applied in the [010] direction, parallel to the strain induced anisotropy.

Figure 6.32 shows switching field increases as a function of strain induced anisotropy indicating that vortex core switching may be retarded using a strain induced anisotropy. Figure 6.32 also shows that the switching field for cores with negative and positive polarisation follow the same trend as a function of the strain induced anisotropy with the variation between the two switching fields never differing by more than 2mT. The switching field also appears to decrease when 10kJm^{-3} of strain induced anisotropy is applied to the system however indicating that a small strain induced anisotropy may help to reduce the switching field when it acts to counteract the effects of the material magnetic anisotropies. Further investigations may focus on the 0-20kJm^{-3} range of strain induced anisotropy in order to fully understand this effect. Since the uniaxial anisotropy is at 45^o to the strain anisotropy the largest reduction in switching field may be expected at $\sim$8.7kJm^{-3} due to the component of the uniaxial anisotropy in the direction of the vortex core's movement being equal to that of the strain induced anisotropy.

In order to investigate whether the angle between the magnetic field pulse and the strain induced anisotropy had an effect on the switching field the effect of applying the field pulse in the [100] direction was investigated. The results of this investigation are shown in figure 6.33.

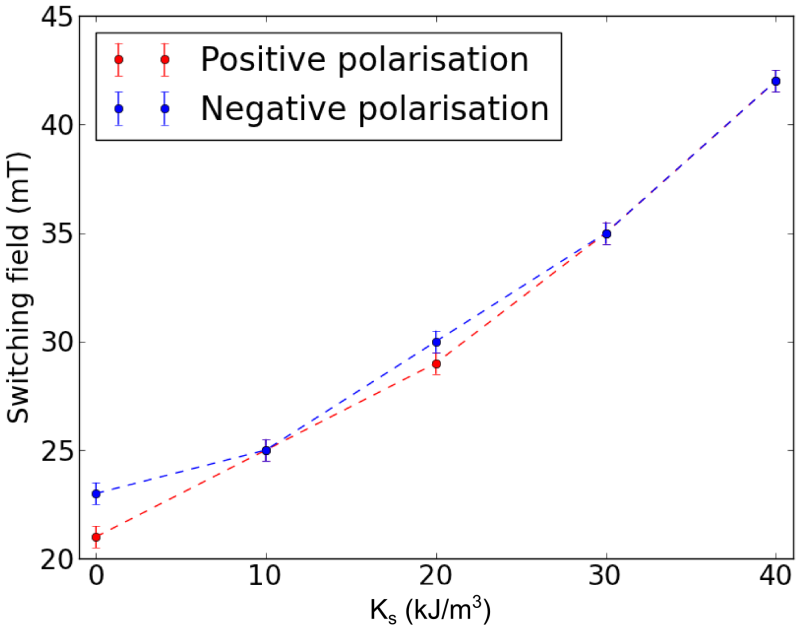

Fig. 6.33 Amplitude of magnetic field pulse required to induce vortex core switching as a function of the strain induced anisotropy when the magnetic field pulse was applied in the [100] direction.

Figure 6.33 shows that when the field was applied perpendicular to the strain induced anisotropy the switching field consistently increased as the strain induced anisotropy increased, the switching field was also consistently larger than when the magnetic field pulse was applied in the [010] direction. The lack of a drop in the switching field when the strain induced anisotropy is at 10kJm^{-3} is unexpected as the uniaxial anisotropy is at 45^{o} to both the magnetic field pulse and the strain induced anisotropy. The effect of varying the amplitude and direction of the uniaxial anisotropy on the switching field may therefore be an interesting avenue for further investigation.

The effect of the strain induced anisotropy on the vortex core switching field and its dependence on the angle between the strain induced anisotropy and the applied magnetic field pulse may be understood by examination of the switching requirements for the vortex core. The polarisation of the vortex core will flip when the vortex core's velocity has exceeded its critical velocity [31], as described in section 2.11. In these simulations this occurs due to the velocities reached by the core during its initial displacement due to the force of the magnetic field pulse. A larger magnetic field pulse causes the initial displacement to increase and therefore the core's velocity during this displacement to increase. The strain induced anisotropy alters the magnetic susceptibility of the material in a specific direction and therefore the cores effective mass in that direction as described in equation 2.33. This is why the vortex core's switching field is altered by the presence of the strain induced anisotropy which alters the velocities reached by the vortex cores during their initial displacements. This theory also explains the variation in the switching field when the angle between the strain induced anisotropy and the magnetic field pulse is altered.

The reasons for this variation in switching field could be confirmed with simulations of the switching events with much higher time and spatial resolution so that more information could be collected on the formation of an anti-vortex in the presence of a strain induced anisotropy. It may also be interesting to reproduce these results experimentally using a waveguide arrangement similar to that used in chapter 5 however the polarisation of the vortex core may be studied using MFM rather than using XMCD PEEM since only the z-component of the magnetisation of the sample would need to be measured and there is no need for a time resolved measurement.

6.4 Effect of shape anisotropy on oscillation

The effects of strain induced anisotropy on the magnetisation dynamics in square objects with widths of 1000nm, 1500nm and 2000nm was studied. In these samples we saw that the strain anisotropy had a much larger effect on the magnetic configurations of the ground state

of the samples as demonstrated in section 6.1. We therefore decided to first look at the effects of size on the frequency profiles of the samples. Shown in figure 6.34 are frequency profiles for the x component of the magnetisation in the 500nm, 1000nm, 1500nm and 2000nm simulations all with a pulse amplitude of 1mT and no strain induced anisotropy.

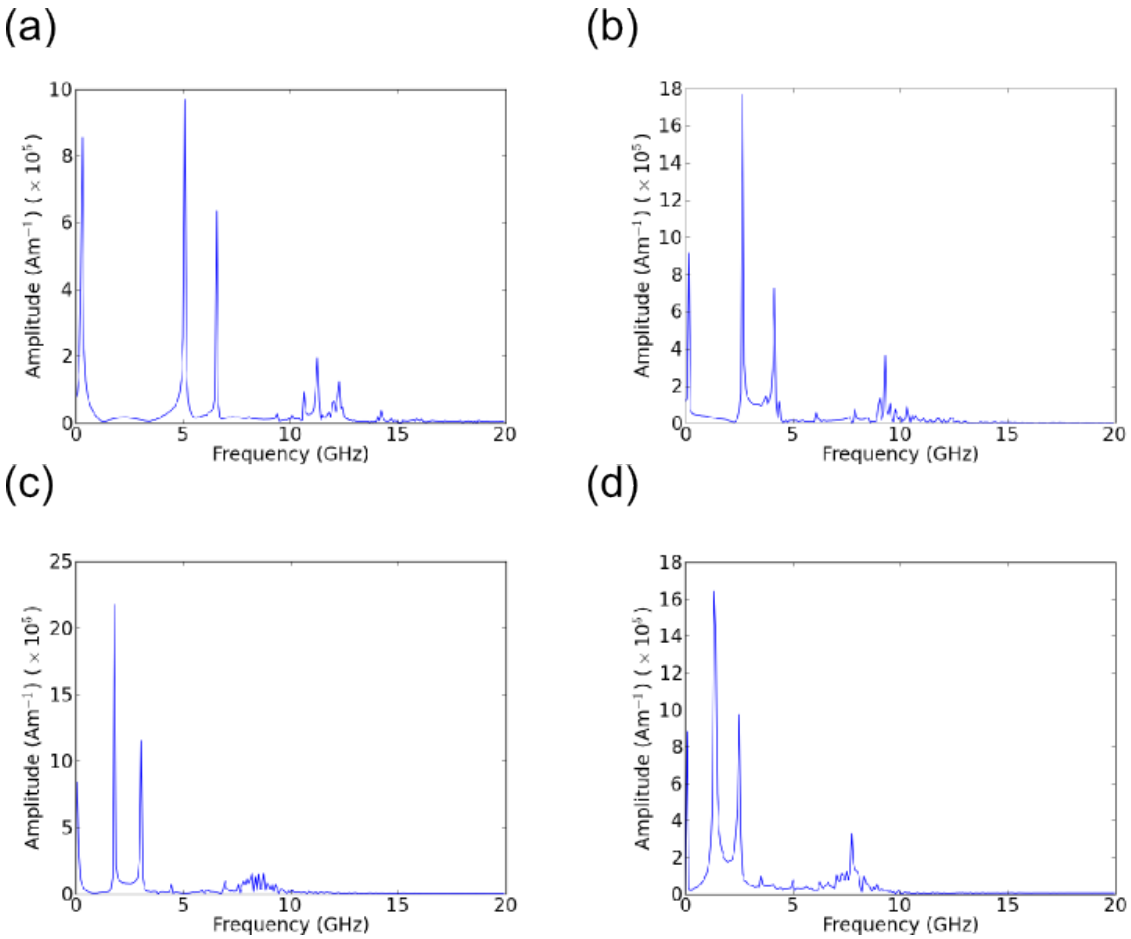

Fig. 6.34 Fourier transformation profiles for the magnetisation of squares of various sizes in the x direction. The squares were a)500nm, b)1000nm, c)1500nm and d)2000nm and were excited with a 1mT magnetic pulse.

Figure 6.34 shows that as the size of the objects increases the frequency of the resonant modes decreases, with the distance between the primary and secondary modes decreasing and the frequency spacing between the secondary modes remaining roughly constant. In order to investigate this relation further the frequencies of the primary and secondary modes were extracted from the frequency profiles shown in figure 6.34. The primary mode frequencies are shown in figure 6.35.

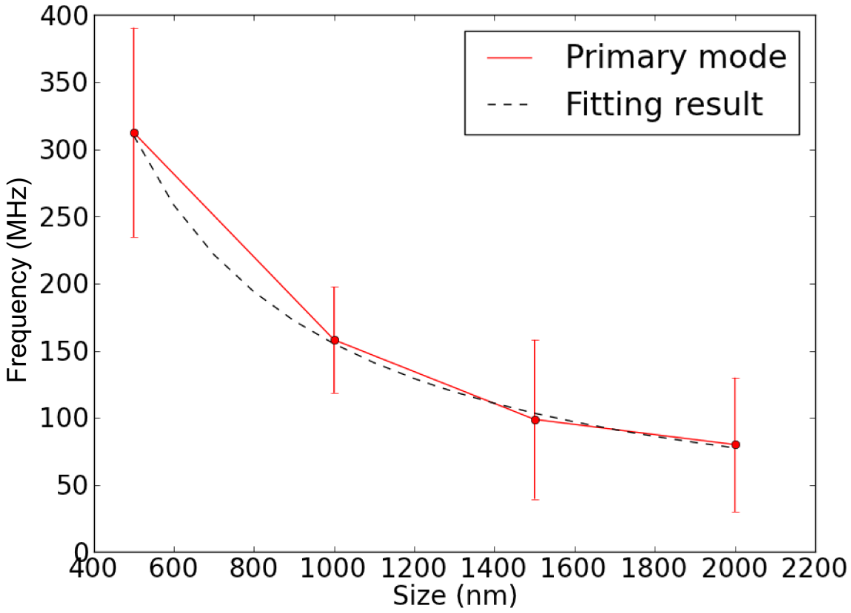

Fig. 6.35 Plot of the frequency found for the primary mode of oscillation from the Fourier transformation profiles shown in figure 6.34 as a function of the object's size. The fit to this data is shown as a black dotted line.

Figure 6.35 shows that the oscillation frequency of the central core decreases as the size of the structure increases. Indeed the oscillation frequency for the central core of the 2000nm sample is so low that the core does not complete a full oscillation within the 500 frames of the simulation and the frequency had to be calculated using the time taken for the core to complete half an oscillation. The frequency of oscillation of the primary core is inversely proportional to the size of the square as expected due to the directly proportional relationship between objects size and magnetic susceptibility [111]. This is demonstrated by the black dotted line in figure 6.35 which demonstrates fitting to the data yielding a constant of proportionality of 155.1 ± 4.4 Hz/m.

Examining the frequency at which the secondary modes oscillate in the samples we again see a similar relation as shown in figure 6.36 which also shows the fitting to the data as black dotted lines. As before the errors are found using the full width at half maximum of the peaks in the frequency spectrum.

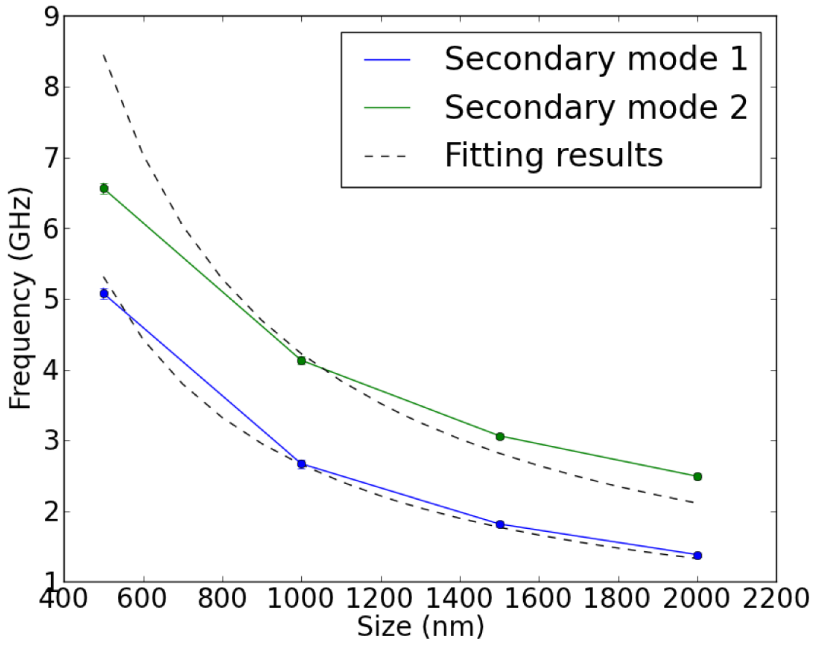

Fig. 6.36 Plot of the frequency found for the secondary modes of oscillation from the Fourier transformation profiles shown in figure 6.34 as a function of the object's size. The error bars in this plot are typically smaller than the markers. The fits to these data are shown as black dotted lines.

Figure 6.36 shows that the frequency of oscillation decreases as a function of size in the secondary oscillations similar to the effect seen in the primary oscillations. The results of fitting to these curves give constants of 2657.5 $\pm$ 78.8 Hz/m for the lower frequency modes and 4225 $\pm$ 550 Hz/m for the higher frequency modes. The large errors in these values indicate that the model of inverse proportionality begins to break down when applied to the higher frequency domain wall modes, possibly due to the effects of the cubic and uniaxial anisotropies dominating over the shape anisotropy in larger objects. The frequency splitting between these two modes is due to the uniaxial anisotropy as previously discussed. This explains why it remains constant regardless of the object's size.

In order to investigate this relationship further Fourier transformation maps were produced for the samples with no strain induced anisotropy when excited with a 1mT pulse. The first sample to be examined in this manner was the 1000nm square. The resulting heat maps are shown in figure 6.37.

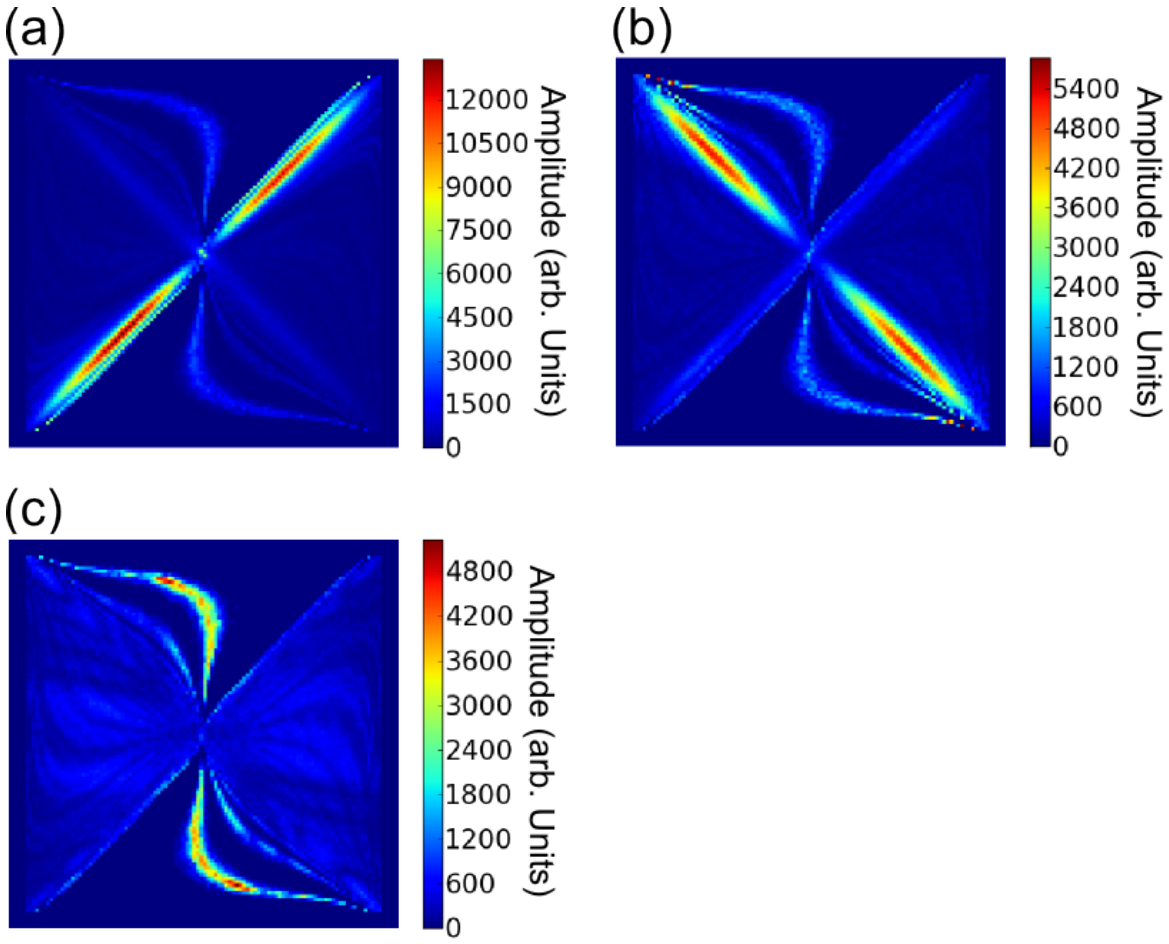

Fig. 6.37 Fourier transformation heat maps for the magnetisation of a 1000nm square in the x direction when a pulse of 1mT was used to excite the system. Shown are heatmaps with windows of 200MHz and central frequencies of a)2.67GHz, b)4.13GHz, c)9.313GHz.

The heatmaps shown in figure 6.37 demonstrate that the secondary modes do indeed continue to form along the domain walls however it also shows the s waves which form in the regions of uniform magnetisation form further away from the domain walls. This may be due to the larger size of the square leading to less confinement of the s-wave meaning it forms with a larger k value.

Also visible in figure 6.37 is an asymmetry in the width of the modes lying along the domain walls with the mode lying parallel to the uniaxial anisotropy being wider than that perpendicular to the uniaxial anisotropy.

In order to see if the wavevector of the s wave continues to increase when the size is increased further heatmaps were produced showing the secondary and tertiary modes for the 1500nm square. These heatmaps are shown in figure 6.38.

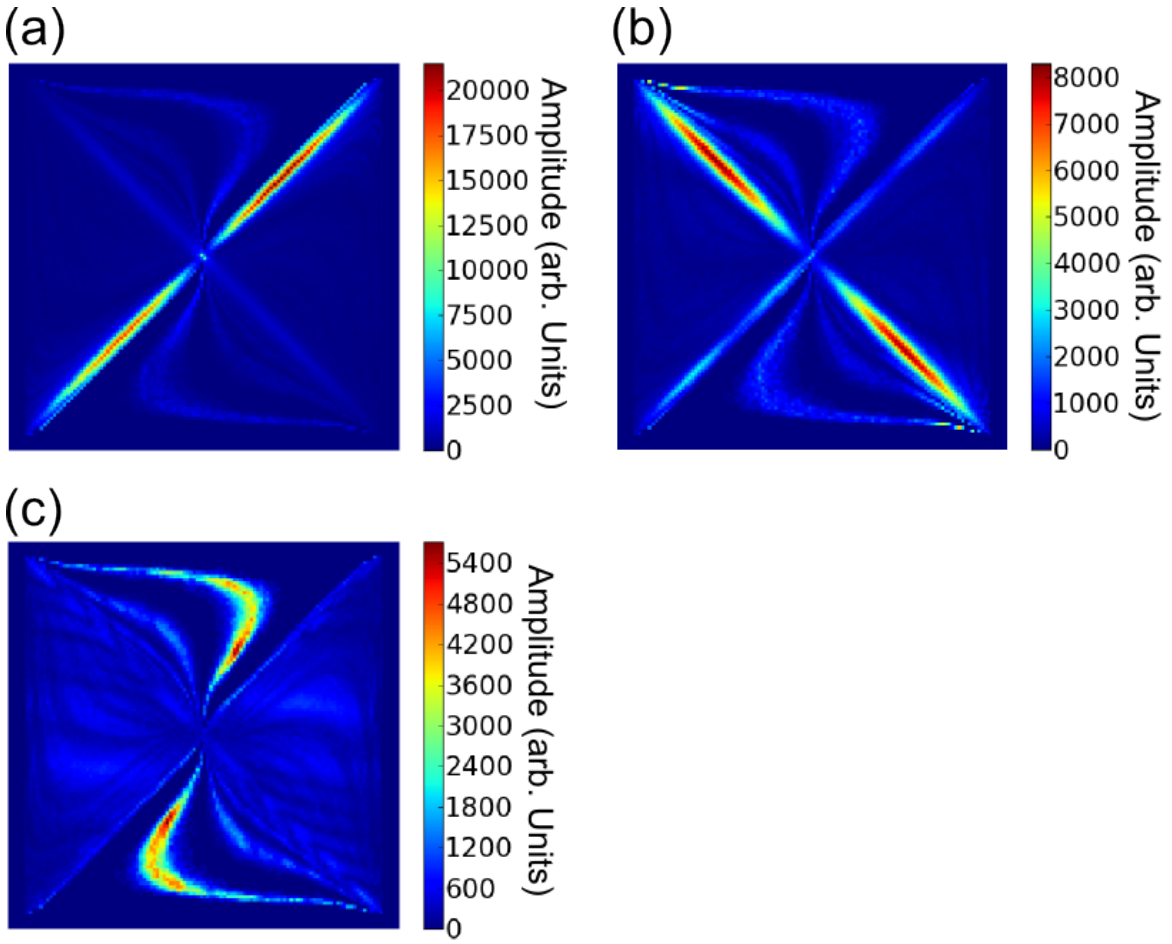

Fig. 6.38 Fourier transformation heat maps for the magnetisation of a 1500nm square in the x direction when a pulse of 1mT was used to excite the system. Shown are heatmaps with windows of 200MHz and central frequencies of a)1.80GHz, b)3.05GHz, c)8.27GHz.

Figure 6.38 shows that the wave vector of the s wave has increased again in response to the increase in available space for the modes to exist within the sample. Once again there is visible asymmetry in the width of the domain modes lying parallel and perpendicular to the uniaxial anisotropy. Finally, we perform a Fourier transform analysis of the 2000nm square shown in figure 6.39.

In figures 6.39a) and b) we can see that the domain wall spin waves form as before however in c) a domain wall mode can be seen perpendicular to the uniaxial anisotropy forming with an additional stationary point halfway between the edge of the sample and the vortex core. This represents a n=2 resonant mode which is why it exhibits a higher frequency of oscillation than the n=1 mode we have seen previously forming along the domain wall. Figures 6.39a) and b) also show a second s wave has begun to form indicating that the first

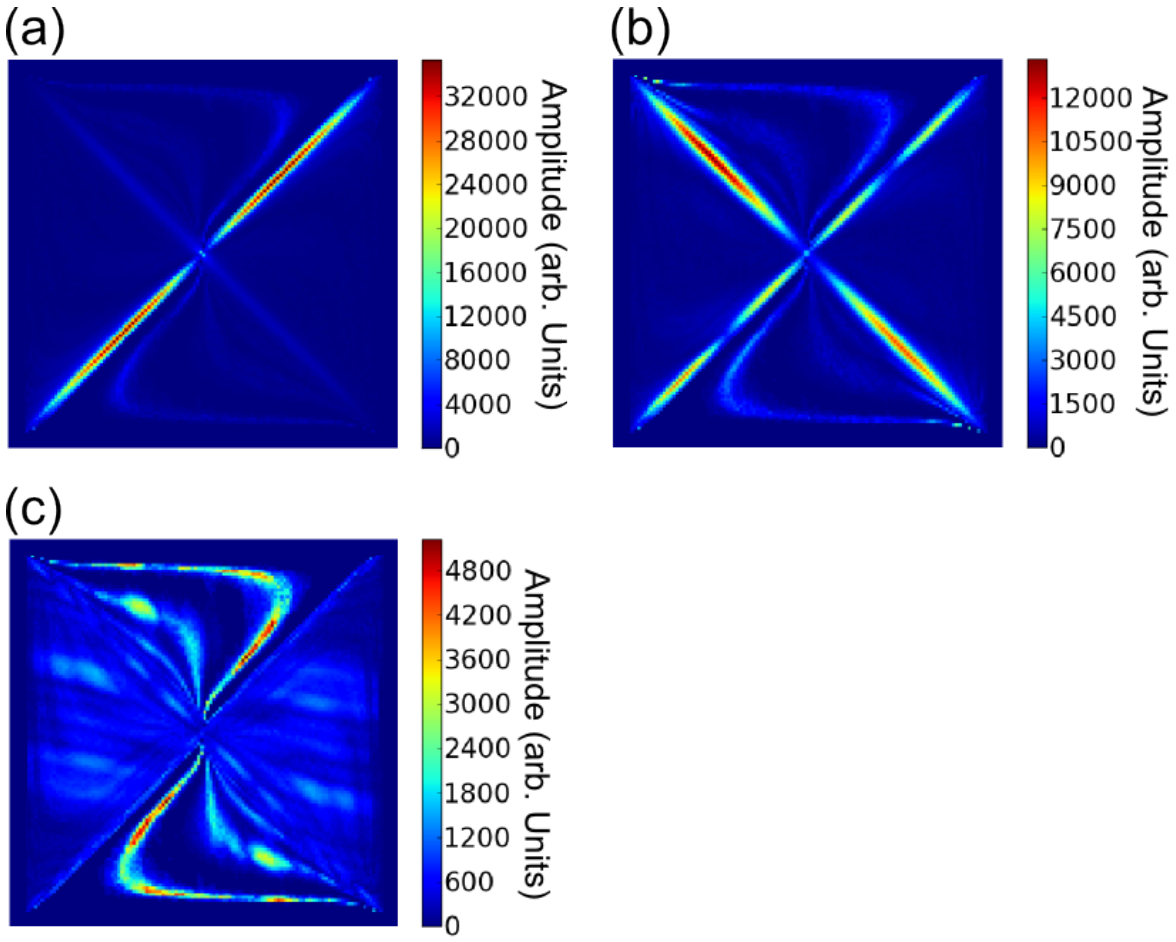

Fig. 6.39 Fourier transformation heat maps for the magnetisation of a 2000nm square in the x direction when a pulse of 1mT was used to excite the system. Shown are heatmaps with windows of 200MHz and central frequencies of a)1.26GHz, b)2.49GHz, 7.79GHz.

s-wave has moved sufficiently far from the domain walls that a second s-wave mode can form in the space between the first and the domain wall modes. This will be further investigated in the next section which will examine the spatial character of the tertiary modes in more detail.

6.5 Study of the tertiary modes

This section details a brief examination of the tertiary modes. Whilst these modes will be strongly suppressed in samples with realistic damping, as discussed in section 6.7, these high frequency modes may be excited by the use of a specific frequency oscillatory magnetic field. The first sample to be examined for the tertiary modes is the 500nm square with no uniaxial anisotropy. This sample was chosen to be examined first due to the system being simplified

by the removal of the uniaxial anisotropy meaning that it most closely resembles the sample investigated in reference [104]. Heat maps were produced focusing on the tertiary modes using a logaritmic scale to examine the lower intensity tertiary modes. The result of this examination are shown in figure 6.40.

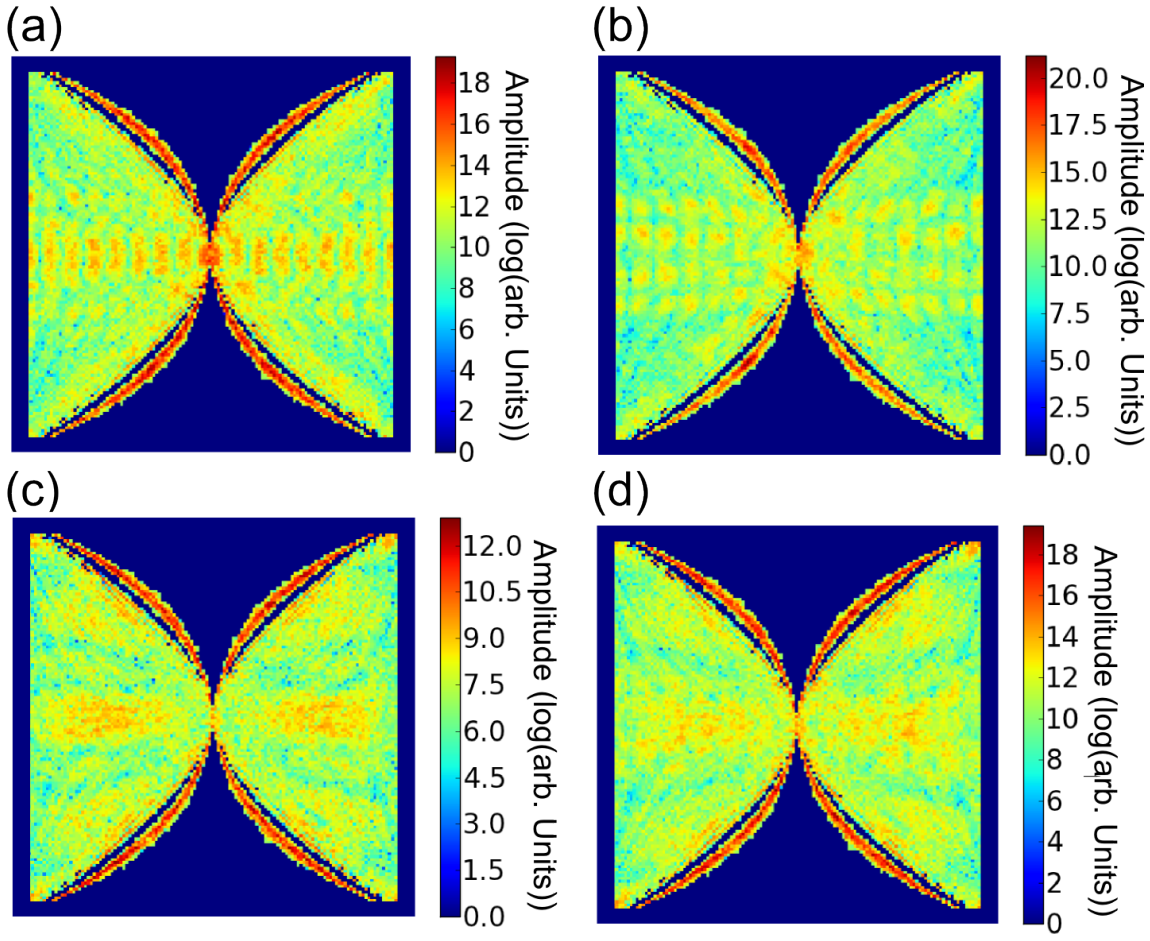

Fig. 6.40 Fourier transformation heat maps for the magnetisation of a 500nm square with no uniaxial anisotropy present in the x direction when a pulse of 1mT was used to excite the system. Shown are heatmaps with windows of 100MHz and central frequencies of a)8.52GHz, b)10.31GHz, c)11.24GHz, d)12.19GHz.

Here we can see standing waves forming in the areas of uniform magnetisation as described in [104]. These waves have their peak intensities in the centre of the areas of uniform magnetisation due to the non-uniformity of the confinement potential constraining these spin wave modes. Whist describing the edges of the shape as infinite potential wells works well when describing the spin wave modes which lie along the domain walls we

must consider the the triangular regions of uniform magnetisation as potential wells when describing the tertiary modes which form in these regions leading to the variation in intensity shown in figure 6.40.

In figure 6.40 we can also see four spin wave modes which form in the areas of uniform magnetisation close to the domain walls. These c shaped waves (c-waves) have a broad linewidth in their frequency of oscillation and appear to be standing waves pinned at the corners of the square and the vortex core. They appear to be similar to the domain wall modes in that they are standing waves with pinning in the same areas but with a higher wavevector leading to a higher frequency. The fact that the waves do not form along a uniform area of effective magnetisation may be what causes the large linewidth of their oscillation frequency which has led to them appearing strongly in all 4 of these frequency maps.

Introducing the uniaxial anisotropy to the system and looking at the Fourier transform maps we see the results shown in figure 6.41.

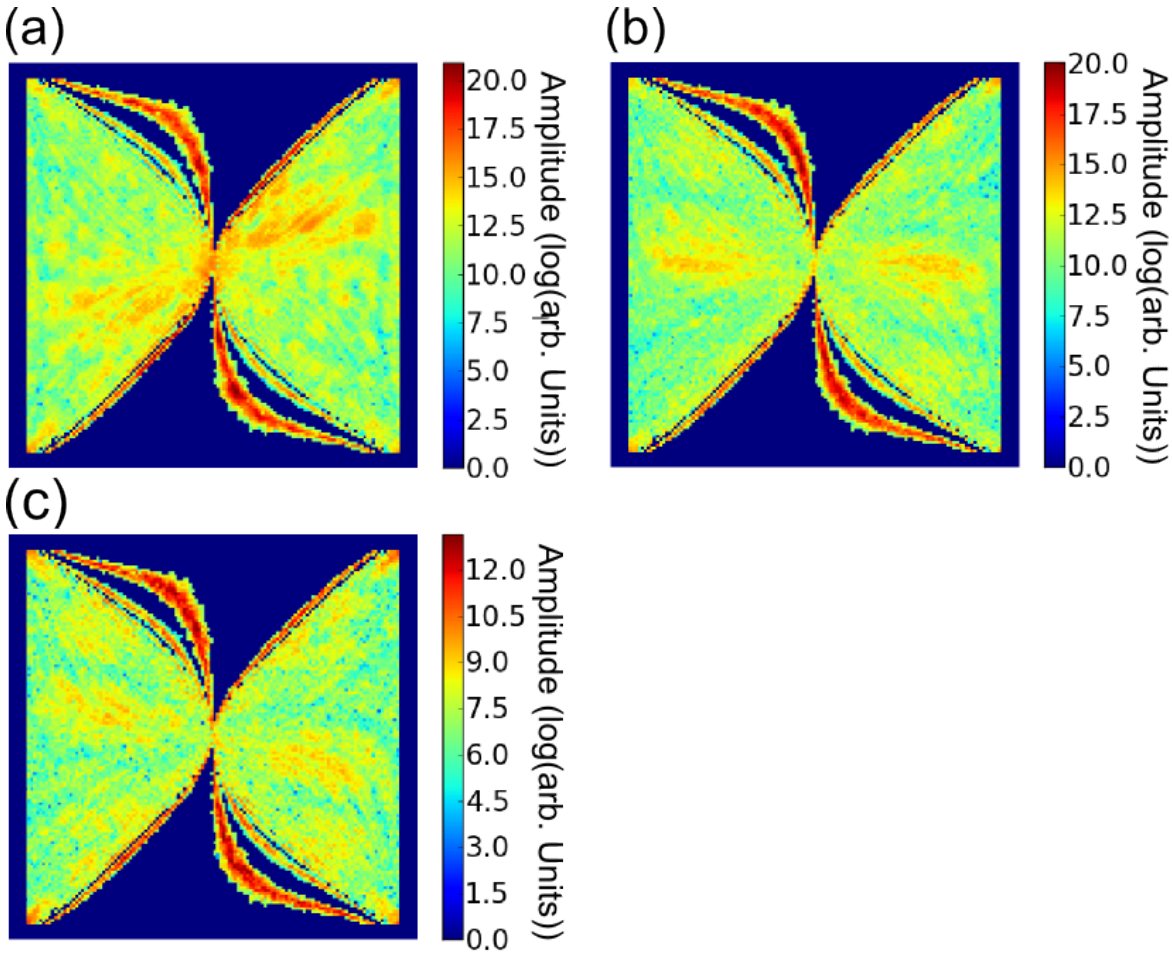

Fig. 6.41 Fourier transformation heatmaps for the 500nm square with no strain induced anisotropy. Uniaxial anisotropy was present for these simulations in contrast with figure 6.40. a) shows the heatmap centred around 11.24GHz, b) is centred around 12GHz and c) is centred around 12.26GHz. All have a window of 100MHz.

The most striking change induced by the reintroduction of the uniaxial anisotropy is that a new s-wave mode has appeared. This appears to be similar to a c wave but with a higher wavevector as the c-waves still appear to be present but with a lower intensity along the [110] axis.

The spin wave modes in the areas of uniform magnetisation have been visibly distorted by the presence of the uniaxial anisotropy. The intensity has also been lowered and the wave vector of the spin wave has been rotated by the uniaxial anisotropy. The reduction in spin wave intensity is probably due to the potential wells being distorted meaning that the wavevector cannot form at 90^o to the magnetisation.

Next we examine the results of increasing the size of the object on the tertary modes and the results are shown for 1000nm in figure 6.42.

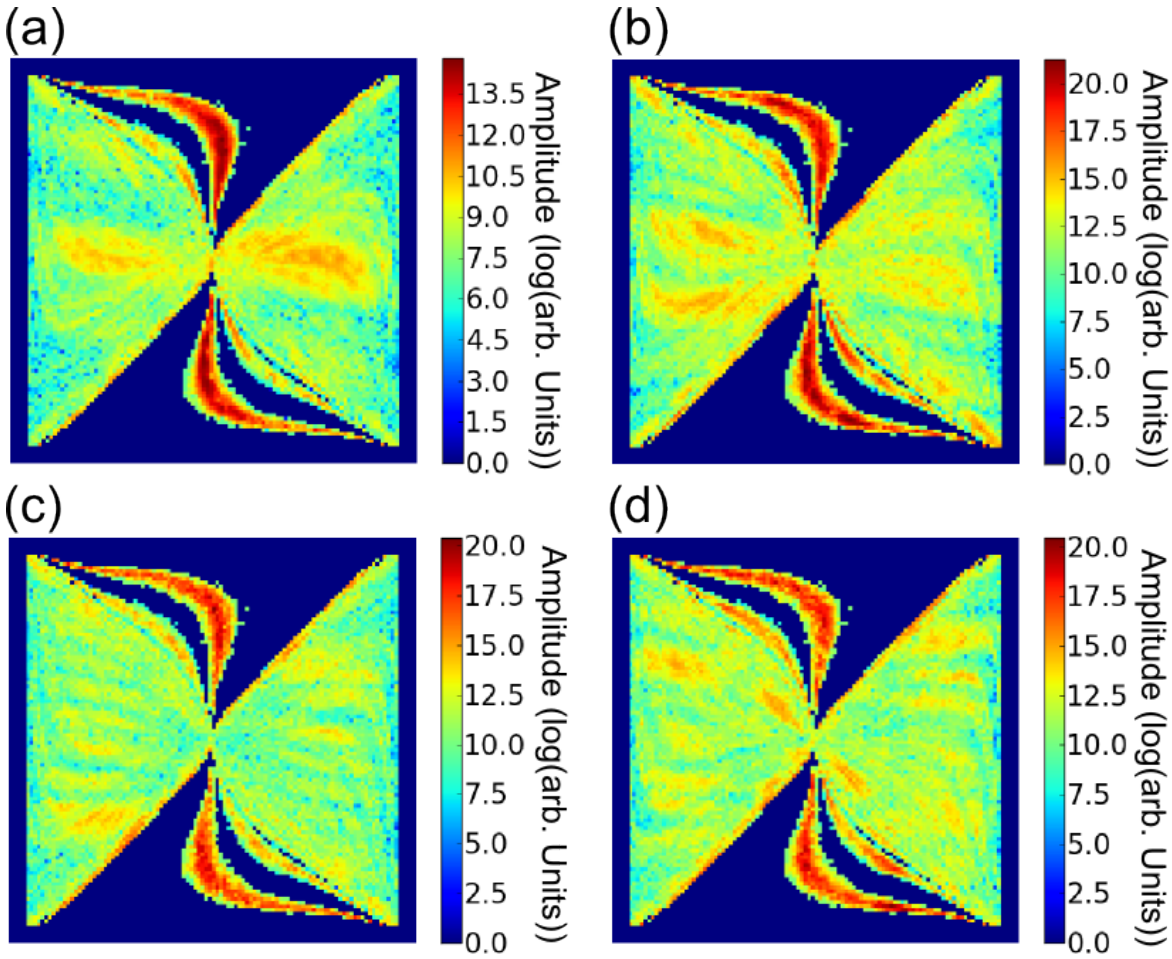

Fig. 6.42 Fourier transformation heatmaps for the 1000nm square with no strain induced anisotropy. a) shows the heatmap centred around 9.03GHz, b) is centred around 9.3GHz, c) is centred around 9.76GHz and d) is centred around 10.31GHz. All have a window of 100MHz.

When the size of the sample is increased we can see that there are more tertiary modes visible in the areas of uniform magnetisation. The modes are again distorted by the presence of the uniaxial anisotropy and in figure 6.42c) we can see what looks like the beginnings of a second s-wave forming close to the domain wall. This may indicate that as the primary s-wave moves away from the domain walls it makes room for a second s-wave to form. To see if this trend continues as size increases we turn our attention to the heatmaps showing the tertiary modes for the 1500nm square shown in figure 6.43.

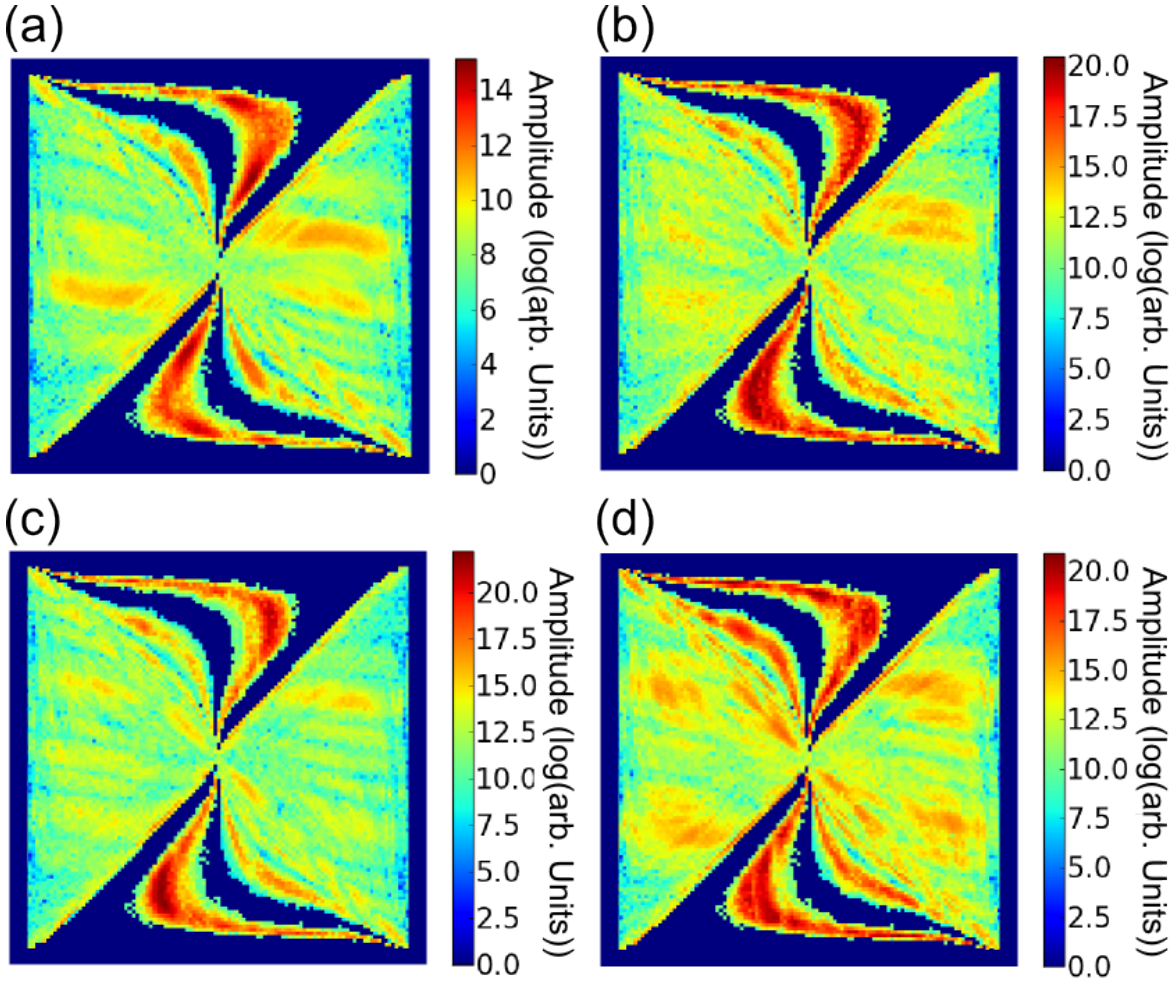

Fig. 6.43 Fourier transformation heatmaps for the 1500nm square with no strain induced anisotropy. a) shows the heatmap centred around 8.18GHz, b) is centred around 8.36GHz, c) is centred around 8.51GHz and d) is centred around 8.75GHz. All have a window of 100MHz.

In figure 6.43) d) we can clearly see the formation of a second s-wave as the first moves away from the domain wall. Finally, we investigated the tertiary modes in a 2000nm square as shown in figure 6.44.

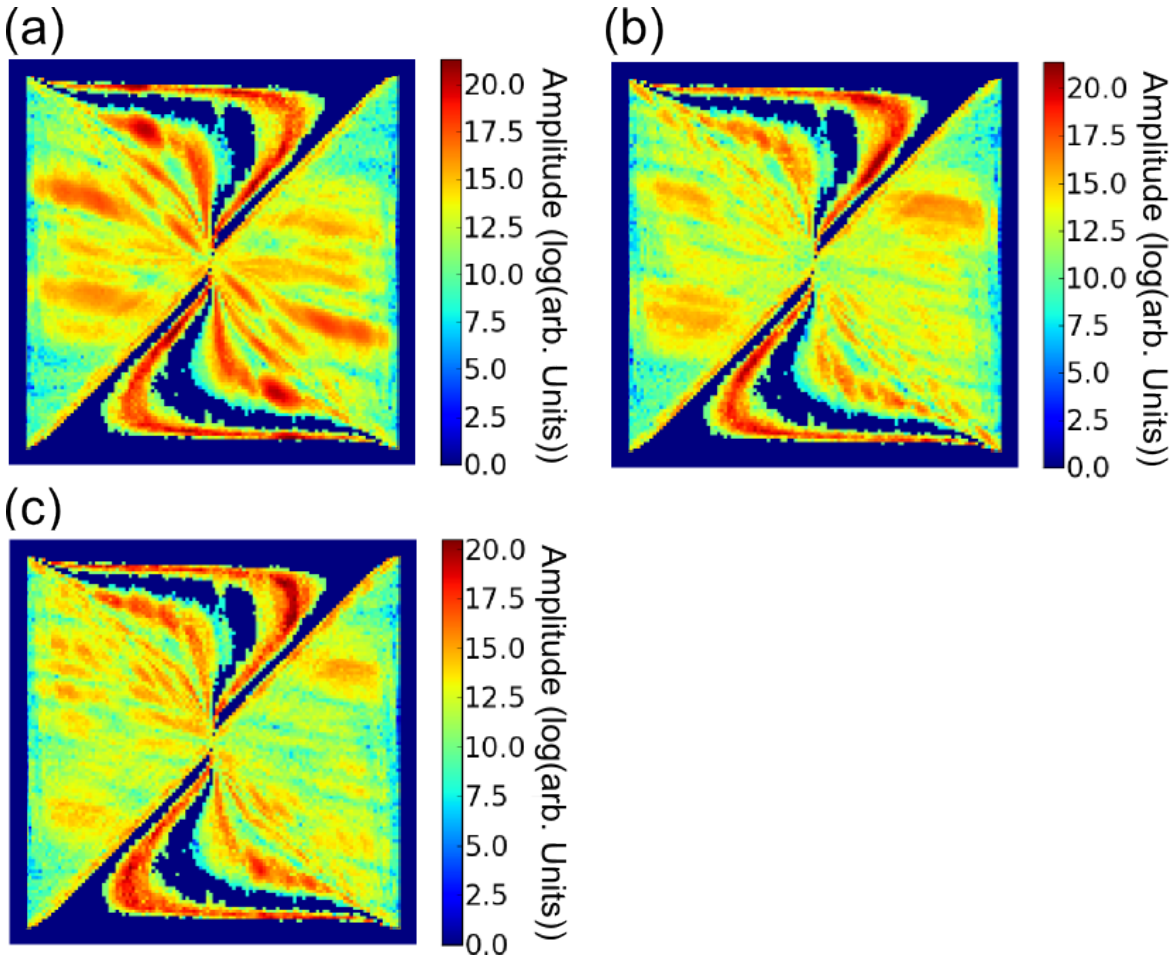

Fig. 6.44 Fourier transformation heatmaps for the 2000nm square with no strain induced anisotropy. This map is centred around a)7.73GHz, b)7.96GHz, c)8.28GHz with a window of 100MHz.

Looking at the heatmaps for the 2000nm sample we can see that the tertiary modes in the areas of uniform magnetisation are overlapping. This indicates that producing more Fourier transformation maps for this sample with a greater sampling rate could be a useful avenue for future work however this process requires extensive processing resources. Also shown in figure 6.44 we can see that a second s-wave has clearly formed however unlike in the other samples in which the second s-wave could be seen it appears to oscillate at a higher frequency than the modes in the areas of uniform magnetisation. However, given the aforementioned frequency resolution problem, this observation is not reliable.

The effect of a strain induced anisotropy on these tertiary spin wave modes may provide an interesting avenue for future work. Figure 6.25 shows reduction in the amplitude of the tertiary modes amplitudes however the frequency appears to remain roughly constant.

6.6 Core breakdown at high field

In section 6.2 as the field applied to the sample increases the area described by the motion of the core increases and in section 6.3 we saw that the size of the shape described would also increase with the size of the object being simulated. When both of these factors are increased at the same time we begin to see that the core breaks up into multiple cores at high field in large samples as was observed experimentally in reference [27]. This effect is shown in the 1000nm, 1500nm and 2000nm samples in figure 6.45.

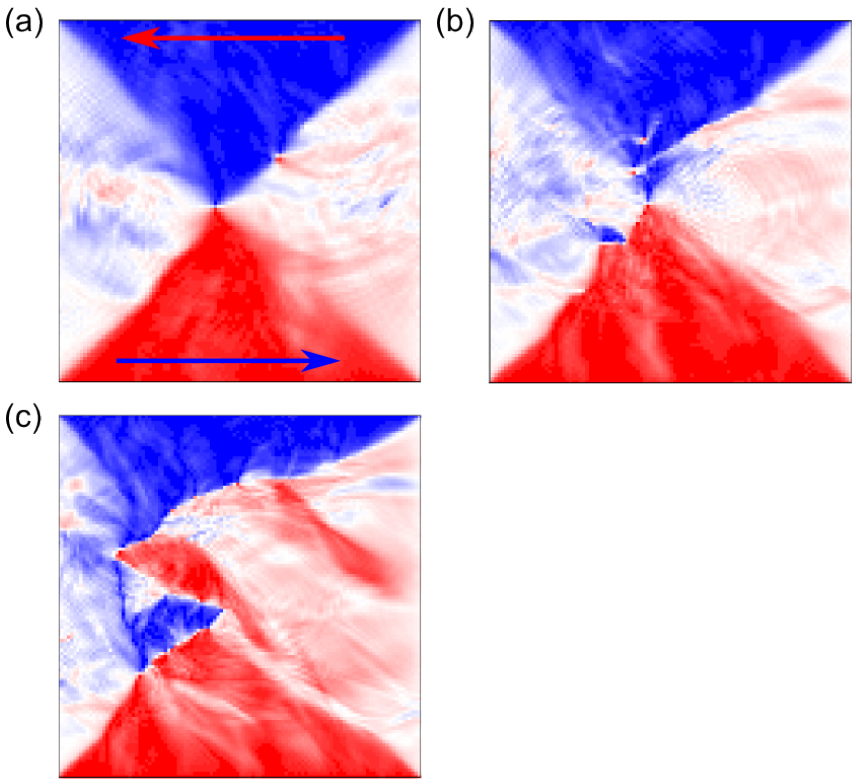

Fig. 6.45 Frames of simulations of squares of various sizes showing the x-component of the magnetisation in frame 20, t=0.5ns when excited with a 25mT amplitude magnetic field pulse. Both uniaxial and cubic anisotropy terms were present in these simulations. The orientation of the magnetisation represented by the red and blue regions is demonstrated by the arrows in a). White indicates zero magnetisation in the x-direction. The squares were a)1000nm, b)1500nm and c)2000nm.

We can see the locations of the vortex cores in these images more clearly by finding the Sobel gradient of the images. The Sobel operator is an edge detection image filter which calculates the difference in pixel intensity between adjacent points in the x and y directions, G_x and G_y respectively. Then by finding the gradient magnitude of the two using equation 6.3 the edge intensity at that pixel can be calculated.

$$G = \sqrt{G_x^2 + G_y^2} \tag{6.3}$$

This process is described in more detail in appendix E however here it must be stated that the use of a Sobel operator to identify vortex cores allows for multiple cores to be found and tracked, unlike a simple measurement of the z-component of the magnetisation which provides too many false positives along the domain walls to be effectively used for tracking of multiple cores. Applying the Sobel operator to the images shown in figure 6.45 produces figure 6.46 in which the cores are highlighted with white circles.

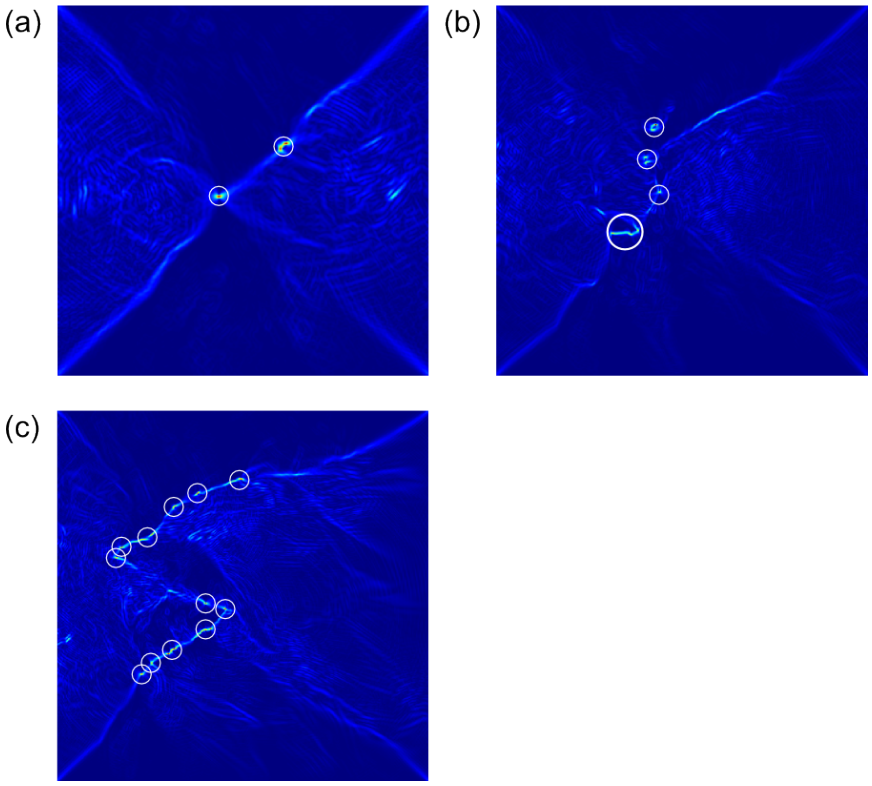

Fig. 6.46 Repeat of the images from figure 6.45 once the sobel operator has been applied in order to show the cores. The cores have been highlighted with white circles as an aid to the eye.

In order to examine the emergence of these cores we can plot the positions of the cores at a certain time in the simulation as a function of the amplitude of field applied to the sample. Shown in figure 6.47 are plots of the positions of the cores in the x-direction as a displacement from the starting position of the central core at time t=0.5ns.

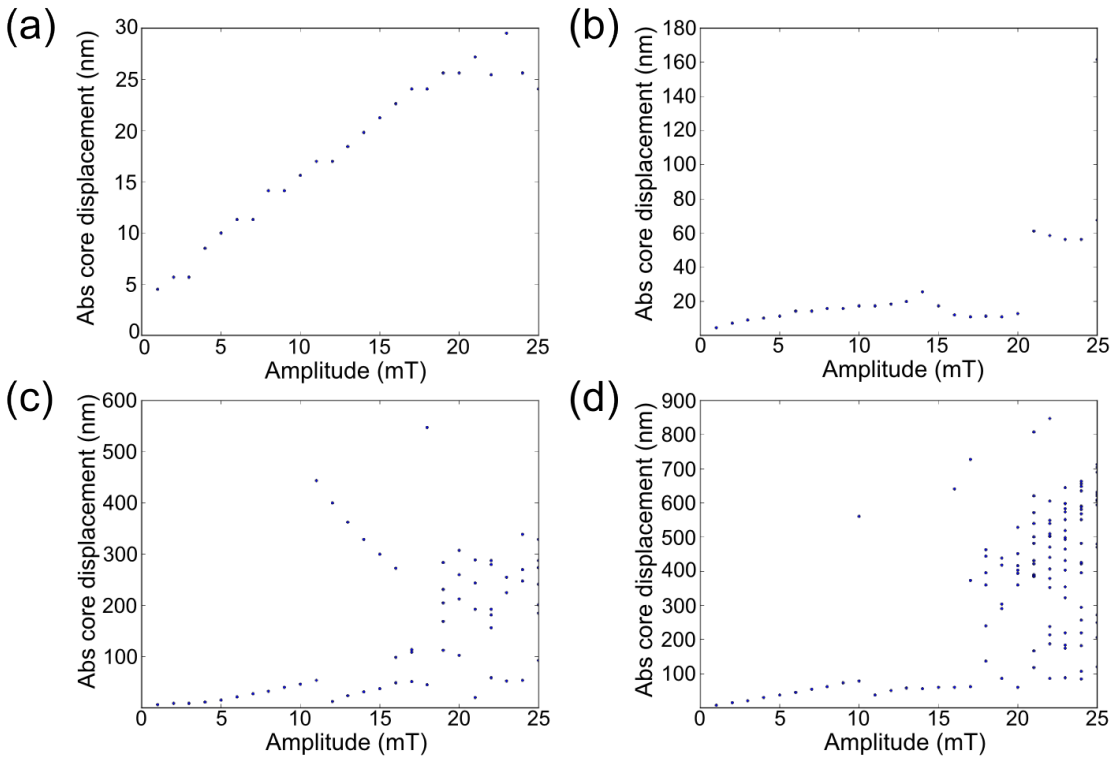

Fig. 6.47 Core displacement from the center of the object as a function of excitation pulse amplitude for squares measuring a)500nm, b)1000nm, c)1500nm and d)2000nm. The core locations were taken from frame 20, t=0.5ns after the exciting magnetic pulse began.

These breakdowns occur in the early frames of the simulation but as the simulations progress the cores tend to recombine into a single core as demonstrated by figure 6.48 which shows the location of a set of found cores in a 2000nm square with no strain induced anisotropy when excited with a 25mT pulse. The cores' movements were tracked using the program described in appendix E.

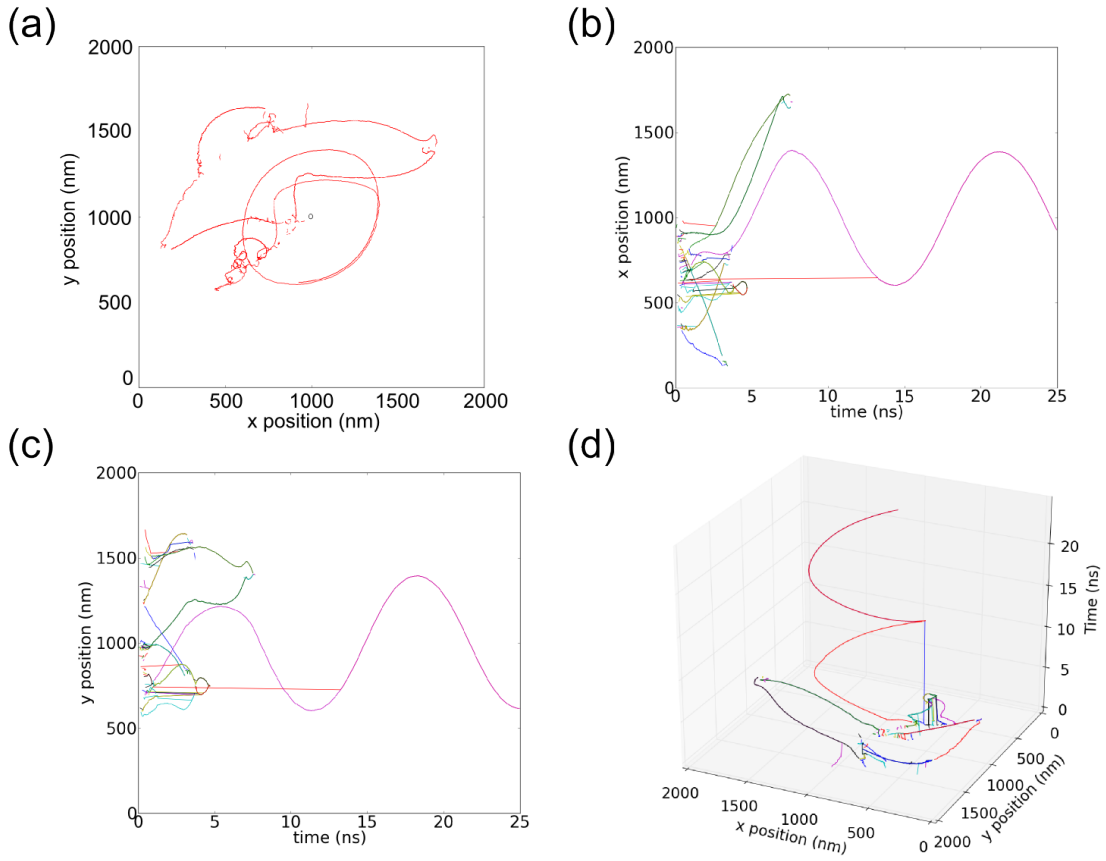

Fig. 6.48 Tracking results for a 2000nm sample with no strain induced anisotropy applied to the sample and a 25mT magnitude magnetic pulse was used to excite core movement. In a) we can see a phase diagram of the core's movements with the starting position of the core being indicated by the black circle at (1000, 1000), in b) we can see the cores' positions as a function of time and in c) we can see the cores' positions in y as a function of time. Finally in d) the cores' positions in x and y is shown as a function of time in a 3D line plot.

Here we can see that the core breaks down when the amplitude of the magnetic field pulse is 25mT. The core does recombine however and when it does it performs oscillations which are much larger than the oscillations observed in previous samples where no core breakdown was observed.

In order to examine the transition to these large oscillations the movement of the primary core as a function of the amplitude of the exciting pulse was examined as demonstrated in figure 6.49 which shows the area described by the movement of the core in the 2000nm sample with no strain induced anisotropy as a function of the amplitude of the field applied to the sample in a) the change in $\dot{\theta}$ as a function of excitation pulse amplitude in b) and the change in $\dot{S}$ as a function of excitation pulse amplitude in c). The polarisation of the primary

core after the cores have recombined is also indicated by the colour of the markers in b. The core's properties were calculated using data taken after t=7.5ns to allow for the cores to recombine after the breakdown event.

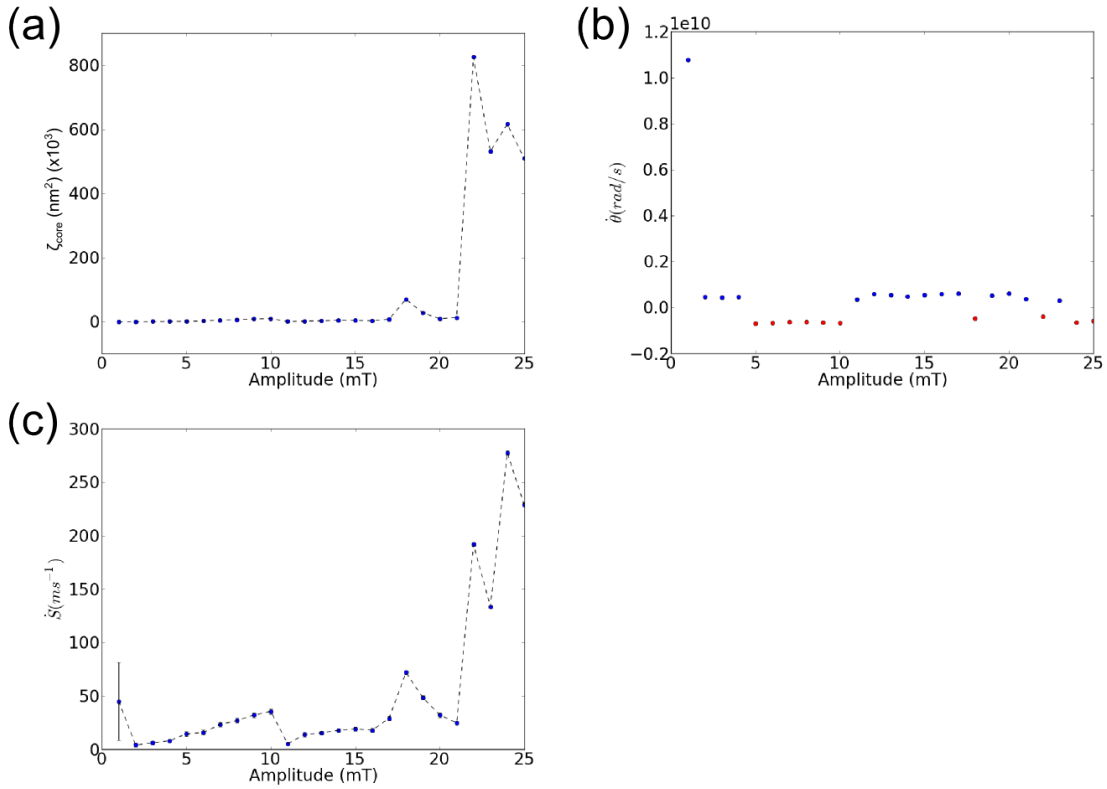

Fig. 6.49 Properties of the core oscillations for the 2000nm square with no strain induced anisotropy as a function of excitation pulse amplitude. In a) the area described by the motion of the core is plotted as a function of the magnetic field pulse amplitude. b) shows $\dot{\theta}$ as a function of excitation pulse amplitude and c) shows $\dot{S}$ as a function of the excitation pulse amplitude. The colour of the markers indicates the chirality of the core at t=7.5ns with red indicating positive chirality and blue indicating negative chirality

Looking at the properties of the core's motion the most striking conclusion we can make from figure 6.49 is that when the excitation pulse amplitude exceeds 21mT the area of the circle described by the core increases by over 8 times. This is coupled with the frequency of oscillation of the core remaining roughly constant as evidenced by figure 6.49b) in which we can see that the value of $\dot{\theta}$ remains roughly constant regardless of the pulse amplitude with the only variance being a move from positive to negative depending on the chirality of the core. The value of $\dot{S}$ also increases eightfold, however this can be explained as the core displacement velocity increasing since whilst the circumference of the core has increased the

frequency has not leading to the core's speed increasing with the distance which it covers. In order to examine the transition in the areas described by the cores we examine the phase space diagrams for the samples at various excitation pulse amplitudes in figure 6.50.

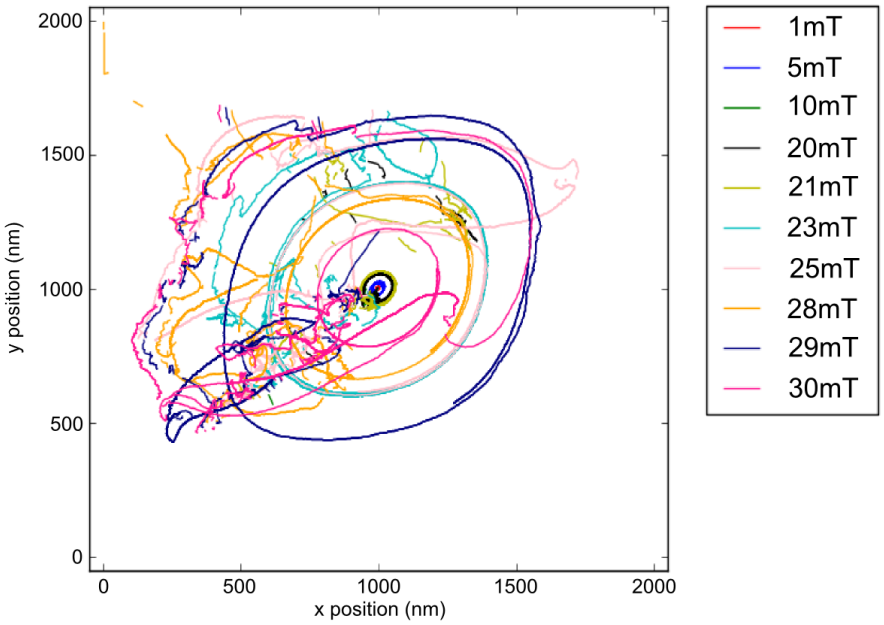

Fig. 6.50 Plot of the x and y positions of the cores in a series of simulations of a 2000nm square with no strain induced anisotropy. The amplitude of the exciting pulse is indicated by the colour of the lines indicating the core movements. The simulations represented here were allowed to evolve over 50ns.

It can be seen that there is a large jump in the amplitude of the oscillations when the core breaks down early in the simulation caused by the cores breaking down and then recombining. We also see that as the pulse amplitude continues to increase the size of the oscillations begins to decrease again as the energy of the oscillation is expended in the multiples of cores produced by the breakdown. This indicates that there may be a resonance frequency for the largest amplitude oscillations and therefore the largest power output of a VCO based STO.

6.7 Effect on the oscillations resulting from realistic damping

In order to examine whether the observations made from the undamped samples may be applied to real world devices the calculations for the 500nm square were repeated with a realistic damping co-efficient of 0.017. This value was taken from FMR measurements described in reference [61].

The simulation of the 500nm square with zero strain induced anisotropy and an excitation pulse amplitude of 25mT were repeated and run for 50ns in order to show the decay of the core oscillations. The core's position was tracked as before and is shown in figure 6.51.

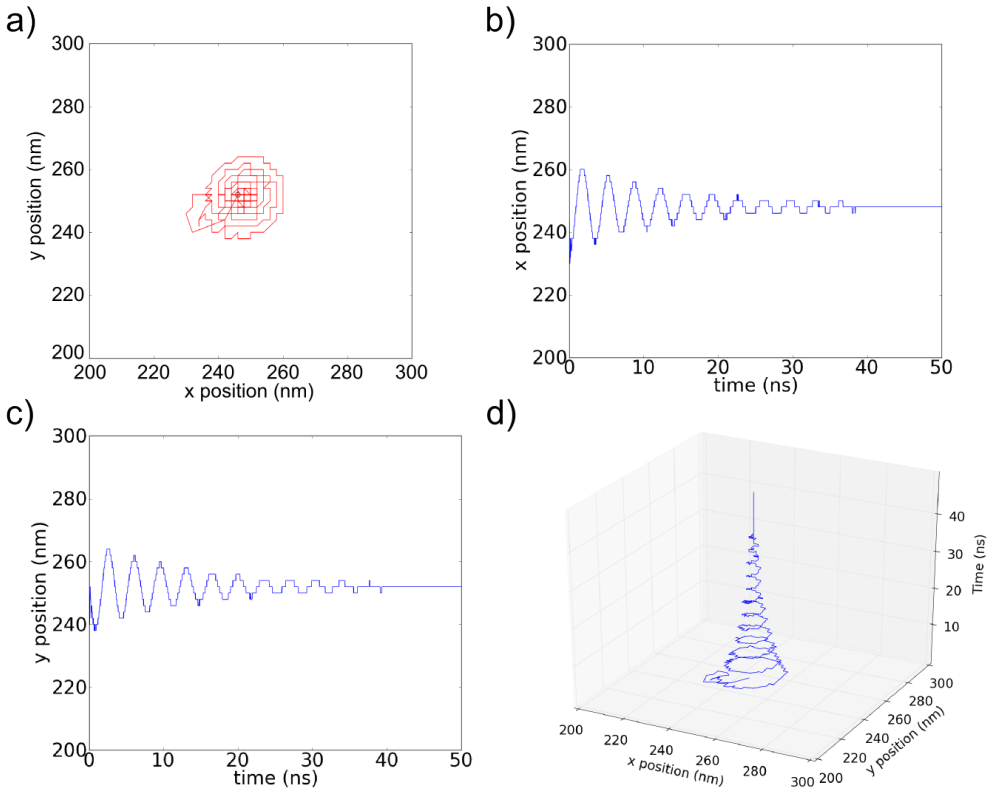

Fig. 6.51 Result of core tracking for primary core in 500nm square with no strain induced anisotropy when excited with a 25mT magnetic field pulse. The core's x and y positions are shown in a), b) shows the core's movement in x as a function of time, c) shows the core's movement in y as a function of time and d) is a 3D plot showing the core's movement in both x and y as a function of time.

Figure 6.51 shows that as time goes on the amplitude of the core oscillation decreases. The initial amplitude of these oscillations is comparable to the simulation with low damping

shown in figure 6.9 and the period of the oscillations is also equal to the period of the oscillations shown in figure 6.9. This decay may also be visualised as the reduction in the fluctuation in the magnetisation across the sample as a function of time, which is demonstrated in figure 6.52.

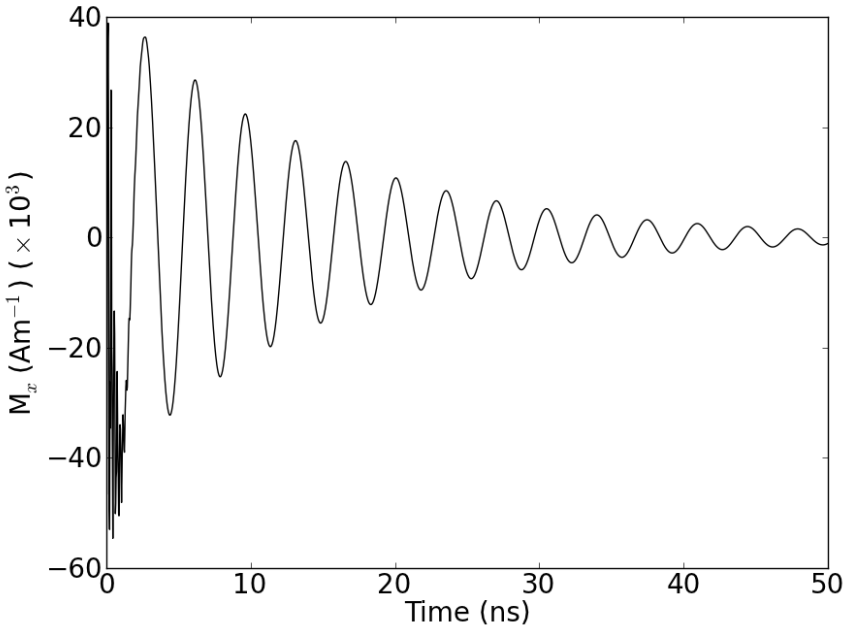

Fig. 6.52 Change in the M_x component of the magnetisation in a 500nm square with a realistic level of damping when excited with a pulse with a peak amplitude of 25mT.

Comparing figure 6.52 to the evolution of the magnetisation of the system with a low level of damping shown in figure 6.10 a) it can be observed that the damped system does not exhibit the secondary oscillations seen when the system experiences low damping.

The effect of damping on the frequency modes of the oscillation were examined by performing a Fourier transformation of the magnetisation in the x direction of the 500nm square with and without damping as shown in figure 6.53.

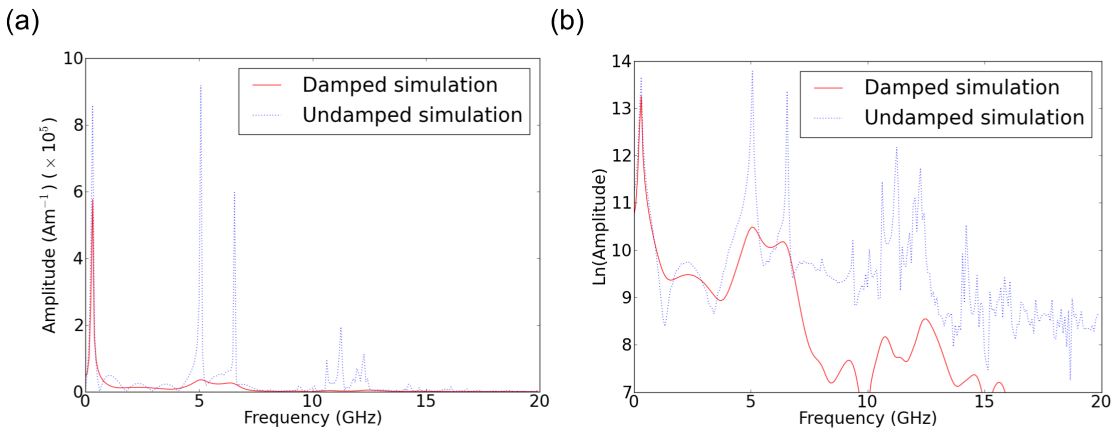

Fig. 6.53 Fourier transformation profiles for the x component of the magnetisation of 500nm samples with no strain induced anisotropy with damping parameters of 0.017 for the damped simulations, shown as a solid red line and 0.0001 for the undamped simulations shown as a dotted blue line. a) shows the raw results of the Fourier transformations and b)shows the natural logarithm of these profiles. The pulse used to excite these oscillations had an amplitude of 1mT.

Looking at these two data sets we can see that the frequency of oscillation of the primary core remains 300MHz indicating that the frequency of oscillation is independent of the damping coefficient of the system. The amplitude of the secondary and tertiary modes are almost totally extinguished however, an effect that can be seen clearly when a 3D Fourier transformation of the 500nm square with a 1mT excitation pulse is performed as shown in figure 6.54.

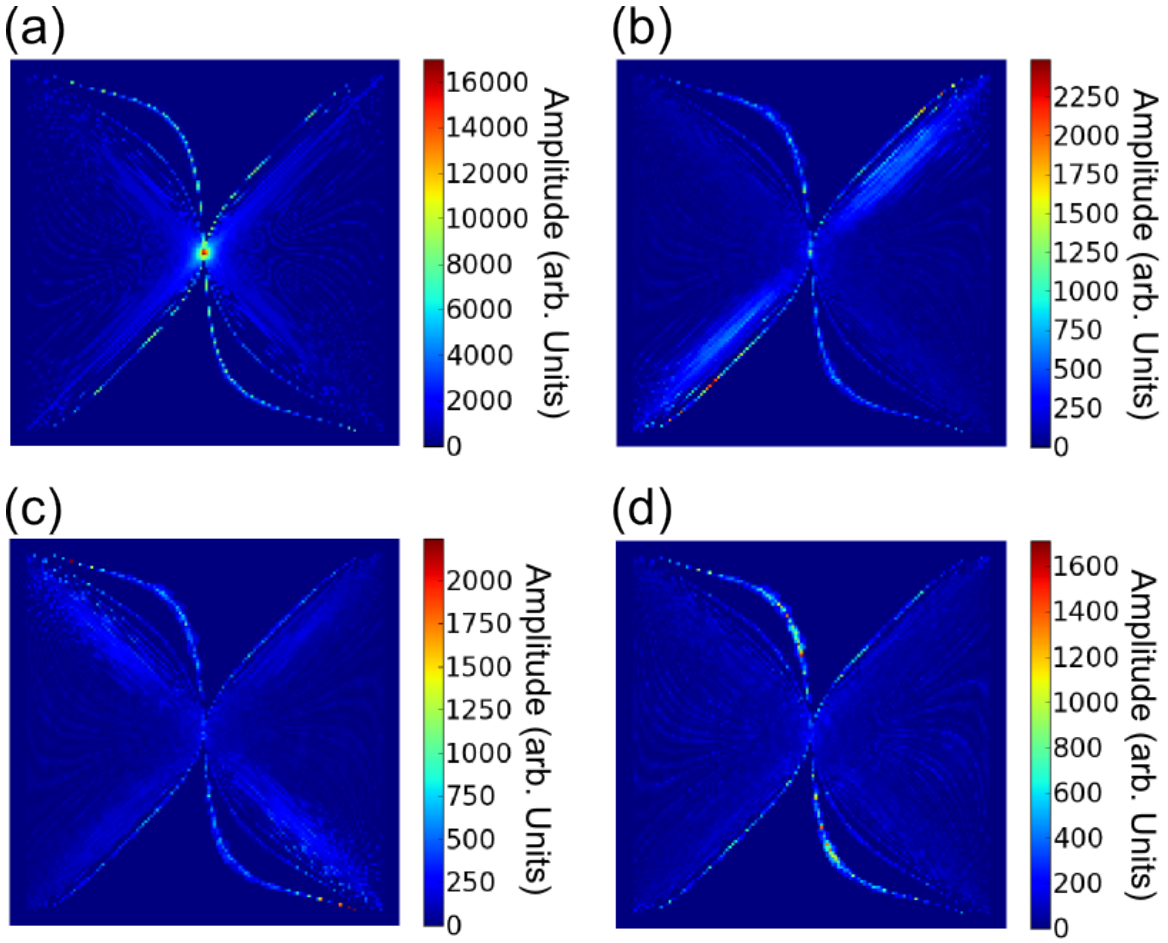

Fig. 6.54 Fourier transformation heatmaps for the 500nm square with no strain induced anisotropy applied to the sample and a damping coefficient of 0.017. The system was excited with a 1mT magnetic field pulse. a) shows the heatmap centred around 300MHz, b) is centred around 5GHz, c) is centred around 6.5GHz and d) is centred around 12.3GHz. All heatmaps have a window of 200MHz.

We can see here that the secondary and tertiary modes in the simulation are still present however the amplitude of the oscillations is reduced indicating that the physics of these modes is unchanged and should be observable in real world devices however their low intensity may make observation of these modes difficult. These modes have previously been observed experimentally however with domain wall modes being observed experimentally both by XMCD PEEM [138] and Kerr microscopy [142]. The high frequency modes are much harder to produce and observe however some observations have potentially been made previously using Kerr microscopy on permaloy discs [142] and using XMCD PEEM in a 2μm $Fe_{1-x}Ga_x$ square in chapter 5. In order to observe these high frequency modes reliably however the system should be excited with a pulse train of a frequency matched to the frequency of the desired modes.

Next we look at the effects of damping on the samples with the core oscillation amplitude amplification due to core breakdown. In order to study this, simulations were performed with realistic damping on 2000nm squares with excitation pulse amplitudes between 1mT and 25mT. By looking at the circles described by the motion of the primary core as a function of excitation pulse amplitude for various field pulse amplitudes we can see the effects shown in figure 6.55. These results were found by finding the mean value of r across the entire simulation after t=7.5ns in order to determine values for ζ_{core} and $\dot{S}$. The errors for these measurements of ζ_{core} and $\dot{S}$ were determined using the size of the vortex core in this figure due to the decay of the radius, and therefore ζ_{core} and $\dot{S}$, of the core's movement over time.

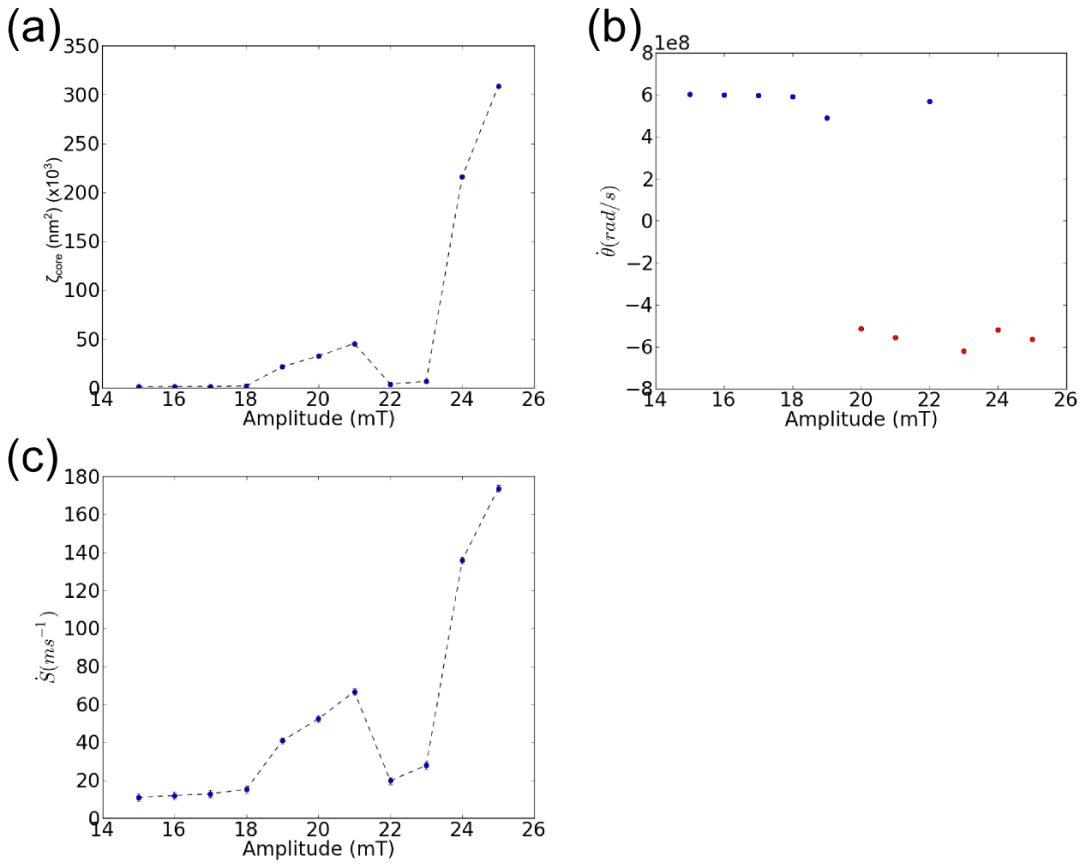

Fig. 6.55 Properties of the core movement in the 2000nm sample with various amplitudes of excitation pulse used to excite the core movement. In a) we can see that the area described by the core increases greatly when the amplitude of the excitation pulse reaches and exceeds 21mT but we can also see in the plot of $\dot{\theta}$ versus excitation pulse amplitude shown in b) that this has no effect on the angular velocity. This means that the core moves at a much higher velocity once the excitation pulse reaches 24mT as we can see in c) where the core's displacement velocity is plotted against the amplitude of the excitation pulse. In the $\dot{\theta}$ plot the polarisation of the core is indicated by the colour of the markers with red indicating positive polarisation and blue indicating negative polarisation. The error bars in these measurements are smaller than the markers.

This shows us that even when the system is damped the core breakdown event leads to an increase in the area described by the core increasing by an order of magnitude. We also see that the core's direction of motion is tied to its polarisation and that the frequency of oscillation remains constant regardless of the amplitude of the exciting pulse. The value of $\dot{\theta}$ is also unaffected by the introduction of damping into the system. The core velocity is reduced however this is due to the reduction in the area described by the core seen in a).

Finally the simulations for the 2000nm square with no strain induced anisotropy and pulse amplitudes of 10mT and 25mT were repeated with the simulation time extended to 50ns in order to show core decay in the 2000nm sample with and without core breakdown induced amplification. The sample excited with a 25mT pulse decays as shown in figure 6.56.

We can see by comparing the tracking results the increase in the core amplitude decays over a much longer time period compared to the decay in the 500nm square. This increase in decay time is due to the increase in core displacement due to the core breakdown meaning that the core breakdown leads to more persistent oscillations in core movement. We also see that the damping causes the core to recombine over a shorter time scale of $\sim$5ns rather than $\sim$7.5ns in the undamped simulations due to the reduced velocity of the cores reducing their separation. These simualtions are only valid when the amplitude of the magnetic field pulse are great enough to induce the core breakdown event. When the pulse amplitude is lower than 22mT no core breakdown occurs and the core precession continures much as it does in the 500nm sample shown in figure 6.51.

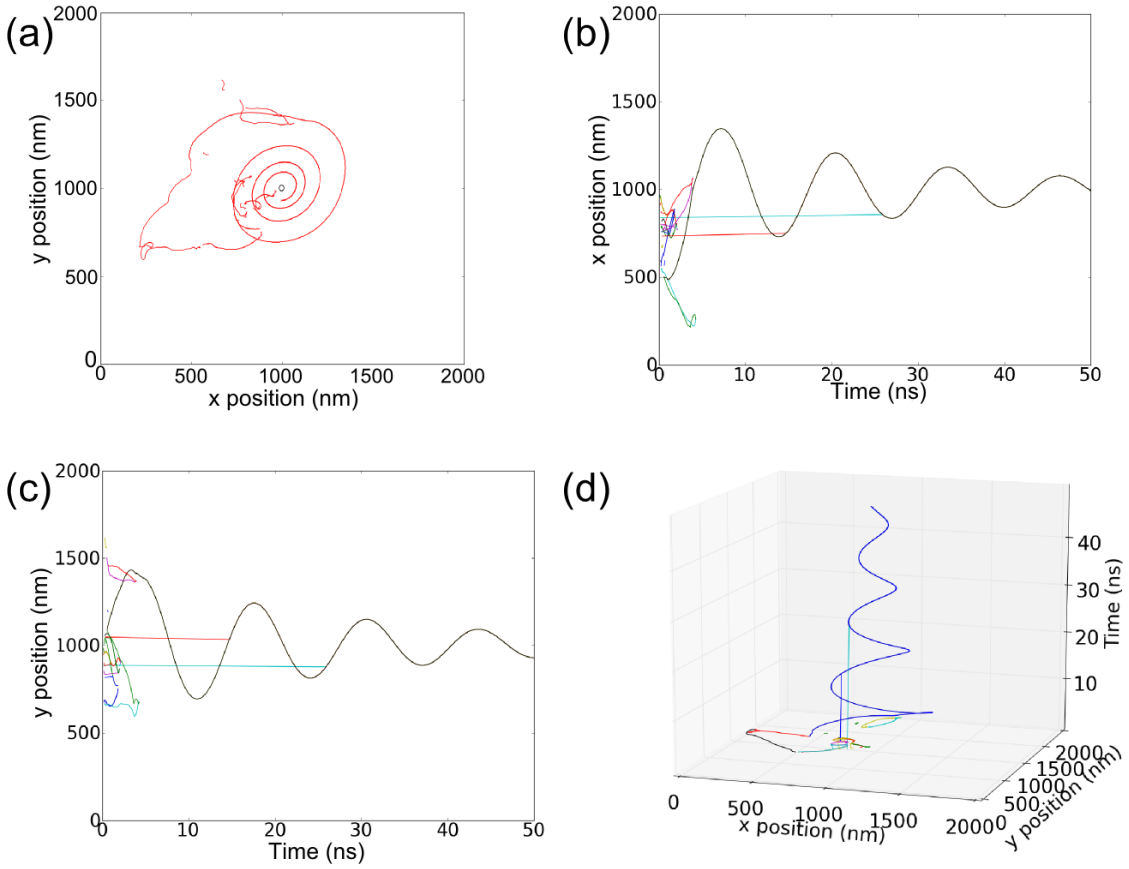

Fig. 6.56 Tracking results for a realistically damped 2000nm sample with zero strain induced anisotropy applied to the sample and a 25mT magnitude magnetic pulse was used to excite core movement. In a) we can see a phase diagram of the core's movement with the starting position of the core being indicated by the black circle at (1000, 1000), in b) we can see the core's position as a function of time and in c) we can see the core's position in y as a function of time. Finally in d) the core's position in x and y is shown as a function of time in a 3D line plot.

6.8 Summary of micromagnetic simulations

This chapter began by establishing the effects of shape anisotropy on magnetisation pinching due to a strain induced anisotropy. It then moved onto describing the results of exciting the oscillatory modes of a Landau flux closure state using a magnetic field pulse, examining the effects of the amplitude of the magnetic field pulse on the motion of the central core and the frequency of oscillation of the various spin modes within the sample. This found that the area described by the motion of the central core and its velocity increased as a function of the amplitude of the exciting magnetic field pulse however when the amplitude of the magnetic field pulse became large enough to induce vortex core switching the area described by the core and its velocity became unpredictable. The frequency of oscillation was shown to be independent of the amplitude of the exciting pulse however the magnitude of the secondary modes was shown to decrease as the amplitude of the pulse increased.

Spatial frequency analysis was used to determine where the oscillatory modes formed and their shapes demonstrating that the secondary modes were standing waves lying along the domain walls with stationary points at the edges of the object and the vortex core. These standing waves were shown to oscillate at different frequencies depending on whether they lay parallel or perpendicular to the uniaxial anisotropy. The system was simulated with no uniaxial anisotropy thereby demonstrating that the frequency of oscillation of the domain wall modes was dependant on their orientation relative to the uniaxial anisotropy.

Increasing the amplitude of the exciting magnetic field pulse was demonstrated to reduce the amplitude of the oscillation of the domain wall modes, most likely due to the effective field along the domain walls becoming non-uniform. An asymmetry in the domain wall modes was also demonstrated when the sample was excited with a magnetic pulse with an amplitude of 25mT however this could not be easily explained without further investigation into the character of the effective field.

The effect of strain on the evolution of the system was investigated and was found to distort the vortex core's motion leading the shape described by the vortex core's motion to become elliptical. The theoretical ability to tune the resonance frequency of a vortex core oscillator based spin torque oscillator by the use of an external physical strain was then demonstrated. It was demonstrated that the frequency of oscillation of both the vortex core and the spin waves within the device may be reduced by the presence of a strain induced anisotropy.

It was also demonstrated that the magnitude of the magnetic field pulse required to induce vortex core switching may increase as a function of the magnitude of a strain induced anisotropy. It was then demonstrated that when the magnetic field pulse was applied perpendicular to the strain induced anisotropy the magnitude of the magnetic field pulse required to

induce core switching increased by up to 16%. The effects of altering the angle between the strain induced anisotropy and the magnetic field pulse may provide an interesting avenue for further research.

An inversely proportional relationship between the frequency of oscillation and the size of the objects was demonstrated for both the oscillation frequency of the vortex core and the domain wall modes. Examination of the spatial characteristics of the domain wall modes in objects of various sizes found asymmetry in the shape of the domain wall modes in larger objects due to the uniaxial anisotropy dominating over the shape anisotropy.

The spatial character of the tertiary modes was examined and it was found that the presence of uniaxial anisotropy distorts the shape of spin wave modes forming in regions of uniform magnetisation. The presence of the uniaxial anisotropy was also demonstrated to produce distorted c-wave modes within the regions of uniform magnetisation, resulting in s-wave modes. As the size of the objects increased multiple of these s-wave modes began to form as the larger sizes allowed the larger s-waves to move away from the domain walls permitting the formation of further, shorter s-waves.

Examination of the effects of high amplitude magnetic pulses on larger objects demonstrated that as the size of the objects increases the vortex core may be induced to break down into multiple vortices and anti-vortices by the application of a strong enough magnetic field pulse. This behaviour has previously been observed experimentally in reference [27].

The cores were shown to collapse into a single vortex state whereupon the remaining vortex oscillated in a circular manner, describing a much larger area than those cores which did not undergo a core breakdown. The frequency of oscillation of this core was demonstrated to be the same as the frequency of oscillation seen in cores which did not undergo core breakdown however meaning the core breakdown also lead to an increase in the core velocity of the remaining core. The effects of the application of strain to this system could potentially form an interesting avenue for further research.

Finally, we demonstrated that introducing damping to the system does not affect the frequency of oscillation of any of the key modes and whilst damping reduces the amplitude of the spin wave modes it does not remove the secondary and tertiary modes from the system. The core breakdown event still occurred in the system with damping and resulted in the same effects observed in the undamped samples indicating that all observations made on the undamped samples may potentially be observed experimentally.

Chapter 7

Conclusions

In this thesis we have extensively studied different methods to alter the frequency of oscillation of VCO STO devices.

In chapter 4 we first investigated the effects of thickness on the magnetocrystaline anisotropy in sputter grown $Fe_{1-x}Ga_x$ thin films grown on GaAs using SQUID magnetometry. It was found that the uniaxial anisotropy increased as a function of thickness and the cubic anisotropy decreased as a function of thickness. At a thickness of 20nm the cubic anisotropy spiked to a unusually high value which was corroborated when a second 20nm sample exhibited the same unusual property. The samples grown as part of the second batch exhibited a very low uniaxial anisotropy, possibly due to a problem with the growth surface however the cubic anisotropy values of the second batch of films were roughly equal to the values found in the first batch. In order to test the fitting procedure, the process was repeated using pure iron films, producing results similar to those found previously indicating that the results found for the $Fe_{1-x}Ga_x$ films are reliable. The iron content in the $Fe_{1-x}Ga_x$ films was tested and found to be higher than expected however the iron concentration did not show any clear relation to the nominal thicknesses of the films indicating that differences in iron concentration were not responsible for the unusual anisotropy results.

Next the magnetostrictive properties of the films were tested using DC transport measurements of hall bars fabricated from some of the films studied by SQUID magnetometry. This study found that the magnetoelastic constants for $Fe_{1-x}Ga_x$ films grown by sputter deposition on a GaAs substrate closely matched those found for $Fe_{1-x}Ga_x$ films grown on GaAs substrates using MBE growth methods. The magnetoelastic constant for the 20nm $Fe_{1-x}Ga_x$ film was unusually high however the reason for the unusually high magnetoelastic constant is unclear. Finally X-ray diffractometry experiments were performed on samples S159, S219,S221 and S227 by Dr. P. Wadley. Whilst sample S159 was found to be too thin for X-ray diffractometry experiments to be performed the lattice constants for S219, S221

and S227 were determined. No clear relation between sample thickness and lattice parameter, lattice mismatch, mosaic block size or mosaic block misalignment could be determined however. Further experiments remain to be performed in order to determine the actual thickness of the films and the density of defects within the lattice. Further diffractomerty studies may also be required in order to study the unusual anisotropy results in samples S219, S411 and S411.

In chapter 5 20nm $Fe_{1-x}Ga_x$ squares were grown on waveguides which were used to study magnetisation precession and core gyrations. Three images sequences of $Fe_{1-x}Ga_x$ squares were successfully collected with device sizes of $10\mu m$, $3\mu m$ and 3.5 μm. Damped Spin wave modes were observed at a frequency of 2GHz in the 10um square as well as movement of the vortex core which persisted after the magnetic field pulse.

Significant core gyrations were observed in the 3um square due to frequency matching between the resonant frequency of gyration of the vortex core and the frequency of the pulse train exciting vortex core motion. This was confirmed by frequency analysis of the vortex core's motion showing that the vortex core oscillated at a frequency of 80$\pm$20MHz which is within error of the exciting pulse frequency of 83MHz. Simulation of the system indicated an oscillation frequency of 90$\pm$40MHz a value which is within error of the exciting pulse frequency. A 3.5μm $Fe_{1-x}Ga_x$ square was examined demonstrating that in a larger object the core only oscillated in the y direction indicating a difference in oscillation frequency due to the increased size of the object. Manual tracking of the vortex core indicated an oscillation frequency of 83$\pm$20MHz, and ROI scans indicated an oscillation frequency of 85.5 $\pm$2.2MHz, simulation of the device gave an oscillation frequency of 90$\pm$40MHz.

The experimental results indicate that the 3μm square experiences much greater frequency matching to the 83MHz pulse train than the 3.5μm square. Further experiments should be performed using the synchrotron in 156 bunch mode in order to determine the relation between object size and natural oscillation frequency across a larger range of object sizes and to determine whether the oscillations observed in these two samples may be reproduced in larger or smaller objects.

These squares did not respond to a stress applied by the transducer however and so the focus of the experiments moved onto Ni objects. These responded well to stress exhibiting the pinching demonstrated in chapter 6 however the damping in the Ni squares was too great to induce gyroscopic motion of the vortex core. Further work could involve the fabrication of waveguides on a piezoelectric material such as PMN-PT allowing for strain to be more directly applied to the samples potentially allowing for strain induced frequency tuning in $Fe_{0.81}Ga_{0.19}$ objects similar to that observed in simulations detailed in chapter 6. For this

to proceed the waveguide would need to be redesigned in order to take into account the difference in dielectric properties between a GaAs substrate and a PMN-PT substrate.

Chapter 6 began by examining the effects of strain on static objects and the sizes at which the strain anisotropy is dominated by the shape anisotropy. This was followed by an examination of the oscillatory modes within a 500nm $Fe_{0.81}Ga_{0.19}$ square with near zero damping using a magnetic field pulse similar to that used to study the $Fe_{0.81}Ga_{0.19}$ squares in chapter 6. Standing spin waves modes were observed to form along the domain walls of the sample at different frequencies depending on whether the domain wall ran along or at 90^o to the direction of the uniaxial anisotropy. Also observed was a s shaped standing spin wave in areas of uniform magnetisation running roughly in the same direction as the uniaxial anisotropy. The properties of the core's movement were studied and it was determined that the area described by the core would increase steadily with field whilst the frequency of oscillation remained constant meaning the vortex core's velocity would continually increase as a function of the amplitude of the exciting magnetic field pulse. Once the the amplitude of the field pulse reached 23mT the vortex core would undergo a vortex core switching event after which it would process in the opposite direction. The relation between magnetic field amplitude and the area described by the vortex core once the vortex core switching event had occurred became non-linear. This means that simulations of the experiment with greater time resolution need to be performed in order to understand the core's behaviour once the amplitude of the magnetic field pulse exceeds the switching field. Studies of the effects of increasing the amplitude of the exciting magnetic field pulse showed that the frequencies of oscillation of the spin modes were unaffected by increasing the amplitude of the magnetic field pulse however the linewidth of the standing spin wave modes was shown to increase due to the decrease in uniformity of the effective field along the domain walls and in areas of uniform magnetisation. Removing the uniaxial anisotropy of the system was observed to cause the domain walls to oscillate at the same frequency. This was followed by tests of the symmetry of the system where it was demonstrated that neither altering the angle of incidence of the magnetic field pulse or the chirality of the Landau flux closure state had any effect on the oscillatory modes of the system.

Next the effects of a strain induced anisotropy on the oscillatory modes of the system were investigated. It was found that a strain induced anisotropy not only reduced the oscillation frequency of the vortex core it also reduced the oscillation frequency of the domain walls of the system. The strain induced anisotropy was also shown to increase the vortex core switching field for both positively and negatively polarised vortex cores. This effect was shown to be amplified when the magnetic field pulse was applied at 90o to the direction of the strain induced anisotropy inviting further work investigating the effect of altering the

angle between strain induced anisotropy and magnetic field pulse as well as reproducing this work experimentally.

This investigation into the effects of strain induced anisotropy was followed by an investigation of the effects of shape anisotropy on the oscillation frequency of the spin modes in the system. This began by studying the frequency of oscillation of the vortex core as the size of the object increased and it was found that the frequency of oscillation was inversely proportional to the width of the square objects. This inverse proportionality was found in the frequency of oscillation of the domain walls as well however the fit of an inversely proportional relationship between object size and frequency of oscillation was found to be weaker for the domain wall modes than the vortex core mode due to the effects of uniaxial anisotropy being more influential on the frequency of oscillation of the domain wall modes than that of the vortex core mode. Images of the spin wave modes showed that as the size of the objects increased the shape of the domain wall modes showed asymmetry due to the uniaxial anisotropy causing domain wall modes along the [110] direction to become narrower and those along the $[1\bar{1}0]$ to become wider. The s-wave spin modes were also observed to form further away from the domain walls in larger objects allowing for a second s-wave to form in the areas of uniform magnetisation.

In order to investigate the spin wave modes forming in the areas of uniform magnetisation the 3D Fourier transformation program was modified to use a logarithmic scale. This allowed spin wave modes in areas of uniform magnetisation to be investigated despite their low intensity. This demonstrated that in the absence of unaxial anisotropy there are a number of spin wave modes with differing wavelengths within the areas of uniform magnetisation. The s-waves were not seen in the system with no uniaxial anisotropy but rather c-waves running close to the domain walls were observed. When the uniaxial anisotropy was re-introduced into the system the spin waves in the areas of uniform magnetisation were distorted by the presence of the uniaxial anisotropy. The c-waves along the [110] axis were also distorted by the presence of the uniaxial anisotropy producing the s-waves observed in previous frequency maps. As the size of the objects increased the s-waves moved away from the domain walls leading to the formation of a second s-wave once the first had moved sufficiently far away from the domain walls. This second s-wave tended to oscillate at a lower frequency than the first due to its shorter length however in the 2000nm square it became unclear which s-wave was oscillating at the highest frequency. Studying these systems in the presence of a strain induced anisotropy may provide an interesting avenue for future work.

Next the effects of high amplitude magnetic field pulses on a 2000nm objects were studied. The vortex core was shown to break down into multiple cores eventually recombining into a single vortex core undergoing gyroscopic motion. This vortex core was shown to describe

a much larger area once it had recombined than vortex cores which did not undergo vortex breakdown events. As the pulse amplitude continued to rise however the area described by the vortex core began to decrease again however indicating an ideal amplitude of magnetic field pulse for inducing vortex core oscillations with high power outputs. This work could be continued by applying a strain induced anisotropy to the system in order to determine the effects of a strain induced anisotropy on the core breakdown event.

Finally, the effects of applying realistic damping to the system were studied and it was determined that whist the amplitudes of the key modes were reduced by the damping it had no effect on the frequency of oscillation of the system. The core breakdown event was also observed in the damped simulations indicating that all observations from the undamped simulations may potentially be reproduced experimentally.

References

[1] M. N. Baibich, J. M. Broto, A. Fert, F. N. Van Dau, F. Petroff, P. Etienne, G. Creuzet, A. Friederich, and J. Chazelas, "Giant magnetoresistance of (001) Fe/(001) Cr magnetic superlattices," *Physical review letters*, vol. 61, no. 21, p. 2472, 1988.

[2] G. Binasch, P. Grünberg, F. Saurenbach, and W. Zinn, "Enhanced magnetoresistance in layered magnetic structures with antiferromagnetic interlayer exchange," *Physical review B*, vol. 39, no. 7, p. 4828, 1989.

[3] M. C. Sekhar, M. Tran, L. Wang, G. Han, and W. Lew, "Enhanced stability against spin torque noise in current perpendicular to the plane self-biased differential dual spin valves," *Journal of Magnetism and Magnetic Materials*, vol. 374, pp. 740–743, 2015.

[4] A. Fert, "Nobel lecture: Origin, development, and future of spintronics," *Reviews of Modern Physics*, vol. 80, no. 4, p. 1517, 2008.

[5] A. Goodman, K. O'Grady, N. Walmsley, and M. Parker, "Magnetisation reversal in spin-valve structures," *IEEE Transactions on Magnetics*, vol. 33, no. 5, pp. 2902–2904, 1997.

[6] R. R. Katti, J. L. Tucker, and A. Kohli, "Magnetoresistive random access memory (MRAM) package including a multilayer magnetic security structure," Aug. 19 2014. US Patent 8,811,072.

[7] D. Apalkov, A. Khvalkovskiy, S. Watts, V. Nikitin, X. Tang, D. Lottis, K. Moon, X. Luo, E. Chen, A. Ong, *et al.*, "Spin-transfer torque magnetic random access memory (stt-mram)," *ACM Journal on Emerging Technologies in Computing Systems (JETC)*, vol. 9, no. 2, p. 13, 2013.

[8] J. Heidecker, "Mram technology status," 2013.

[9] J. Manschot, A. Brataas, and G. E. Bauer, "Reducing the critical switching current in nanoscale spin valves," *Applied physics letters*, vol. 85, no. 15, pp. 3250–3252, 2004.

[10] K. C. Chun, H. Zhao, J. D. Harms, T.-H. Kim, J.-P. Wang, and C. H. Kim, "A scaling roadmap and performance evaluation of in-plane and perpendicular mtj based stt-mrams for high-density cache memory," *IEEE Journal of Solid-State Circuits*, vol. 48, no. 2, pp. 598–610, 2013.

[11] E. Grimaldi, R. Lebrun, A. Jenkins, A. Dussaux, J. Grollier, V. Cros, A. Fert, H. Kubota, K. Yakushiji, A. Fukushima, *et al.*, "Spintronic nano-oscillators: Towards nanoscale and tunable frequency devices," in *2014 IEEE International Frequency Control Symposium (FCS)*, pp. 1–6, IEEE, 2014.

[12] K. D. Sattler, *Handbook of nanophysics: functional nanomaterials*. CRC Press, 2010.

[13] R. Lehndorff, D. Bürgler, S. Gliga, R. Hertel, P. Grünberg, C. Schneider, and Z. Celinski, "Magnetization dynamics in spin torque nano-oscillators: Vortex state versus uniform state," *Physical Review B*, vol. 80, no. 5, p. 054412, 2009.

[14] P. Muduli, O. Heinonen, and J. Åkerman, "Temperature dependence of linewidth in nanocontact based spin torque oscillators: Effect of multiple oscillatory modes," *Physical Review B*, vol. 86, no. 17, p. 174408, 2012.

[15] A. Slavin, "Microwave sources: Spin-torque oscillators get in phase," *Nature nanotechnology*, vol. 4, no. 8, pp. 479–480, 2009.

[16] A. Slavin and V. Tiberkevich, "Nonlinear auto-oscillator theory of microwave generation by spin-polarized current," *IEEE Transactions on Magnetics*, vol. 45, no. 4, pp. 1875–1918, 2009.

[17] V. Pribiag, I. Krivorotov, G. Fuchs, P. Braganca, O. Ozatay, J. Sankey, D. Ralph, and R. Buhrman, "Magnetic vortex oscillator driven by dc spin-polarized current," *Nature Physics*, vol. 3, no. 7, pp. 498–503, 2007.

[18] T. Silva and W. Rippard, "Developments in nano-oscillators based upon spin-transfer point-contact devices," *Journal of Magnetism and Magnetic Materials*, vol. 320, no. 7, pp. 1260–1271, 2008.

[19] T. Taniguchi, H. Arai, H. Kubota, and H. Imamura, "Theoretical study of spin-torque oscillator with perpendicularly magnetized free layer," *IEEE Transactions on Magnetics*, vol. 50, no. 1, pp. 1–4, 2014.

[20] B. S. Min Gyu Albert Park, Seung-Heon Chris Baek, "Frequency control of a spin-torque oscillator using magnetostrictive anisotropy," *Applied Physics Letters*, vol. 108, no. 2, p. 023504, 2016.

[21] D. E. Parkes, R. Beardsley, S. Bowe, I. Isakov, P. A. Warburton, K. W. Edmonds, R. P. Campion, B. L. Gallagher, A. W. Rushforth, and S. A. Cavill, "Voltage controlled modification of flux closure domains in planar magnetic structures for microwave applications," *Applied Physics Letters*, vol. 105, no. 6, 2014.

[22] A. Houshang, E. Iacocca, P. Dürrenfeld, S. Sani, J. Åkerman, and R. Dumas, "Spin-wave-beam driven synchronization of nanocontact spin-torque oscillators," *Nature nanotechnology*, vol. 11, no. 3, pp. 280–286, 2016.

[23] T. Qu and R. Victora, "Phase-lock requirements in a serial array of spin transfer nano-oscillators," *Scientific reports*, vol. 5, 2015.

[24] A. Dussaux, A. Khvalkovskiy, J. Grollier, V. Cros, A. Fukushima, M. Konoto, H. Kubota, K. Yakushiji, S. Yuasa, K. Ando, *et al.*, "Phase locking of vortex based spin transfer oscillators to a microwave current," *Applied Physics Letters*, vol. 98, no. 13, p. 132506, 2011.

[25] W. Yu, P. S. Keatley, P. Gangmei, M. K. Marcham, T. Loughran, R. Hicken, S. A. Cavill, G. van der Laan, J. Childress, and J. Katine, "Observation of vortex dynamics in arrays of nanomagnets," *Physical Review B*, vol. 91, no. 17, p. 174425, 2015.

[26] P. Wessels, J. Ewald, M. Wieland, T. Nisius, G. Abbati, S. Baumbach, J. Overbuschmann, A. Vogel, A. Neumann, J. Viefhaus, *et al.*, "Time-resolved soft x-ray microscopy of magnetic nanostructures at the p04 beamline at petra III," in *Journal of Physics: Conference Series*, vol. 499, p. 012009, IOP Publishing, 2014.

[27] A. Kaiser, C. Wiemann, S. Cramm, and C. M. Schneider, "Influence of magnetocrystalline anisotropy on the magnetization dynamics of magnetic microstructures," *Journal of Physics: Condensed Matter*, vol. 21, no. 31, p. 314008, 2009.

[28] P. S. Keatley, V. Kruglyak, P. Gangmei, and R. Hicken, "Ultrafast magnetization dynamics of spintronic nanostructures," *Philosophical Transactions of the Royal Society of London A: Mathematical, Physical and Engineering Sciences*, vol. 369, no. 1948, pp. 3115–3135, 2011.

[29] J. Katine and E. E. Fullerton, "Device implications of spin-transfer torques," *Journal of Magnetism and Magnetic Materials*, vol. 320, no. 7, pp. 1217–1226, 2008.

[30] B. Van Waeyenberge, A. Puzic, H. Stoll, K. Chou, T. Tyliszczak, R. Hertel, M. Fähnle, H. Brückl, K. Rott, G. Reiss, *et al.*, "Magnetic vortex core reversal by excitation with short bursts of an alternating field," *Nature*, vol. 444, no. 7118, pp. 461–464, 2006.

[31] K.-S. Lee, S.-K. Kim, Y.-S. Yu, Y.-S. Choi, K. Y. Guslienko, H. Jung, and P. Fischer, "Universal criterion and phase diagram for switching a magnetic vortex core in soft magnetic nanodots," *Physical Review Letters*, vol. 101, no. 26, p. 267206, 2008.

[32] T. A. Ostler, R. Cuadrado, R. W. Chantrell, A. W. Rushforth, and S. A. Cavill, "Strain induced vortex core switching in planar magnetostrictive nanostructures," *Phys. Rev. Lett.*, vol. 115, p. 067202, Aug 2015.

[33] D. E. Kotecki, "A review of high dielectric materials for dram capacitors," *Integrated Ferroelectrics*, vol. 16, no. 1-4, pp. 1–19, 1997.

[34] D. T. Wang, *MODERN DRAM MEMORY SYSTEMS: PERFORMANCE ANALYSIS AND SCHEDULING ALGORITHM*. PhD thesis, University of Maryland, 2005.

[35] M. Noske, A. Gangwar, H. Stoll, M. Kammerer, M. Sproll, G. Dieterle, M. Weigand, M. Fähnle, G. Woltersdorf, C. H. Back, *et al.*, "Unidirectional sub-100ps magnetic vortex core reversal," *Physical Review B*, vol. 90, no. 10, p. 104415, 2014.

[36] B. Jacob, S. Ng, and D. Wang, *Memory systems: cache, DRAM, disk*. Morgan Kaufmann, 2010.

[37] ARM Ltd., "Single and dual port RAMs for low power and high performance memory implementations," 2016.

[38] L. Sandlund, M. Fahlander, T. Cedell, A. Clark, J. Restorff, and M. Wun-Fogle, "Magnetostriction, elastic moduli, and coupling factors of composite terfenol-D," *Journal of Applied Physics*, vol. 75, no. 10, pp. 5656–5658, 1994.

[39] R. C. Hall, "Single crystal anisotropy and magnetostriction constants of several ferromagnetic materials including alloys of NiFe, SiFe, AlFe, CoNi and CoFe," *Journal of Applied Physics*, vol. 30, pp. 816–819, 1958.

[40] H. Urquhart, K. Azumi, and J. Goldman, "Magnetostriction constants in iron-cobalt alloys," tech. rep., DTIC Document, 1953.

[41] J. Atulasimha and A. B. Flatau, "A review of magnetostrictive iron–gallium alloys," *Smart Materials and Structures*, vol. 20, no. 4, p. 043001, 2011.

[42] A. E. Clark, K. B. Hathaway, M. Wun-Fogle, J. B. Restorff, T. A. Lograsso, V. M. Keppens, G. Petculescu, and R. A. Taylor, "Extraordinary magnetoelasticity and lattice softening in bcc Fe-Ga alloys," *Journal of Applied Physics*, vol. 93, no. 10, 2003.

[43] Q. Xing, Y. Du, R. McQueeney, and T. Lograsso, "Structural investigations of Fe–Ga alloys: phase relations and magnetostrictive behavior," *Acta Materialia*, vol. 56, no. 16, pp. 4536–4546, 2008.

[44] R. Wu, "Origin of large magnetostriction in FeGa alloys," *Journal of Applied Physics*, vol. 91, no. 10, pp. 7358–7360, 2002.

[45] H. Wang, Y. Zhang, R. Wu, L. Sun, D. Xu, and Z. Zhang, "Understanding strong magnetostriction in Fe_{100-x} Ga_x alloys," *Scientific reports*, vol. 3, 2013.

[46] J. Cullen, P. Zhao, and M. Wuttig, "Anisotropy of crystalline ferromagnets with defects," *Journal of applied physics*, vol. 101, no. 12, p. 123922, 2007.

[47] S. Pascarelli, M. Ruffoni, R. S. Turtelli, F. Kubel, and R. Grössinger, "Local structure in magnetostrictive melt-spun Fe_{80} Ga_{20} alloys," *Physical Review B*, vol. 77, no. 18, p. 184406, 2008.

[48] D. Wu, Q. Xing, R. W. McCallum, and T. A. Lograsso, "Magnetostriction of iron-germanium single crystals," *Journal of Applied Physics*, vol. 103, no. 7, 2008.

[49] A. Muñoz-Noval, A. Ordóñez-Fontes, and R. Ranchal, "Influence of the sputtering flow regime on the structural properties and magnetic behavior of Fe-Ga thin films (Ga 30 at.%)," *Physical Review B*, vol. 93, no. 21, p. 214408, 2016.

[50] G. Petculescu, K. B. Hathaway, T. A. Lograsso, M. Wun-Fogle, and A. E. Clark, "Magnetic field dependence of galfenol elastic properties," *Journal of Applied Physics*, vol. 97, no. 10, 2005.

[51] M. J. Donahue and D. G. Porter, *OOMMF User's guide*. US Department of Commerce, Technology Administration, National Institute of Standards and Technology, 1999.

[52] B. D. Cullity, *Introduction to Magnetic Materials*. Menlo Park, California: The Addison-Wesley Publishing Company, 1972.

[53] E. Klokholm and J. A. Aboaf, "The saturation magnetostriction of permalloy films," *Journal of Applied Physics*, vol. 52, p. 2474, 1981.

[54] J. Dean, M. Bryan, N. Morley, G. Hrkac, A. Javed, M. Gibbs, and D. Allwood, "Numerical study of the effective magnetocrystalline anisotropy and magnetostriction in polycrystalline FeGa films," *Journal of Applied Physics*, vol. 110, no. 4, p. 043902, 2011.

[55] L. Daniel and N. Galopin, "A constitutive law for magnetostrictive materials and its application to terfenol-D single and polycrystals," *The European Physical Journal Applied Physics*, vol. 42, no. 2, pp. 153–159, 2008.

[56] R. C. ÓHandley, *Modern Magnetic Materials: Principles and Applications*. Springer, 2000.

[57] R. Gerd Steinle-Neumann, Lards Stixrude, "First-principles elastic constants for the hcp transition metals Fe, Co, and Re at high pressure," *Physical Review B*, vol. 60, pp. 791–799, 1999.

[58] N. G. Einspruch and L. T. Claiborne, "Elastic constants of a (73.8 % Ni-26.2 % Fe) ferromagnetic alloy," *Journal of Applied Physics*, vol. 35, p. 175, 1963.

[59] C. Rossignol, B. Perrin, B. Bonello, P. Djemia, P. Moch, and H. Hurdequint, "Elastic properties of ultrathin permalloy/alumina multilayer films using picosecond ultrasonics and brillouin light scattering," *Physical Review B*, vol. 70, no. 9, p. 094102, 2004.

[60] R. Kellogg, A. B. Flatau, A. Clark, M. Wun-Fogle, and T. A. Lograsso, "Temperature and stress dependencies of the magnetic and magnetostrictive properties of $Fe_{0.81}Ga_{0.19}$," *Journal of applied physics*, vol. 91, no. 10, pp. 7821–7823, 2002.

[61] D. Parkes, L. Shelford, P. Wadley, V. Holỳ, M. Wang, A. Hindmarch, G. Van Der Laan, R. Campion, K. Edmonds, S. Cavill, *et al.*, "Magnetostrictive thin films for microwave spintronics," *Scientific reports*, vol. 3, no. 2220, 2013.

[62] A. T. Hindmarch, "Revealing the volume magnetic anisotropy of Fe films epitaxied on GaAs(001) surface," *Applied Physics Letters*, vol. 98, p. 132505, 2011.

[63] A. T. Hindmarch, "Interface magnetism in ferromagnetic metal–compound semiconductor hybrid structures," in *Spin*, vol. 1, pp. 45–69, World Scientific, 2011.

[64] J. Atulasimha and A. B. Flatau, "Experemental actuation and sensing behaviour of single-crystal iron-gallium alloys," *Journal of Intelligent Material Systems and Structures*, vol. 19, pp. 1371–1381, 2008.

[65] F. J. Giessibl, "Advances in atomic force microscopy," *Reviews of modern physics*, vol. 75, no. 3, p. 949, 2003.

[66] M. Dreyer, M. Löhndorf, A. Wadas, and R. Wiesendanger, "Ultra-high-vacuum magnetic force microscopy of the domain structure of ultra-thin Co films," *Applied Physics A: Materials Science & Processing*, vol. 66, pp. 1209–1212, 1998.

[67] Y. Seo, P. Cadden-Zimansky, and V. Chandrasekhar, "Low-temperature high-resolution magnetic force microscopy using a quartz tuning fork," *Applied Physics Letters*, vol. 87, no. 10, p. 103103, 2005.

[68] J. L. Hockel, A. Bur, T. Wu, K. P. Wetzlar, and G. P. Carman, "Electric field induced magnetization rotation in patterned Ni ring/Pb $(Mg_{1/3}Nb_{2/3})$ O3]$_{(1-0.32)}$-[$PbTiO_3$]$_{0.32}$ heterostructures," *Applied Physics Letters*, vol. 100, no. 2, p. 022401, 2012.

[69] A. Hubert and R. Schäfer, *Magnetic Domains: The analysis of Magnetic Microstructures*. Springer, 1998.

[70] A. Barman, T. Kimura, Y. Otani, Y. Fukuma, K. Akahane, and S. Meguro, "Benchtop time-resolved magneto-optical kerr magnetometer," *Review of Scientific Instruments*, vol. 79, no. 12, p. 123905, 2008.

[71] T. Eimüller, P. Fischer, G. Schütz, P. Guttmann, G. Schmahl, K. Pruegl, and G. Bayreuther, "Magnetic transmission x-ray microscopy: imaging magnetic domains via the x-ray magnetic circular dichroism," *Journal of alloys and compounds*, vol. 286, no. 1, pp. 20–25, 1999.

[72] V. Uhlíř, M. Urbánek, L. Hladík, J. Spousta, M. Im, P. Fischer, N. Eibagi, J. Kan, E. Fullerton, and T. Šikola, "Dynamic switching of the spin circulation in tapered magnetic nanodisks," *Nature nanotechnology*, vol. 8, no. 5, pp. 341–346, 2013.

[73] W. Meyer-Ilse, G. Denbeaux, L. Johnson, W. Bates, A. Lucero, and E. Anderson, "The high resolution x-ray microscope, XM-1," in *X-ray microscopy: Proceedings of the VI International Conference*, vol. 507, pp. 129–134, AIP Publishing, 2000.

[74] C. Kittel and D. F. Holcomb, "Introduction to solid state physics," *American Journal of Physics*, vol. 35, no. 6, pp. 547–548, 1967.

[75] J. C. Slater, "Atomic shielding constants," *Physical Review*, vol. 36, no. 1, p. 57, 1930.

[76] H. Bethe, *Quantenmechanik der Ein-und Zwei-Elektronenprobleme*. Springer, 1933.

[77] M. Getzlaff, *Fundamentals of magnetism*. Springer Science & Business Media, 2007.

[78] G. Wastlbauer and J. A. C. Bland, "Structural and magnetic properties of ultrathin epitaxial Fe films on GaAs(001) and related semiconductor substrates," *Advances in Physics*, vol. 54, pp. 137–219, 2005.

[79] D. Craik, *Magnetism:Principles and applications*. Baffins Lane, Chichester, West Sussex, PO19 IUD, England: John Wiley and sons Ltd., 1995.

[80] B. Heinrich, T. Monchesky, and R. Urban, "Role of interfaces in higher order angular terms of magnetic anisotropies: ultrathin film structures," *Journal of magnetism and magnetic materials*, vol. 236, no. 3, pp. 339–346, 2001.

[81] Y. Xu, E. Kernohan, D. Freeland, M. Tselepi, A. Ercole, and J. Bland, "Structure and magnetic properties of epitaxial Fe films on GaAs (100) and InAs (100)," *Journal of magnetism and magnetic materials*, vol. 198, pp. 703–706, 1999.

[82] B. Lépine, C. Lallaizon, S. Ababou, A. Guivarc'h, S. Députier, A. Filipe, F. N. Van Dau, A. Schuhl, F. Abel, and C. Cohen, "Fe/GaAs (001) and Fe/GaSb (001) heterostructures: epitaxial growth and magnetic properties," *Journal of crystal growth*, vol. 201, pp. 702–706, 1999.

[83] F. Bensch, R. Moosbühler, and G. Bayreuther, "Onset of magnetic anisotropy in epitaxial Fe films on GaAs (001)," *Journal of applied physics*, vol. 91, no. 10, pp. 8754–8756, 2002.

[84] M. Gester, C. Daboo, R. Hicken, S. Gray, and J. Bland, "Thickness-dependent in-plane magnetic anisotropy in epitaxial Fe films on GaAs substrates," *Thin Solid Films*, vol. 275, no. 1, pp. 91–94, 1996.

[85] Y. Xu, E. Kernohan, D. Freeland, A. Ercole, M. Tselepi, and J. Bland, "Evolution of the ferromagnetic phase of ultrathin Fe films grown on GaAs (100)-4$\times$ 6," *Physical Review B*, vol. 58, no. 2, p. 890, 1998.

[86] G. Prinz, G. Rado, and J. Krebs, "Magnetic properties of single-crystal $\{110\}$ iron films grown on GaAs by molecular beam epitaxy," *Journal of Applied Physics*, vol. 53, no. 3, pp. 2087–2091, 1982.

[87] S. Mirbt, B. Sanyal, C. Isheden, and B. Johansson, "First-principles calculations of Fe on GaAs (100)," *Physical Review B*, vol. 67, no. 15, p. 155421, 2003.

[88] M. Brockmann, M. Zölfl, S. Miethaner, and G. Bayreuther, "In-plane volume and interface magnetic anisotropies in epitaxial Fe films on GaAs (001)," *Journal of magnetism and magnetic materials*, vol. 198, pp. 384–386, 1999.

[89] A. Kaiser, C. Wiemann, S. Cramm, and C. M. Schneider, "Influence of magnetocrystalline anisotropy on the magnetization dynamics of magnetic microstructures," *Journal of Physics: Condensed Matter*, vol. 21, no. 31, p. 314008, 2009.

[90] O. Thomas, Q. Shen, P. Schieffer, N. Tournerie, and B. Lépine, "Interplay between anisotropic strain relaxation and uniaxial interface magnetic anisotropy in epitaxial Fe films on (001) GaAs," *Physical review letters*, vol. 90, no. 1, p. 017205, 2003.

[91] M. Shayegan, K. Karrai, Y. Shkolnikov, K. Vakili, E. De Poortere, and S. Manus, "Low-temperature, in situ tunable, uniaxial stress measurements in semiconductors using a piezoelectric actuator," *Applied physics letters*, vol. 83, no. 25, pp. 5235–5237, 2003.

[92] I. Campbell, A. Fert, and O. Jaoul, "The spontaneous resistivity anisotropy in Ni-based alloys," *Journal of Physics C: Solid State Physics*, vol. 3, no. 1S, p. S95, 1970.

[93] T. R. McGuire and R.I.Potter, "Anisotropic magnetoresistance in ferromagnetic 3d alloys," *IEEE Transactions on Magnetics*, vol. 11, 4, pp. 1018–1038, 1975.

[94] C. H. Marrows, "Spin-polarised currents and magnetic domain walls," *Advances in Physics*, vol. 54, pp. 585–713, 2005.

[95] A. Aharoni, *Introduction to the Theory of Ferromagnetism*. Oxford University Press, Great Clarendon Street, Oxford, OX2 6DP: Oxford University Press, 2000.

[96] B. Westerstrand, P. Nordblad, and L. Nordborg, "The magnetocrystalline anisotropy constants of iron and iron-silicon alloys," *Physica Scripta*, vol. 11, no. 6, p. 383, 1975.

[97] A. E.J.Torok and H.N.Oredson, "Transition between Bloch and Néel walls," *Journal of Applied Physics*, vol. 36, pp. 1394–1399, 1964.

[98] J. Stöhr and H. C. Siegmann, "Magnetism," *Solid-State Sciences. Springer, Berlin, Heidelberg*, vol. 5, 2006.

[99] P. Wadley, *X-ray Magnetic Circular Dichromism Studies of III-Mn-V Compounds and Heterostructures*. PhD thesis, University of Nottingham, 2012.

[100] A. A. Freeman, *Magnetic X-ray Spectroscopy Studies of Dilute Magnetic Semiconductors*. PhD thesis, University of Nottingham, 2009.

[101] B. Lenk, H. Ulrichs, F. Garbs, and M. Münzenberg, "The building blocks of magnonics," *Physics Reports*, vol. 507, no. 4, pp. 107–136, 2011.

[102] N. Mecking, *A comprehensive study of the AMR-induced microwave photovoltage, photocurrent and photoresistance in Permalloy microstrips*. Verlag Dr. Hut, 2008.

[103] J. Jorzick, S. Demokritov, C. Mathieu, B. Hillebrands, B. Bartenlian, C. Chappert, F. Rousseaux, and A. Slavin, "Brillouin light scattering from quantized spin waves in micron-size magnetic wires," *Physical Review B*, vol. 60, no. 22, p. 15194, 1999.

[104] M. Bailleul, R. Höllinger, K. Perzlmaier, and C. Fermon, "Microwave spectrum of square permalloy dots: Multidomain state," *Physical Review B*, vol. 76, no. 22, p. 224401, 2007.

[105] K. Wagner, A. Kákay, K. Schultheiss, A. Henschke, T. Sebastian, and H. Schultheiss, "Magnetic domain walls as reconfigurable spin-wave nanochannels," *Nature nanotechnology*, vol. 11, no. 5, pp. 432–436, 2016.

[106] R. Damon and J. Eshbach, "Magnetostatic modes of a ferromagnetic slab," *Journal of applied physics*, vol. 31, no. 5, pp. S104–S105, 1960.

[107] A. Thiele, "Steady-state motion of magnetic domains," *Physical Review Letters*, vol. 30, no. 6, p. 230, 1973.

[108] D. Huber, "Dynamics of spin vortices in two-dimensional planar magnets," *Physical Review B*, vol. 26, no. 7, p. 3758, 1982.

[109] A. Drews, *Dynamics of magnetic vortices and antivortices*. PhD thesis, The University of Hamburg, 2009.

[110] B. Krüger, A. Drews, M. Bolte, U. Merkt, D. Pfannkuche, and G. Meier, "Harmonic oscillator model for current-and field-driven magnetic vortices," *Physical Review B*, vol. 76, no. 22, p. 224426, 2007.

[111] S. Gliga, *Ultrafast vortex core dynamics investigated by finite-element micromagnetic simulations*, vol. 79. Forschungszentrum Jülich, 2010.

[112] R. D. Knight, *Physics for scientists and engineers*, vol. 1. Pearson, 2004.

[113] E. De Ranieri, P. Roy, D. Fang, E. Vehsthedt, A. Irvine, D. Heiss, A. Casiraghi, R. Campion, B. Gallagher, T. Jungwirth, *et al.*, "Piezoelectric control of the mobility of a domain wall driven by adiabatic and non-adiabatic torques," *Nature materials*, vol. 12, no. 9, pp. 808–814, 2013.

[114] A. T. Hindmarch, D. E. Parkes and A. W. Rushforth, "Fabrication of metallic magnetic nanostructures by argon ion milling using a reversed-polarity planar magnetron ion source," *Vacuum*, vol. 86, no. 10, pp. 1600–1604, 2012.

[115] R. L. Fagaly, "Superconducting quantum interference device instruments and applications," *Review of Scientific Instruments*, vol. 77, p. 101101, 2006.

[116] S. Kasap and P. Capper, *Handbook of Electronic and Photonic Materials*. Springer, 2006.

[117] J. W. Cooley and J. W. Tukey, "An algorithm for the machine calculation of complex Fourier series," *Mathematics of Computation*, vol. 19, no. 90, pp. 297–301, 1965.

[118] V. Grant, *Growth and Characterisation of III-V Semiconductor Nanostructures*. PhD thesis, School of Physics and Astronomy, University of Nottingham, 2008.

[119] J. Stöhr, Y. Wu, B. Hermsmeier, M. Samant, G. Harp, S. Koranda, D. Dunham, and B. Tonner, "Element-specific magnetic microscopy with circularly polarized x-rays," *Science-New York then Washington-*, vol. 259, pp. 658–658, 1993.

[120] H. Hopster and H. P. Oepen, *Magnetic Microscopy of Nanostructures*. Germany: Springer, 2005.

[121] J. Stöhr, H. A. Padmore, S. Anders, T. Stammler and M. R. Scheinfein, "Principles of x-ray dichromism spectromicroscopy," *Surface review and letters*, vol. 5, pp. 1297–1308, 1998.

[122] T. Schmidt, S. Heun, J. Slezak, J. Diaz, K. Prince, G. Lilienkamp, and E. Bauer, "Speleem: combining leem and spectroscopic imaging," *Surface Review and Letters*, vol. 5, no. 06, pp. 1287–1296, 1998.

[123] S. Heun, Y. Watanabe, "Photoelectron spectroscopy with a photoemission electron microscope," *Nanoscale Spectroscopy and its Applications to Semiconductor Research*, vol. 588, pp. 157–171, 2002.

[124] S. Nakagawa, "Magnetic objective lens for use in a scanning electron microscope." US Patent, December 1983. US 06/338622.

[125] A. T. J. B. Eppink and D. H. Parker, "Velocity map imaging of ions and electrons using electrostatic lenses: Application in photoelectron and photofragment ion imaging of molecular oxygen," *Review of Scientific Instruments*, vol. 68, pp. 3477–3484, 1997.

[126] S. Hufner, *Photoelectron Spectroscopy*. D-66041 Saarbrucken, Germany: Springer, 1996.

[127] Diamond light source, "Beamlines I06-design specifications," May 2009.

[128] D. Parkes, *Strain Control of Ferromagnetic Thin Films and Devices*. PhD thesis, University of Nottingham, School of Physics and Astronomy, 2016.

[129] Diamond Light Source, "Machine page," May 2015.

[130] L. R. Nivedita, V. V. S. Kumar, K. Asokan, and R. T. Rajendrakumar, "Growth and Magnetic Properties of RF Sputtered Fe-Ga Thin Films," *Materials Research*, vol. 18, pp. 946 – 952, 10 2015.

[131] E. M. Kneedler, B. T. Jonker, P. M. Thibado, R. J. Wagner, B. V. Shanabrook, and L. J. Whitman, "Influence of substrate surface reconstruction on the growth and magnetic properties of Fe on GaAs(001)," *Phys. Rev. B*, vol. 56, pp. 8163–8168, Oct 1997.

[132] K.-Y. Wang, M. Sawicki, K. Edmonds, R. Campion, S. Maat, C. Foxon, B. Gallagher, and T. Dietl, "Spin reorientation transition in single-domain (Ga, Mn) As," *Physical review letters*, vol. 95, no. 21, p. 217204, 2005.

[133] D. E. Parkes, S. A. Cavill, A. T. Hindmarch, P. Wadley, F. McGee, C. R. Staddon, K. W. Edmonds, R. P. Campion, B. L. Gallagher and A. W. Rushforth, "Non-volatile voltage control of magnetization and magnetic domain walls in magnetostrictive epitaxial thin films," *Applied Physics Letters*, vol. 101, p. 072402, 2012.

[134] P. Shepley, A. Rushforth, M. Wang, G. Burnell, and T. Moore, "Modification of perpendicular magnetic anisotropy and domain wall velocity in pt/co/pt by voltage-induced strain," *Scientific reports*, vol. 5, 2015.

[135] J. C. Fuggle and N. Mårtensson, "Core-level binding energies in metals," *Journal of Electron Spectroscopy and Related Phenomena*, vol. 21, no. 3, pp. 275–281, 1980.

[136] Centronic, *AEPX65 Datasheet*.

[137] S.-B. Choe, Y. Acremann, A. Scholl, A. Bauer, A. Doran, J. Stöhr, and H. A. Padmore, "Vortex core-driven magnetization dynamics," *Science*, vol. 304, no. 5669, pp. 420–422, 2004.

[138] J. Raabe, C. Quitmann, C. Back, F. Nolting, S. Johnson, and C. Buehler, "Quantitative analysis of magnetic excitations in landau flux-closure structures using synchrotron-radiation microscopy," *Physical review letters*, vol. 94, no. 21, p. 217204, 2005.

[139] Photon Design, "FIMMWAVE product website," December 2012.

[140] A. Wee, D. B. Grayden, Y. Zhu, K. Petkovic-Duran, and D. Smith, "A continuous wavelet transform algorithm for peak detection," *Electrophoresis*, vol. 29, no. 20, pp. 4215–4225, 2008.

[141] K.-W. Moon, B. S. Chun, W. Kim, Z. Qiu, and C. Hwang, "Duffing oscillation-induced reversal of magnetic vortex core by a resonant perpendicular magnetic field," *Scientific reports*, vol. 4, 2014.

[142] J. Park, P. Eames, D. Engebretson, J. Berezovsky, and P. Crowell, "Imaging of spin dynamics in closure domain and vortex structures," *Physical Review B*, vol. 67, no. 2, p. 020403, 2003.

Appendix A

SQUID magnetometry Fitting comparisons

This appendix contains the loops fitted to the SQUID data in chapter 4. In each figure the experimental data is represented by the black line and the simulated data by the blue line.

Fig. A.1 Demonstration of the relation between simulated data and experimental data collected using a SQUID magnetometer used to find K_c and K_u for a 10nm $Fe_{1-x}Ga_x$ film grown on GaAs at a temperature of 2K. The magnetic hysteresis loop produced with decreasing field is shown in black in a) with its fit in blue. b) shows the magnetic hysteresis loop with increasing field and its fit.

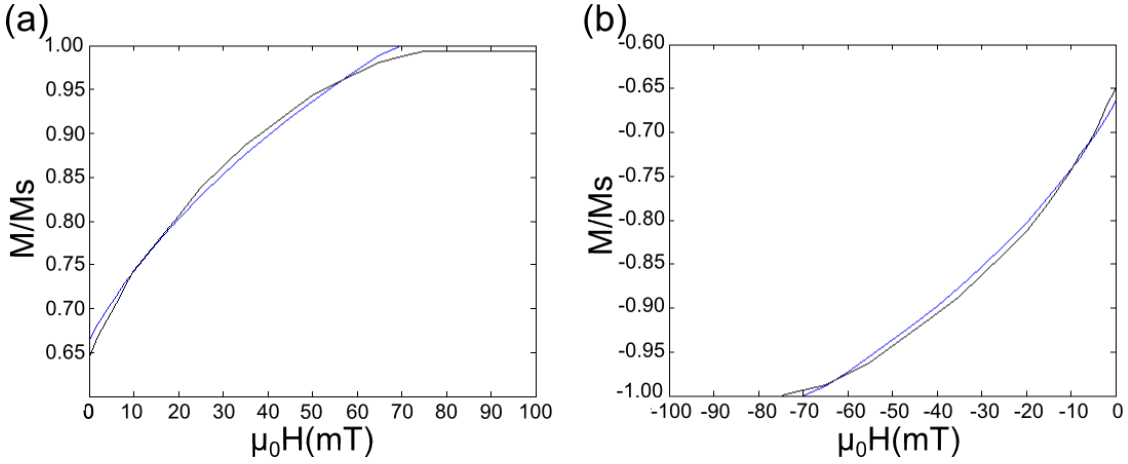

Fig. A.2 Demonstration of the relation between simulated data and experimental data collected using a SQUID magnetometer used to find K_c and K_u for a 20nm $Fe_{1-x}Ga_x$ film grown on GaAs at a temperature of 2K.The magnetic hysteresis loop produced with decreasing field is shown in black in a) with its fit in blue. b) shows the magnetic hysteresis loop with increasing field and its fit.

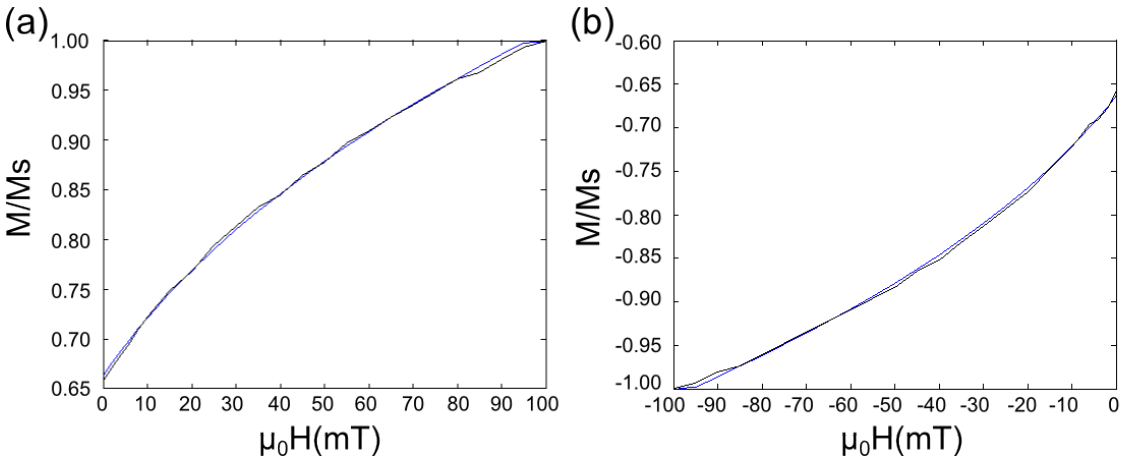

Fig. A.3 Demonstration of the relation between simulated data and experimental data collected using a SQUID magnetometer used to find K_c and K_u for a 30nm $Fe_{1-x}Ga_x$ film grown on GaAs at a temperature of 2K.The magnetic hysteresis loop produced with decreasing field is shown in black in a) with its fit in blue. b) shows the magnetic hysteresis loop with increasing field and its fit.

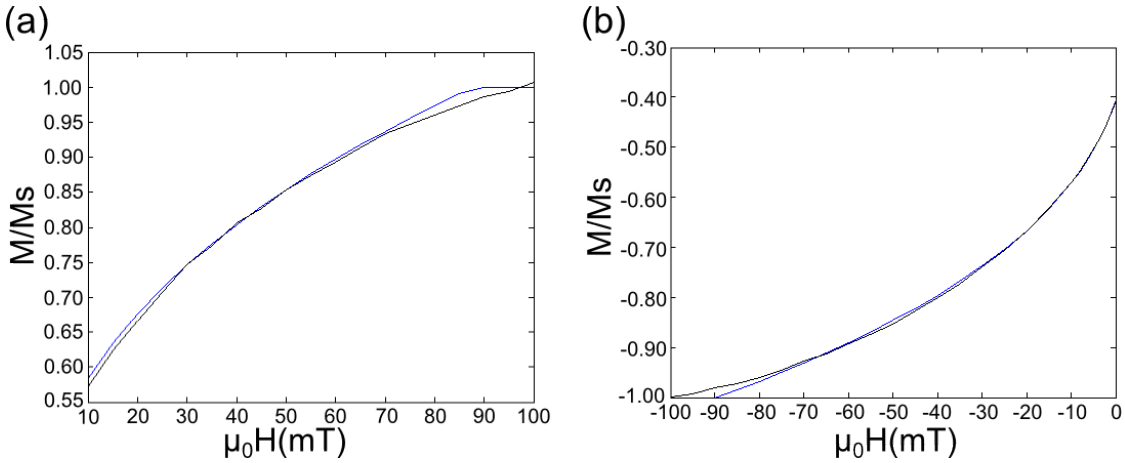

Fig. A.4 Demonstration of the relation between simulated data and experimental data collected using a SQUID magnetometer used to find K_c and K_u for a 100nm $Fe_{1-x}Ga_x$ film grown on GaAs at a temperature of 2K. The magnetic hysteresis loop produced with decreasing field is shown in black in a) with its fit in blue. b) shows the magnetic hysteresis loop with increasing field and its fit.

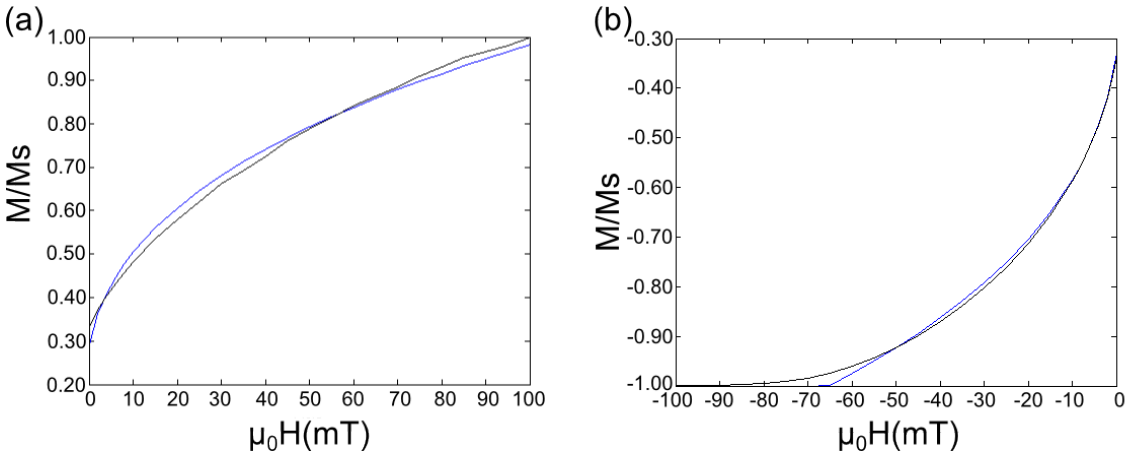

Fig. A.5 Demonstration of the relation between simulated data and experimental data collected using a SQUID magnetometer used to find K_c and K_u for a 10nm $Fe_{1-x}Ga_x$ film grown on GaAs at a temperature of 300K. The magnetic hysteresis loop produced with decreasing field is shown in black in a) with its fit in blue. b) shows the magnetic hysteresis loop with increasing field and its fit.

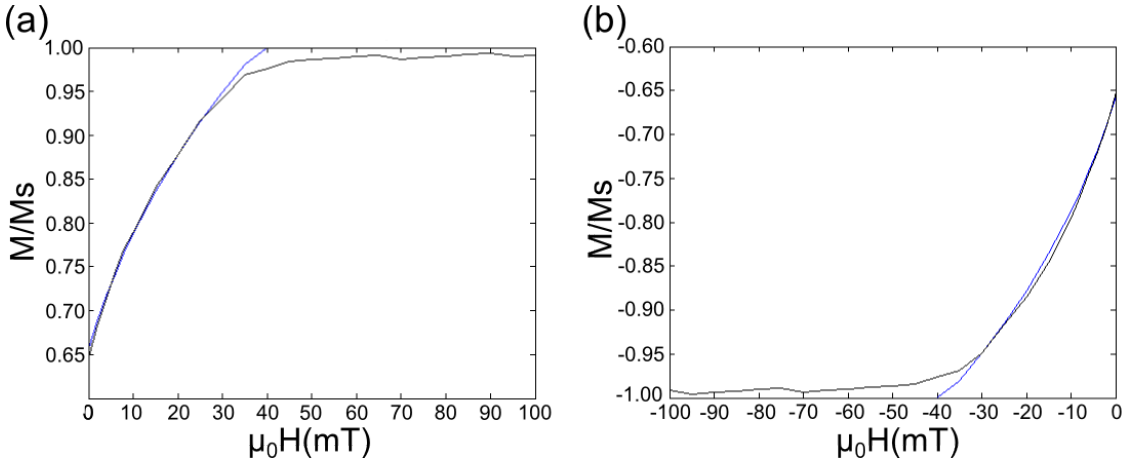

Fig. A.6 Demonstration of the relation between simulated data and experimental data collected using a SQUID magnetometer used to find K_c and K_u for a 20nm $Fe_{1-x}Ga_x$ film grown on GaAs at 300K. The magnetic hysteresis loop produced with decreasing field is shown in black in a) with its fit in blue. b) shows the magnetic hysteresis loop with increasing field and its fit.

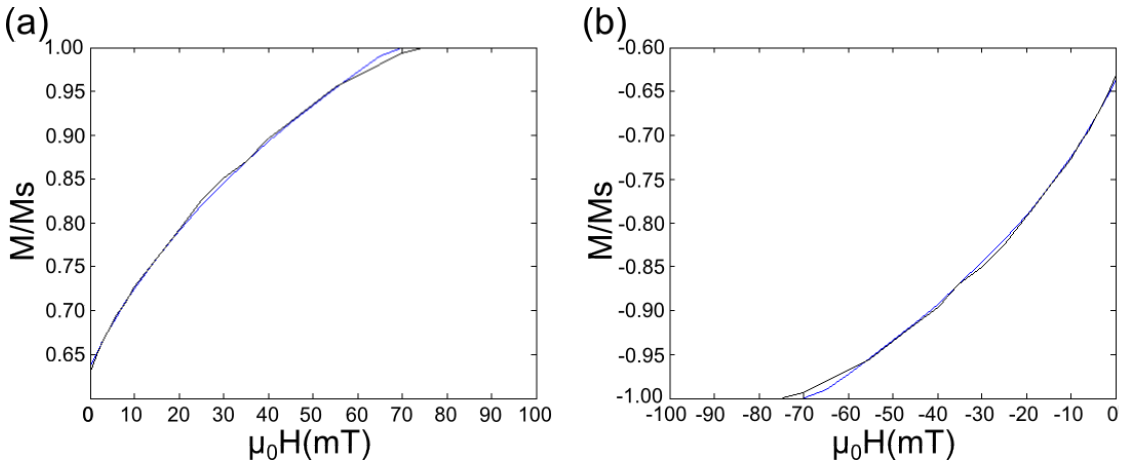

Fig. A.7 Demonstration of the relation between simulated data and experimental data collected using a SQUID magnetometer used to find K_c and K_u for a 30nm $Fe_{1-x}Ga_x$ film grown on GaAs at 300K. The magnetic hysteresis loop produced with decreasing field is shown in black in a) with its fit in blue. b) shows the magnetic hysteresis loop with increasing field and its fit.

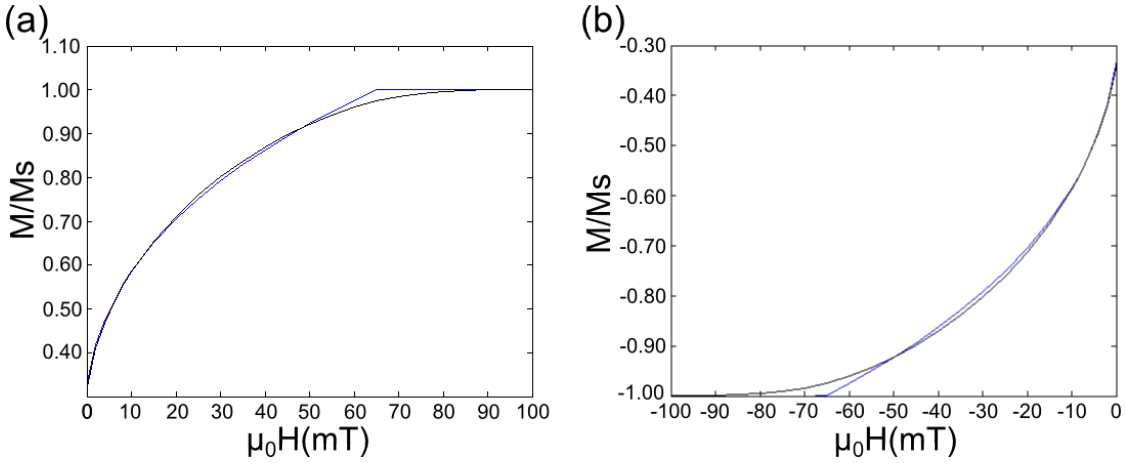

Fig. A.8 Demonstration of the relation between simulated data and experimental data collected using a SQUID magnetometer used to find K_c and K_u for a 100nm $Fe_{1-x}Ga_x$ film grown on GaAs at 300K. The magnetic hysteresis loop produced with decreasing field is shown in black in a) with its fit in blue. b) shows the magnetic hysteresis loop with increasing field and its fit.

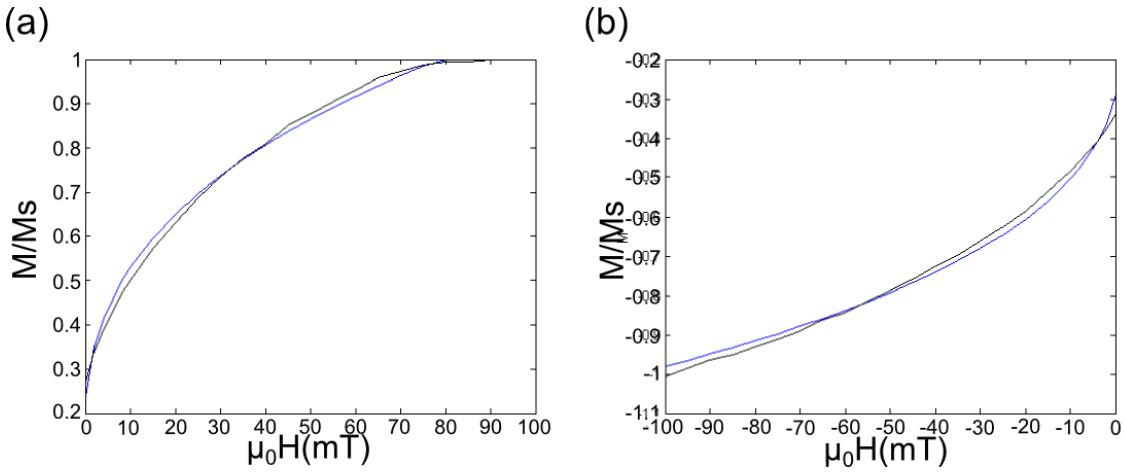

Fig. A.9 Demonstration of the relation between simulated data and experimental data collected using a SQUID magnetometer used to find K_c and K_u for a 10nm Fe film grown on GaAs at a temperature of 2K. The magnetic hysteresis loop produced with decreasing field is shown in black in a) with its fit in blue. b) shows the magnetic hysteresis loop with increasing field and its fit.

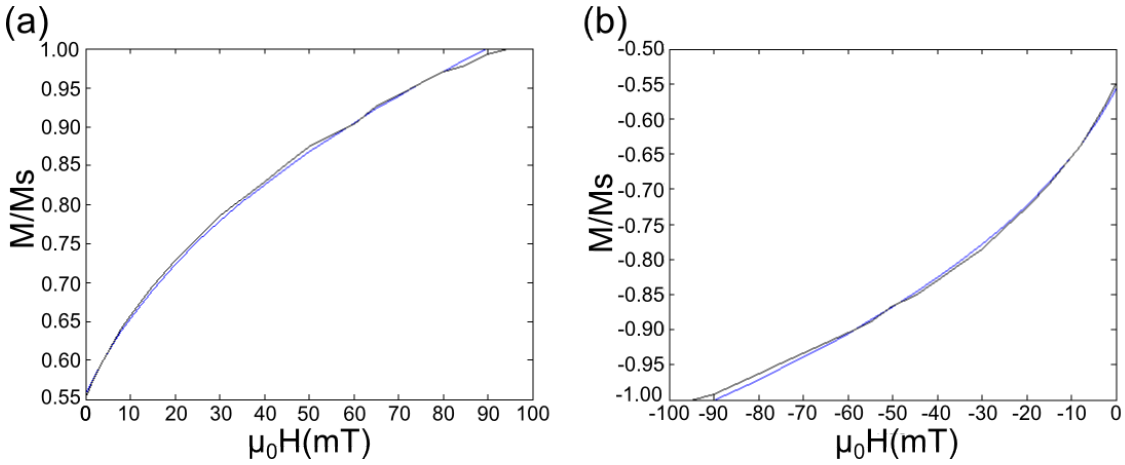

Fig. A.10 Demonstration of the relation between simulated data and experimental data collected using a SQUID magnetometer used to find K_c and K_u for a 20nm Fe film grown on GaAs at a temperature of 2K. The magnetic hysteresis loop produced with decreasing field is shown in black in a) with its fit in blue. b) shows the magnetic hysteresis loop with increasing field and its fit.

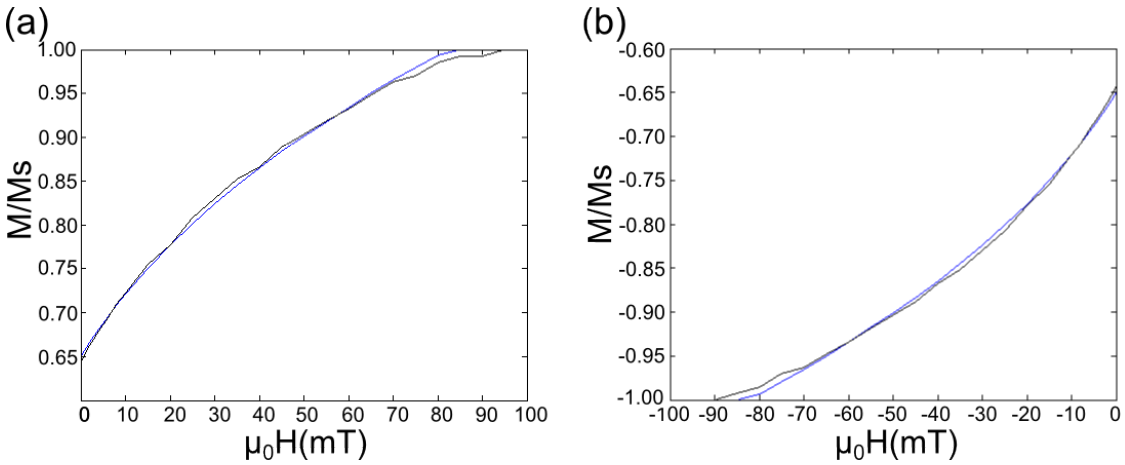

Fig. A.11 Demonstration of the relation between simulated data and experimental data collected using a SQUID magnetometer used to find K_c and K_u for a 30nm Fe film grown on GaAs at 2K. The magnetic hysteresis loop produced with decreasing field is shown in black in a) with its fit in blue. b) shows the magnetic hysteresis loop with increasing field and its fit.

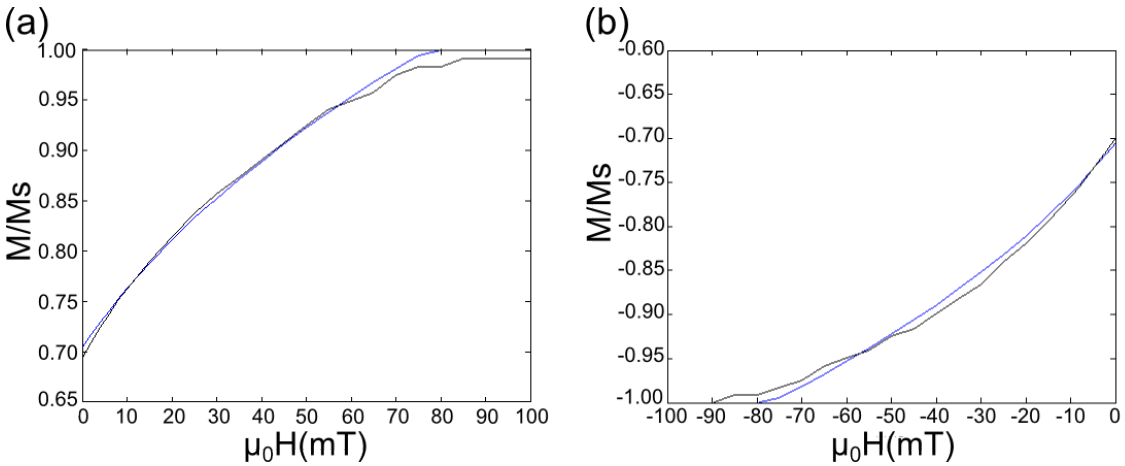

Fig. A.12 Demonstration of the relation between simulated data and experimental data collected using a SQUID magnetometer used to find K_c and K_u for a 10nm Fe film grown on GaAs at 300K. The magnetic hysteresis loop produced with decreasing field is shown in black in a) with its fit in blue. b) shows the magnetic hysteresis loop with increasing field and its fit.

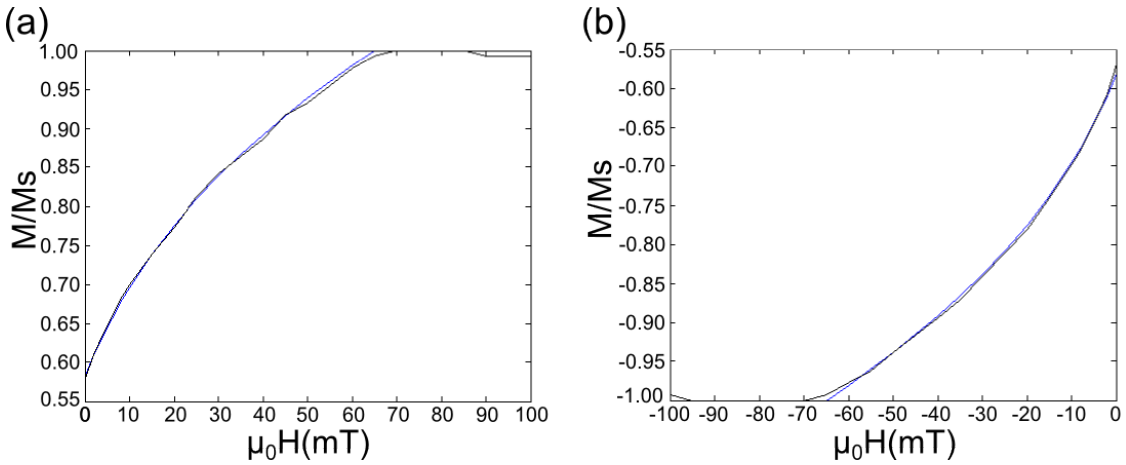

Fig. A.13 Demonstration of the relation between simulated data and experimental data collected using a SQUID magnetometer used to find K_c and K_u for a 20nm Fe film grown on GaAs at 300K. The magnetic hysteresis loop produced with decreasing field is shown in black in a) with its fit in blue. b) shows the magnetic hysteresis loop with increasing field and its fit.

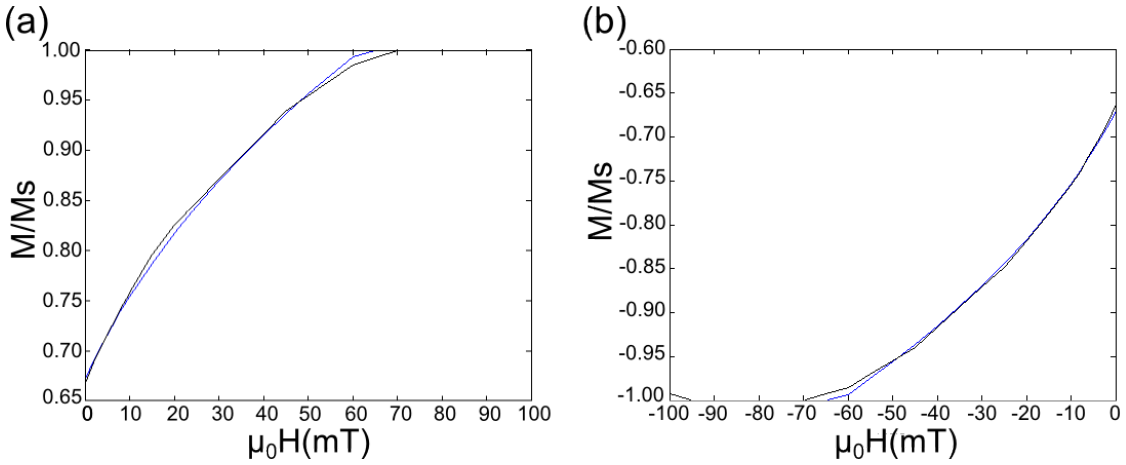

Fig. A.14 Demonstration of the relation between simulated data and experimental data collected using a SQUID magnetometer used to find K_c and K_u for a 30nm Fe film grown on GaAs at a temperature of 300K. The magnetic hysteresis loop produced with decreasing field is shown in black in a) with its fit in blue. b) shows the magnetic hysteresis loop with increasing field and its fit.

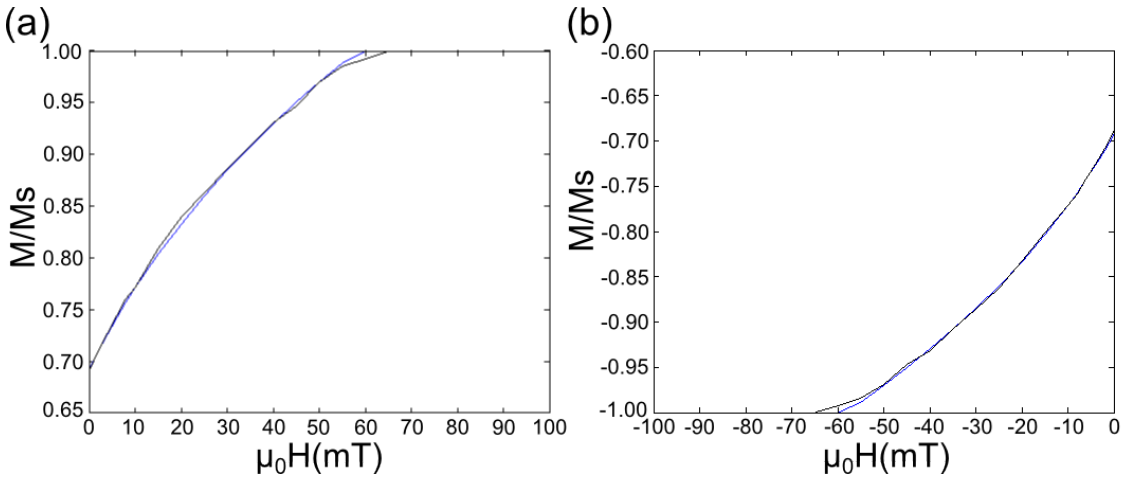

Fig. A.15 Demonstration of the relation between simulated data and experimental data collected using a SQUID magnetometer used to find K_c and K_u for the first secondary 20nm $Fe_{1-x}Ga_x$ film grown on GaAs at a temperature of 300K. The magnetic hysteresis loop produced with decreasing field is shown in black in a) with its fit in blue. b) shows the magnetic hysteresis loop with increasing field and its fit.

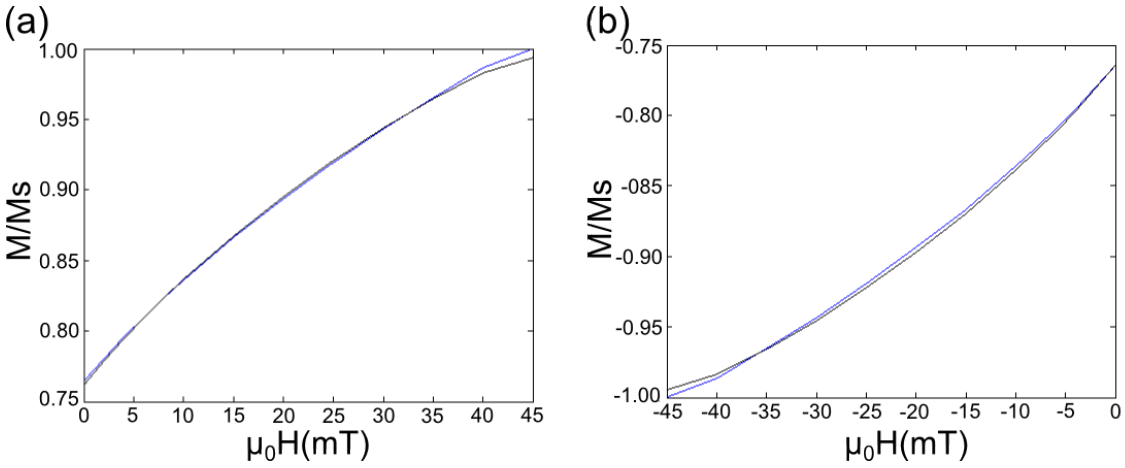

Fig. A.16 Demonstration of the relation between simulated data and experimental data collected using a SQUID magnetometer used to find K_c and K_u for the first secondary 30nm $Fe_{1-x}Ga_x$ film grown on GaAs at a temperature of 300K. The magnetic hysteresis loop produced with decreasing field is shown in black in a) with its fit in blue. b) shows the magnetic hysteresis loop with increasing field and its fit.

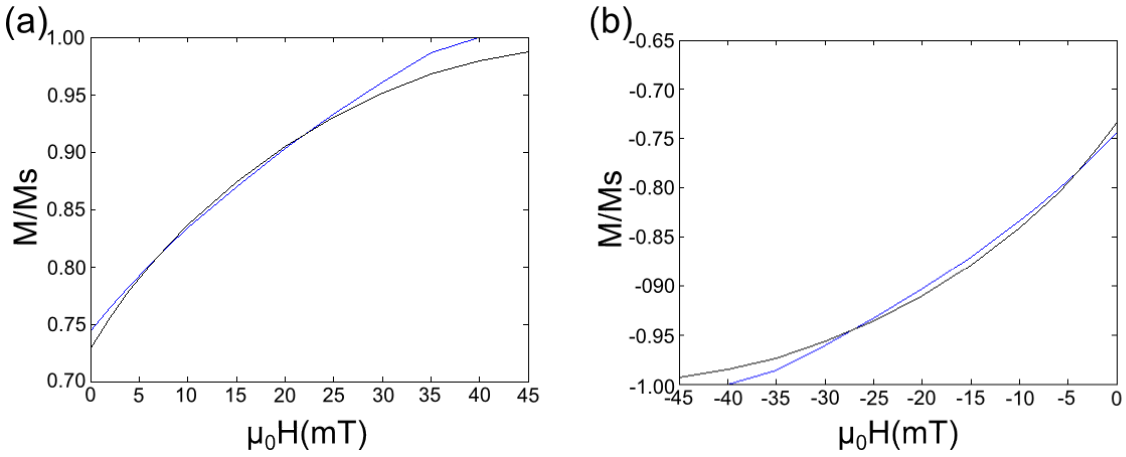

Fig. A.17 Demonstration of the relation between simulated data and experimental data collected using a SQUID magnetometer used to find K_c and K_u for the first secondary 20nm $Fe_{1-x}Ga_x$ film grown on GaAs at a temperature of 2K. The magnetic hysteresis loop produced with decreasing field is shown in black in a) with its fit in blue. b) shows the magnetic hysteresis loop with increasing field and its fit.

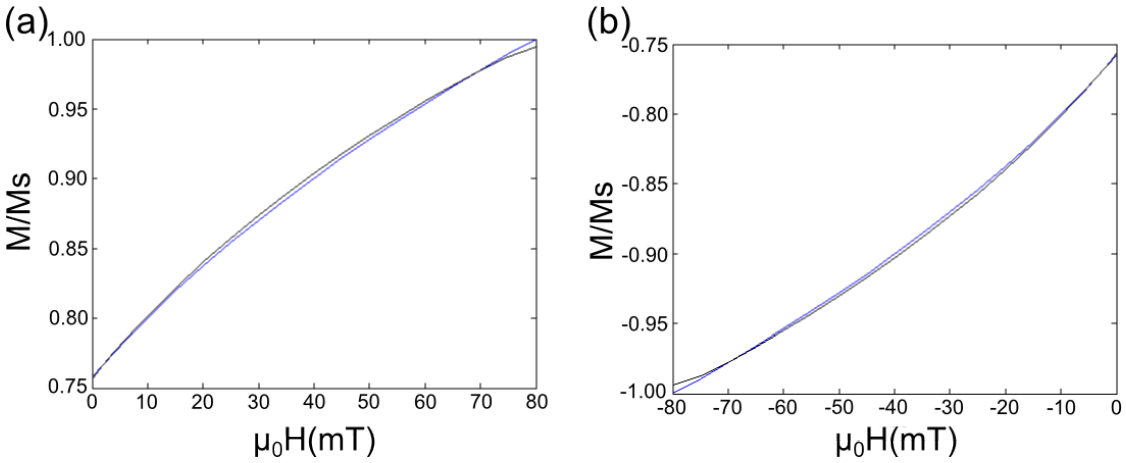

Fig. A.18 Demonstration of the relation between simulated data and experimental data collected using a SQUID magnetometer used to find K_c and K_u for the first secondary 30nm $Fe_{1-x}Ga_x$ film grown on GaAs at a temperature of 2K. The magnetic hysteresis loop produced with decreasing field is shown in black in a) with its fit in blue. b) shows the magnetic hysteresis loop with increasing field and its fit.

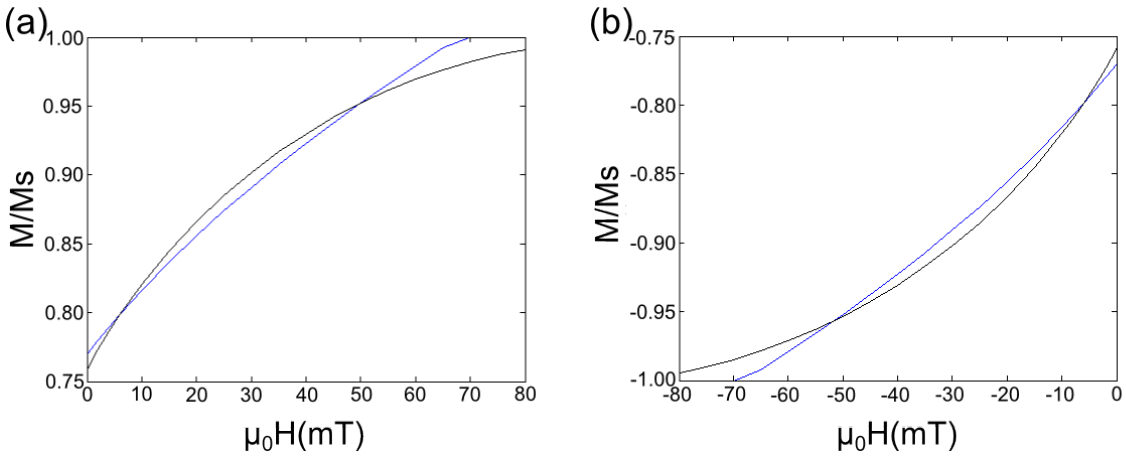

Fig. A.19 Demonstration of the relation between simulated data and experimental data collected using a SQUID magnetometer used to find K_c and K_u for the second secondary 20nm $Fe_{1-x}Ga_x$ film grown on GaAs at a temperature of 300K. The magnetic hysteresis loop produced with decreasing field is shown in black in a) with its fit in blue. b) shows the magnetic hysteresis loop with increasing field and its fit.

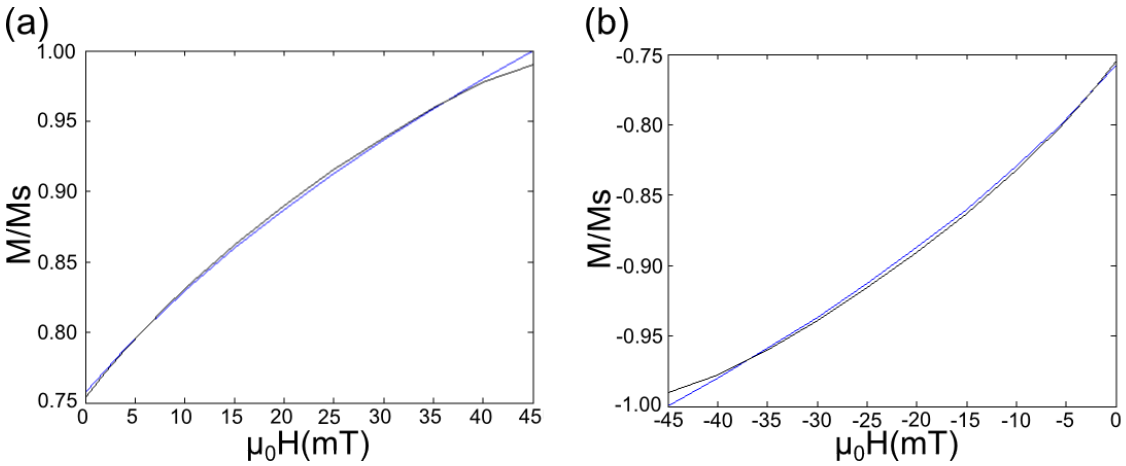

Fig. A.20 Demonstration of the relation between simulated data and experimental data collected using a SQUID magnetometer used to find K_c and K_u for the second secondary 30nm $Fe_{1-x}Ga_x$ film grown on GaAs at 300K. The magnetic hysteresis loop produced with decreasing field is shown in black in a) with its fit in blue. b) shows the magnetic hysteresis loop with increasing field and its fit.

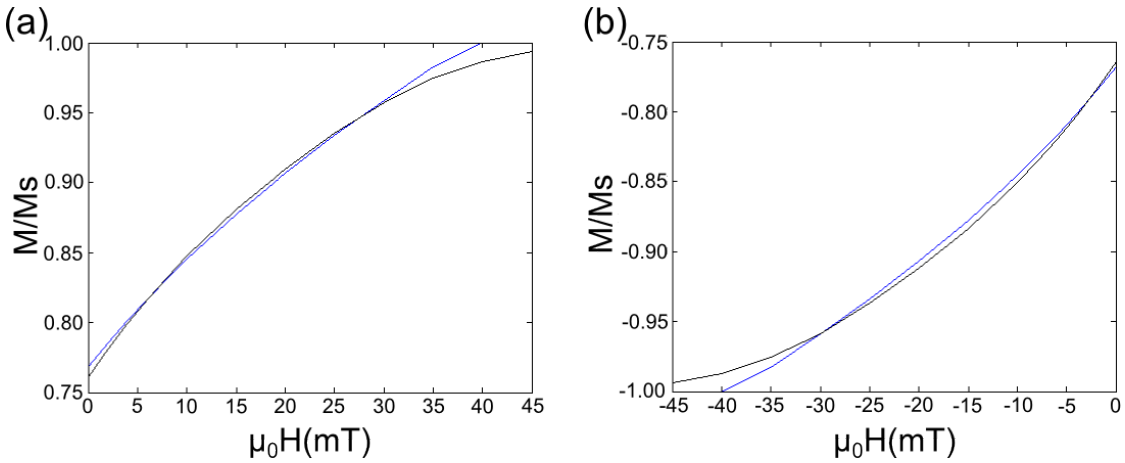

Fig. A.21 Demonstration of the relation between simulated data and experimental data collected using a SQUID magnetometer used to find K_c and K_u for the second secondary 20nm $Fe_{1-x}Ga_x$ film grown on GaAs at 2K. The magnetic hysteresis loop produced with decreasing field is shown in black in a) with its fit in blue. b) shows the magnetic hysteresis loop with increasing field and its fit.

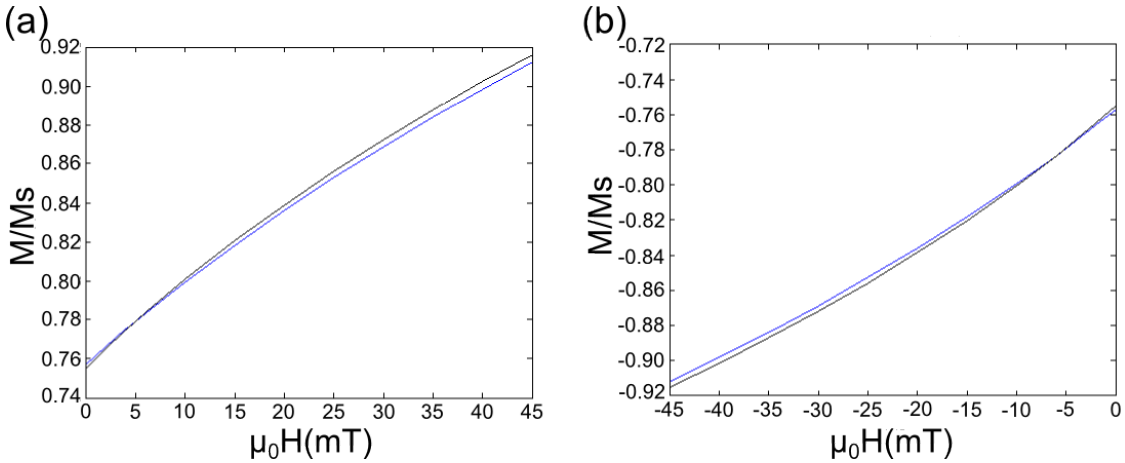

Fig. A.22 Demonstration of the relation between simulated data and experimental data collected using a SQUID magnetometer used to find K_c and K_u for the second secondary 30nm $Fe_{1-x}Ga_x$ film grown on GaAs at a temperature of 2K. The magnetic hysteresis loop produced with decreasing field is shown in black in a) with its fit in blue. b) shows the magnetic hysteresis loop with increasing field and its fit.

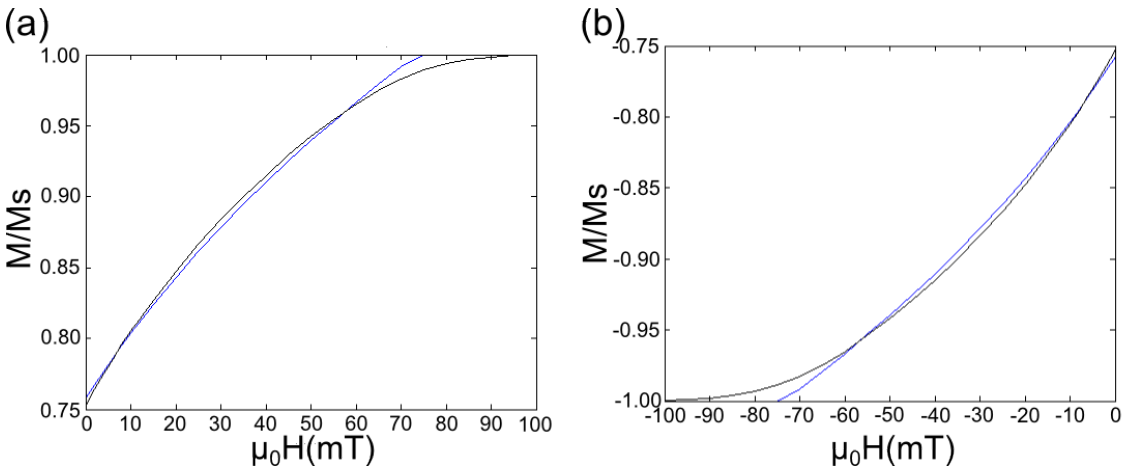

Appendix B

Transport measurement data pre-processing procedure

The first task was to perform a correction to take into account the field offset due to the persistent magnetisation of the iron core of the magnet. This was done by identifying the switching events and then finding the average of these values which was assumed to be the offset. This value was then subtracted from the field values for all the data points in the field sweep, the results of this correction are shown in figure B.1.

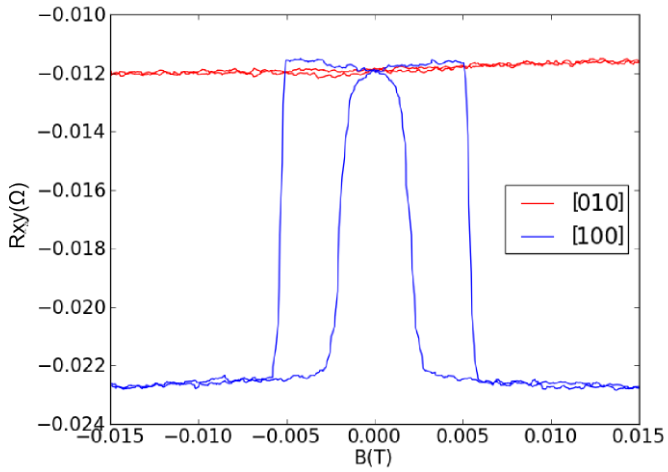

Fig. B.1 R_{xy} field sweep data for the 10nm $Fe_{1-x}Ga_x$ sample, S159, with $(2.3 \pm 0.01) \times 10^{-4}$ strain once the field offset correction had been applied. The field sweeps when the field was swept along the [100] direction are shown in blue whilst the measurement of R_{xy} when the field was swept along the [010] direction is shown in red.

The next process to be performed was a correction to the data in order to remove the effects of temperature drift. This involved finding the mean of the first 8 and last 8 data points in the scan and then assuming that the difference between these two values was entirely due to a temperature drift which was linear with respect to time. In order to remove this effect the difference between the two mean values was divided by the number of data points in the field sweep to find a factor which was multiplied by the index of each data point and then subtracted from the R_{xy} value of that point. The result of this process is shown in figure B.2.

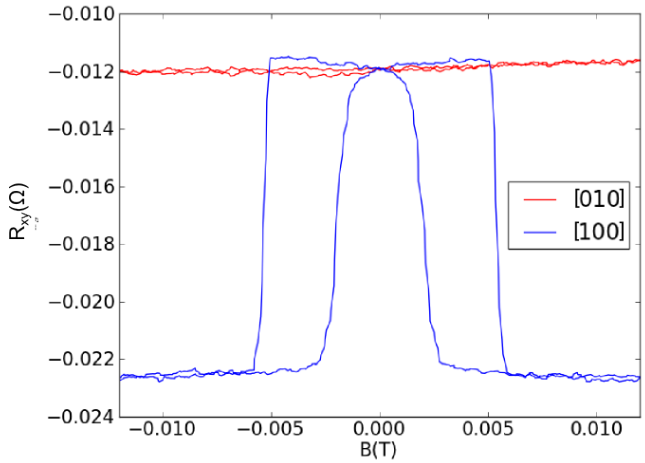

Fig. B.2 R_{xy} field sweep data for the 10nm $Fe_{1-x}Ga_x$ sample, S159, with $(2.3 \pm 0.01) \times 10^{-4}$ strain once the linear correction had been applied. The field sweeps when the field was swept along the [100] direction are shown in blue whilst the measurement of R_{xy} when the field was swept along the [010] direction is shown in red.

The next correction performed was designed to account for any out of plane Hall effect due to the bar being canted relative to the direction of the field. This cant was due to a number of combining factors, including the epoxy layer being uneven, the varnish layer holding the transducer to the sample holder and an uneven etching during the back thinning process. This cant leads to the introduction of a contribution to the resistance which is antisymmetric with respect to the field. In order to correct for this a process known as symmetrisation was used. This process involved viewing the hysteresis loops as four distinct quadrants. The first division being to separate the loops for increasing and decreasing field. These two loops were then separated into regions where field was positive and negative as demonstrated in figure B.3.

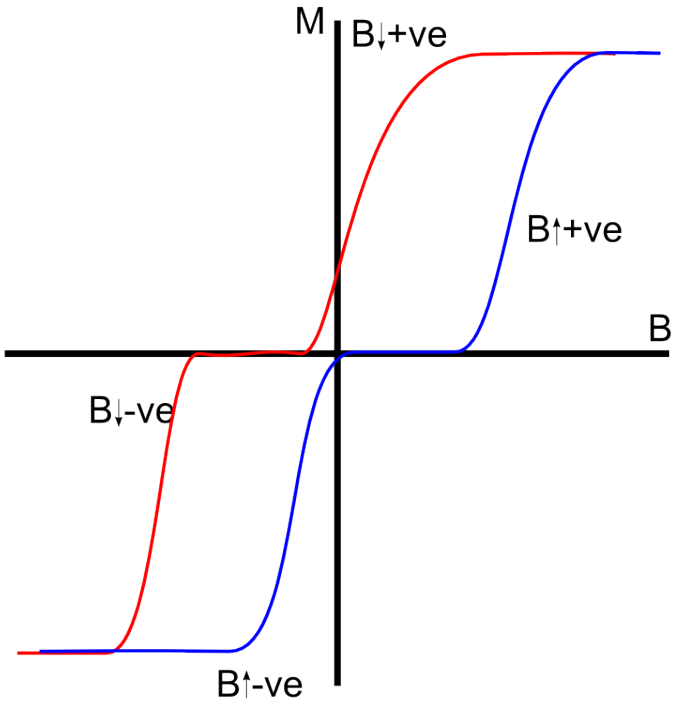

Fig. B.3 Demonstration of the four regimes used for the symmetrisation process. The loop produced with increasing field is shown in blue and the loop produced by decreasing field is shown in red.

Since the loops produced for increasing and decreasing field would be symmetrical in the absence of a cant equations B.1 and B.2 were used to find the symeterised component for the resistance measurements with field decreasing, $R_{sym}(\downarrow$+ve) and field increasing, $R_{sym}(\uparrow$+ve).

$$R_{sym}(\downarrow +ve) = \frac{R(\downarrow +ve) + R(\uparrow -ve)}{2} \tag{B.1}$$

$$R_{sym}(\uparrow +ve) = \frac{R(\uparrow +ve) + R(\downarrow -ve)}{2} \tag{B.2}$$

These two symmetrised sections of the loop were then recombined in order to form up and down loops which were entirely symmetrical as shown in figure B.4.

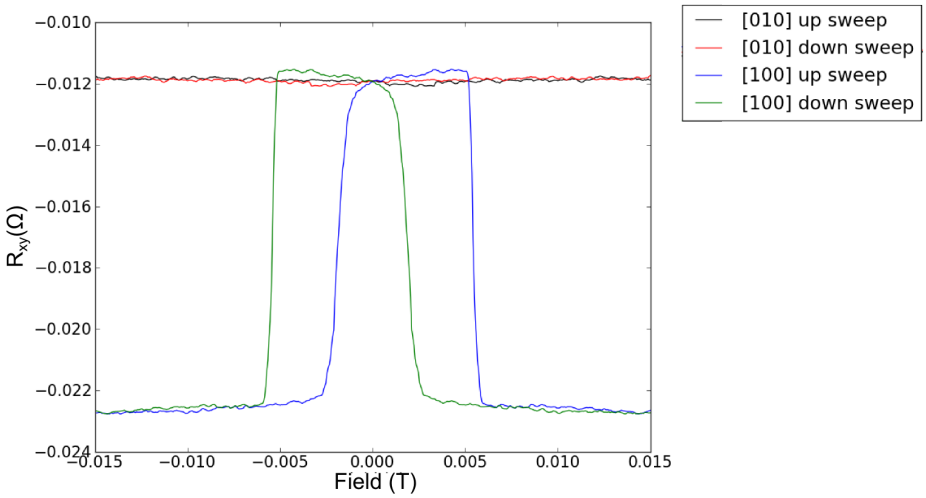

Fig. B.4 R_{xy} field sweep data for the 10nm $Fe_{1-x}Ga_x$ sample, S159, with $(2.3 \pm 0.01) \times 10^{-4}$ strain. The field sweeps when the field was swept along the [100] direction are shown in a) in which the blue line indicates the up loop and the green line indicates the down loop. The R_{xy} measurement when the field was swept upwards along the [010] direction is shown in black, downwards in the [010] is shown in red, upwards in the [100] direction is shown in blue and downwards in the [100] direction is shown in green.

The next step was correcting for mixing of the longitudinal resistance into the measured transverse resistance, hereafter referred to as the V_{xx} correction once the symmetrisation correction had been applied. This can arise due to an offset in the alignment of the voltage probes as illustrated in figure B.5, or due to inhomogeniety of the resistivity tensor in the region between the voltage probes.

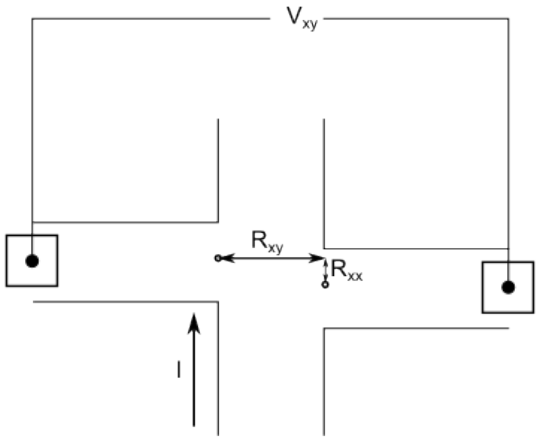

Fig. B.5 Figure showing the reasoning behind the V_{xx} correction. Two arms of a hall bar are shown with an exaggerated mismatch between the positions of the arms along the main bar. This leads to a small R_{xx} component being mixed into the R_{xy} measurement which is corrected for using the V_{xx} correction. The current is indicated by the black arrow in the bottom left of the diagram.

The correction took the form of equation B.3 in which α is a correction factor found by the ratio of the mean R_{xy} measurement and the mean R_{xx} measurement.

$$R_{xy}^{corrected} = R_{xy} + \alpha R_{xx} \tag{B.3}$$

The result of this final correction is shown in figure B.6.

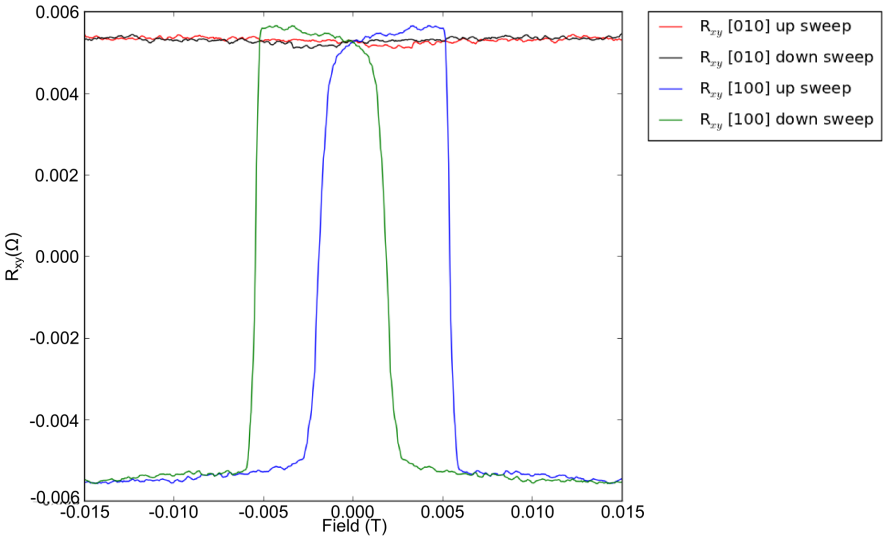

Fig. B.6 R_{xy} measurement taken as field was swept along the [100] axis, shown in blue for the up sweep and green for the down sweep, and the [010] axis, shown in black for the up sweep and red for the down sweep. Both the field sweeps are shown on the same axes once all corrections have been performed. This measurement was taken with a strain of $(2.3 \pm 0.01) \times 10^{-4}$.

Appendix C

Fitting results for the transport data

This appendix shows the fits used to infer the results shown in the transport analysis in chapter 4

C.1 Fits for the primary 10nm sample, S159

Fig. C.1 Fit used to find the values of K_s and the domain wall energy of the transport loop collected from the primary 10nm sample, S159, with -30V applied to the transducer corresponding to strain of $[-1.383\times10^{-4}\pm7.47\times10^{-7}]$. The cost of this fit is 3.390×10^{-1}.

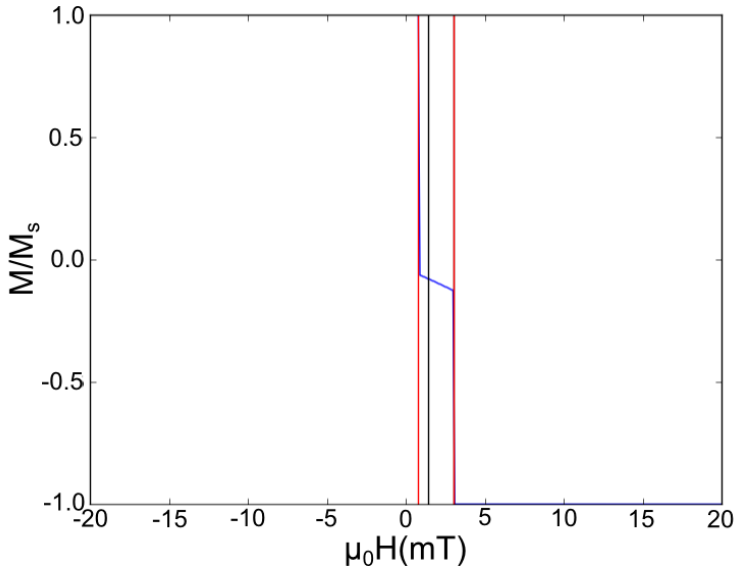

Fig. C.2 Fit used to find the values of K_s and the domain wall energy of the transport loop collected from the primary 10nm sample, S159, with -25V applied to the transducer corresponding to strain of $[-1.1525 \times 10^{-4} \pm 6.23 \times 10^{-7}]$. The cost of this fit is 9.031×10^{-1}.

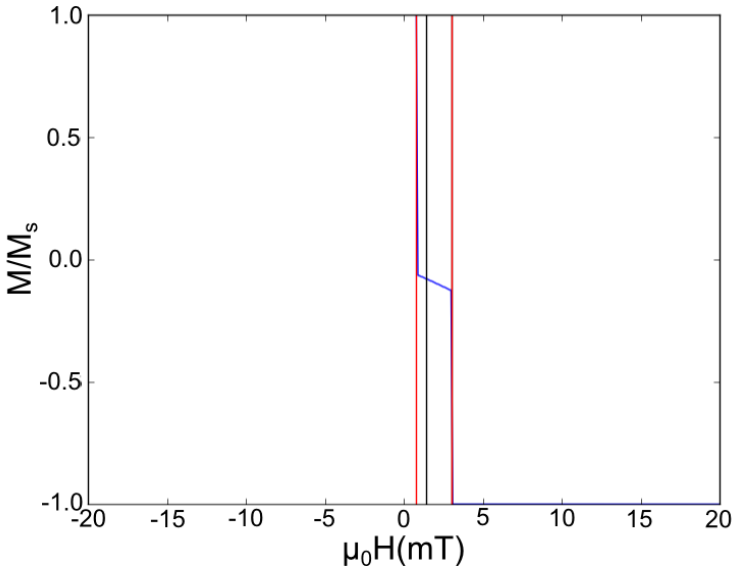

Fig. C.3 Fit used to find the values of K_s and the domain wall energy of the transport loop collected from the primary 10nm sample, S159, with -20V applied to the transducer corresponding to strain of $[-0.922 \times 10^{-4} \pm 4.98 \times 10^{-7}]$. The cost of this fit is 4.375×10^{-1}.

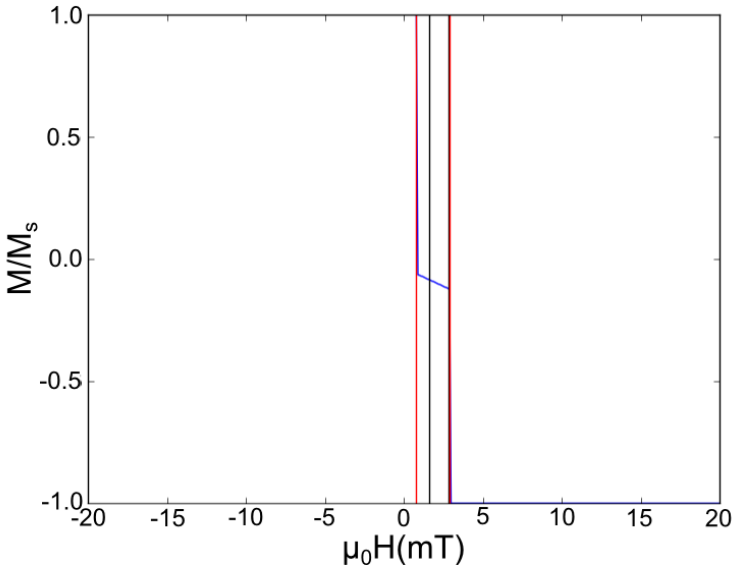

Fig. C.4 Fit used to find the values of K_s and the domain wall energy of the transport loop collected from the primary 10nm sample, S159, with -15V applied to the transducer corresponding to strain of $[-0.6915 \times 10^{-4} \pm 3.73 \times 10^{-7}]$. The cost of this fit is 8.607×10^{-1}.

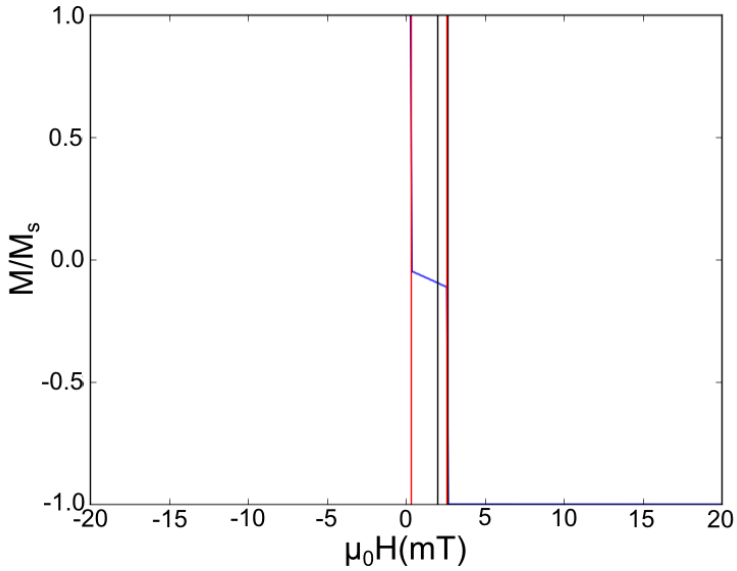

Fig. C.5 Fit used to find the values of K_s and the domain wall energy of the transport loop collected from the primary 10nm sample, S159, with -10V applied to the transducer corresponding to strain of $[-0.461 \times 10^{-4} \pm 2.49 \times 10^{-7}]$. The cost of this fit is 6.393×10^{-1}.

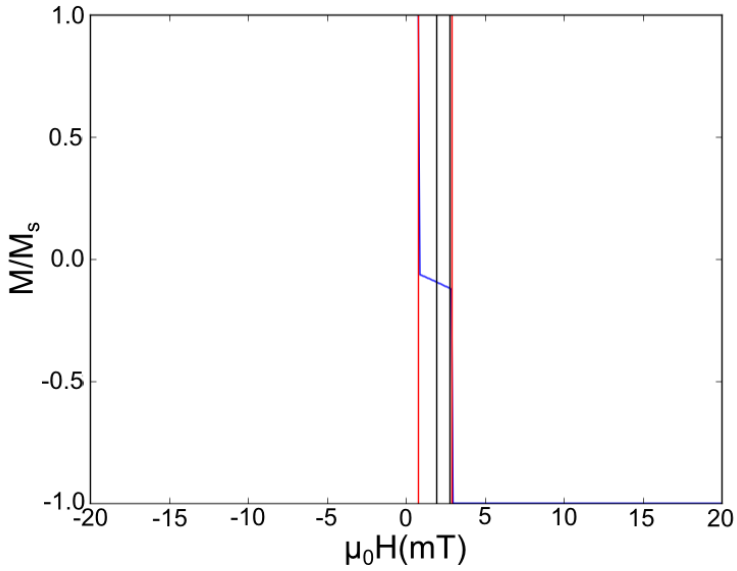

Fig. C.6 Fit used to find the values of K_s and the domain wall energy of the transport loop collected from the primary 10nm sample, S159, with -5V applied to the transducer corresponding to strain of $[-0.2305 \times 10^{-4} \pm 1.25 \times 10^{-7}]$. The cost of this fit is 4.980×10^{-1}.

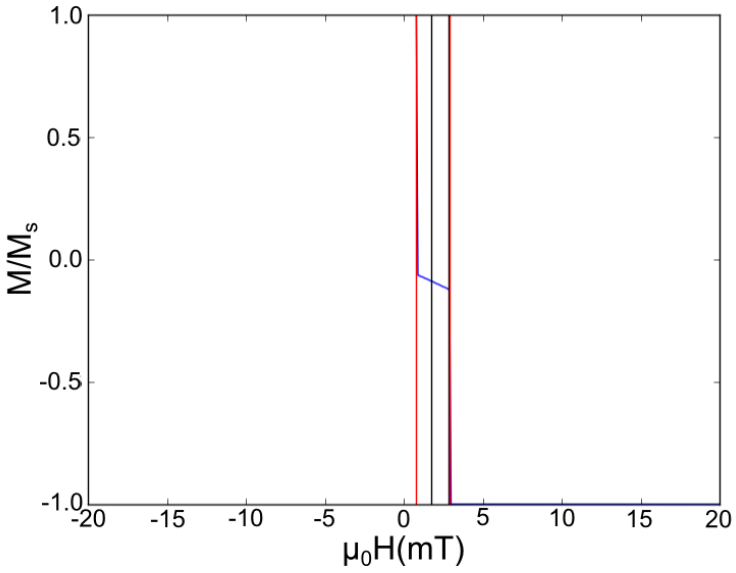

Fig. C.7 Fit used to find the values of K_s and the domain wall energy of the transport loop collected from the primary 10nm sample, S159, with 0V applied to the transducer corresponding to strain of 0. The cost of this fit is 2.883×10^{-1}.

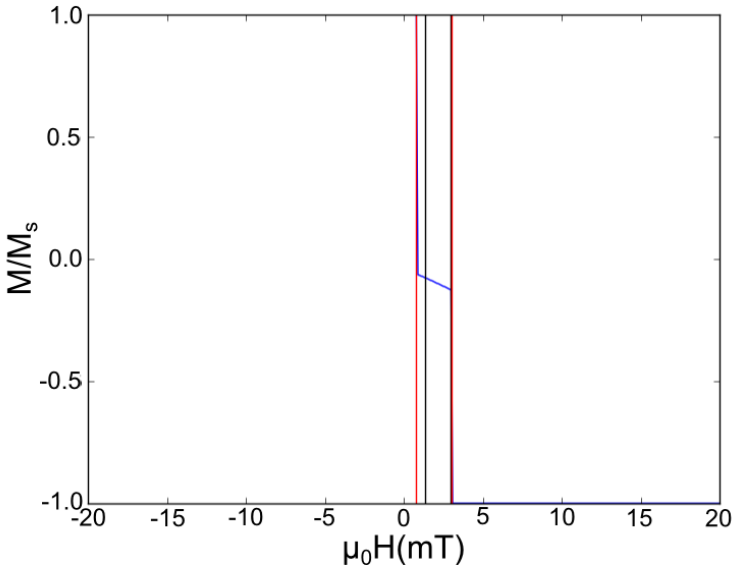

Fig. C.8 Fit used to find the values of K_s and the domain wall energy of the transport loop collected from the primary 10nm sample, S159, with 5V applied to the transducer corresponding to strain of $[0.231 \times 10^{-4} \pm 1.24 \times 10^{-7}]$. The cost of this fit is 1.593×10^{-1}.

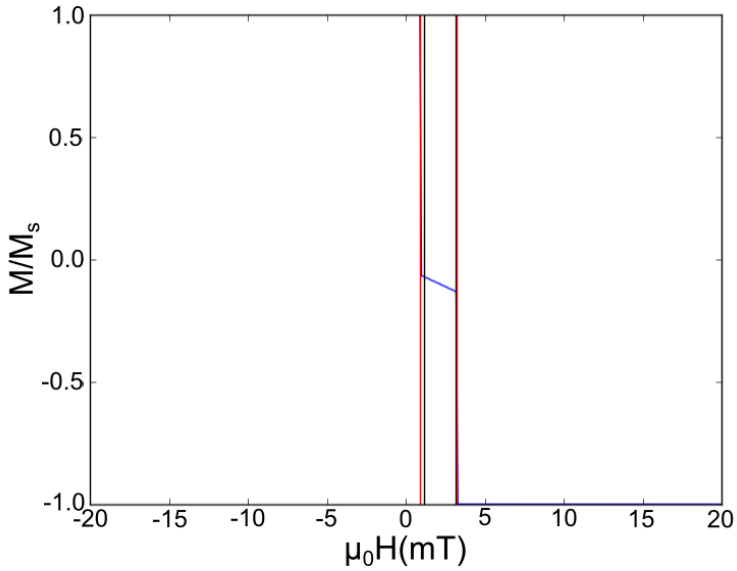

Fig. C.9 Fit used to find the values of K_s and the domain wall energy of the transport loop collected from the primary 10nm sample, S159, with 10V applied to the transducer corresponding to strain of $[0.461 \times 10^{-4} \pm 2.49 \times 10^{-7}]$. The cost of this fit is 1.227×10^{-1}.

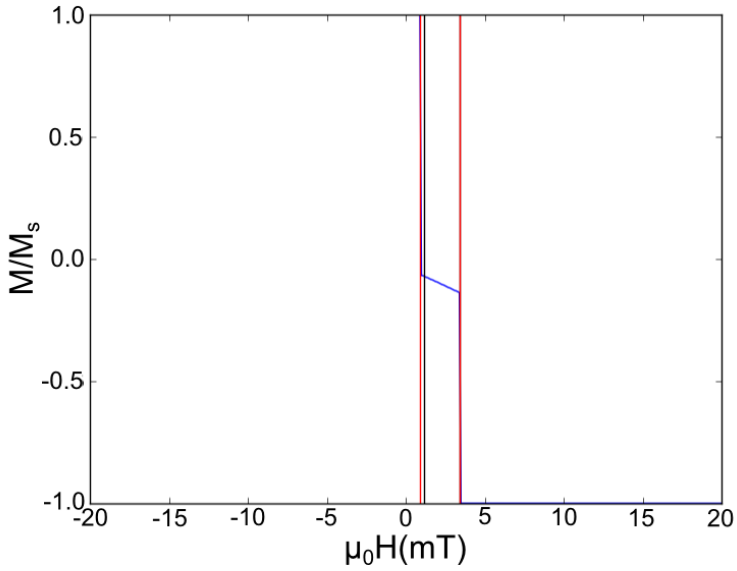

Fig. C.10 Fit used to find the values of K_s and the domain wall energy of the transport loop collected from the primary 10nm sample, S159, with 15V applied to the transducer corresponding to strain of $[0.6915 \times 10^{-4} \pm 3.73 \times 10^{-7}]$. The cost of this fit is 0.525×10^{-1}.

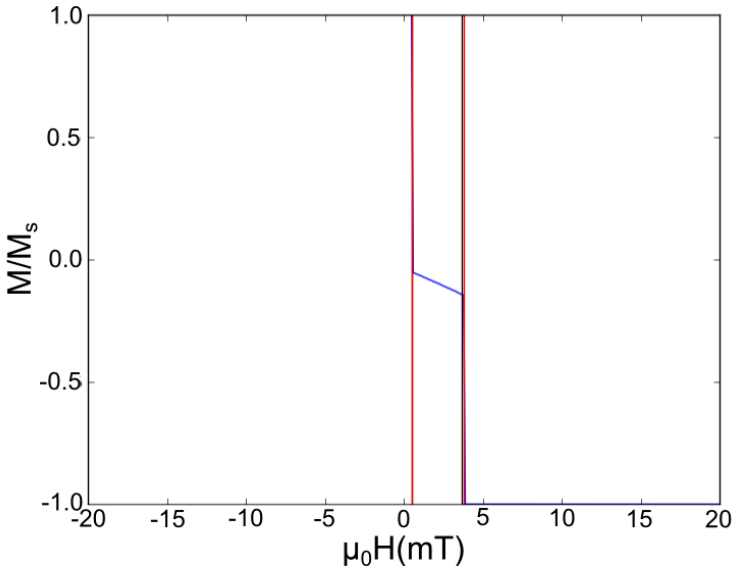

Fig. C.11 Fit used to find the values of K_s and the domain wall energy of the transport loop collected from the primary 10nm sample, S159, with 20V applied to the transducer corresponding to strain of $[0.922 \times 10^{-4} \pm 4.98 \times 10^{-7}]$. The cost of this fit is 0.350×10^{-1}.

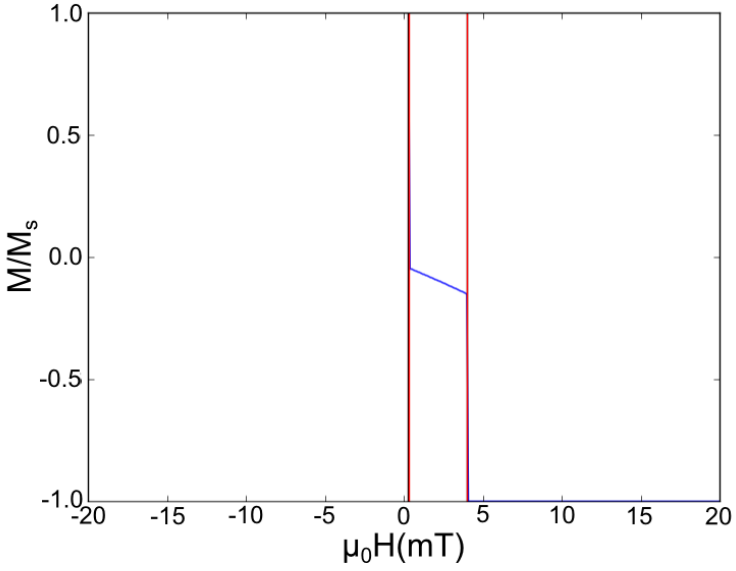

Fig. C.12 Fit used to find the values of K_s and the domain wall energy of the transport loop collected from the primary 10nm sample, S159, with 25V applied to the transducer corresponding to strain of $[1.1525 \times 10^{-4} \pm 0.00624 \times 10^{-7}]$. The cost of this fit is 0.225×10^{-1}.

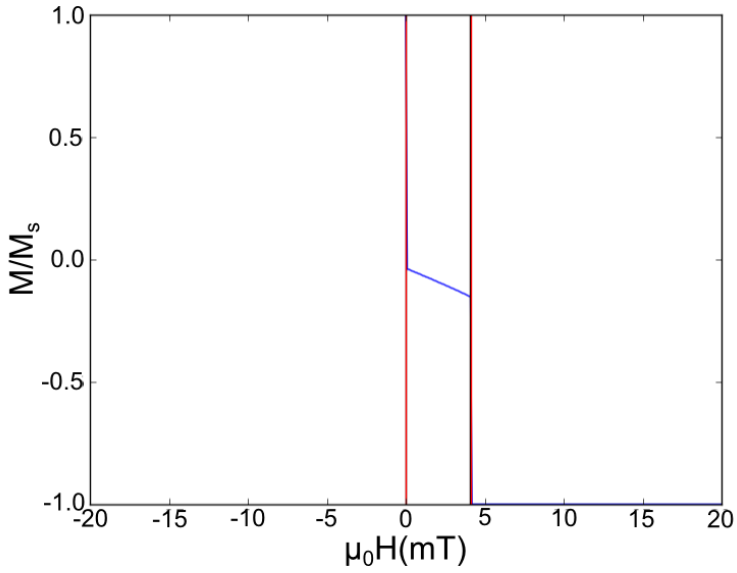

Fig. C.13 Fit used to find the values of K_s and the domain wall energy of the transport loop collected from the primary 10nm sample, S159, with 30V applied to the transducer corresponding to strain of $[1.383 \times 10^{-4} \pm 7.47 \times 10^{-7}]$. The cost of this fit is 0.475×10^{-1}.

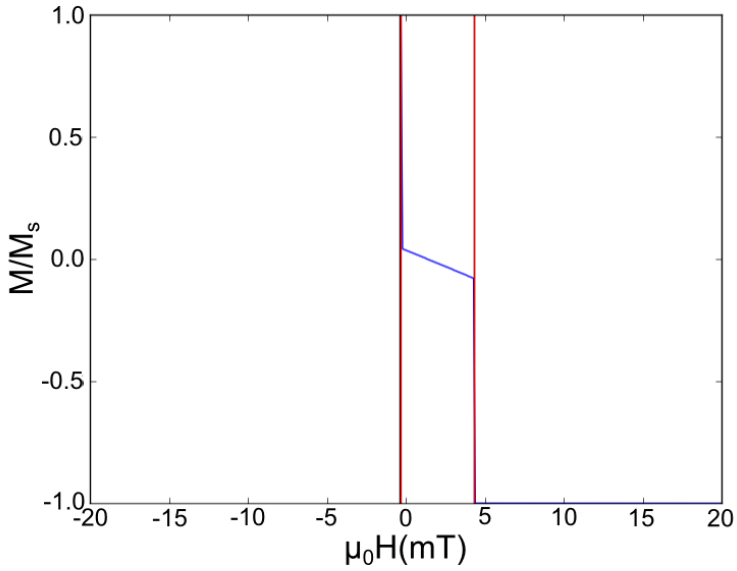

Fig. C.14 Fit used to find the values of K_s and the domain wall energy of the transport loop collected from the primary 10nm sample, S159, with 35V applied to the transducer corresponding to strain of $[1.6135 \times 10^{-4} \pm 8.72 \times 10^{-7}]$. The cost of this fit is 0.496×10^{-1}.

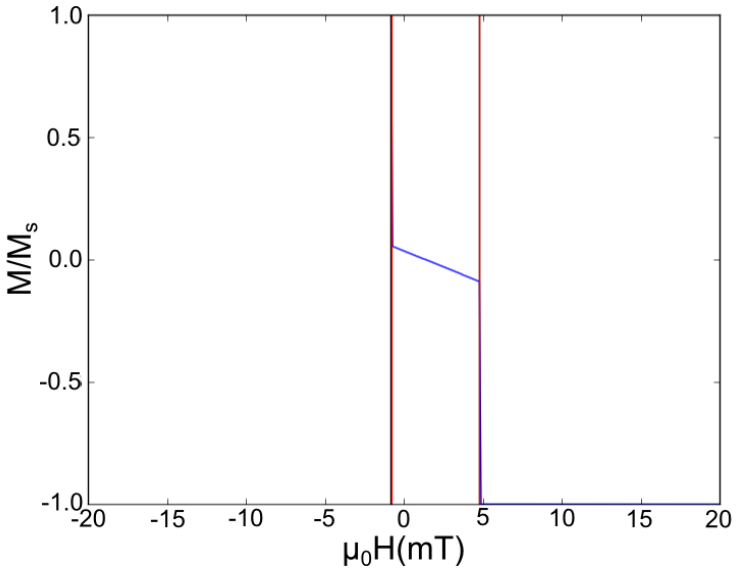

Fig. C.15 Fit used to find the values of K_s and the domain wall energy of the transport loop collected from the primary 10nm sample, S159, with 40V applied to the transducer corresponding to strain of $[1.844 \times 10^{-4} \pm 9.96 \times 10^{-7}]$. The cost of this fit is 0.176×10^{-1}.

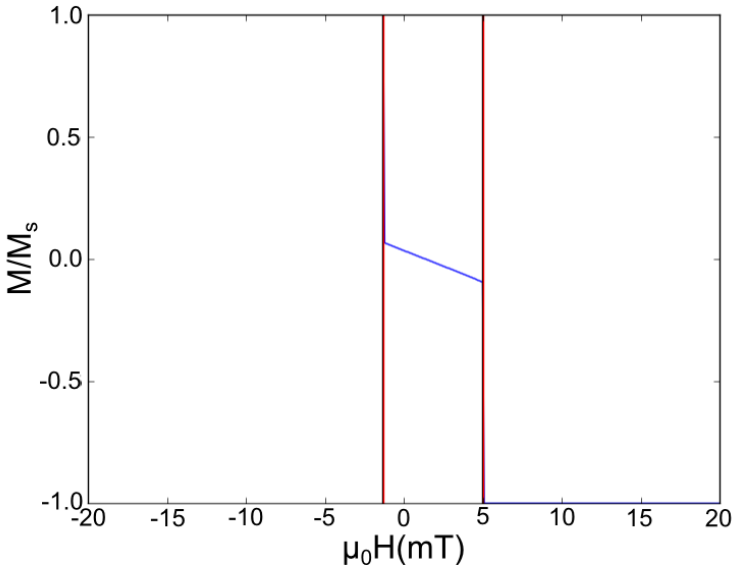

Fig. C.16 Fit used to find the values of K_s and the domain wall energy of the transport loop collected from the primary 10nm sample, S159, with 45V applied to the transducer corresponding to strain of $[2.0745 \times 10^{-4} \pm 1.12 \times 10^{-6}]$. The cost of this fit is 0.544×10^{-1}.

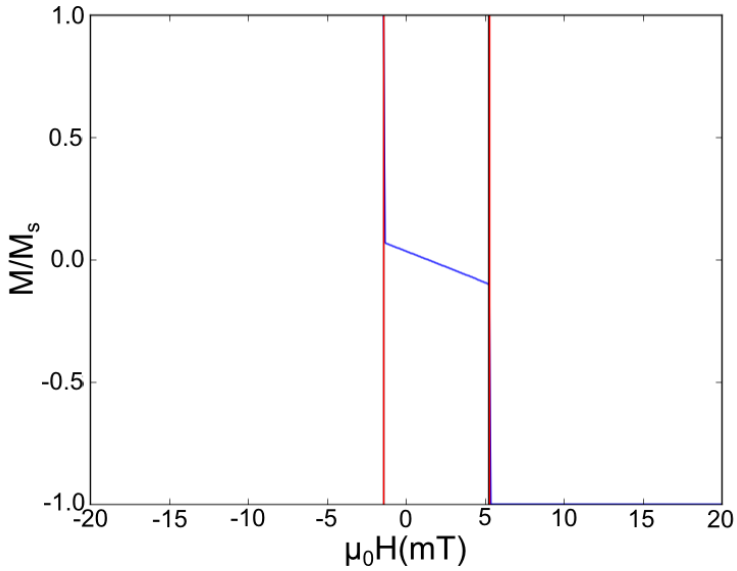

Fig. C.17 Fit used to find the values of K_s and the domain wall energy of the transport loop collected from the primary 10nm sample, S159, with 50V applied to the transducer corresponding to strain of $[2.305 \times 10^{-4} \pm 1.25 \times 10^{-6}]$. The cost of this fit is 0.2277×10^{-1}.

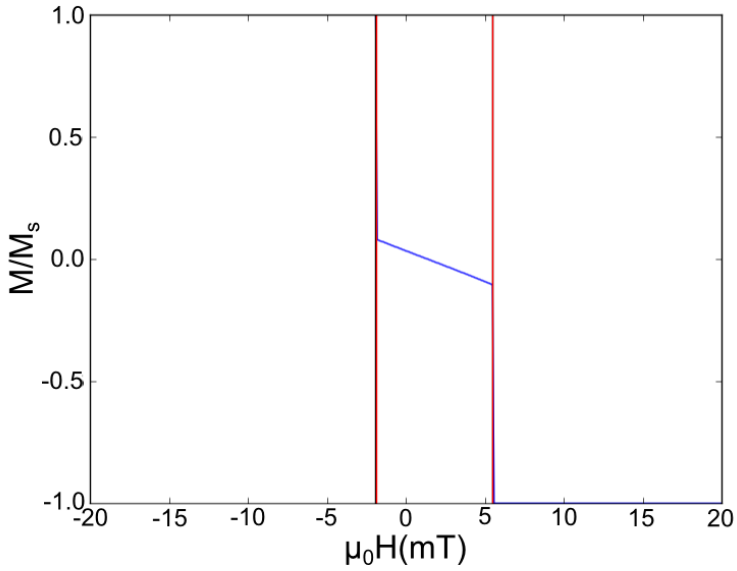

C.2 Fits for the primary 20nm sample, S219

Fig. C.18 Fit used to find the values of K_s and the domain wall energy of the transport loop collected from the primary 20nm sample, S219, with -30V applied to the transducer corresponding to strain of $[-0.881 \times 10^{-4} \pm 1.23 \times 10^{-7}]$. The cost of this fit is 6.578×10^{-1}.

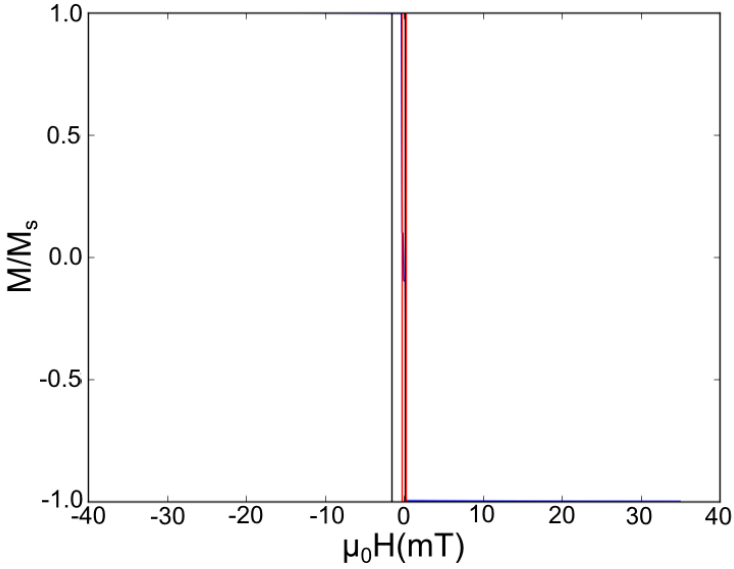

Fig. C.19 Fit used to find the values of K_s and the domain wall energy of the transport loop collected from the primary 20nm sample, S219, with -20V applied to the transducer corresponding to strain of $[-0.587 \times 10^{-4} \pm 8.2 \times 10^{-8}]$. The cost of this fit is 4.100×10^{-1}.

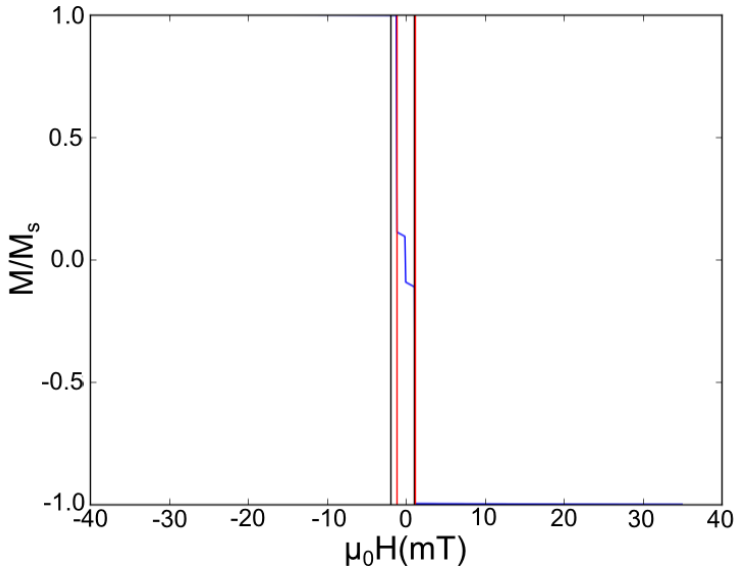

Fig. C.20 Fit used to find the values of K_s and the domain wall energy of the transport loop collected from the primary 20nm sample, S219, with -10V applied to the transducer corresponding to strain of $[-0.294 \times 10^{-4} \pm \times 10^{-6}]$. The cost of this fit is 2.242×10^{-1}.

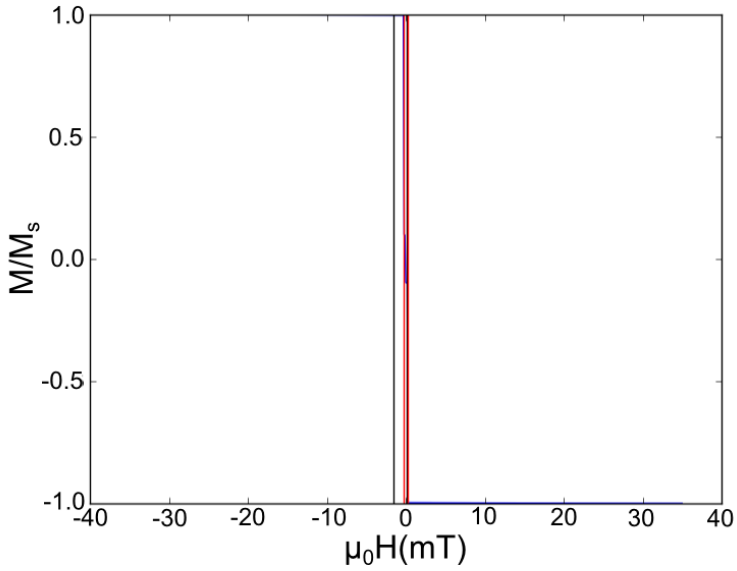

Fig. C.21 Fit used to find the values of K_s and the domain wall energy of the transport loop collected from the primary 20nm sample, S219, with 0V applied to the transducer corresponding to strain of 0. The cost of this fit is 0.407×10^{-1}.

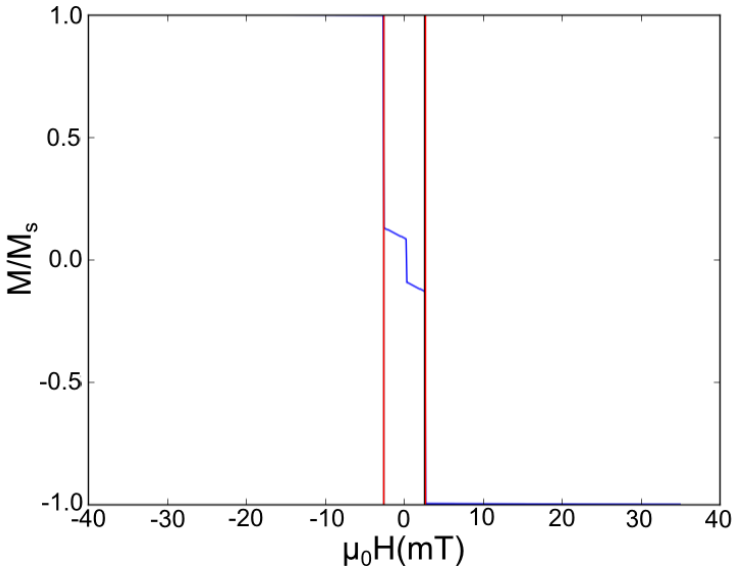

Fig. C.22 Fit used to find the values of K_s and the domain wall energy of the transport loop collected from the primary 20nm sample, S219, with 10V applied to the transducer corresponding to strain of $[0.2936\times10^{-4}\pm4.1\times10^{-8}]$. The cost of this fit is 0.450×10^{-1}.

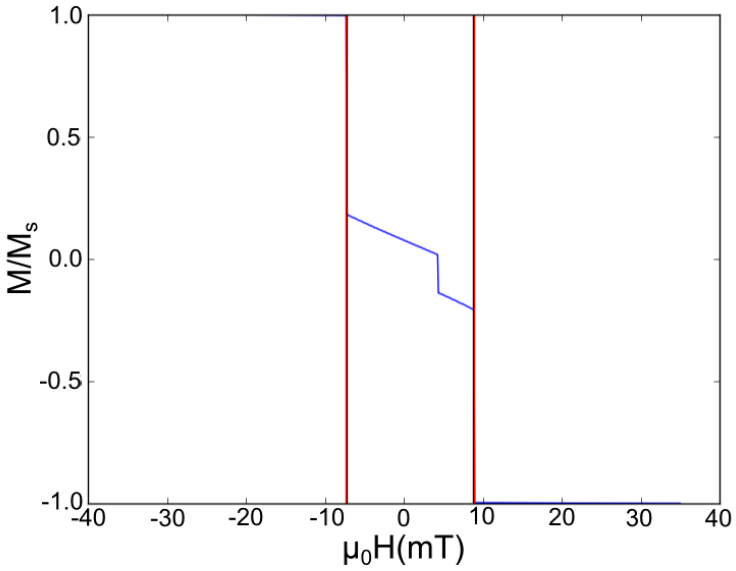

Fig. C.23 Fit used to find the values of K_s and the domain wall energy of the transport loop collected from the primary 20nm sample, S219, with 20V applied to the transducer corresponding to strain of $[0.5872 \times 10^{-4} \pm 8.2 \times 10^{-8}]$. The cost of this fit is 0.525×10^{-1}.

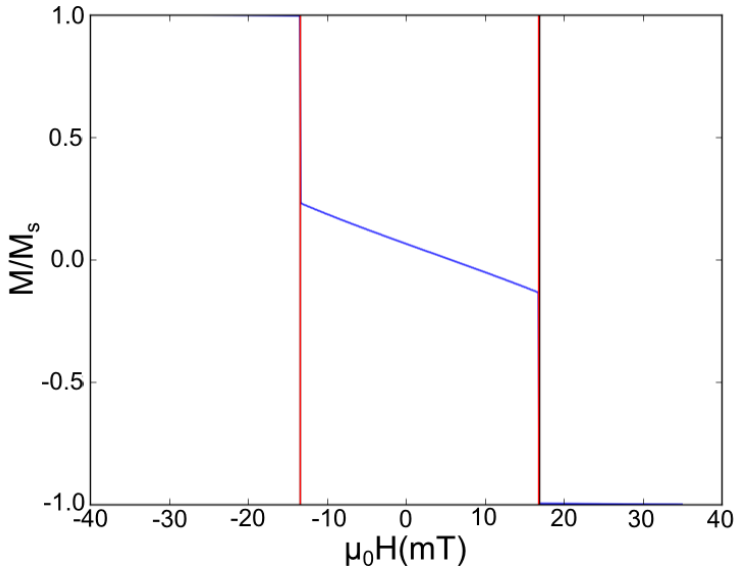

Fig. C.24 Fit used to find the values of K_s and the domain wall energy of the transport loop collected from the primary 20nm sample, S219, with 30V applied to the transducer corresponding to strain of $[0.881 \times 10^{-4} \pm 1.23 \times 10^{-7}]$. The cost of this fit is 0.450×10^{-1}.

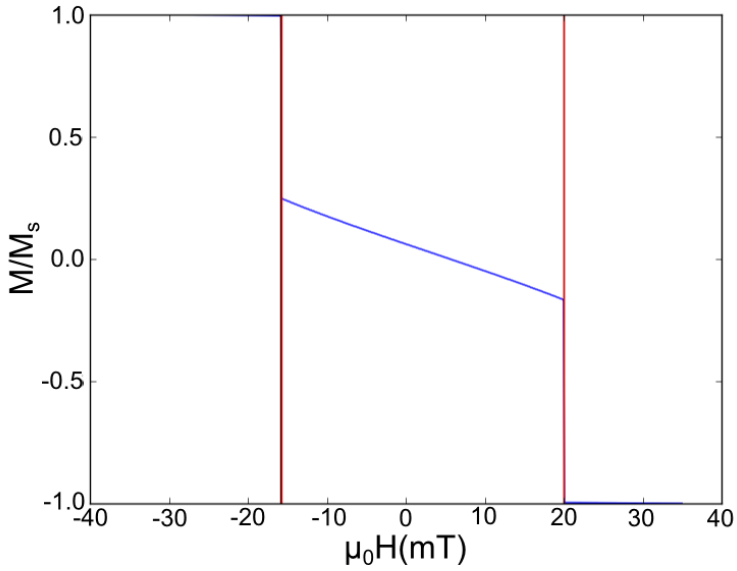

Fig. C.25 Fit used to find the values of K_s and the domain wall energy of the transport loop collected from the primary 20nm sample, S219, with 40V applied to the transducer corresponding to strain of $[1.174 \times 10^{-4} \pm 1.64 \times 10^{-7}]$. The cost of this fit is 0.375×10^{-1}.

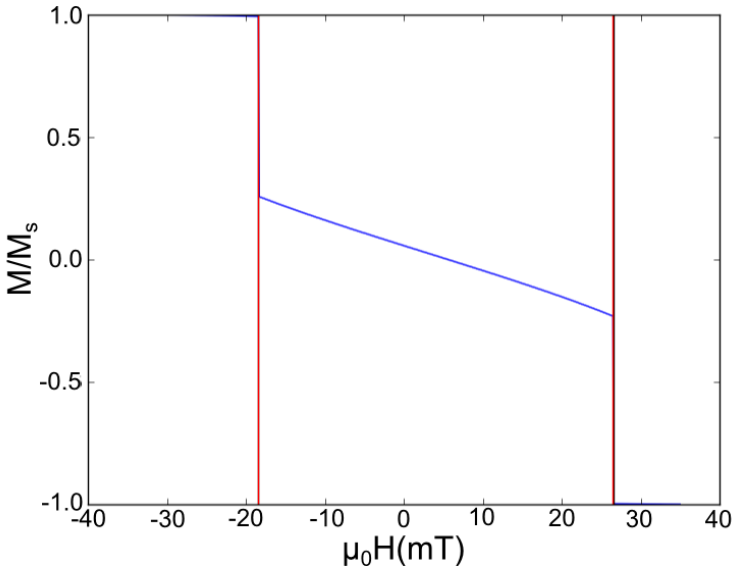

Fig. C.26 Fit used to find the values of K_s and the domain wall energy of the transport loop collected from the primary 20nm sample, S219, with 50V applied to the transducer corresponding to strain of $[1.468 \times 10^{-4} \pm 2.05 \times 10^{-7}]$. The cost of this fit is 0.375×10^{-1}.

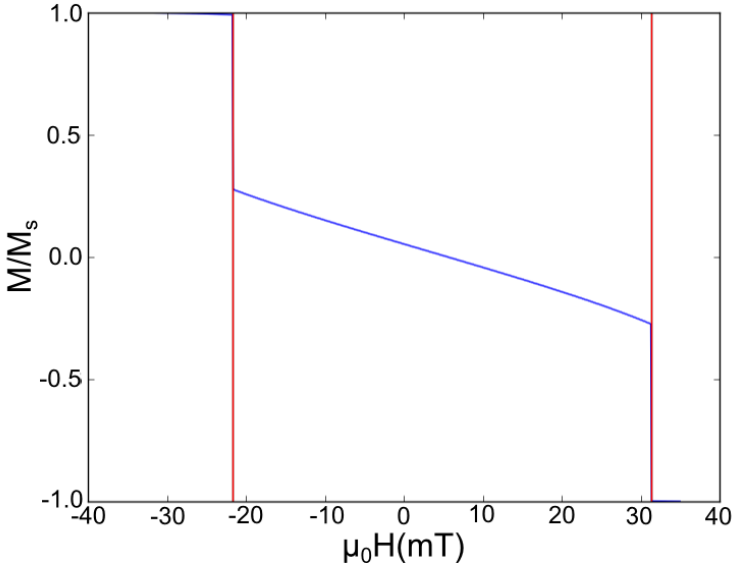

C.3 Fits for the secondary 20nm sample, S411

Fig. C.27 Fit used to find the values of K_s and the domain wall energy of the transport loop collected from the secondary 20nm sample, S411, with -30V applied to the transducer corresponding to strain of $[-2.535\times10^{-4}\pm3.34\times10^{-6}]$. The cost of this fit is 3.171×10^{-1}.

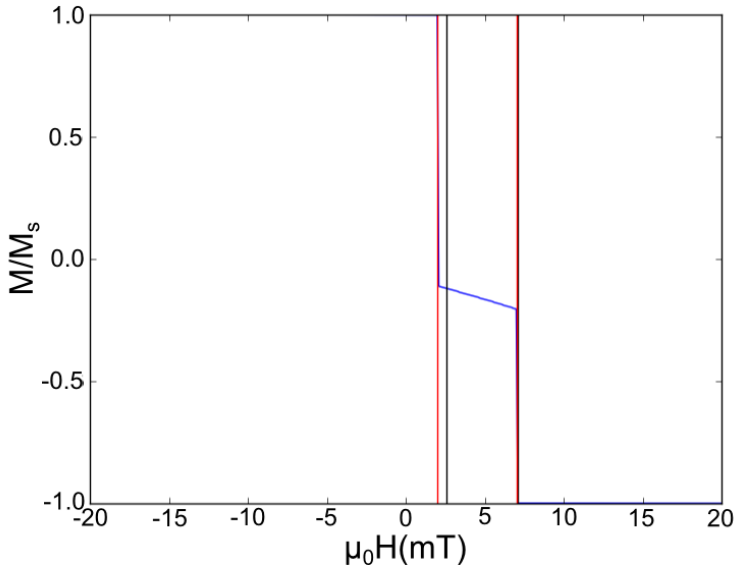

Fig. C.28 Fit used to find the values of K_s and the domain wall energy of the transport loop collected from the secondary 20nm sample, S411, with -20V applied to the transducer corresponding to strain of $[-1.69 \times 10^{-4} \pm 2.23 \times 10^{-6}]$. The cost of this fit is 8.081×10^{-1}.

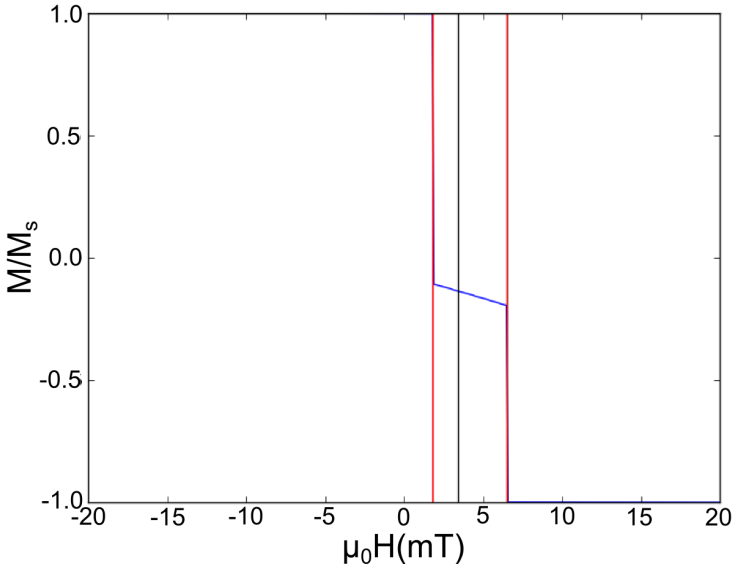

Fig. C.29 Fit used to find the values of K_s and the domain wall energy of the transport loop collected from the secondary 20nm sample, S411, with -10V applied to the transducer corresponding to strain of $[-0.85 \times 10^{-4} \pm 1.11 \times 10^{-6}]$. The cost of this fit is 7.252×10^{-1}.

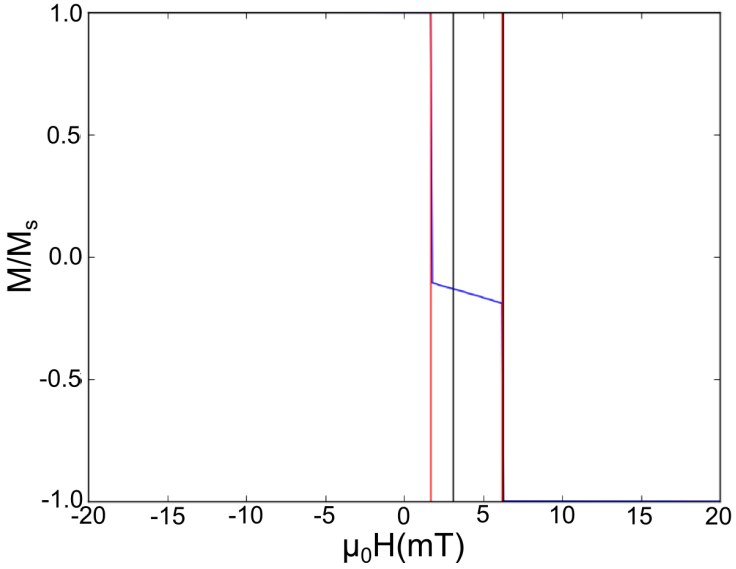

Fig. C.30 Fit used to find the values of K_s and the domain wall energy of the transport loop collected from the secondary 20nm sample, S411, with 0V applied to the transducer corresponding to strain of 0. The cost of this fit is 1.667×10^{-1}.

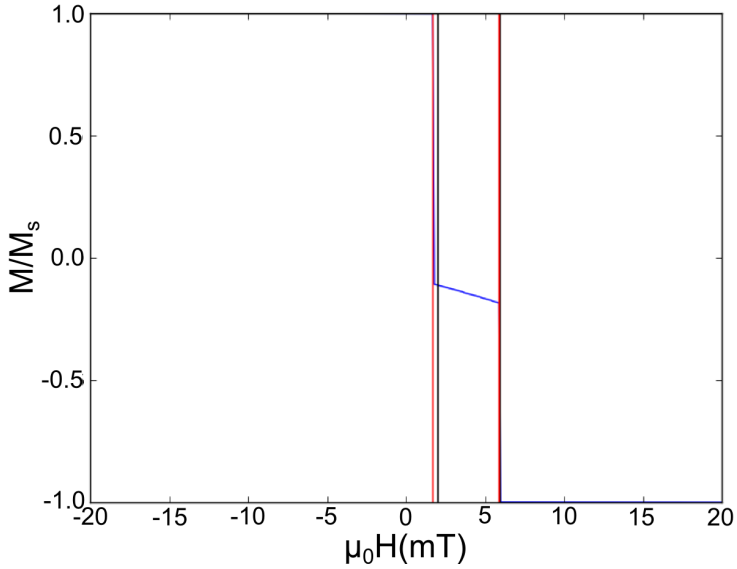

Fig. C.31 Fit used to find the values of K_s and the domain wall energy of the transport loop collected from the secondary 20nm sample, S411, with 10V applied to the transducer corresponding to strain of $[0.845 \times 10^{-4} \pm 1.11 \times 10^{-6}]$. The cost of this fit is 0.248×10^{-1}.

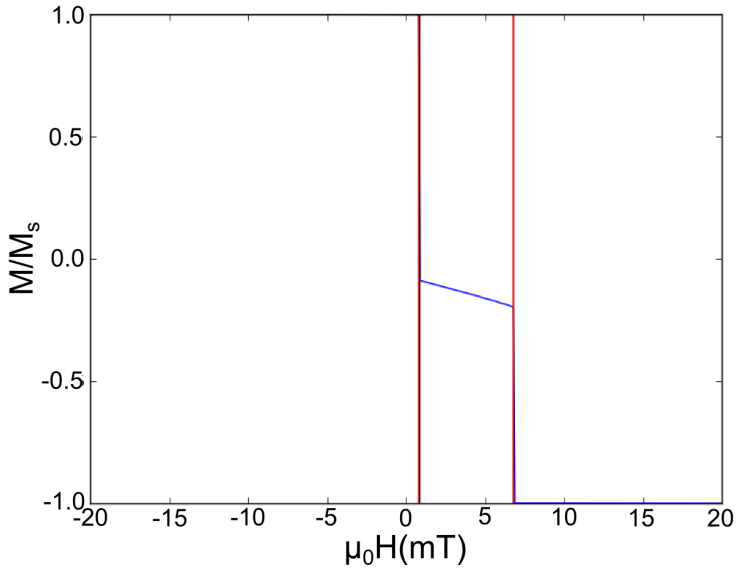

Fig. C.32 Fit used to find the values of K_s and the domain wall energy of the transport loop collected from the secondary 20nm sample, S411, with 20V applied to the transducer corresponding to strain of $[1.69 \times 10^{-4} \pm 2.23 \times 10^{-6}]$. The cost of this fit is 0.259×10^{-1}.

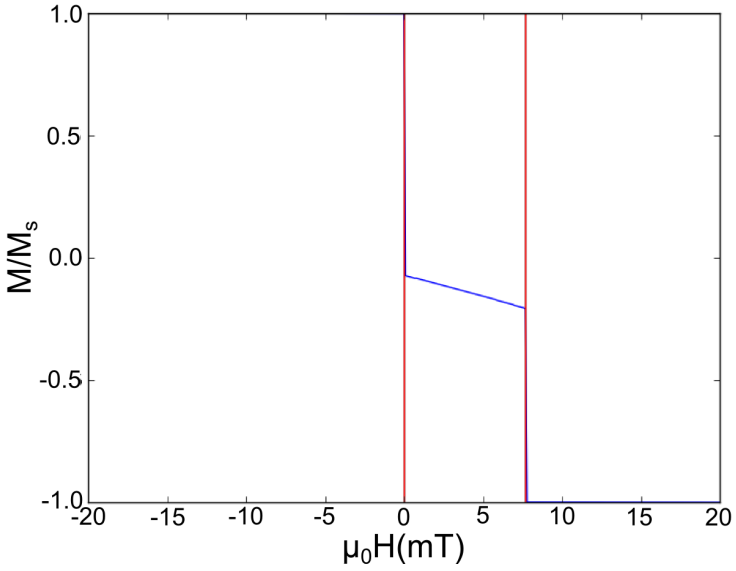

Fig. C.33 Fit used to find the values of K_s and the domain wall energy of the transport loop collected from the secondary 20nm sample, S411, with 30V applied to the transducer corresponding to strain of $[2.54 \times 10^{-4} \pm 3.34 \times 10^{-6}]$. The cost of this fit is 0.167×10^{-1}.

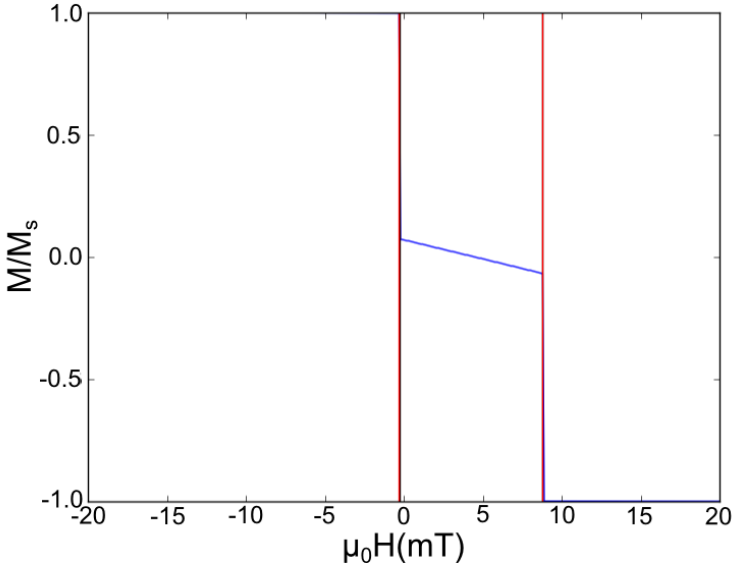

Fig. C.34 Fit used to find the values of K_s and the domain wall energy of the transport loop collected from the secondary 20nm sample, S411, with 40V applied to the transducer corresponding to strain of $[3.38 \times 10^{-4} \pm 4.46 \times 10^{-6}]$. The cost of this fit is 0.252×10^{-1}.

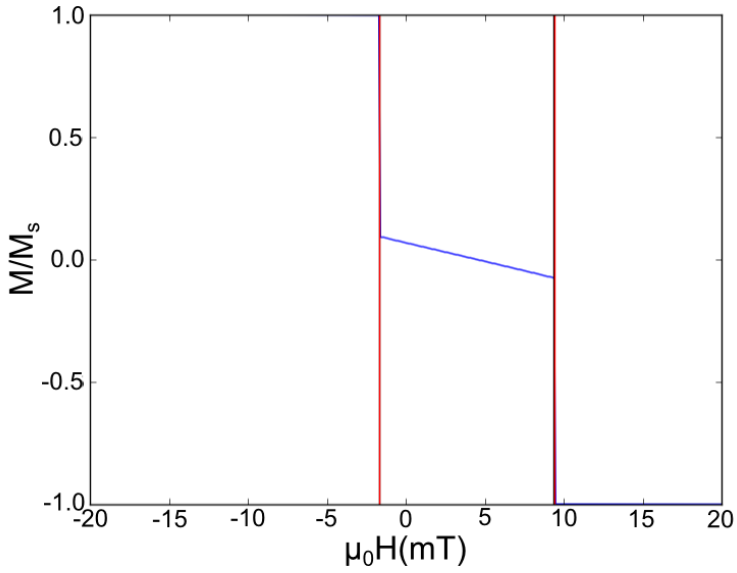

Fig. C.35 Fit used to find the values of K_s and the domain wall energy of the transport loop collected from the secondary 20nm sample, S411, with 50V applied to the transducer corresponding to strain of $[4.225 \times 10^{-4} \pm 5.57 \times 10^{-6}]$. The cost of this fit is 0.093×10^{-1}.

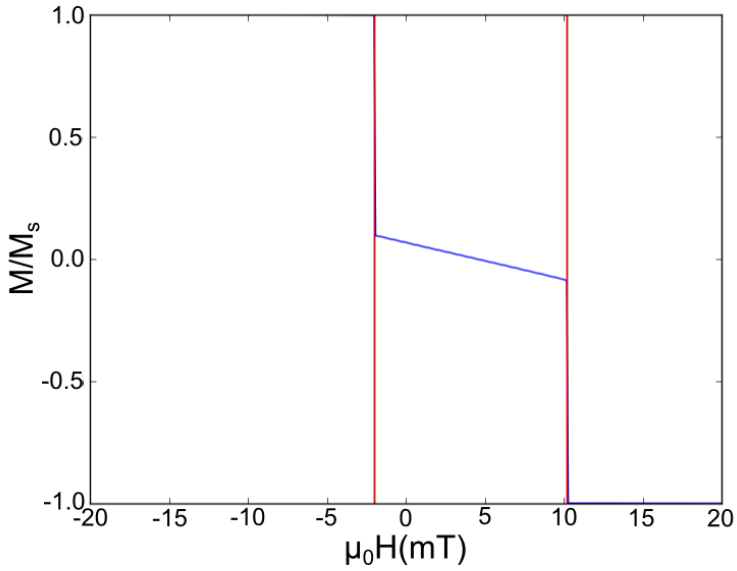

C.4 Fits for the secondary 30nm sample, S410

Fig. C.36 Fit used to find the values of K_s and the domain wall energy of the transport loop collected from the secondary 30nm sample, S410, with -30V applied to the transducer corresponding to strain of $[-1.56 \times 10^{-4} 6.07 \pm \times 10^{-5}]$. The cost of this fit is 11.589×10^{-1}.

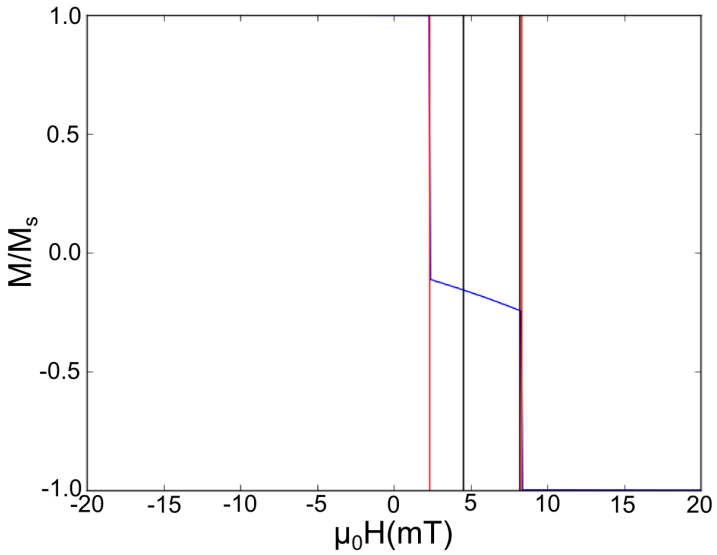

Fig. C.37 Fit used to find the values of K_s and the domain wall energy of the transport loop collected from the secondary 30nm sample, S410, with -25V applied to the transducer corresponding to strain of $[-1.30\times10^{-4}\pm5.06\times10^{-5}]$. The cost of this fit is 10.407×10^{-1}.

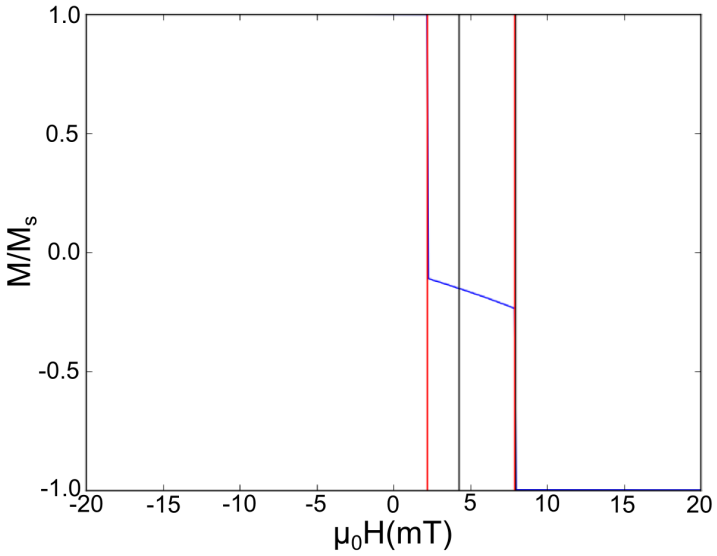

Fig. C.38 Fit used to find the values of K_s and the domain wall energy of the transport loop collected from the secondary 30nm sample, S410, with -20V applied to the transducer corresponding to strain of $[-1.04\times10^{-4}\pm4.05\times10^{-5}]$. The cost of this fit is 14.166×10^{-1}.

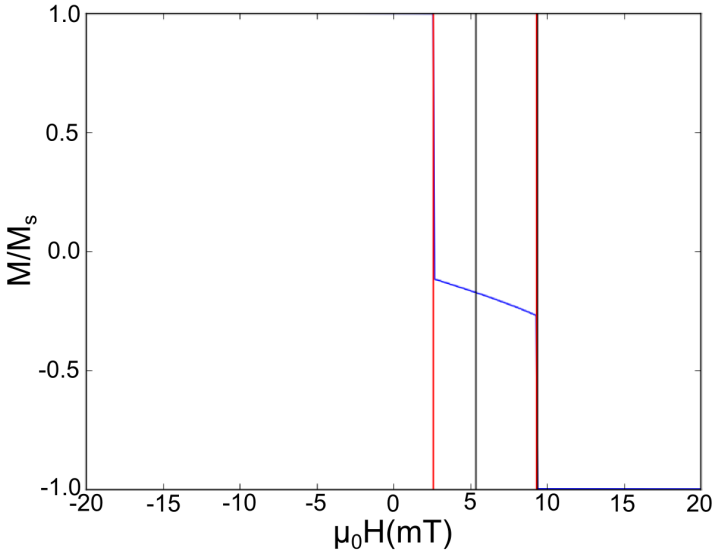

Fig. C.39 Fit used to find the values of K_s and the domain wall energy of the transport loop collected from the secondary 30nm sample, S410, with -15V applied to the transducer corresponding to strain of $[-0.78\times10^{-4}\pm3.04\times10^{-5}]$. The cost of this fit is 11.752×10^{-1}.

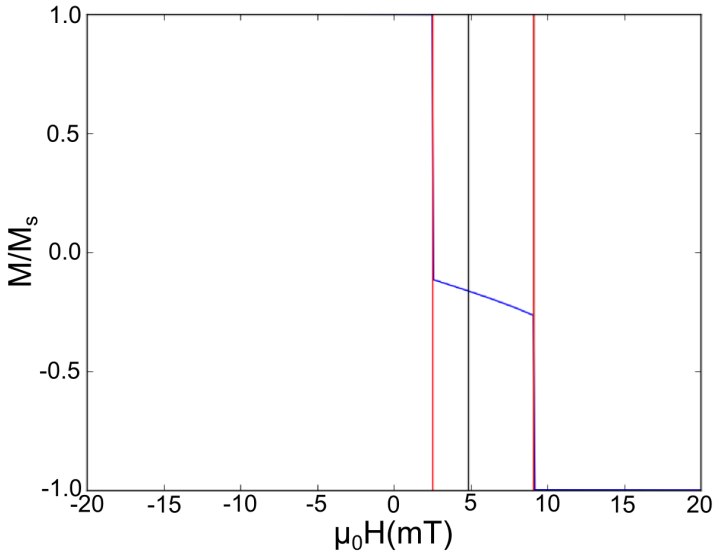

Fig. C.40 Fit used to find the values of K_s and the domain wall energy of the transport loop collected from the secondary 30nm sample, S410, with -10V applied to the transducer corresponding to strain of $[-0.52\times10^{-4}\pm2.02\times10^{-5}]$. The cost of this fit is 12.170×10^{-1}.

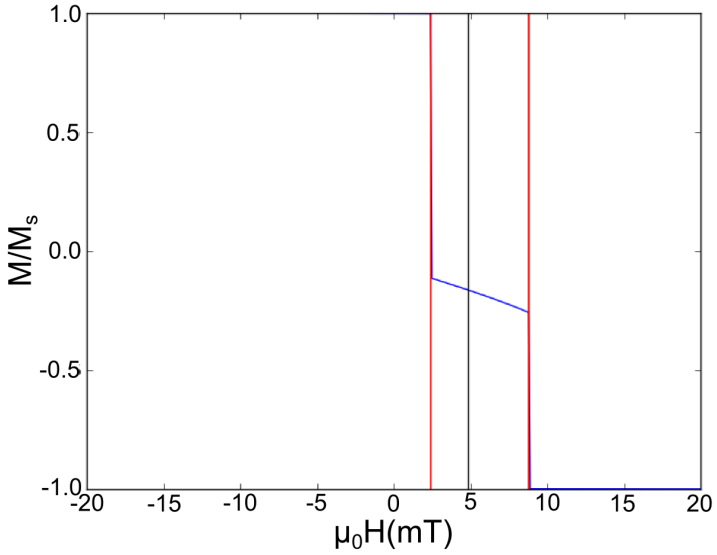

Fig. C.41 Fit used to find the values of K_s and the domain wall energy of the transport loop collected from the secondary 30nm sample, S410, with -5V applied to the transducer corresponding to strain of $[-0.26 \times 10^{-4} \pm 1.01 \times 10^{-5}]$. The cost of this fit is 6.415×10^{-1}.

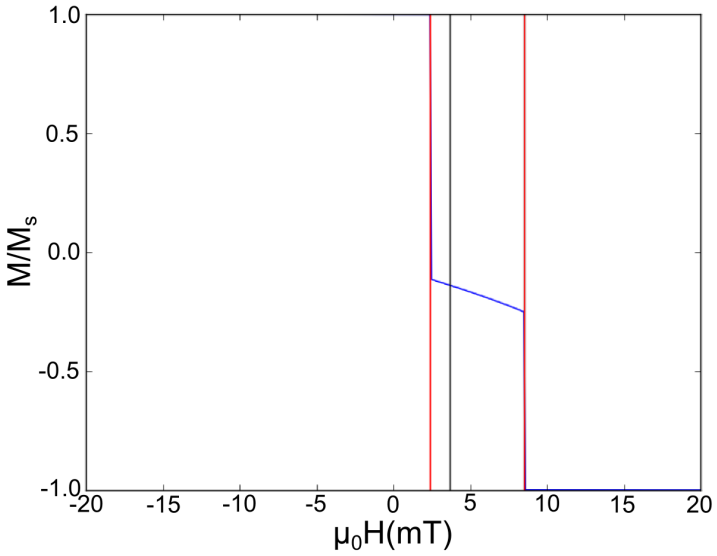

Fig. C.42 Fit used to find the values of K_s and the domain wall energy of the transport loop collected from the secondary 30nm sample, S410, with 0V applied to the transducer corresponding to strain of 0. The cost of this fit is 12.089×10^{-1}.

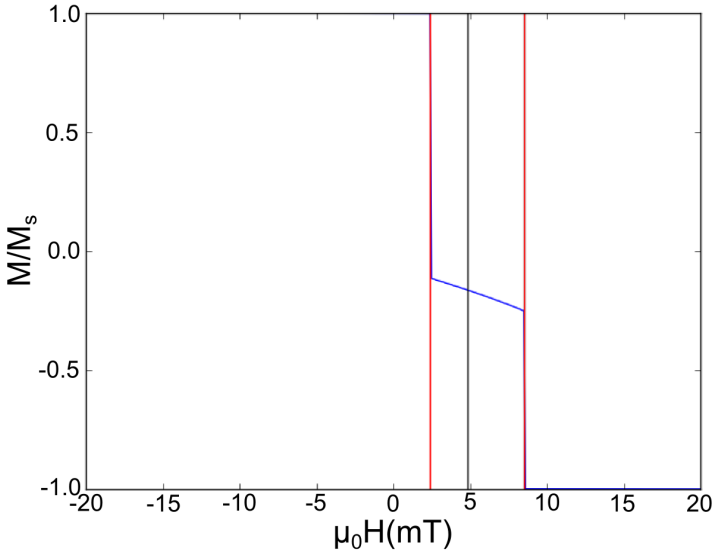

Fig. C.43 Fit used to find the values of K_s and the domain wall energy of the transport loop collected from the secondary 30nm sample, S410, with 5V applied to the transducer corresponding to strain of $[0.26 \times 10^{-4} \pm 1.01 \times 10^{-5}]$. The cost of this fit is 4.511×10^{-1}.

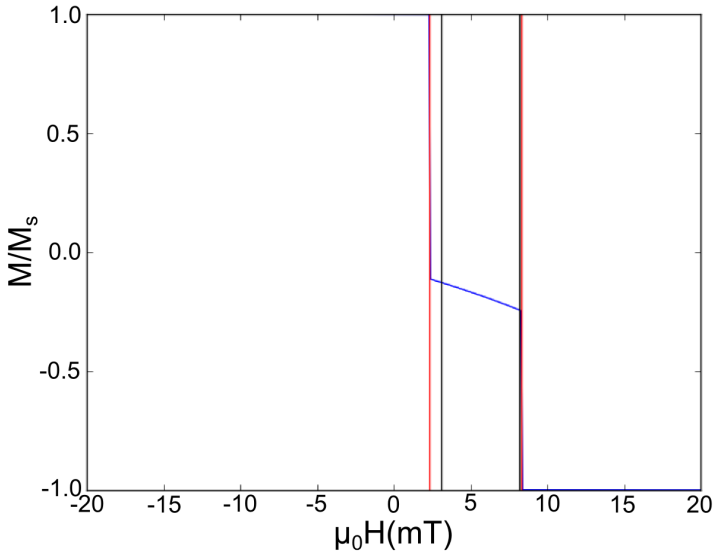

Fig. C.44 Fit used to find the values of K_s and the domain wall energy of the transport loop collected from the secondary 30nm sample, S410, with 10V applied to the transducer corresponding to strain of $[0.52 \times 10^{-4} \pm 2.02 \times 10^{-5}]$. The cost of this fit is 3.674×10^{-1}.

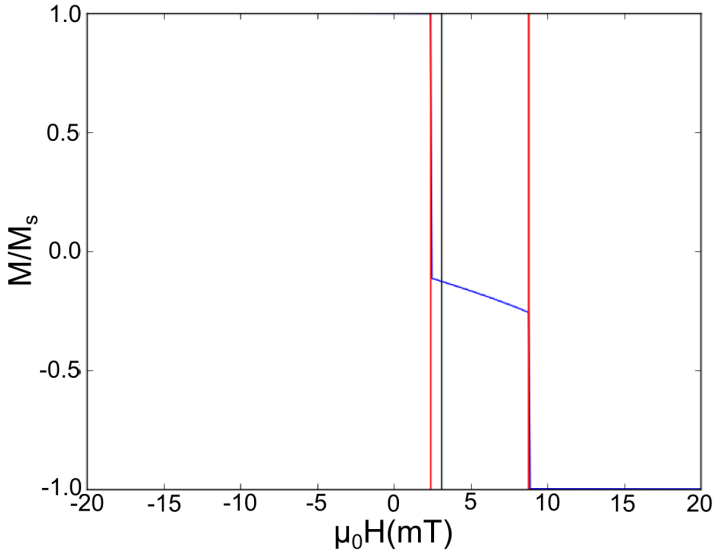

Fig. C.45 Fit used to find the values of K_s and the domain wall energy of the transport loop collected from the secondary 30nm sample, S410, with 15V applied to the transducer corresponding to strain of $[0.78 \times 10^{-4} \pm 3.04 \times 10^{-5}]$. The cost of this fit is 0.011×10^{-1}.

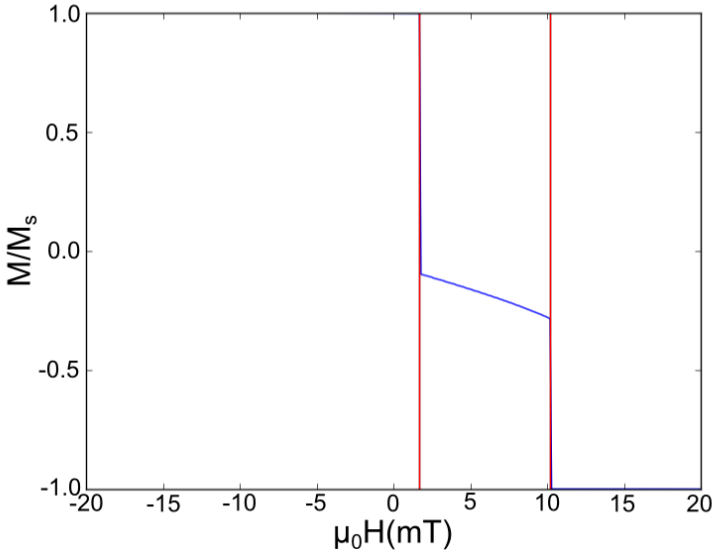

Fig. C.46 Fit used to find the values of K_s and the domain wall energy of the transport loop collected from the secondary 30nm sample, S410, with 20V applied to the transducer corresponding to strain of $[1.04 \times 10^{-4} \pm 4.05 \times 10^{-5}]$. The cost of this fit is 0.178×10^{-1}.

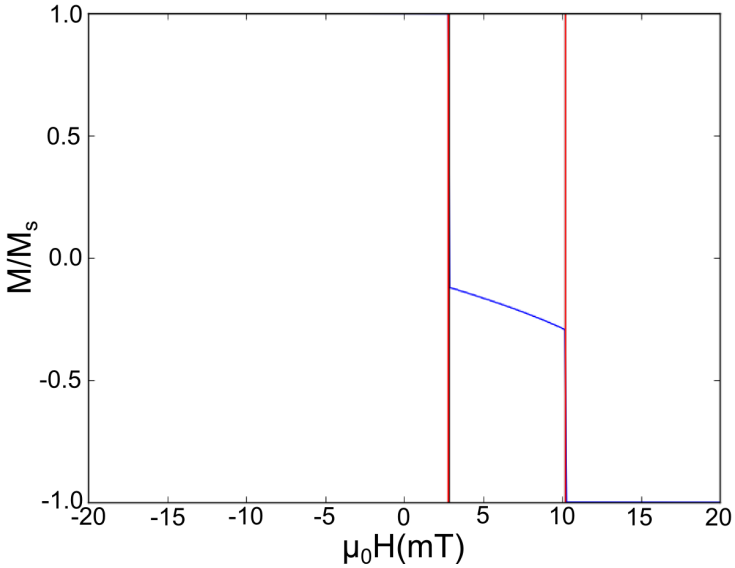

Fig. C.47 Fit used to find the values of K_s and the domain wall energy of the transport loop collected from the secondary 30nm sample, S410, with 25V applied to the transducer corresponding to strain of $[1.30 \times 10^{-4} \pm 5.06 \times 10^{-5}]$. The cost of this fit is 0.496×10^{-1}.

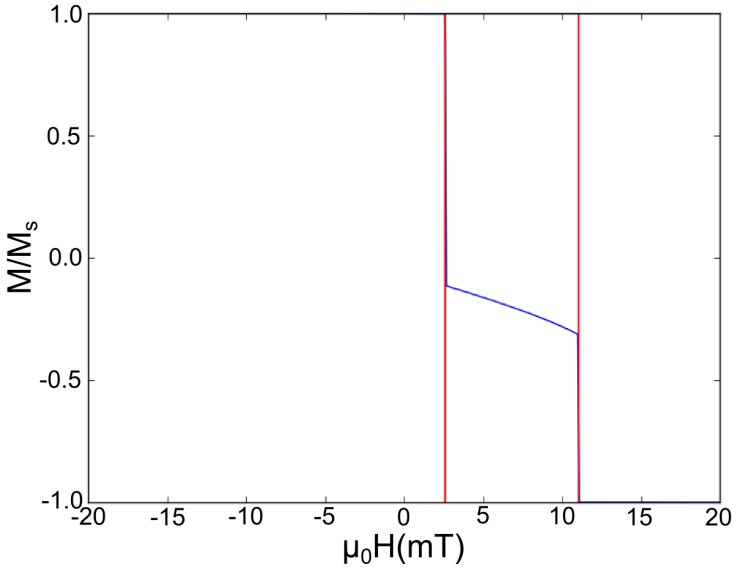

Fig. C.48 Fit used to find the values of K_s and the domain wall energy of the transport loop collected from the secondary 30nm sample, S410, with 30V applied to the transducer corresponding to strain of $[1.56 \times 10^{-4} \pm 6.07 \times 10^{-5}]$. The cost of this fit is 0.333×10^{-1}.

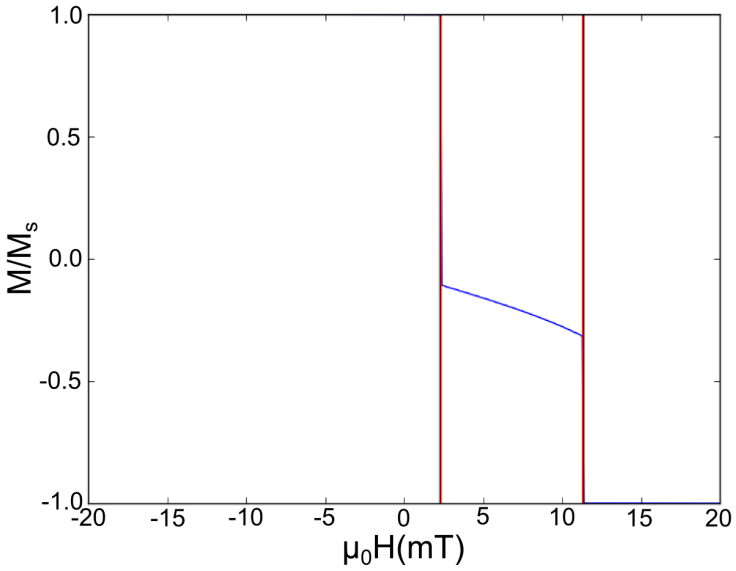

Fig. C.49 Fit used to find the values of K_s and the domain wall energy of the transport loop collected from the secondary 30nm sample, S410, with 35V applied to the transducer corresponding to strain of $[1.82 \times 10^{-4} \pm 7.08 \times 10^{-5}]$. The cost of this fit is 0.167×10^{-1}.

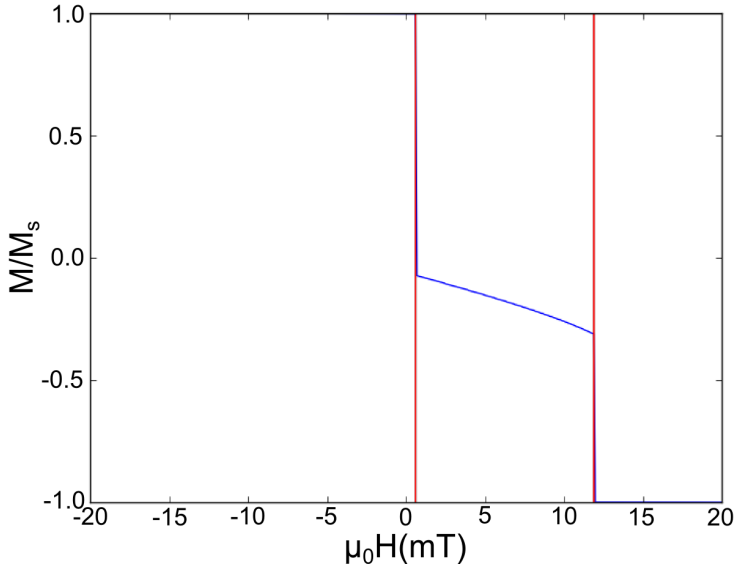

Fig. C.50 Fit used to find the values of K_s and the domain wall energy of the transport loop collected from the secondary 30nm sample, S410, with 40V applied to the transducer corresponding to strain of $[2.08 \times 10^{-4} \pm 8.10 \times 10^{-5}]$. The cost of this fit is 0.166×10^{-1}.

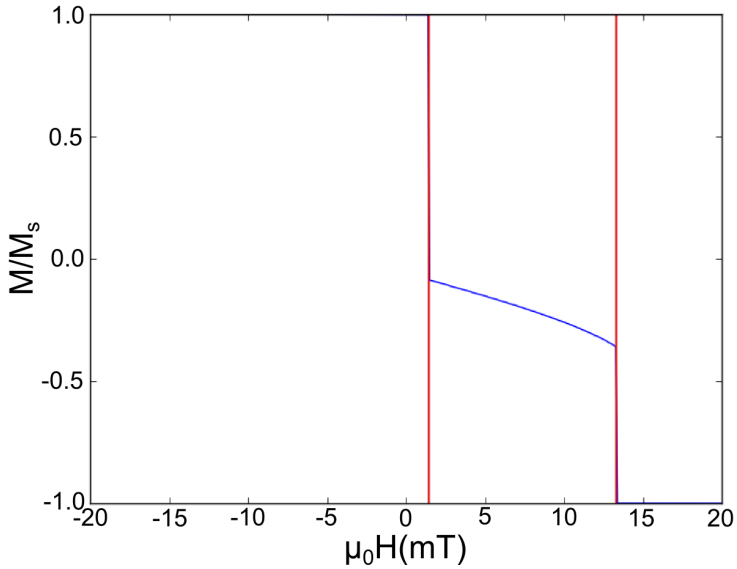

Fig. C.51 Fit used to find the values of K_s and the domain wall energy of the transport loop collected from the secondary 30nm sample, S410, with 45V applied to the transducer corresponding to strain of $[2.34 \times 10^{-4} \pm 9.11 \times 10^{-5}]$. The cost of this fit is 0.415×10^{-1}.

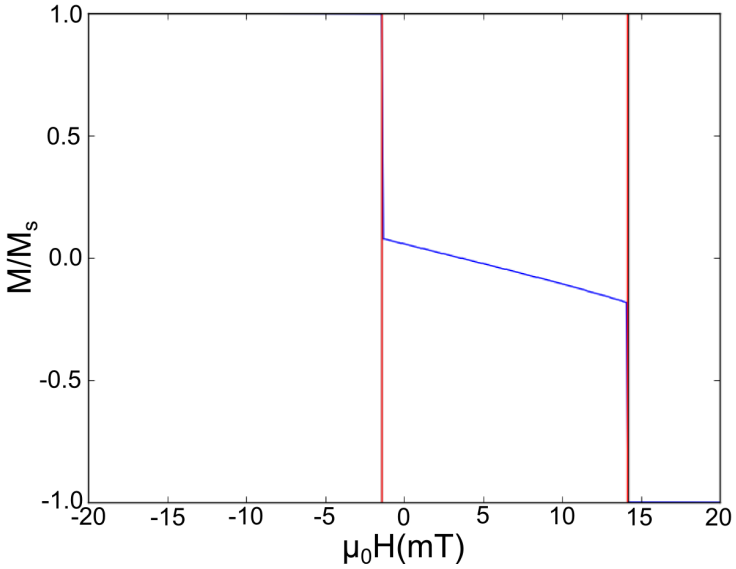

Fig. C.52 Fit used to find the values of K_s and the domain wall energy of the transport loop collected from the secondary 30nm sample, S410, with 50V applied to the transducer corresponding to strain of $[2.60 \times 10^{-4} \pm 1.012 \times 10^{-4}]$. The cost of this fit is 0.410×10^{-1}.

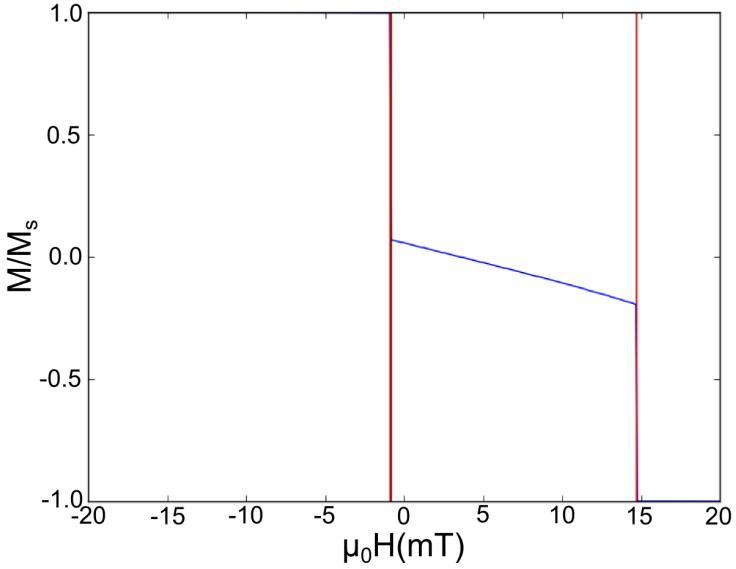

Appendix D

Time resolved simulations consistency checks

The results of various simulations used to check the effects of altering the angle of incidence of the magnetic field pulse and the chirality of the magnetic vortex state are detailed here.

In order to check for further asymmetries in the results of the simulations the y component of the magnetisation with the uniaxial anisotropy included was subjected to the same 3D Fourier transform process, the results of which are shown in figure D.1.

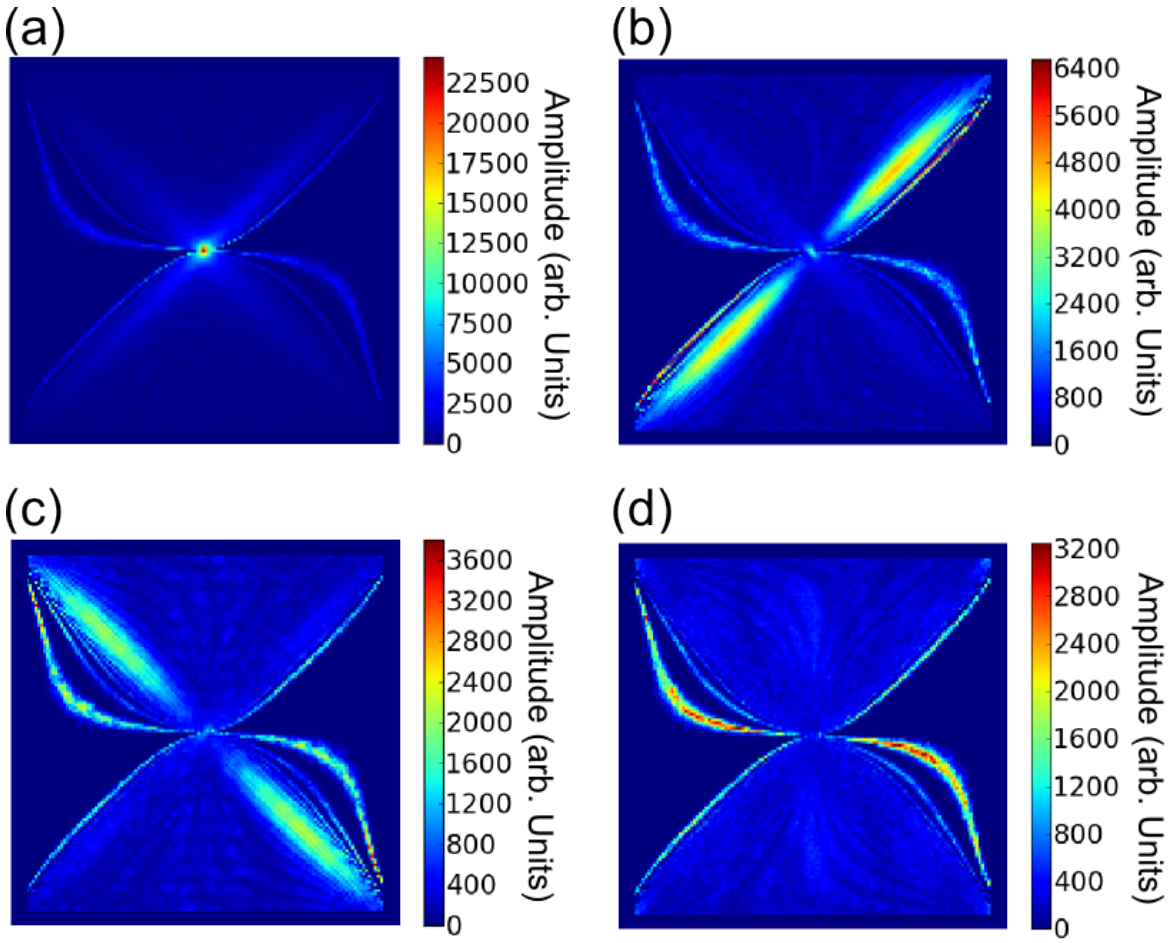

Fig. D.1 Fourier transformation heat maps for the magnetisation of a 500nm square in the y direction when a magnetic field pulse of 1mT was used to excite the system. Shown are the heatmaps with windows of 200MHz and central frequencies of a) 300MHz, b) 5GHz, c) 6.5GHz and d) 12.3GHz.

This shows that the simulations display 90^o symmetry meaning that the y component of the magnetisation behaves exactly the same as the x-component. We would expect this since the cubic anisotropy lies in both the x and the y directions making the two directions symmetrical. We are also looking at the same waves we saw in figure 6.19 meaning we would not expect any asymmetry.

In order to test whether any anisotropy was introduced by changing the orientation of the exciting magnetic field pulse the magnitude of the pulse was reversed to act in the negative [010] direction. The results of this test are shown in figure D.2.

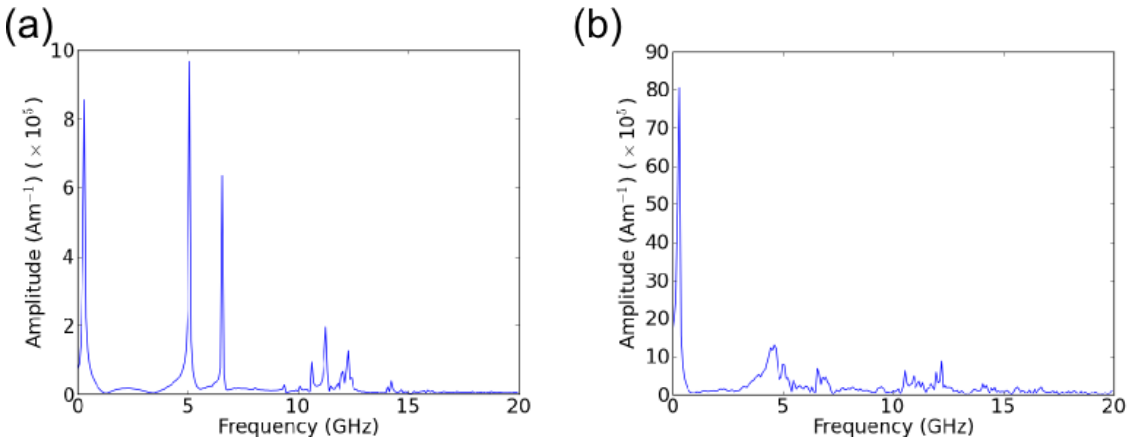

Fig. D.2 Fourier transform profile of the x component of magnetisation of a 500nm square when subjected to a a)-1mT and b)-25mT exciting pulse in the [010] direction.

The frequency profile is identical as the frequency profile produced when a positive magnetic field pulse was used to excite motion and this pattern continued into the spatial frequency maps of the samples shown in figure D.3.

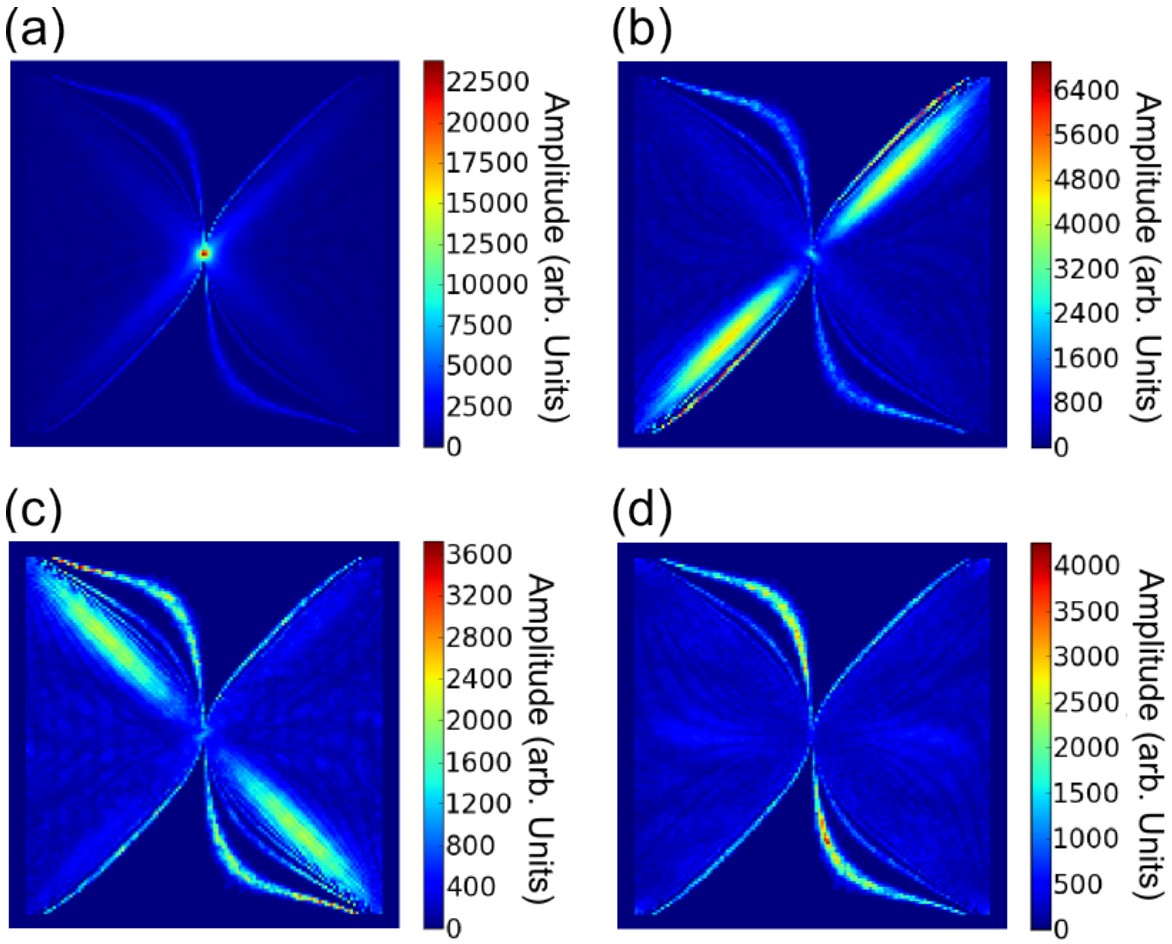

Fig. D.3 Fourier transformation heat maps for the magnetisation of a 500nm square in the x direction when a magnetic field pulse of -1mT was used to excite the system. Shown are the heatmaps with windows of 200MHz and central frequencies of a) 300MHz, b) 5GHz, c) 6.5GHz and d) 12.3GHz.

This produced the same results as our initial simulations indicating reflective symmetry so the pulse was applied in the [100] direction in order to investigate the 90^o symmetry of the system, the results are shown in figure D.4.

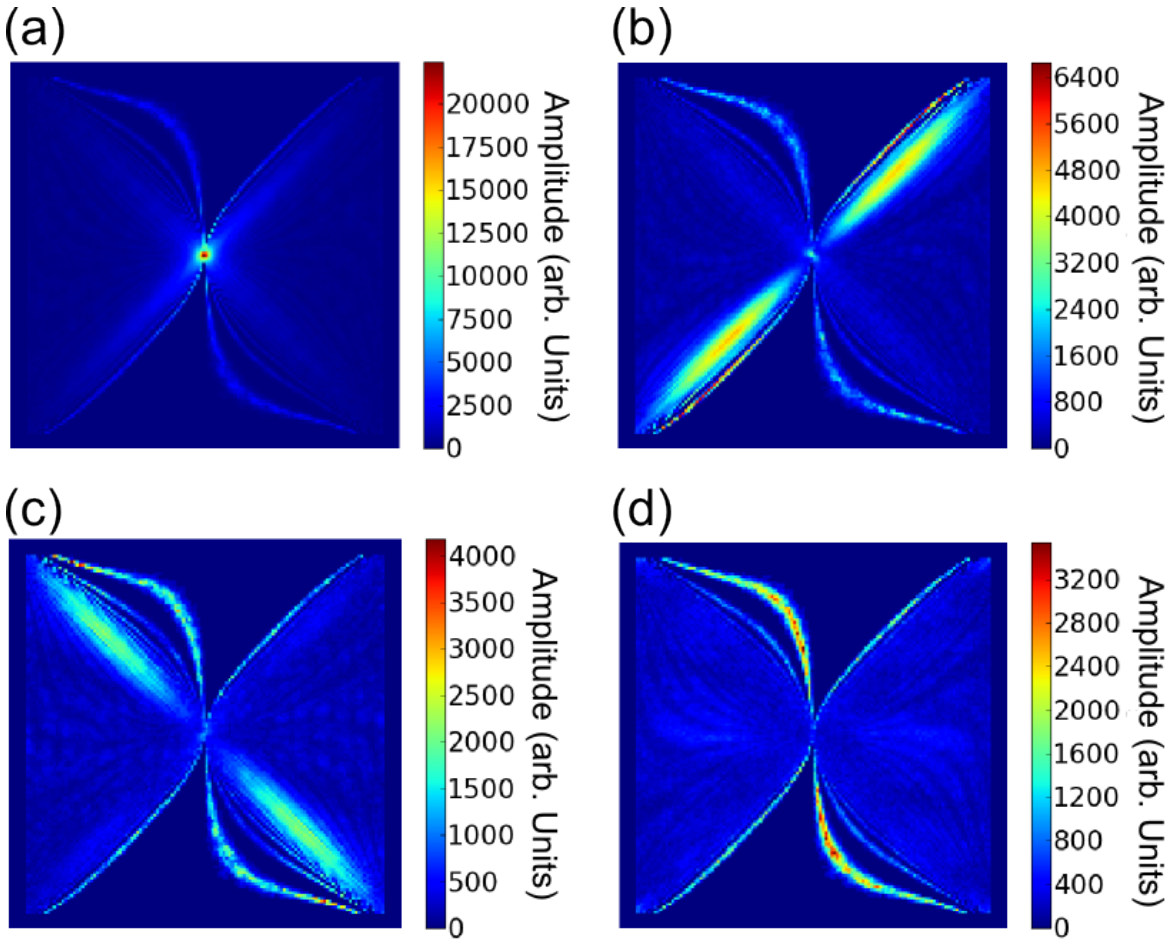

Fig. D.4 Fourier transformation heat maps for the magnetisation of a 500nm square in the x direction when a magnetic field pulse of 1mT applied in the [100] direction was used to excite the system. Shown are the heatmaps with windows of 200MHz and central frequencies of a) 300MHz, b) 5GHz, c) 6.5GHz and d) 12.3GHz.

The magnetic field pulses applied in the [100] direction produced identical results as found when the pulse was applied in the [010] direction indicating 90^o symmetry. Reversal of the chirality of the domain pattern was also studied in order to investigate the chiral symmetry of the system. Initial magnetisation for this simulation is shown in figure D.5.

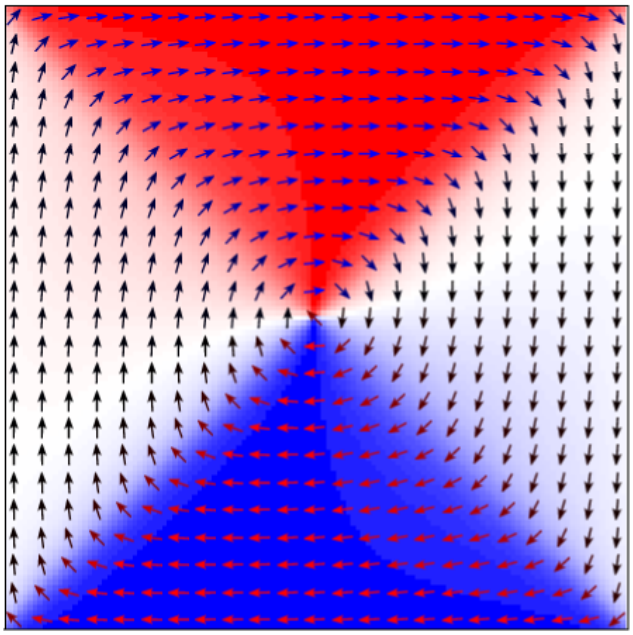

Fig. D.5 Starting magnetisation for simulation with the magnetisation reversed. The arrows indicate the direction of the magnetisation and the colours are set to indicate the colours shown in the images of the simulation in progress.

This led to the oscillatory modes behaving as previously measured as shown in figure D.6 indicating the system exhibits chiral symmetry.

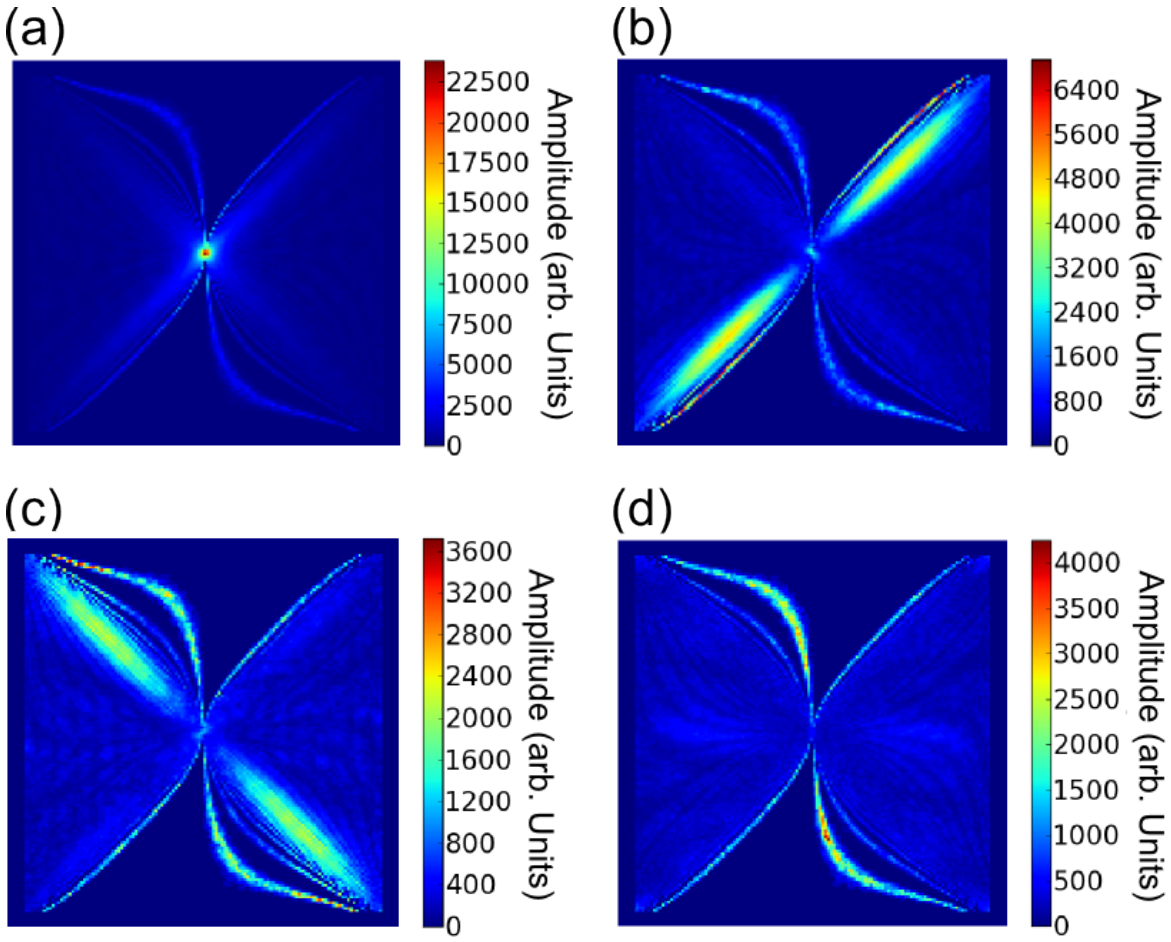

Fig. D.6 Fourier transformation heat maps for the magnetisation of a 500nm square in the x direction when a magnetic field pulse of 1mT in the [010] direction was used to excite the system. The initial magnetisation was reversed with respect to the starting magnetisation used to produce the simulations performed to produce the heatmaps shown in figures 6.19, D.1, D.3 and D.4. Shown are the heatmaps with windows of 200MHz and central frequencies of a) 300MHz, b) 5GHz, c) 6.5GHz and d) 12.3GHz.

Appendix E

Core finding program

In order to track the way cores moved over the course of a given video two programs had to be produced. The first was a program to find the cores within any given image and the second was a program designed to track their location as they moved in time. The cores were found by first of all finding the Sobel operator of the image in x and y. The result shows the areas in which there are large transitions in the intensity of the image. An example of the Sobel operator is shown in figure E.1.

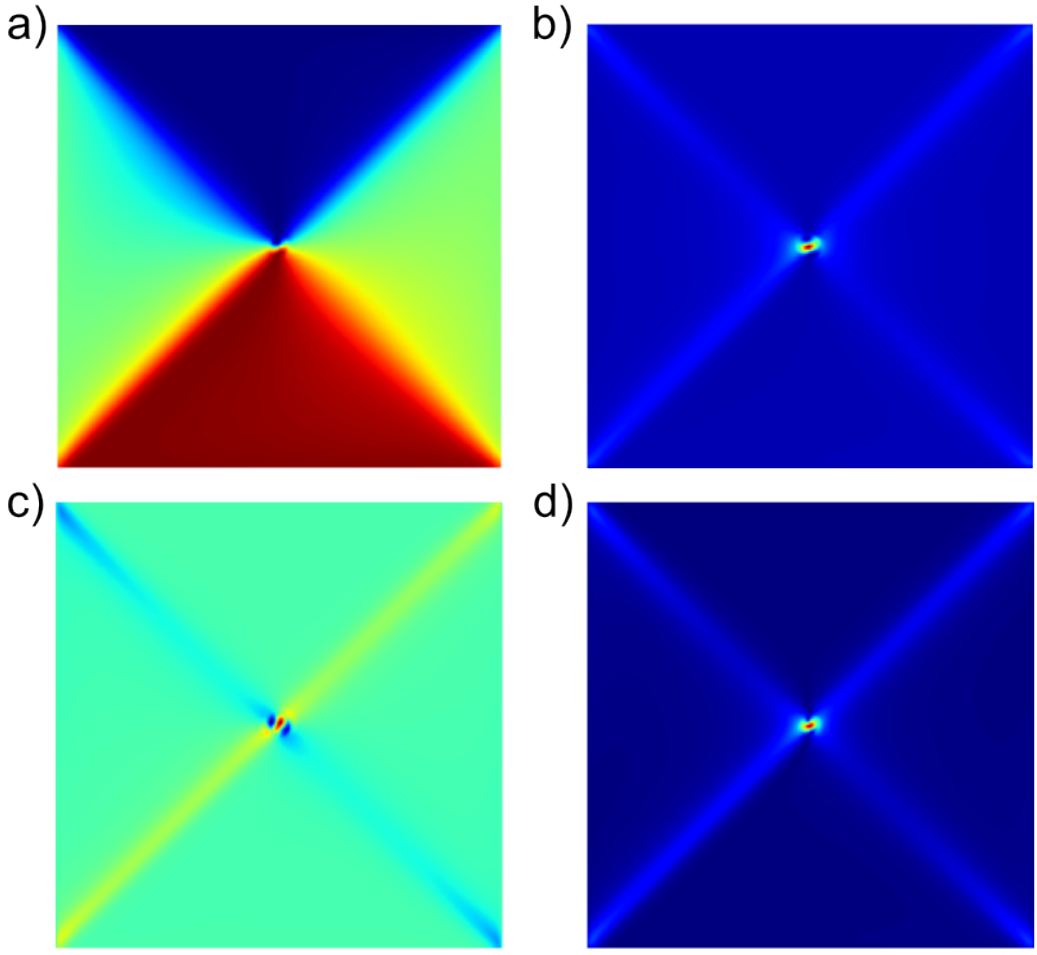

Fig. E.1 Demonstration of the Sobel operator. Shown in a) is the domain structure of a 500nm square in which the x component of the magnetisation is demonstrated with red being left to right and blue being right to left. The Sobel operator has been applied in the x direction in b) and in the y direction in c). Panel d) shows the magnitude of the Sobel operator demonstrating the high magnitude of the core in contrast to the Sobel magnitude of the domain walls.

By using the Sobel operator we can detect only the cores since whilst the domain walls are areas of high contrast in intensity the contrast is unidirectional. The Sobel operator overcomes this problem since the cores exhibit much higher intensity since the contrast is in multiple directions. The cores now show up as areas of high intensity but some of these areas contain multiple pixels which would read as multiple cores in close proximity if we were to simply locate the high intensity pixels. In order to avoid this we use a cluster finding process of increasing squares. This method was chosen since it does not require any human intervention beyond setting what counts as a point, other clustering procedures need to know in advance how many clusters they're looking for or else how dense a cluster needs to be before it can be considered such. The method of increasing squares avoids these problems however it is weak in data sets with overlapping clusters, this will not be a problem in analysing our data however.

First a list of all the high intensity pixels is complied. The first element of this list is then considered a 'core' object and a box is drawn around it 1 pixel in every direction meaning it is surrounded by a 9 pixel box. If these 9 pixels addresses appear in our list of the high intensity pixels that pixel is said to be part of the core and is moved from the list of high intensity pixels and onto a list of pixels within this core. The box is then redrawn with a width 2 pixels larger than the one before it. If the new box contains more high intensity pixels than the one before it then the box grows again and the check is repeated. If however the new box contains no more pixels than the box which preceded it the core is defined as containing the pixels already found and the box stops growing, this core is then added to a list of cores. These 'core' objects hold the upper and lower limits of the x and y positions of the pixels within them, the mean position of the high intensity pixels within them, the total volume of the core and finally the time step of the frame in which the core was captured (this will gain relevance when we track the cores over time). The program then moves to the next high intensity pixel in its high intensity pixel list and repeats the operation until all the high intensity pixels have been assigned to cores. This process is illustrated in figure E.2.

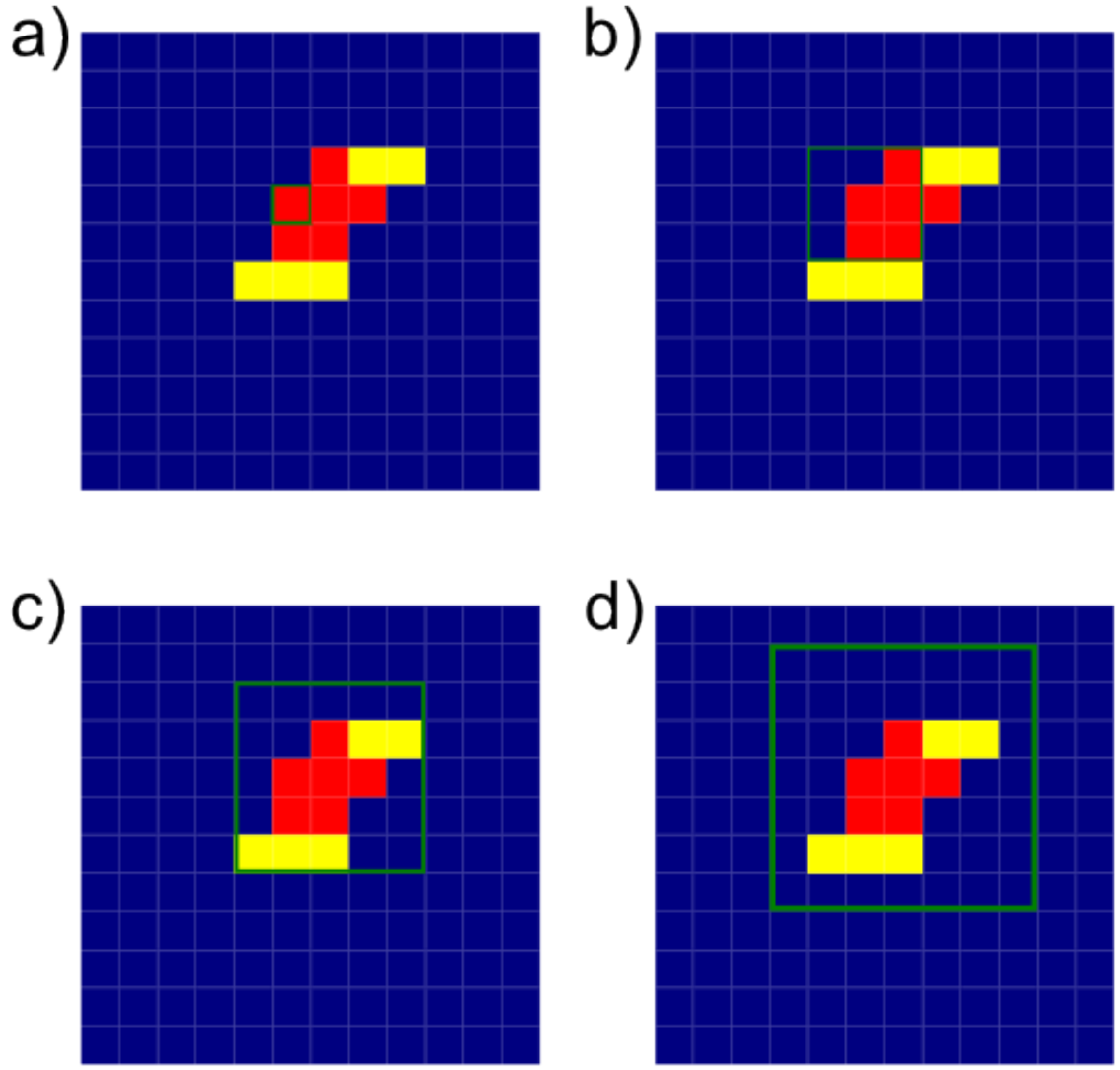

Fig. E.2 Demonstration of the increasing squares methods of tracking clusters. in a) a high intensity pixel has been identified and a square has been drawn around it. In b) the square has expanded to 1 square from the central pixel in every direction. In c) the square has expanded again by another square in every direction. The intensity need to count as a high intensity pixel is set by the user so the yellow squares may or may not count as high intensity pixels depending on the user's preference. In this example the yellow squares are not intense enough to be counted. Finally in d) the square contains no more squares than the square in c) so the cluster is said to include only the squares within the square and the core is added to the list of cores. The program will now move onto the next high intensity pixel not identified as part of a pre-existing core.

The cores were then tracked as a function of time as they moved throughout the simulation. This was done by breaking the problem down and tracking the core's movements from frame to frame. In order to describe this process we will look at two images which occur consecutively. We will refer to these images as frame 1 and frame 2. The difference in location between each core in frame 1 and each core in frame 2 is found by equation E.1 in which the distance between the cores is RMSD. The core in frame 1 in equation E.1 is at the position (x_1, y_1) and the core in frame 2 is at position (x_2, y_2).

$$RMSD = \sqrt{(x_2 - x_1)^2 + (y_2 - y_1)^2} \tag{E.1}$$

The program then looks for the frame 1 core, frame 2 core pairing that produces the lowest RMSD between the two cores, if this distance is lower than some pre-set upper limit then the core in frame 2 is defined as the core in frame one after one timestep has elapsed. The position of the core in frame 2 is added to the list of positions of core 1. If there are no cores within the upper limit of the core in frame 1 then it is assumed that the core has decayed and the tracking for that core is ended. If there are multiple cores equidistant from the core in frame 1 then the core is assumed to have split. The list of previous core objects is duplicated and the cores in frame 2 are added to both lists. This process is then repeated for all the frames in the sequence in order to track the movement of the cores over time. The process of finding the distance between the cores from one frame to the next is demonstrated in figure E.3.

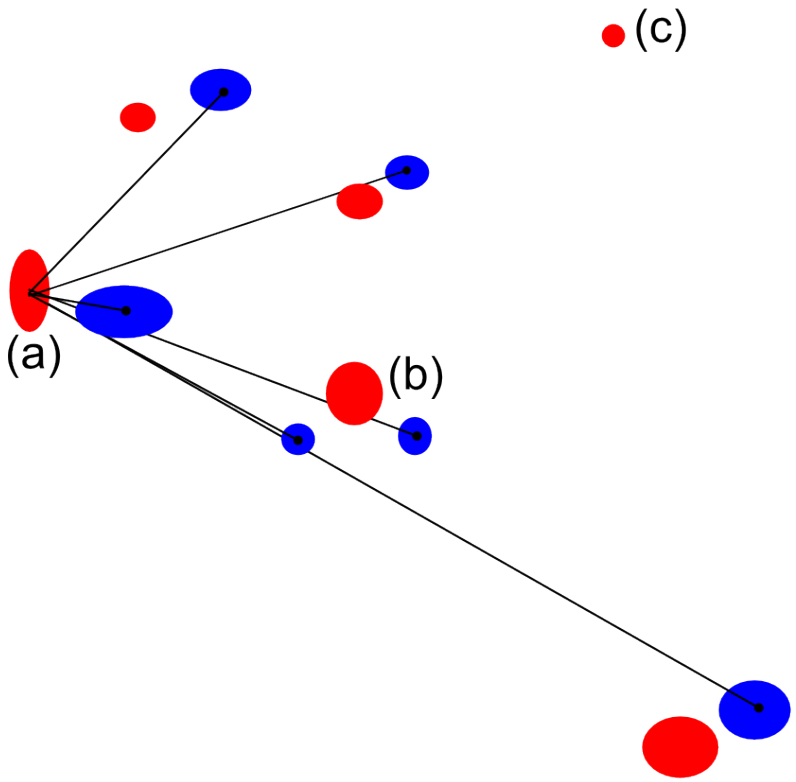

Fig. E.3 Demonstration of the core tracking procedure. Shown in red are the cores in frame 1 and shown in blue are the cores in frame 2. The black lines represent the distance between the core in frame 1 at (a), these line will be drawn for each of the cores in frame 1 in turn so that the progress of each core can be monitored. Shown at (b) is an instance where a core in frame 1 has split into two cores in frame 2. In this instance the list tracking the core in frame 1 will be duplicated so that the core tracking for the two new cores can continue. The core in frame 1 at (c) has died. The list tracking its progress will cease to be appended to in frames 2 onwards. If the a core appears in the region with a timeframe defined by the user later in the simulation the tracking will continue as before.